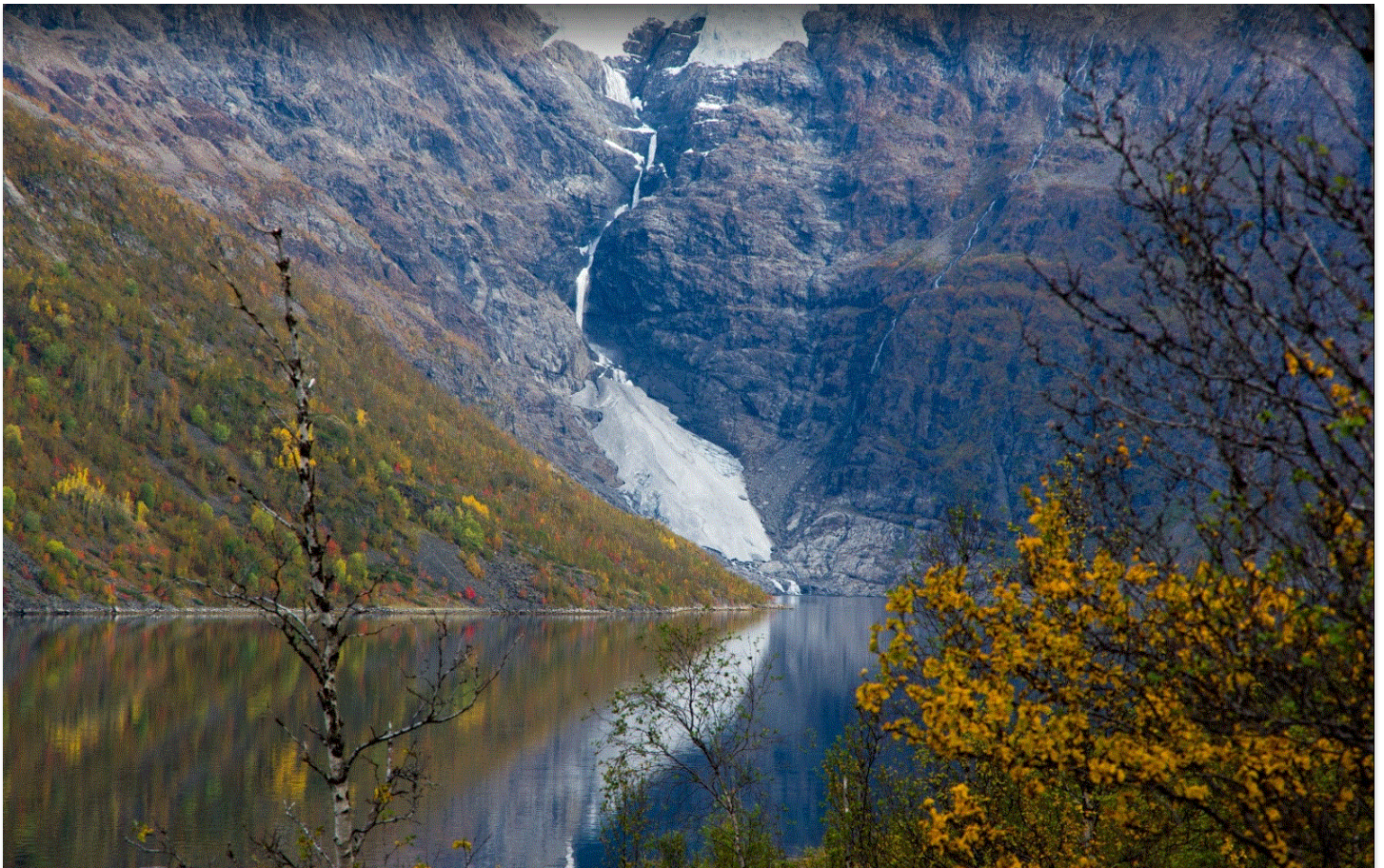Faculty of Science and Technology

Department of Geosciences

Sedimentary processes and paleoenvironment reconstructions in fjords comprising the Bergsfjord peninsula, Northern Norway

—

Christine Tømmervik Kollsgård
GEO-3900 Master thesis in Marine Geology
May 2018

Abstract

Low-resolution bathymetry, high-resolution seismic data (chirp) and multi-proxy analyses of three sediment gravity cores were integrated to study sedimentary processes with the purpose of reconstructing paleoenvironments in the three north Norwegian fjords Øksfjorden, Bergsfjorden and Jøkelfjorden since the last glacial. These three fjords are located on the Bergsfjorden peninsula and surround the ice cap Øksfjordjøkelen.

The multi-proxy analyses of the sediment cores included measurements of the physical properties (e.g. wet-bulk density, magnetic susceptibility), X-radiography, X-ray fluorescence (XRF) core scanning, grain-size distribution analyses and visual descriptions of the sediment cores.

The results suggest that four sedimentary processes occurred in the fjords: glacier-proximal sedimentation with repeated changes of physical conditions in a glacimarine environment, suspension settling in an open-marine environment with occasional ice rafting, mass wasting, as well as deltaic processes.

Furthermore, the results suggest that Bergsfjorden was deglaciated prior to c. 11,090 cal. yrs. BP and that a large-scale mass-transport event took place shortly before this time. The glacier Øksfjordjøkelen has terminated in Jøkelfjorden during the last at least 8.7 ka cal. yrs. BP. An advance of Svartfjelljøkelen and Øksfjordjøkelen occurred presumably around 8.2 ka cal. yrs. BP. Glacial activity was very reduced or absent in Bergsfjorden between 7.3 and 5.0 ka cal. yrs. BP in Bergsfjorden. Relatively steady sedimentary environments are observed after 4.2 ka cal. yrs. BP in Bergsfjorden, 5.1 ka cal. yrs. BP Øksfjorden and 5.0 ka cal. yrs. BP in Jøkelfjorden.

Acknowledgements

Table of Contents

1   Introduction

1.1   Motivation

The climate has naturally been varying throughout the history of the Earth (e.g. Friis-Christensen & Lassen, 1991). Change of movements in the solar system, tectonic drifting, the composition of the atmosphere and oceans, and the distribution of the hydrosphere all affect the global climate (e.g. Ruddiman, 2007). However, studies of the climate for the past century indicate an anthropogenic induced acceleration of change in the climate configuration (IPCC, 2014). Effects of increasing amounts of greenhouse gases released into the atmosphere by humans enhance the natural variations of the climate (e.g. Jacoby & D'Arrigo, 1989; Bradley & Jonest, 1993; Francey et al., 2013). The oceans are acidifying (e.g. Gattuso et al., 2011), the permafrost is thawing (e.g. Overpeck et al., 1997), and the amounts of precipitation, storms and floods are increasing (Fowler & Hennessy, 1995) leading to increased secondary effects such as mass wasting and tsunamis (Crozier, 2010). Melt of glaciers and ice sheets due to increased atmospheric temperatures contribute to sea level rise (Overpeck et al., 1997). In order to approach the climatic issues of the future, predictions of feedback effects are needed (e.g. Jakobsson et al., 2014). There is a demand on high-resolution paleoclimatic reconstructions (Bradley & Jonest, 1993) as a means to better understand the climate of the past and help predict future climate change (e.g. Raymo, 1994). The marine sediment cores analysed in this thesis are high-resolution records that tell about how the paleo-environment varied in the fjords of the Bergsfjord peninsula after the latest deglaciation.

1.2   Background
Climatic variations followed the Last Glacial Maximum (LGM), where the ice masses covering northern Norway reached its maximum extent around 19,000 cal. yrs. BP (Winsborrow et al., 2010). Glaciers are largely influenced by the local climate, and react fast to changes (Benn & Evans, 2014). Fjords trap relatively undisturbed sediment inhering organic material that allow for accurate dating. These deposits provide sedimentary records with relatively high temporal resolution, reflecting both local terrestrial and marine processes (Syvitski et al., 1987). Marine sediment cores retrieved from fjords are stratigraphic archives providing data available for proxy-analysis. Interpretations of these give insight in climatic and environmental variations of the past (Cottier et al., 2010). Hence, Holocene fjord records may provide tools applicable for climate models (Howe et al., 2010).

The study area in this thesis is the Bergsfjord peninsula (Figure 1). Today, three ice caps (Øksfjordjøkelen, Svartfjelljøkelen and Lansgfjelljøkelen) exist at the peninsula. These are assumed to have been decoupled from the Fennoscandian Ice Sheet during Younger Dryas (Sollid et al., 1973). Studies suggest that Øksfjordjøkelen had marine terminating outlets at the heads of surrounding fjord at that time

(Evans et al., 2002). Most probably, Øksfjordjøkelen, the largest of the glaciers, had a rapid response to the cooling in the Younger Dryas stadial, leaving traces in the terrain as it advanced towards the fjord heads (B. R. Rea & Evans, 2007). Continuous records of the climatic fluctuations following the deglaciation is expected to be preserved in the sediment deposited in the fjords comprising this study: Øksfjorden, Bergsfjorden and Jøkelfjorden.

Previous studies in the area include mapping of glacier extent (L. M. Andreassen et al., 2012; Whalley & Parkinson, 2016), dating and correlations of terminal moraines (Andersen, 1968; Winsborrow et al., 2010; Stokes et al., 2014), reconstruction of the glacier extent of Øksfjordjøkelen (Evans et al., 2002; B. R. Rea & Evans, 2007) and Svartfjelljøkelen (Eeg, 2012). Eeg suggest little or no glacigenic sediment input into the Bergsfjord lake between 7000 and 5200 cal. yrs. BP.

1.3   Objectives

The overall goal of the project is to investigate sedimentary processes in Øksfjorden, Bergsfjorden and Jøkelfjorden. The study is based on the analyses of high-resolution seismic profiler data combined with three sediment cores, one from each fjord, and the purpose is to:

1) Reconstruct the post-glacial palaeo-environmental conditions of the ice cap Øksfjordjøkelen located in the drainage areas of the three fjords.

2) Identify the sedimentary processes affecting the three fjords and compare thes

2 Study area

2.1 Physiographic setting

The Bergsfjorden peninsula is located immediately north of 70° N at the border of Troms and Finnmark Counties in Northern Norway (Figure 1). There are several fjords in the area. This study comprise of three of them; (1) Øksfjorden (70°10'N, 22°16'E) a 28 km long fjord with an inner orientation from E-W before turning S-N in the outer part; (2) Bergsfjorden (70°17'N, 21°48'E), a SSW-NNE oriented, 12 km outer part of Langfjorden and; (3) Jøkelfjorden (70°4'N, 21°58'E) a 16 km long fjord oriented NNE-SSW in the inner part and NEE-SWW in the outer (Figure 1). Three ice caps are located at the peninsula; Øksfjordjøkelen (70°9'N, 22°4'E), Svartfjelljøkelen (70°14'N, 21°57'E) and Langfjordjøkelen (70°7'N, 21°43'E), covering approximately 50 km^2 (NVE, 2006; L. M. Andreassen et al., 2012). Øksfjordjøkelen lies in the catchment area of all the three fjords.

The region is high relief mountainous with peaks and arêtes reaching higher than 1000 m a.s.l. It includes several fjords with depths of maximum 250 m b.s.l. (Kartverket). The topography comprises preserved plateaus of pre-Quaternary bedrock overlain by ice caps, isolated by glacially eroded valleys and cirques (Østrem et al., 1973). The highest summit is a point at Øksfjordjøkelen reaching 1191 m a.s.l. (SNL). Loppatind, 1175 m a.s.l, is the highest point of Finnmark county in solid rock (Kartverket). A lot of snow avalanche activity and a few rock falls has been registered in all the fjords of the peninsula (Sandersen & Domaas, 2014; NGU, 2018a).
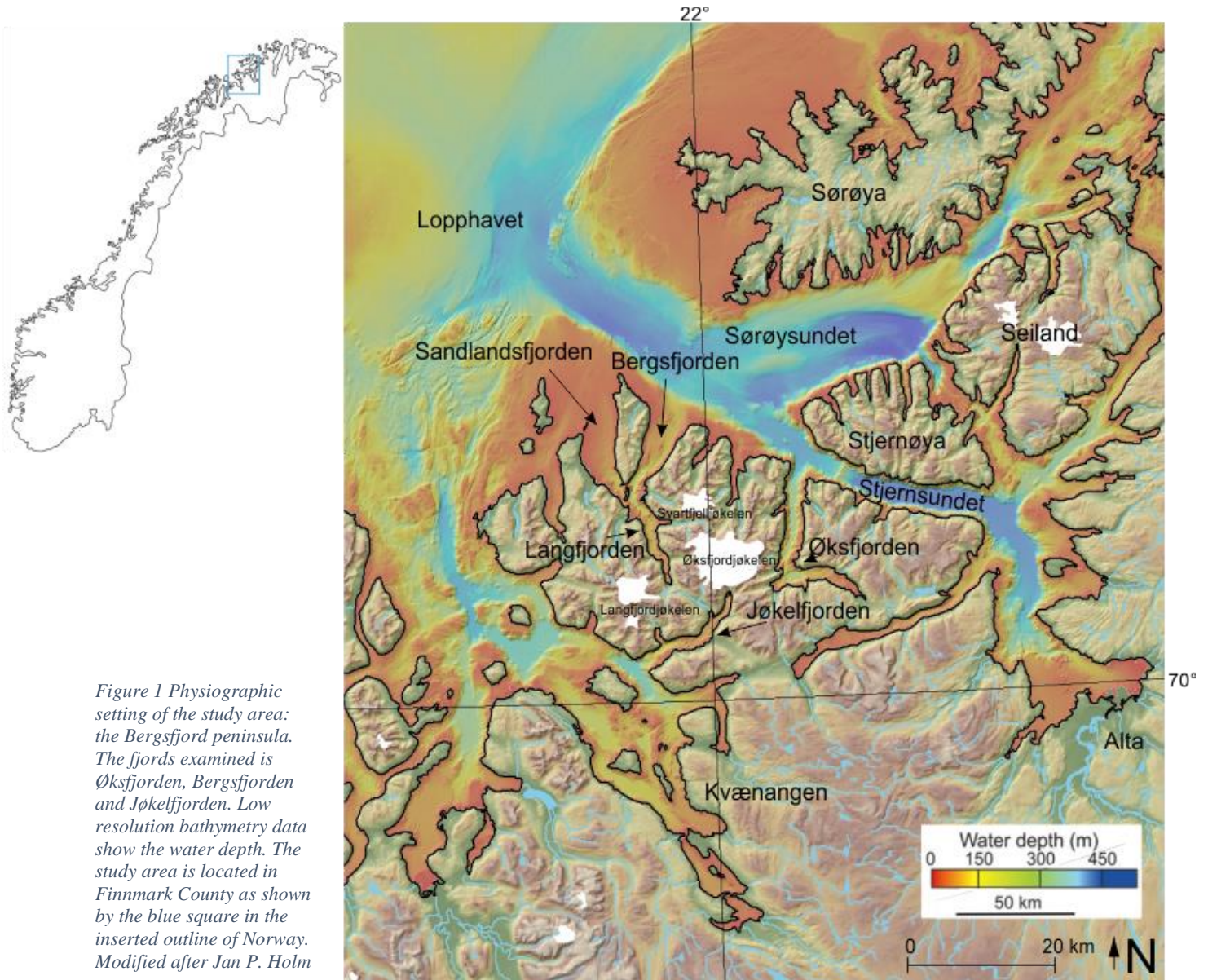
Figure 1 Physiographic setting of the study area: the Bergsfjord peninsula. The fjords examined is Øksfjorden, Bergsfjorden and Jøkelfjorden. Low resolution bathymetry data show the water depth. The study area is located in Finnmark County as shown by the blue square in the inserted outline of Norway. Modified after Jan P. Holm

2.2 Geology

2.2.1 *Bedrock*

The bedrock in the study area is of Proterozoic age and consists mainly of metamorphosed plutonic rock that intruded into an older metamorphosed sedimentary succession (Figure 2) (P. Bøe, 2011). These constitute the upper part of the Kalak Nappe Complex (KNC) (Sturt et al., 1975). Underlying Precambrian Raipas basement is exposed East and South of the study area (Robins & Gardner, 1975; Pharaoh et al., 1982). The metasedimentary host rock consists of Metasandstone (yellow), Gneisses (beige), Mica gneisses and -schists (green) (Figure 3) (D. Roberts, 1973). The plutonic intrusive rocks are a part of the Seiland Igneous Province (SIP) (Figure 2) (Sturt et al., 1975; Chroston et al., 1976; Stephens et al., 1985). Mafic Gabbro (burgundy) make up most of the magmatic province in the study area, with presence of younger ultramafic Peridotite intrusions (purple) and even younger alkaline intrusions of Syenite (pink) and Carbonatite/Marble (light blue) (Figure 3) (Krauskopf, 1954; Sturt et al., 1975).

Figure 2 Major geological features of and nearby the Seiland Igneous Province (SIP) (Robins & Gardner, 1975). The Seiland Igneous Province (SIP) is shown as Intrusive Igneous rocks, the root of a plutonic intrusion emplaced into the Kalak Nappe Complex (KNC), shown as Overthrust Metamorphic rocks. A window of Precambrian Basement is present S and E of the study area.
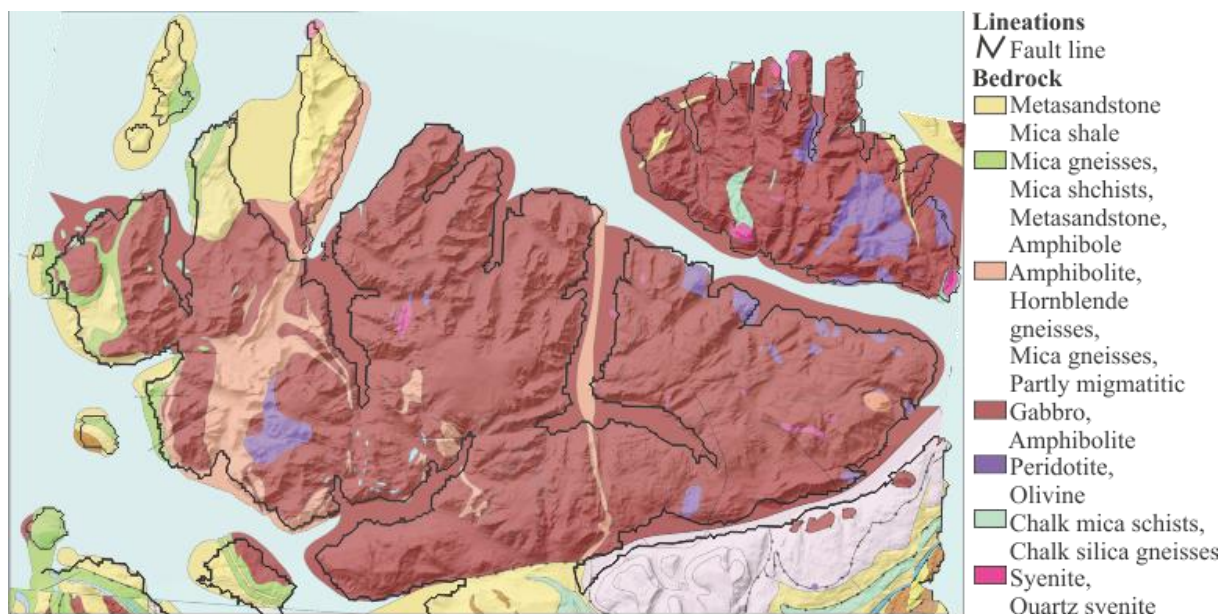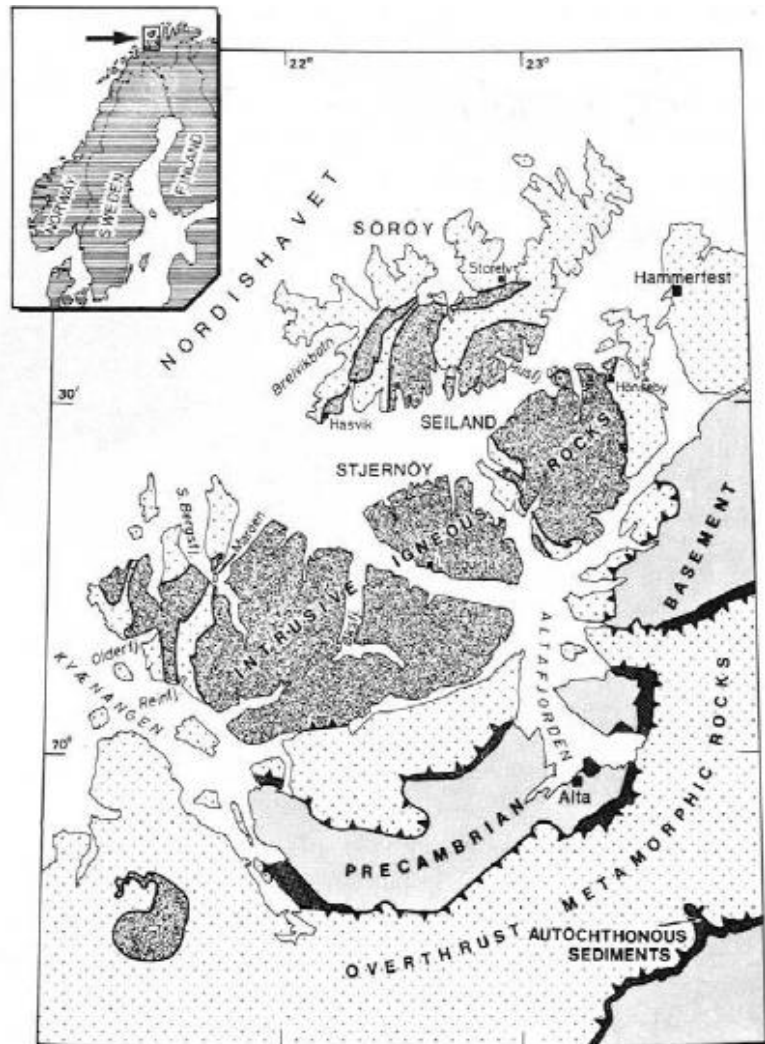
Figure 3 Geological map of the Bergsfjord peninsula. The bedrock of the study area consists of Garnet-rich Banded Gneisses (beige), Metasandstone (yellow), Garnet-rich Mica gneisses and -schists (green), mafic Gabbro (burgundy), ultramafic Peridotite (purple) and alkaline intrusions of Syenite (pink) and Carbonatite Limestone (light blue). The reverse thrust fault marking the contact between the SIP and the KNC is exposed SE of the study area. Modified after (NGU, 2011) with the water surface from Jan P. Holm.

R. J. Roberts et al. (2006) found that the emplacement of the mafic and ultramafic intrusions making up the Bergsfjord peninsula occurred between 570 – 560 Ma in a single tectonic regime, most likely related to intracontinental rifting. They assumed that the alkaline intrusions where emplaced in the same event, all intruding the KNC before deformation and displacement onto the Baltic Shield during the Caledonian orogeny 420 Ma ago. Because of the denudation following the Caledonian orogeny only the root of the plutonic rocks are preserved, making it difficult to interpret its origin (R. J. Roberts et al., 2006).

During the Mesozoic era (251 – 65 Ma) large-scale weathering and erosion created a palaeic surface close to the sea-level at the time (Bryhni, 2015). Preserved left-overs of this surface are found several places in Norway, amongst them the high plateaus at the Bergsfjord peninsula (Whalley et al., 2004). The following isostatic uplift resulted in a dome-shaped landscape, the Baltic Shield. The uplift caused an extension of the bedrock that may have induced bifurcation and faulting, determing the position of todays fjords (Syvitski et al., 1987).

The Seiland Intrusive Complex is well studied, though at Seiland island and not on the Bergsfjord peninsula. Krauskopf 1954 (Krauskopf, 1954) thouroghly mapped the eastern part of the peninsula. However, a geological map of the entire peninsula does not exsits in higher resolution than 1:250 000 (D. Roberts, 1973).

The Gabbro and Amphibolite is generally very resistant (B. R. Rea et al., 1996), thus mass wasting of rocks will generally occur due to joint patterns in relation to the geometry of the slopes (Sandersen & Domaas, 2014). Unstable rock slopes in Troms county are being mapped south on the peninsula north in Kvænangen. In Finnmark county possible unstable rock slopes have not been investigated (NGU, 2018c)

2.2.2   Marine geology

The fjords of the peninsula are relatively shallow and consist of basins confined by sills (Figure 6). Jøkelfjorden is a fjord arm of Kvænangen. A distal transition into deeper troughs are inferred offshore of the northern fjord inlets (Figure 4), these troughs are interpreted to be erosional zones of paleo ice streams (Ottesen et al., 2005). Sandlandsfjorden, and the area West of Bergsfjorden, is defined as a strandflat (Buhl-Mortensen, 2006; Mareano, 2006b) (Figure 4), a shallow plateau seemingly not as affected by the erosional effect of the paleo ice streams. Glacial lineations are mapped north of the peninsula (Figure 6) possibly indicating the direction of ice stream movement. A detailed survey of marine landforms and a grain size distribution of the sea floor of Sørøysundet, Stjernsundet and areas toward Lopphavet was carried out by Buhl-Mortensen (2006) (Figure 5). However, detailed investigations and the acquisition of high-resolution swath bathymetry data from the fjords in this study remain to be performed.
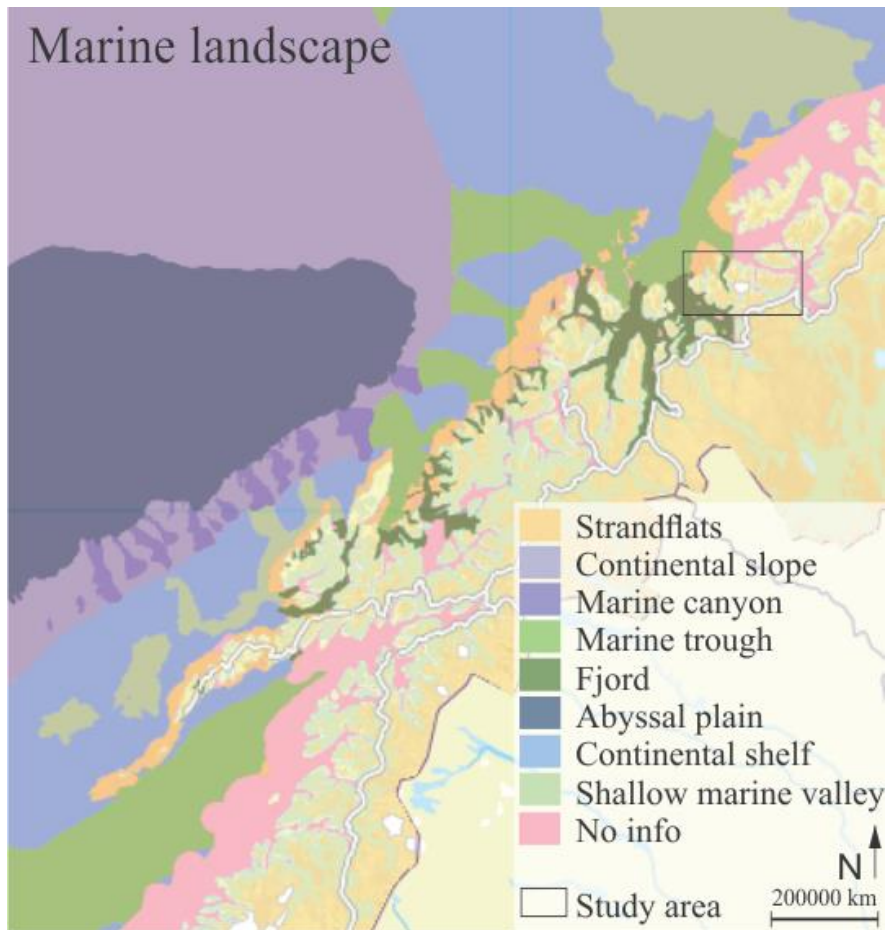
Figure 4 Marine landscape adapted from (Mareano, 2006b) showing the study area and its surrounding marine landscape of fjords, strandflats and marine valleys
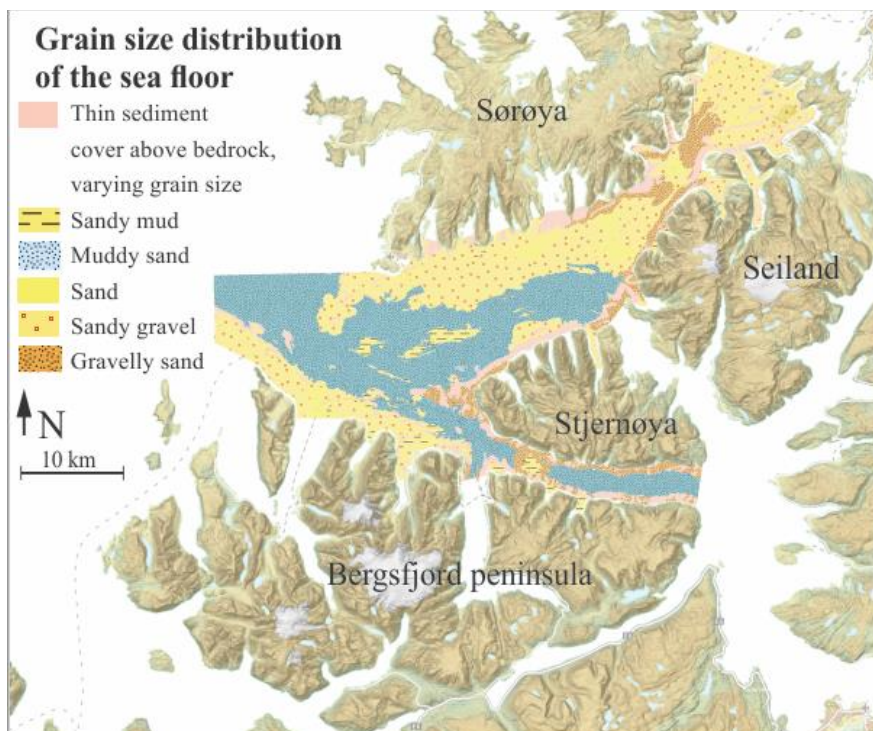
Figure 5 Grain size distribution of the sea floor. A detailed survey of the marine landforms, fjords and grain size distribution of the sea floor were made in 2006 covering Sørøysundet, Stjernsundet and areas toward Lopphavet (Buhl-Mortensen, 2006). 1100 km2 were mapped using detailed video analysis and sediment sampling. Figure adapted from (Mareano, 2006a).

11
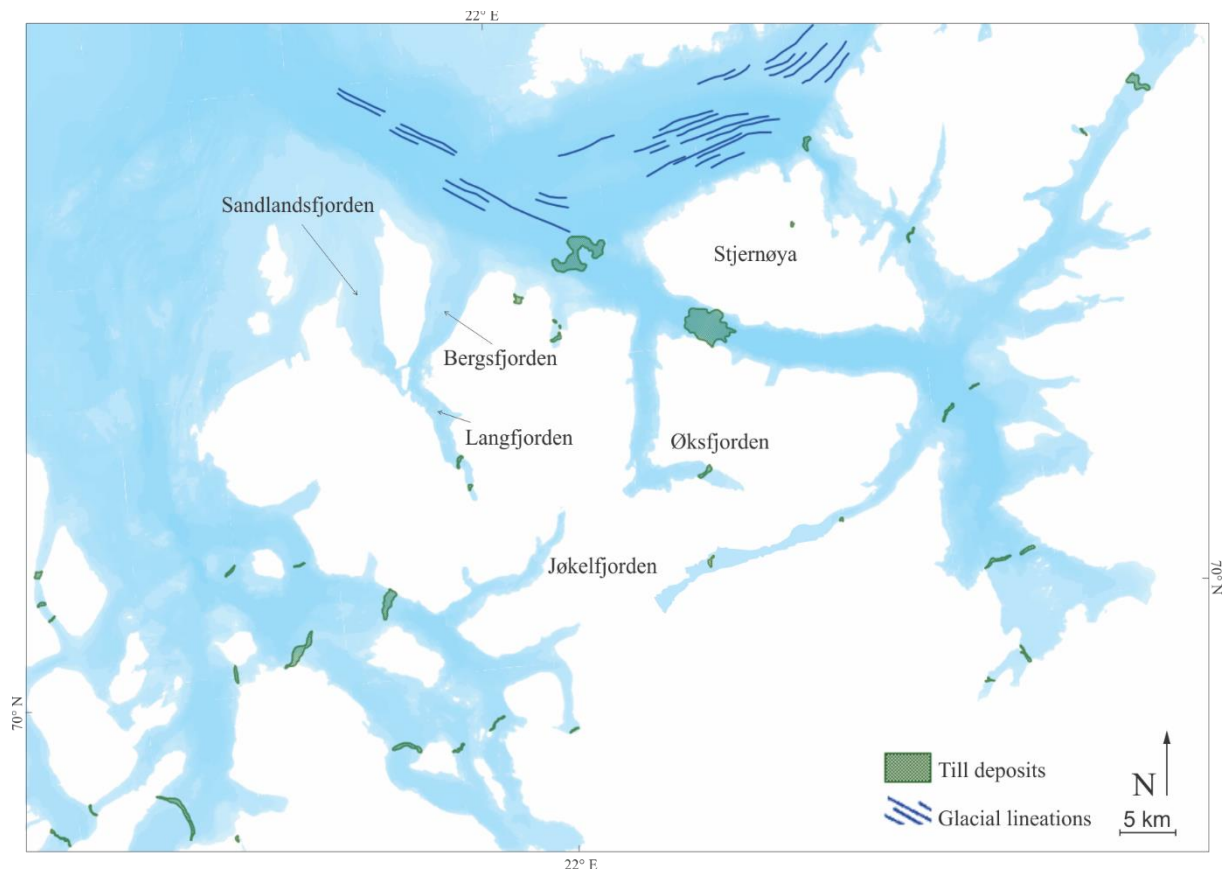
Figure 6 Terminal moraines and parallel ridges and grooves. More landforms than the ones mapped are expected. From Mareano. The deposits in Øksfjorden and Langfjorden interpreted as till in Mareano are, however, interpreted as rock avalanche deposits by NGU (NGU, 2018a). Figure modified after (Mareano, 2018)

2.3 Climate

2.3.1 Glaciations

Cenozoic glaciations deformed the landscape by erosion of grounded ice advancing along weak zones (Østrem et al., 1973). A gradual global cooling initiated 50 Ma yrs. BP (Zachos et al., 2001). The cooling intensified before the onset of the Northern Hemisphere Glaciation ~2.75 Ma yrs. BP in the late Pliocene (Haug et al., 1999; Ravelo et al., 2004). This mark the beginning of the Quaternary (Figure), a period when ice rafted debris (IRD) first appeared in the marine records (Ruddiman, 2007). Milankovitch cycles of 100,000, 41,000 and 23,000 years are represented in the climate records, and prove the solar impact on the global climate (Raymo, 1994). The Quaternary contained large scale climatic variations with interglacial periods of warmer climate in between the cold glacials, primarily caused by the changing insolation (Vorren et al., 2007).
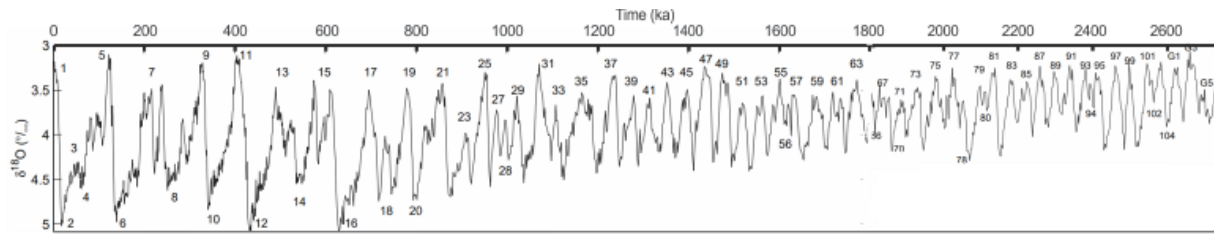
Figure 7 Globally combined benthic δ18O records through the Quaternary as an indicator for paleoclimate (Lisiecki & Raymo, 2005). Odd numbers and lower δ18O values represent warmer marine isotope stages, and vice versa. A transition interval from a domination of 41,000 to 100,000 yr. cycles occurred between 1250 and 700 ka yrs. BP, increasing the strength of the climatic variations and hence also the erosional forces (P. U. Clark et al., 2006).

Intense erosion in the Northern Hemisphere are observed to have occurred around 1.8 Ma yrs. BP, and is probably caused by the global shift toward an increased climate variability (Shuster et al., 2005). A transition from dominating 100,000 yr cycles to 41,000 occurred in the mid-Pliocene, further increasing the variability (Figure). Temperate glaciers are the main glacier-type to perform large-scale excavations by abrading and segregating ice in the underlying bedrock (Nesje, 2017). Hence the formation of the fjords in the study area is likely to have initiated in the glacial-interglacial transitions in Pleistocene (Nesje & Whillans, 1994; Kessler et al., 2008), when large scale ice flows drained the ice sheets that came and went. (B. R. Rea et al., 1996) suggest evidence of a cold-based glacier situated on top of the Paleic surface and hence preserving it.

Flutes along the sea floor in troughs and transverse ridges may imply presence of grounded ice flow (Rydningen et al., 2013). Winsborrow et al. (2010) and Ottesen et al. (2005) have mapped flow sets providing evidence of warm based ice and ice streams focused out through Altafjorden and the sounds north of the Bergsfjord peninsula (Figure 8). The glacial lineations and transverse moraine ridges show a stepwise retreat of the fronts of grounded ice streams during the deglaciation (Figure 9) (Winsborrow et al., 2010). Some flow sets are superimposed on the former, representing different periods of erosion (1, 8 and 9, 10, 7, respectively). These indicate that the Fennoscandian Ice Sheet advanced out through fjords and cross-shelf troughs, onto the continental shelf and to the shelf edge along the entire continental margin offshore Norway during Weichsel, the last glacial period (e.g. Ottesen et al., 2005).
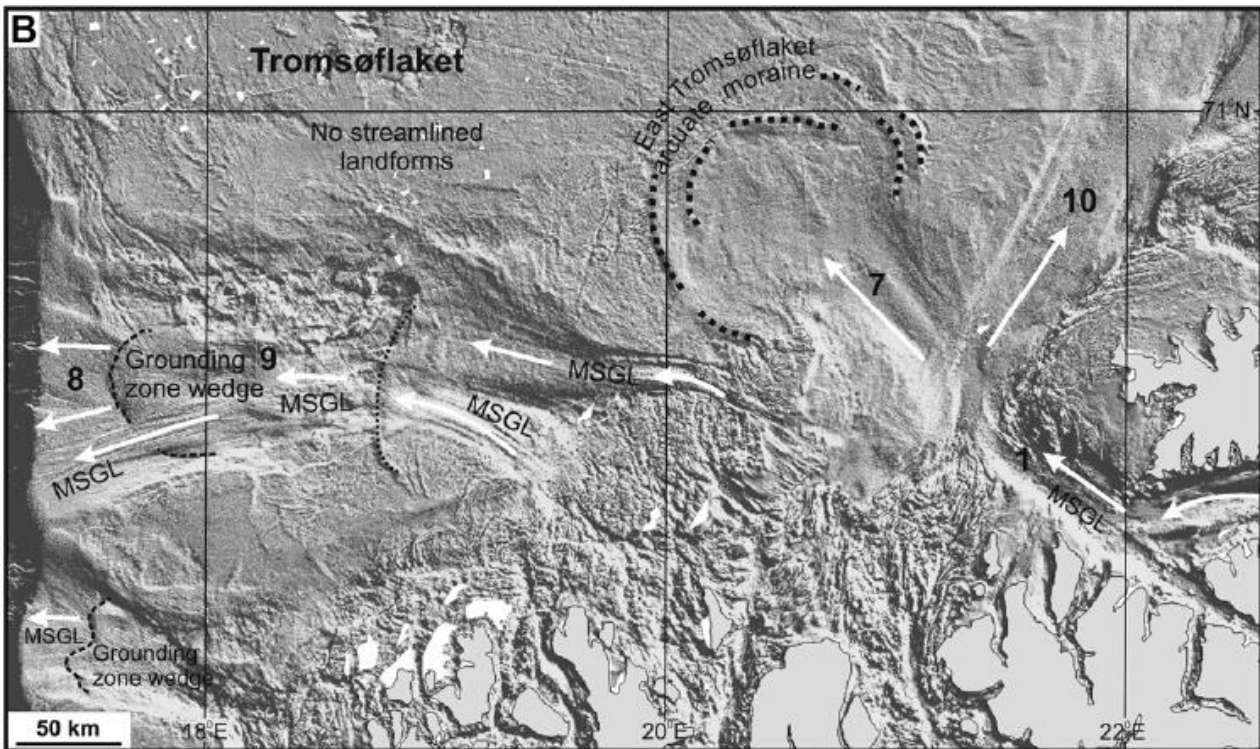
Figure 8 Numbers refer to designated flow sets. MSGL = Mega-Scale Glacial Lineations. Numbers show superimposed flow sets, representing different periods of erosion (1, 8 and 9, 10, 7, respectively). After Winsborrow et al. (2010).
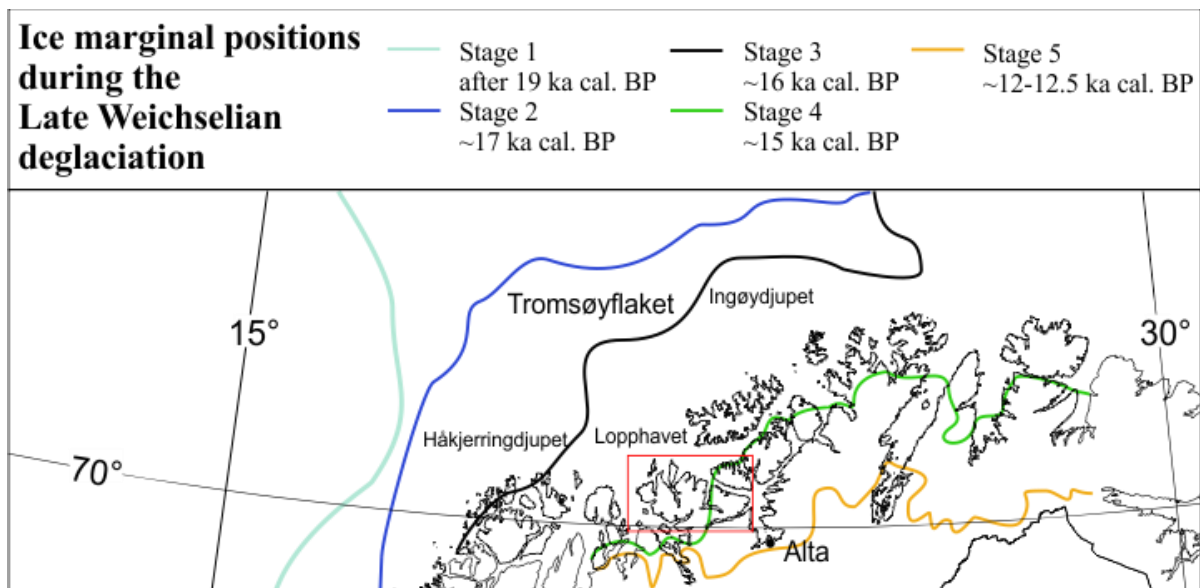
Figure 9 Five-stage reconstruction of the LGM and subsequent deglaciation of shelf outside the study area. The stages show the extent of the ice sheet, based on megascale geomorphic mapping. Red square show the position of the study area. Figure based on studies made by Winsborrow et al. (2010).

During the late Weichselian, the latest largest extent of the Fennoscandian Ice Sheet occurred between 25,000 and 18,000 yrs. BP on the Northern Hemisphere (Ottesen et al., 2005). This outer limit represents the Last Glacial Maximum (LGM) that occurred at a time of almost equal solar insolation as at present (Ruddiman, 2007). However, the preceding lower annual insolation probably helped in building up global ice sheets responding to the forcing with a delay (Ruddiman, 2007). Subsequently, higher amounts of annual insolation toward the end and shortly after the last glacial contributed to the drawdown of the Fennoscandian Ice Sheet (Ruddiman, 2007). The entire Bergsfjord peninsula is assumed to have been covered by ice during the LGM (B. R. Rea et al., 1996; Stokes et al., 2014) (Figure 9)

2.3.2 Deglaciation

The ice sheet retreat following the LGM has left traces corresponding to ice-front positions in the deglaciation (Figure 9 and Figure 10A). Moraine systems, marine limits and raised shorelines on the Bergsfjord peninsula and surrounding areas have been mapped, dated and correlated by Andersen (1965, 1968); Sollid et al. (1973); and Evans et al. (2002). Stokes et al. (2014) found an asynchronous response in the eight major retreat systems mapped in northern Norway based on further datings and morphological studies (Figure 10B). Of these, the Skarpnes, Tromsø-Lyngen and Stordal sub-stages are the most prominent in the study area. Egga II moraines, corresponding to LGM, are found as submarine ridges far out on the continental shelf. These are estimated to an age of 17.8 (± 0.3) cal. ka BP (Andersen, 1968; Vorren & Plassen, 2002; Stokes et al., 2014).

The only well-dated event on the continental shelf is the Flesen Moraine in Andfjorden, a marine trough south in the county, at 17.3 cal. ka yrs. BP (Vorren & Plassen, 2002) (Figure 10B). However, investigations from Ersfjorden and Kaldfjorden, west of Tromsø, suggest ice-free conditions prior to ~18 cal. ka yrs. BP (Hermansen, 2015; Olsen, 2015).

Bølling and Allerød interstadials followed the last glacial, two warmer periods from approximately 14.7 ka cal. yrs. BP e.g. (Hughen et al., 2000) (Figure 10C). The Skarpnes moraine sub-stage deposited 14.2 (± 0.3) ka cal. yrs. BP. Andersen (1968); and Vorren and Plassen (2002) represent a period of still-stand or re-advance of the ice sheet, probably corresponding to the colder stadial of Older Dryas briefly separating the Bølling and Allerød interstadials (Vorren et al., 2007). The Skarpnes moraine is situated directly north-east of the Øksfjord inlet and mark the deglaciation of the trough north of the Bergsfjord peninsula (Figure 10A).

According to Stokes et al. (2014) Altafjorden was deglaciated before 13.5 ka cal. yrs. BP and the onset of the colder Younger Dryas stadial initiated about 12.8 ka cal. yrs. BP. An advance in the glacier front and the deposition of the Tromsø-Lyngen sub-stage is assumed to have occurred 12.1 (± 0.2) ka cal. yrs. BP, presumably corresponding to the Younger Dryas terminal moraines, the Main stage, mapped all over north-western Europe (Figure 9 and Figure 10) (e.g. Andersen, 1980; Corner, 1980; Andersen et al., 1995; Vorren & Plassen, 2002; Vorren et al., 2007; Stokes et al., 2014).
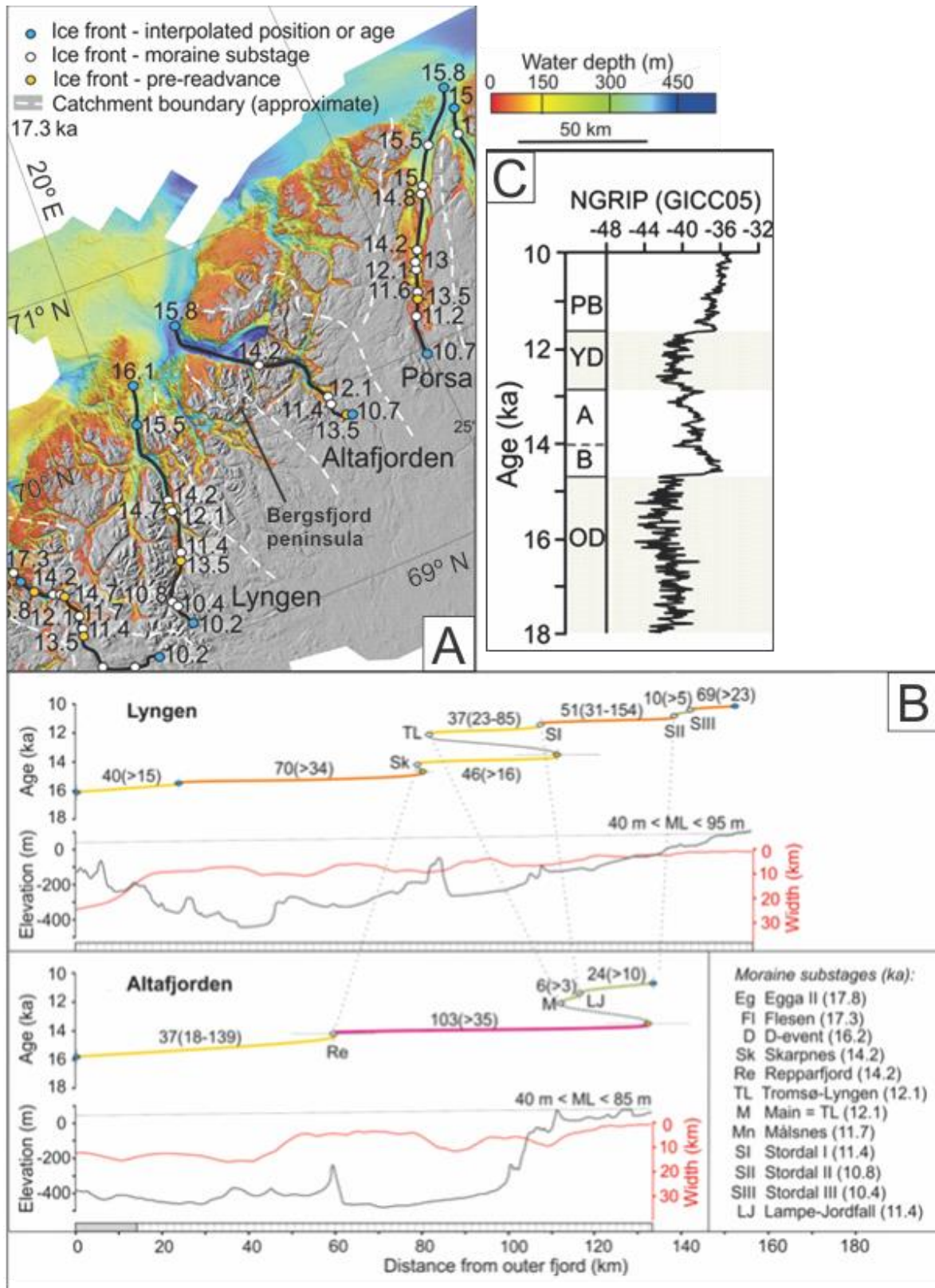
Figure 10 A) Show the location of transects in B) showing time-distance diagrams of the glacier terminus position along with the width and depth of the fjords. Both A) and B) show known and interpolated ka cal. yrs BP dates and the location of the ice-front positions. The retreat rate between the moraine sub-stages (linked from Lyngen to Altafjorden with dashed lines) are calculated in meter per year (m/a). The white dashed lines in A) represent estimated catchment areas at LGM. Marine limit (ML) show approximate relative sea level during glacier retreat. C) Show the stable oxygen isotopes ($\delta^{18}O$) North Greenland Ice Core Project (NGRIP et al., 2004) along with interstadials and stadials GICC05 (Greenland Ice Core Chronology, 2005); OD: Oldest Dryas, B: Bølling, A: Allerød, YD: Younger dryas and PB: Preboreal. Lower $\delta^{18}O$ represent colder periods, and vice versa. Modified from (Stokes et al., 2014).

Øksfjordjøkelen was decoupled from the rest of the Scandinavian Ice Sheet during Younger Dryas, with the terminal moraine situated south of the peninsula (Figure 9) (Sollid et al., 1973; B. R. Rea & Evans, 2007). However, an advance in the ice front presumably occurred locally. Evans et al. (2002) mapped moraines and correlated them with shore lines in order to reconstruct the glacier extent (Figure 11). Ten major outlet glaciers drained Øksfjordjøkelen, descending close to, or below, sea level at ~40-55 m above present-day sea level (increasing inland) during both Older and Younger Dryas (B. R. Rea & Evans, 2007). However, the fjords as we know them today were still free of glacial ice.
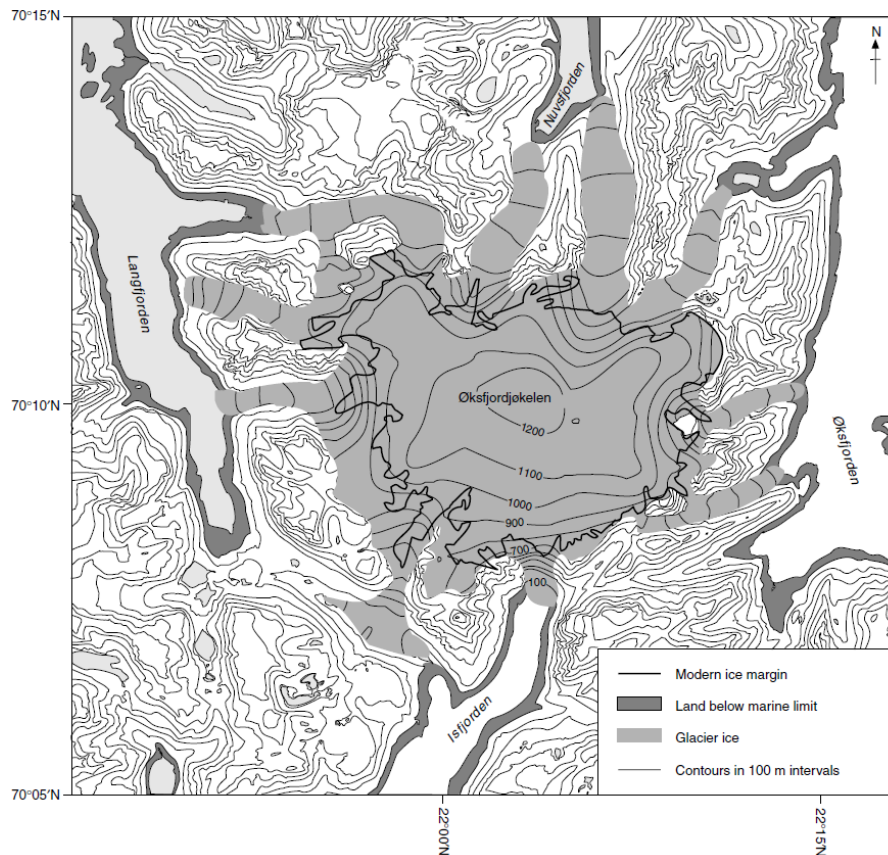
Figure 11 The reconstructions of the extent of Øksfjordjøkelen during Younger Dryas have been made by mapping moraines and combining evidence of 14C-datings, sea-level chronology, glacial geology and glaciology executed by themselves and others. From (Evans et al., 2002).

2.3.2   Interglacial

A warming period called the Preboreal followed after the termination of Younger Dryas around 11,500 years BP (Friedrich et al., 1999; Hughen et al., 2000). This was the first period of the interglacial *Holocene* that we are still situated in. The Younger Dryas/Preboreal-transition mark the end of the former ice age and Pleistocene (Andersen, 1980). A rapid retreat through 1,000 years affected the main ice sheet, with some halts and re-advances depositing moraines along its path (Evans et al., 2002; Vorren et al., 2007). The high melt rate produced extreme meltwater rivers and transported huge amounts of sand and gravel out to the glacier front (Vorren & Plassen, 2002). Glacigenic clay and silt were transported away from the sand and gravel by rivers and currents further out in the fjords and offshore.

Three sub-stages are distinguished in the Preboreal (Andersen, 1968): Stordal I, Stordal, II and Stordal III, with estimated ages of 11.4 (± 0.2), 10.8 (± 0.2) and 10.4 (± 0.2) ka cal. yrs. BP, respectively (Corner, 1980; Stokes et al., 2014). The Lampe-Jordfall moraine mark a sub-

stage corresponding to the Stordal I moraine 11.4 (± 0.2) ka cal. yrs. BP (Figure stokes). All the sub-stages may have been caused by minor climatic fluctuations (Andersen, 1968). (Evans et al., 2002) found that the rapid reaction to the changing climate following the Younger Dryas shows that the ice cap was in equilibrium with the climate.

Active geological processes such as tectonics (Fjeldskaar et al., 2000; Stewart et al., 2000), as well as eroding glaciers and rivers carving out the landscape, creating deltas, floods, mass-wasting (R. Bøe et al., 2003) and tsunamis (Bondevik et al., 1997) characterize the Holocene epoch (Forwick & Vorren, 2002). Holocene has been defined by isostatic uplift following the melting of the ice sheet (Walcott, 1972), along with rising sea level due to the increased input of meltwater into the oceans (Fairbridge, 1961; J. A. Clark et al., 1978).

2.3.3 Isostatic rebound and eustasy

The load from the massive ice sheets present during LGM pushed the rigid lithosphere into the viscous asthenosphere. The Fennoscandian Ice Sheet was presumably 3,000 m thick at its thickest above Botnvika, pushing the crust down about 1,000 m (R. Dahl et al., 2004). (Walcott, 1972), among others, showed that the subsequent reduce in ice load resulted in a gravitational (isostatic) disequilibrium due to the rheology of the mantle, and hence caused a marine shoreline regression, a relative sea level fall, due to the rising crust (Figure 12). The process of the lithospheric restoration is called glacial isostatic adjustment (GIA) (Lund et al., 2009).

In an isostatically deformed region such as Fennoscandia, the isostatic rebound is still going on post LGM (Walcott, 1972). The isostatic uplift has a lagged response time after the change in load (Benn & Evans, 2014). Complete adjustments of the crust may take more than 10,000 years. Hence, it will most likely never be in equilibrium with the loading of ice due to the faster changing climate. Once the ice retreats, the rate of the postglacial uplift in an area may be estimated by mapping deposits indicating the former sea level (Goudie et al., 2005). Displaced geomorphological features such as deltas, beaches, shingle ridges (storm deposits) and erosional platforms mark former shorelines with varying heights relative to the present sea level (Corner, 2006; Vorren et al., 2007; Benn & Evans, 2014).
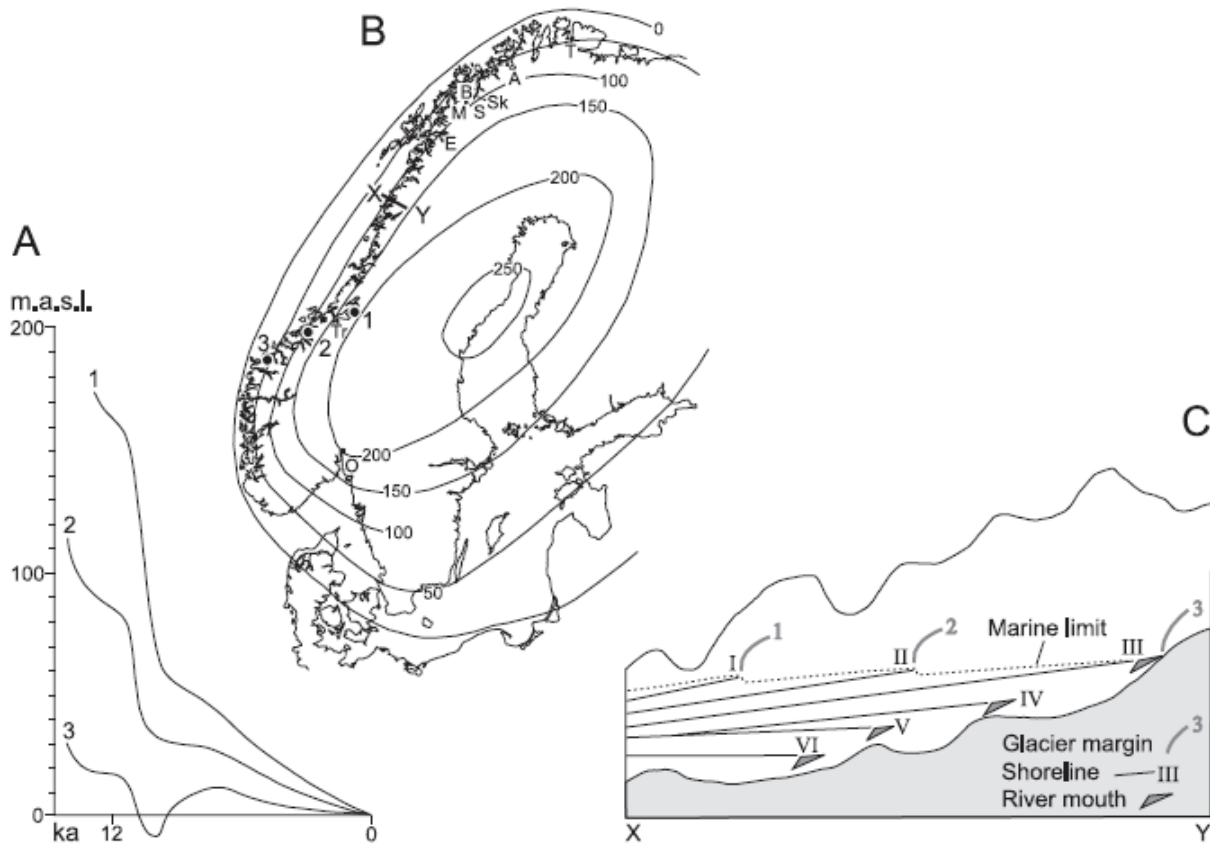
Figure 12 Relative sea-level change in Fennoscandia through 14 ka yrs. A) Show regional shoreline displacement curves with an increasing distance from the uplift center (position seen in B and C). B) Isobases of 50 m. C) raised shorelines formed during glacier retreat (I, II and III) and delta progradation and fjord head regression (IV, V and VI). Older shorelines have a greater tilt due to a longer time of subsequent uplift and a higher velocity of the uplift in the center where the ice was at its thickest. Shoreline V represent the Tapes transgression in the outer fjords. After (Corner, 2006).

However, eustasy (the change in sea level) will also affect the position of the former shoreline along with the rebound in the crust (Fairbridge, 1961), creating a need for sea level reconstructions independent of evidence found in sediment deposits (J. A. Clark et al., 1978). If the past sea level of a region can be explained, the raised shorelines may work as accurate evidence of the GIA of an area in time (Walcott, 1972) and isobases indicating the rate of the isostatic rebound may be created from this data (Fossen, 2009).

A regional sea level history has been constructed by (Grønlie, 1951; Marthinussen, 1960; Andersen, 1965, 1968; Sollid et al., 1973; Evans et al., 2002). Evans et al. (2002) made an updated equidistant shoreline diagram (Figure 14) based on the mapping and correlation of the former shorelines and a sea level reconstruction made by Corner (1980) for Lyngen, further south in the county. The isobases for the Main shoreline is seen in Figure 13.

21,000 years BP the eustatic sea level was 125 (± 5) m lower than at present (Fleming et al., 1998; Fairbanks, 1989). Approximately 17,500 years BP, the retreat of the North American glaciers along with the deglaciation of the Barents Sea Ice cover and the Bear Island Through begun, resulted in a higher global mean sea level (Fairbanks, 1989). Raised shorelines give indications of the sea level of the past. The marine limit (ML) is the shoreline with the highest altitude after the deglaciation.

In Scandinavia, the crust rose faster than the sea level, causing a post-glacial relative sea level regression (Marthinussen, 1960; J. A. Clark et al., 1978). Rebound began earlier along the coasts, due to an earlier deliquescence of the ice sheet and an initial, relatively smaller load due to less ice in these areas (Benn & Evans, 2014). Rates of uplift along the coast of northern Norway are about 1 mm/year, while the rate at Botnvika is about 8 mm/year (Dehls et al., 2000a; Fjeldskaar et al., 2000). This is reflected in the lower marine limit and raised shorelines out by the coast as compared to locations with closer proximity to the ice center (Benn & Evans, 2014). As seen in Figure 14, the older shorelines have a greater tilt than the younger due to the decreasing amounts of differential uplift through time. The raised shorelines formed subsequently during glacier retreat, extend further inland as the ice sheet had a relatively steady retreat.
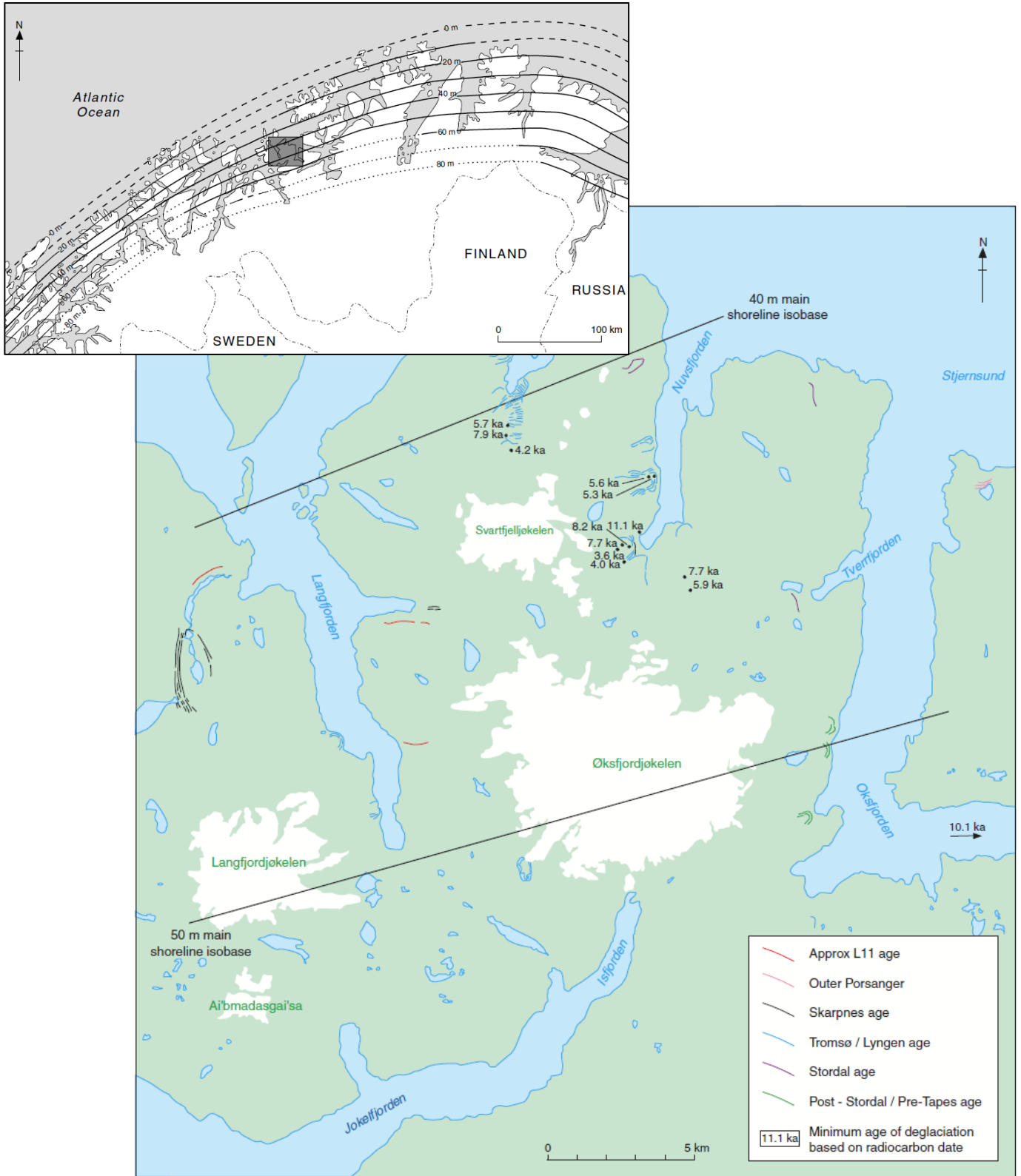
Figure 13 Map showing the isobases of the Main shoreline after Marthinussen (1960), corresponding to the Younger Dryas and the Tromsø-Lyngen substage. B) show a close up of the study area along with dated glacier margins associated with specific shorelines. After (Evans et al., 2002).

Raised shorelines in the study area have been mappen and include shorelines corresponding to the Skarpnes event, the Main substage, the Stordal substage and the Tapes shoreline. These are mapped with a decreasing altitude, respectively (Figure 14) (Evans et al., 2002). Sandlandsfjorden is mapped as a strandflat (Figure 4), thus representing a continuation of a shoreline stage predating the present (Holtedahl, 1967).
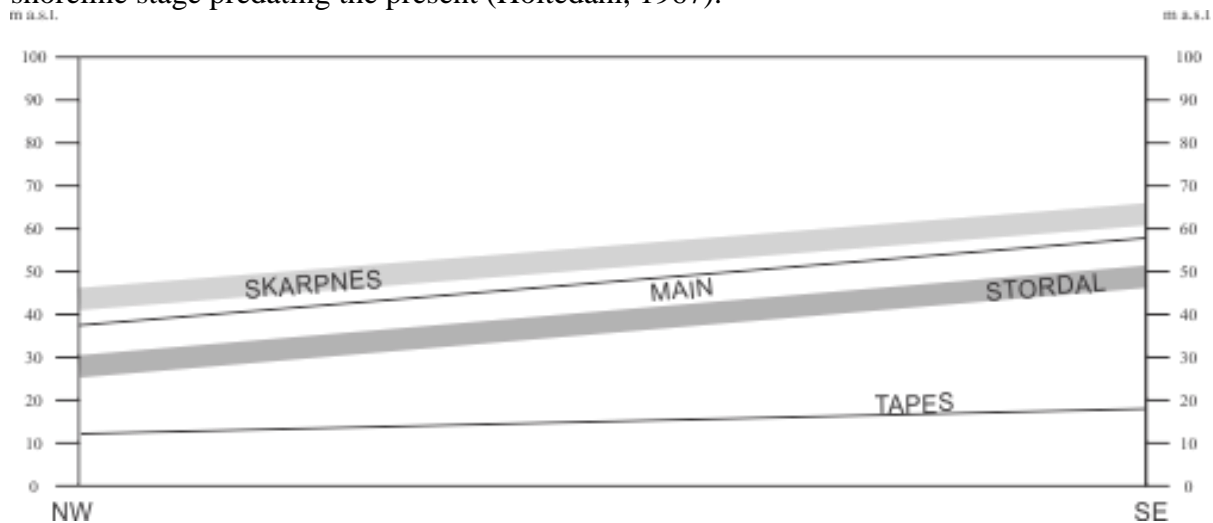
Figure 14 Equidistance map of raised shorelines in m above the present day sea level. Perpendicular on the isobases mapped in Figure. Modified after (Evans et al., 2002)

The Skarpnes shoreline is found 7-10 m above the Main shoreline (Andersen, 1968; Evans et al., 2002). The Main shoreline represent the sea level During Older and Younger Dryas ~40-55 m above the present-day sea level (increasing inland) (B. R. Rea & Evans, 2007). A period of relative sea level transgression occurred some places along the outer coast of Norway between 6,600 and 4,800 years BP called the Tapes-transgression (Marthinussen, 1962). The ice sheet melted at a higher rate than the land rose, leading to submergence of land presently above sea level, possibly due to a preceding warmer period (Vorren et al., 2007). The Tapes shore line is present beneath the Marine Limit and the Younger Dryas shore line and is seen crosscutting post-glacial shorelines some places (Marthinussen, 1960)

2.3.4 Post-deglaciation

(Andersen, 1980) made an attempt in summing up the deglaciation of Norway the past 10,000 ^{14}C yrs. based on pollen records from southwestern Norway. He stated that most of Norway was deglaciated about 9,000 ^{14}C yrs. BP, leaving only a discontinuous ice cover (Andersen, 1980). When entering the Boreal, a dry and warm climate 8,500- 8,000 ^{14}C yrs. BP is suggested. (S. O. Dahl & Nesje, 1996) propose higher winter precipitation 10,000 – 8,300 cal. yrs. BP, increasing the latter 200 years along with warmer temperatures, resulting in a retreat in the glaciers in southwestern Norway. With the continued melting throughout the country, (Andersen, 1980) imply that no glaciers existed in Norway at that time. (S. O. Dahl & Nesje, 1996) assume that the glaciers melted away around 7,000 cal. yrs. BP, as they recorded warm summer temperatures until 7,850 cal. yrs. BP. (Eeg, 2012) demonstrated a retreat in Svartfjelljøkelen ice cap between 9,000 and 7,000 cal. yrs. BP.

A regional cooling event is inferred in northwestern Europe 8200 cal. yrs. BP (Barber et al., 1999) and is also found in Bergsfjordvatnet (Eeg, 2012). A drier and colder Norway forced glaciers to retreat, and the pine tree-limit to drop (Klitgaard-Kristensen et al., 1998). The lake Agassiz event occurred around this time, so did the Storegga submarine slide (Ruddiman, 2007; Vorren et al., 2007).

The glaciers were very small between ~8000 to 4000 cal. yrs. BP, and most glaciers in Norway were completely melted away at least once due to high summer temperatures and/or reduced winter precipitation (Vorren et al., 2007; Nesje et al., 2008). Little or no glacial input were found in Bergsfjordvatnet between 7,000 and 5,200 cal. yrs. BP (Eeg, 2012). The warmer, more humid period from 8,000- 5,300 ^{14}C yrs. BP, represent the Atlantic period and the Tapes transgression (Andersen, 1980). It is possible that some small glaciers accumulated in the mountainous regions during these times (Andersen, 1980). (S. O. Dahl & Nesje, 1996) also found a small advance in glacier extent up until 6,200 cal. yrs. BP. From 5,300 ^{14}C yrs. BP (Andersen, 1980) recorded a dryer phase preceding a humid 4,900- 3,500 ^{14}C yrs. BP.

After ~4,000 cal. yrs. BP the glaciers are assumed to have grown again (Nesje et al., 2008) as a result of the increased amounts of precipitation. Several rock avalanche events are dated to have occurred around 4,000 cal. yrs. BP, presumably caused be the same reason.

(Andersen, 1980) recorded a short period of less humid climate 3,500- 2,800 ^{14}C yrs. BP. He inferred that many mountain glaciers started to grow from 2,800 ^{14}C yrs. BP, entering the Sub-Atlantic period of moist and cool climate with glacier maximums at 1,900 ^{14}C yrs. BP, 1,500-1,300 ^{14}C yrs. BP, 1,100 ^{14}C yrs. BP and 600 ^{14}C yrs. BP.

(Bradley & Jonest, 1993) made a proxy record of composite temperature anomalies combining five series of tree-ring-, instrumental- and melt records from 1400 to 1975 CE (Fig). They interpreted that Northern Scandinavia was coldest between 1550-1750 CE, marking the Little Ice Age (LIA) (S. O. Dahl & Nesje, 1996). (S. O. Dahl & Nesje, 1996) found the highest winter precipitation rates in the same period to have preceded the LIA 1250- 1750 CE (Eeg, 2012) found that Svartfjelljøkelen had its maximum extent in the LIA, after the advance initiating around 5,200 cal. yrs. BP. A following retreat of most Norwegian glaciers has occurred subsequently (Nesje et al., 2008). Small, discontinuous moraines located around the Øksfjordjøkelen ice cap, are assumed deposited following the LIA maximum (Whalley et al., 1989).
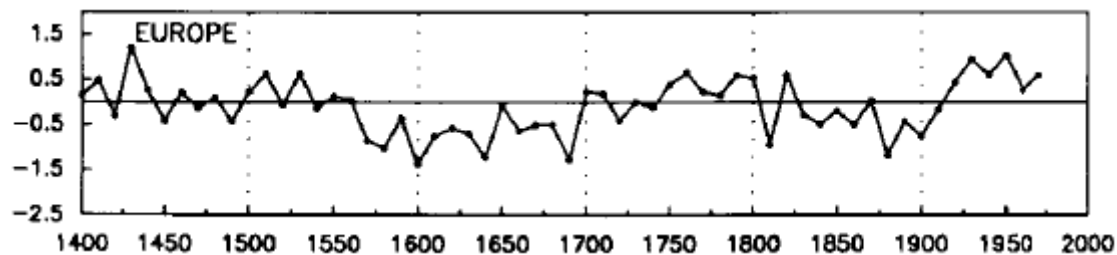
Figure 15 A proxy record of composite temperature anomalies combining five series of tree-ring-, instrumental- and melt records from 1400 CE to 1975. They interpreted that Northern Scandinavia was coldest between 1550-1750 CE, marking the LIA. After (Bradley & Jonest, 1993).

2.3.5   Present climate

Norway is significantly warmer than other countries at the same latitude due to the Gulf Stream (OECD, 2001) with a mean annual temperature (1961-1990) of 1.0 ℃ (Yr, 2018). The western part of Norway is considered a maritime climate, and the eastern Norway continental due to the protection by the Scandinavian Caledonides. The climate at the Bergsfjord peninsula is situated in the sub-arctic zone (Krauskopf, 1954) and is characterized as a weak oceanic section (Halvorsen et al., 2009) with precipitation rates averaging between 1,500 and 2,000 mm per year (Kjøllmoen et al., 2000). The mean annual temperature rates measured at Nuvsvåg station in Loppa (27 m a.s.l.) from 1961-1990 was 0.5 °C (Yr, 2018). The Köppen-Geiger climate classification defines the Bergsfjord peninsula as a fully humid, snow climate with cool summers (Kottek et al., 2006).

Weather stations at the peninsula include Øksfjord observation station (92860) 560 m a.s.l., measuring temperature and wind (since 2013), Sopnesbukt observation station (92910) 8 m a.s.l measuring precipitation, Nuvsvåg observation station (92650) 27 m a.s.l. measuring precipitation, temperature and snow depths (since 2015), and Langfjordjøkelen observation station (92500) 915 m a.s.l. measuring temperature (since 2004)
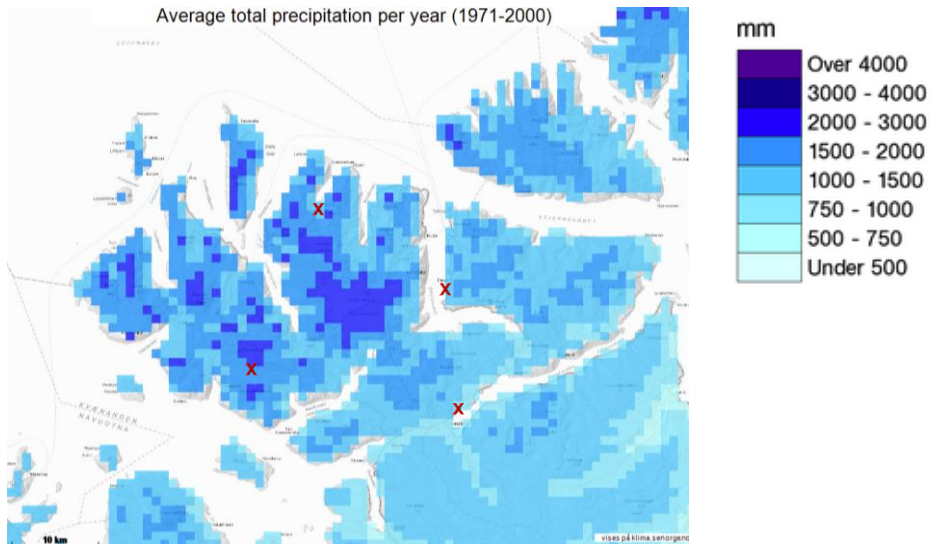
Figure 16 Mean annual precipitation (mm) averaged for 1 km x 1 km from 1971-2000, shown along with the weather stations in the area. From (seNorge, 2018).
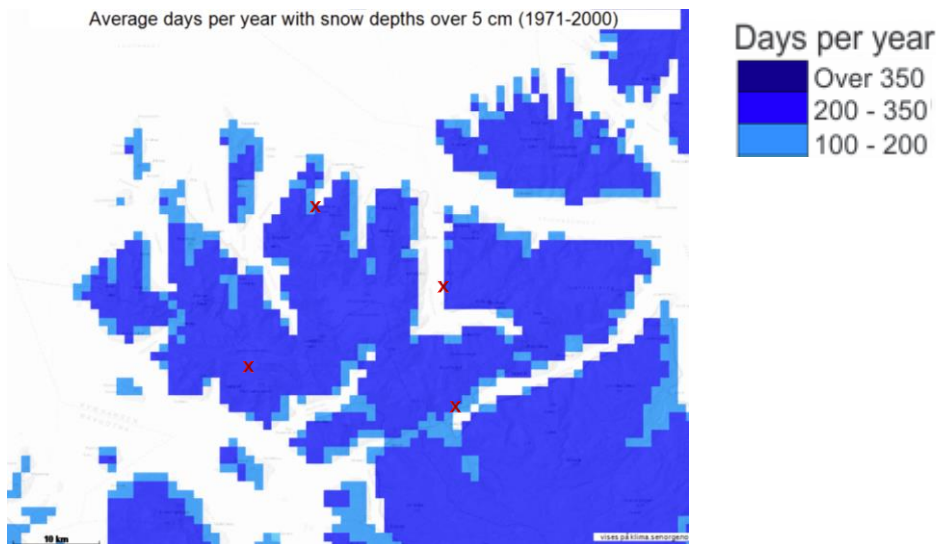
Figure 17 Mean annual maximum snow depth over 5 cm averaged for 1 km x 1 km from 1971-2000, shown along with the weather stations. From (seNorge, 2018).
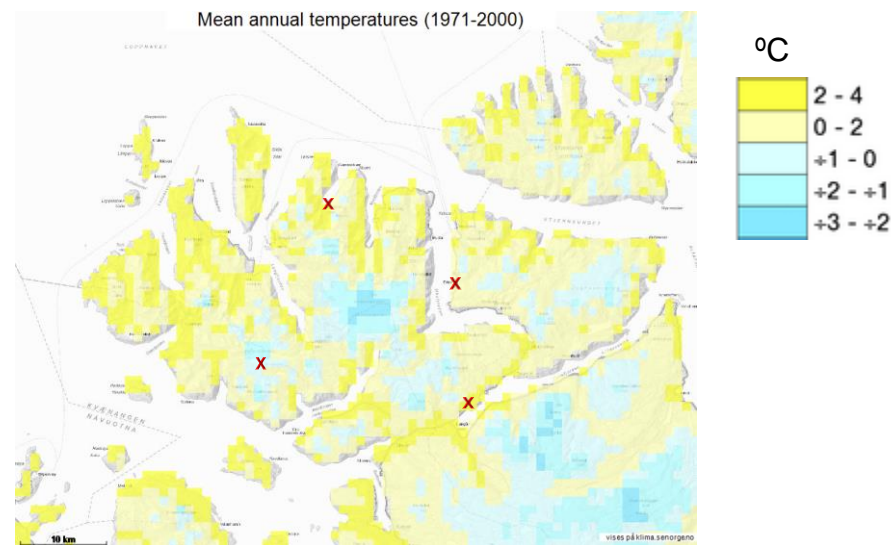
Figure 18 Mean annual temperatures (℃) km from 1971-2000, shown along with the weather stations. From (seNorge, 2018).

25

2.4 Geomorphology of fjords

2.4.1   Definition and distribution
The deep, elongated troughs, carved by glaciers and occupying a mixture of marine and fresh waters, are what we define as fjords e.g. (Holtedahl, 1967). Typically, fjords are situated along the coastline in (previously glaciated) high-latitude regions such as Chile, New Zealand, Alaska, Canada, Russia, Greenland, Scandinavia and the British Isles e.g. (Syvitski et al., 1987). Their process of formation, morphology and often limited exchange with marine water separate them in definition from the other types of estuaries e.g. (Hansen & Rattray, 1966).

2.4.2   Formation mechanisms
Rivers flow in the least resisting path. So does glaciers. They either follow lithology with lower strength of resistance against erosion than the surrounding bedrock or valleys of negative topography due to faulting (Holtedahl, 1967). Increased fluvial erosion due to the isostatic uplift following the Mesozoic denudation created deep valleys with a V-profile (Bryhni, 2015). Later when the glaciers advanced in the valleys, the valleys were eroded even further, modifying the profile towards a parabola later filled in and creating the general U-shape of fjords (Syvitski et al., 1987). Glaciers may erode deep below the water surface, over-deepening the fjords, as seen by ice bergs floating with 9/10 of its mass beneath the water surface (Monroe & Wicander, 2011). Subsequent sea level rise has increased the depth of the fjords (IPCC, 2014). The presence of a fjord indicate a pre-glaciated landscape (Vorren et al., 2007).

Excavation of fjords are assumed initiated in the Pleistocene (Nesje & Whillans, 1994; Ravelo et al., 2004; Shuster et al., 2005; Kessler et al., 2008) by warm-based glacier action (Vorren et al., 2007). Not only did the glacial culminations of the epoch carve out the fjords. At times of average glaciations glaciers have been present, deepening and widening the fjords (Porter, 1989). Mass movements may also have contributed to valley widening and non-glacial erosion in the landscape (Whalley et al., 2004).

2.4.3   Classification
Multiple classification systems of fjords exist based on glacier dynamics, sediment and meltwater supply and the influence of rivers, waves, tides and water circulation in fjords (e.g. (Skei, 1983; Syvitski et al., 1987; Hambrey, 1994; Syvitski & Shaw, 1995). (Howe et al., 2010) use a classification based on the climatic regime, i.e. polar, subpolar and temperate. The climate affect the presence of glaciers and sea ice, the amount of fresh-water input and hence the sediment supply. Fjords in *polar* regimes are permanently covered by sea ice or an ice shelf. *Subpolar* regimes provide fjords with sea ice breaking up in some part of the year with mean summer temperatures > 0 ℃. *Temperate* fjords only have locally distributed sea ice if present, and may be either glaciated or non-glaciated. This study is in a temperate climate regime, with seasonal sea ice in the head of the fjords. The fjords are non-glaciated, but they all have glaciers in their catchment area.

2.4.4   Large scale morphology
As the geology and climate affect the morphology of fjords, a large variety of forms exist. Their elongated alignment is based on the geology in the area and the drainage aspects. Fjords can comprise of several deep basins confined by transverse, shoal sills e.g. (Skei, 1983). These consist of either deposited glacial till covered by glaciomarine deposits, or more resistant bedrock. Sills are often present at the mouth, confining the fjord basin from the outer marine valley. Sometimes traces of it is found on each side of the fjord.

In general, fjords are deeper than they are wide (Farmer & Freeland, 1983). The width is presumably decided by the variations in resistance in the bedrock restricting the lateral erosion of the fjords. Generally, the steepness of the fjord sides depend on the composition of the bedrock. Presumably, there is an interconnection between high gradients on the side walls and narrower, deeper fjords based on the high resistant composition of the bedrock, and vice versa.

Fjords are braided systems of fjord arms often connected to a main fjord (Syvitski et al., 1987). These are formed by converging or diverging valley glaciers. As with the glaciers forming the fjords, the main contributing rivers most often enter at the fjord head. Due to the glacier dynamics fjords are often narrowing at the fjord mouth, and are deepest directly on the inside of the sills. The presence of glaciers also form deeper basins further in the fjord, closer to the fjord head (Vorren et al., 2007).

Climatic variations influence the formation of fjords by varying the presence of glaciers and then also sea level and the rate of erosion. The thermal regime of the present and the past, hence, affect the morphology of the fjords. Cold-based glaciers are also less erosive than warm-based. The postglacial climate affect the evolution of the sediment deposits by the varying precipitation rates and hence the weathering and sediment supply it may have induced. Slope failures are also affected by the climate, with increasing slope activity at times of high precipitation rates. Post-glacial sidewall talus cones, lateral moraines and terraces created by old shorelines are often found along the sides of the fjord (Syvitski et al., 1987).

The morphology of the fjords affect the hydrography and the processes affecting the sedimentation (Chapter 2.6 and 2.7).

2.4.5   *The fjords of the Bergsfjord peninsula*
The large variation in the alignment of the fjords are probably due to the ice cap draining toward all aspects down from the high plateau. As the plateau probably is preserved due to the resistant bedrock, the structural geology is inferred to be the dominating factor affecting the alignment (Figure 3). As the fjords are not thoroughly mapped it is difficult to evaluate the presence of sills in the fjords. Figure show some till deposits, but these have also been classified as mass-wasted deposits (NGU, 2018a).

The fjords surrounding the Bergsfjord peninsula are high-relief types, presumably restricting sediment deposition to the basins (Boulton, 1990; Benn & Evans, 2014). Slumping from steeper slopes are likely to have occurred due to both the relief of the bathymetry and the precipitous rock-slopes comprising the sides of the fjord (Benn & Evans, 2014).

Today all the fjords are temperate, non-glaciated fjord as direct contact between the glaciers and the fjords no longer influence the sedimentation except through proglacial rivers and the paraglacial deposits available for erosion. The catchment areas of each fjord may be seen in Figure 19. Large rivers enter at the fjord head in Langfjorden and at Sør-Tverrfjord, transporting sediment from Langfjordjøkelen into the fjord. Both Øksfjordjøkelen and Svartfjelljøkelen drain into Langfjorden down Nord-Tverrfjord. Svartfjellfkelen also drain through Bergsfjordvatnet entering Bergsfjorden at Bergsfjord (Figure 19). Øksfjorden catch proglacial river input from Øksfjordjøkelen in Tverrfjorden and Bac'cavuonvag'gi, and non-glacial influenced rivers at Storelvdalen, Kolsokkerelva, Øksfjordbotn and Øksfjord (Figure 19). Jøkelfjorden retrieve fluvial input from the southern side of the fjord and both proglacial

and non-glacially affected rivers enter on the northern side. Until very recently Øksfjordjøkelen calved directly into the fjord (Askheim, 2016). Today the regenerated Nerisen retrieves the ice calving off the main ice cap.
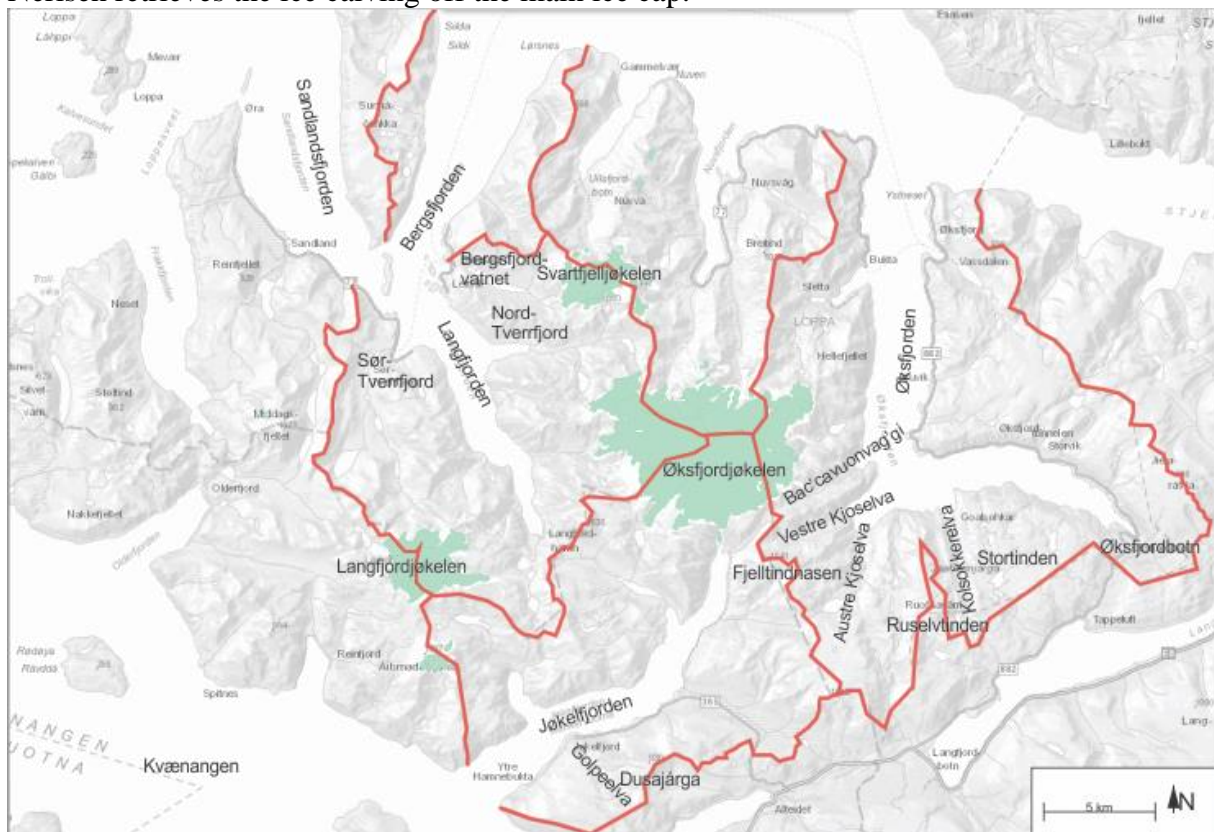
Figure 19 Catchment area for the three fjords. Øksfjordjøkelen drain into all of them. All three glaciers drain into Langfjorden. Modified after (Østrem et al., 1973; NVE, 2018b).

2.4.5.1 Øksfjorden (70°10'N, 22° 16'E)

Morainal till deposits are previously mapped in the inner part of the fjord (Figure 6). Evans et al., (2002) mapped subaerial moraines in the southern and eastern part of Øksfjorden. They indicated a local glacier ice feeding into Austre Kjoselva from the plateau of Stortinden, Ruselvfjellet and Fjelltindnasen during the Younger Dryas stadial, in addition to Øksfjordjøkelen draining down Tverrfjorddalen, Storelvdalen and Bac'cavuonvag'gi (Figure 19). The outlet glaciers most likely grounded in water close to the fjord head at this time, calving into the fjord, as the water most places are too deep for the glacier to ground far out in the fjords (Evans et al., 2002). Hence, the moraines in the fjord most likely predate the Younger Dryas stadial.

The geographical direction of the fjords may have been determined by geological structures providing bedrock of varying strength of resistance against erosion (Syvitski et al., 1987). These structures include fault zones, igneous intrusions and general variations in composition of the bedrock. As the Bergsfjord peninsula comprise of massive intrusions this seem to be a good explanation of the L-form of Øksfjorden.

2.4.5.2 Bergsfjorden (70°17'N, 21° 48'E)

Morainal till deposits are previously mapped in the inner part of the fjord (Figure 6). Inflow of organic material from 'outside' the fjords, seem to in particularly affect Bergsfjorden, due to its proximation to the main ocean and the width of the fjord. Bergsfjorden is an outer continuation of Langfjorden, here included in the study. Sandlandsfjorden to the east of

28

Bergsfjorden is classified as a strandflat, thus the shallow inlet represents a previous shoreline not subducted under water.

2.4.5.3 Jøkelfjorden (70°4'N, 21° 58'E)

Jøkelfjorden is especially affected by the high proximity to the Øksfjordjøkelen, with subglacial rivers transitioning into a waterfall draining down in the reconstituted glacier located at the head of the fjord. Not long ago, the glacier calved directly into the fjord.

2.5 Glaciology

2.5.1 Introduction

Mainland Norway, with its large area of 323 781 km^2 (Kartverket, 2017) today has a glaciated cover of 2692 km^2 (L. M. Andreassen et al., 2012). A reduction of 11 % is found to have occurred over a mean period of ~30 years, with the northernmost glaciers retreating with the highest rate (Winsvold, 2017). Measurements to estimate the size of the plateau glaciers at the Bergsfjord peninsula has sporadically been made the past 100 years along with measurements and reconstructions of the equilibrium line altitude (ELA).

2.5.2 Definitions

Plateau glaciers or *ice caps* are defined as a broad, upstanding glaciated areas possibly with the underlying land being a topographic high. Similarly, *Ice sheets* are also dome-shaped, but cover areas greater than 50 000 km^2. *Outlet glaciers* are channels of ice radiating out from the ice caps or ice sheets, occupying troughs or valleys. A glaciers *mass balance* is the best overall measure of annual changes in mass storage (water equivalent). ELA (equilibrium line altitude) is the boundary between the *ablation-* and *accumulation zone*. When the ELA is situated above the highest point of a glacier and the situation persists for many successive years, rapid glacier recession may occur. (Benn & Evans, 2014). It is important to keep in mind that glacial retreat occur faster than build up (Raymo, 1992), thus glaciers have a faster response to a climate conditions leading to ablation.

2.5.3 Movement

As one of the most effective erosional agents, glaciers excavate troughs and fjords (Benn & Evans, 2014). Especially fast flowing ice streams erode great amounts of rock and transport it out to the continental shelf. Due to the dome shape of the Fennoscandian Ice Sheet, the main movement of the ice sheets were from the center and out toward the ocean. Hence deciding the location and alignment of the fjords. The alignment of the fjords at the Bergsfjord peninsula indicate radiating streams of ice from Øksfjordjøkelen.

2.5.4 Thermal regime

Due to findings of striated bedrock surfaces and moraine sequences the plateau glaciers in the study area are defined as warm-based (Gellatly et al., 1988; Whalley et al., 1989). Preserved blockfields surrounding Øksfjordjøkelen have been investigated and are assumed to predate the Pleistocene glaciations, or possibly interglacial periods, as warm and humid-type of weathering is inferred (Whalley et al., 1997). The preservation of the blockfields might imply that a cold-based ice sheet has been present in earlier times (B. R. Rea et al., 1996), however it can also indicate that it was above the ice as nunataks (Vorren et al., 2007). No other evidence of cold-based ice has yet been found at Øksfjordjøkelen (Whalley et al., 2004).

2.5.5 Glacier extent

Reconstructions of glacier extent may be carried out based on various proxy analyses. Sediment from the deep sea, the continental shelf and fjords may preserve evidence of glacier- and sea ice extent (Howe et al., 2010). Locally, past glacier extent may be decided by the location of moraines.

Maps of the ice caps at the Bergsfjord peninsula were first published as a quadrangle map in 1907 (Angell et al., 1907), stating that areas of the glaciers were as seen in Table 1. These maps were updated in 1940 and 1965. In 1973, the Atlas73 was published by (Østrem et al., 1973), including estimations of size (as seen in italic in the table), but also an estimated volume of 4.4 km^3 for Øksfjordjøkelen (using a mean thickness of 200 m). Existing maps and aerial images were used when the extents of the glaciers in northern Norway were mapped for Atlas73 (Østrem & Haakensen, 1993). The sizes from 1988 and 2006 were measured by NVE (NVE, 2006). In 2006 the areas were measured by a Landsat sensor measuring with an accuracy of 3 % (L. M. Andreassen et al., 2012). A general trend of growing glaciers was observed in the 1990's, but during the past 30 years the glaciers in northern Norway were estimated to have been reduced by 17 % (Winsvold & Andreassen, 2015). All over, the glaciers in northern Norway has reduced its size by more than 50 %, since the beginning of 1900 CE, from 139 to 65 km^2 (Winsvold & Andreassen, 2015).

Table 1. Estimated and measured area of the glaciers at the Bergsfjord peninsula. The earlier sizes have a higher source of error than the ones measured in 2006. Areas after (NVE, 2006) and (Østrem et al., 1973).

Year (CE)	1907	1966	1973	1988	2006
Øksfjordjøkelen (km^2)	49.7	47.1	41.1	42.0	38.6
Svartfjelljøkelen (km^2)	8.5	6.9	5.0	5.5	4.13
Langfjelljøkelen (km^2)	21.5	13.5	9.9	9.2	7.5

2.5.6 Equilibrium line altitude

Reconstructions of past ELA of ice caps may be calculated from accurate glacier extent estimates if the glacier was in sync with the climate at the time (Benn & Evans, 2014). The rapid reaction to the changing climate after Younger Dryas show that Øksfjordjøkelen was in equilibrium with the climate (Evans et al., 2002). (B. R. Rea & Evans, 2007) estimated the ELA of Øksfjordjøkelen to be between 498 and 590 m above the present sea level during the largest Younger Dryas extent. Today, glaciated ice is situated between ~400 and 1200 m a.s.l. With an ELA above 900 m a.s.l. (B. R. Rea & Evans, 2007).

2.5.7 Øksfjordjøkelen (70°9'N, 22°4'E)

With its 38.6 km^2, Øksfjordjøkelen is the 9th largest glacier In Norway (Østrem & Haakensen, 1993). Its ice thickness is believed to be at least 100 m and reflect the underlying slope of the plateau surface (Whalley et al., 1989). A regenerated glacier, Nerisen, is situated at the head of Jøkelfjorden (Figure 20). The calving down to Nerisen previously also went directly into the fjord, this ceased in the 1990's. Øksfjordjøkelen was the last glacier on main land Europe

to calve into the ocean (Askheim, 2016). Presently, Øksfjordjøkelen drain to all three fjords comprising this study, with 10 small outlet glaciers (B. R. Rea & Evans, 2007).

Figure 20 Jøkelfjord and the regenerated Nerisen, 1973. The photograph on the front page represent the present conditions, with a small, non-calving glacier. From the early 20th century fishermen retrieved ice here. The calving glacier generated tsunamis up to 30 meters when calving into the fjord. From (Østrem et al., 1973).

2.5.8 Langfjordjøkelen (70°7'N, 21°43'E)

In Norway, Langfjordjøkelen is the glacier with the largest recession, presently covering an area of approximately 7.5 km² (L. M. Andreassen et al., 2016). Mass balance measurements are being conducted in order to examine the glacier fluctuations (Figure 21). This has been done since 1989 with a break from 1993 to 1996. In 1996 length-, thickness- and velocity measurements were initiated (NVE, 2018a). The ice cap is relatively small, and therefore has a short response on climate variations.
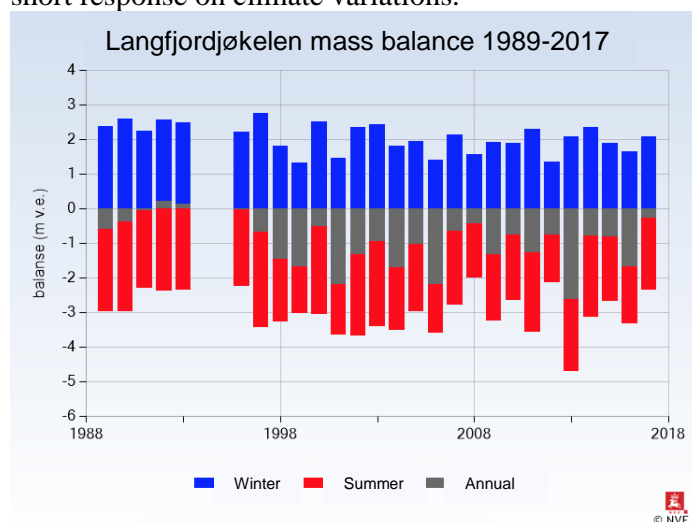
Figure 21 Mass balance measurements from Lansgfjordjøkelen 1989-1993 and 1996-2017. The glacier is retreating, more than any other glacier in Norway. Figure modified after (NVE, 2018a).

2.5.9   Svartfjelljøkelen (70°14'N, 21°57'E)

The approximate 4.13 km^2 glacier today has an ELA sitauted at ~870 m a.s.l. A small lake
called Bergsfjordvatnet is in the catchment area of Svartfjelljøkelen. Eeg (2012) reconstructed
the ELA through Holocene, and found little or no glacigenic sediment supplied to
Bergsfjordvatnet between 7,000 and 5,200 cal. yrs. BP. Svartfjelljøkelen drains directly into
Langfjorden. Bersfjordsvatnet drains to Bergsfjorden, thus sediment be trapped in the lake.

2.6 Hydrography

2.6.1   Oceanography

The North Atlantic Current (NAC), an extension of the Gulf Stream, flows northeastward
towards Norway, branching into several relatively warm and steady currents (Rossby, 1996)
(Figure 22). Warm (2–13 ºC) and salty (≥ 35 PSU) Atlantic Water (AW) is carried into the
northern North Atlantic by the Norwegian Current (NC) and continues both into the Arctic
Ocean as the West Spitsbergen Current and into the Barents Sea as the North Cape Current
(Figure 22) (Hopkins, 1991). Coastal Water (CW) is influenced by freshwater run off from
the Norwegian mainland and thus characterized by reduced salinities (< 35 PSU). It overlies
the AW as a westward thinning wedge (Figure). The salinity increases northward along with
the mixing of the two water masses, thus preventing sea ice to form in northern Norway
(Sætre & Ljøen, 1972). AW of the NC and CW of the Norwegian Coastal Current (NCC)
constitute the surface waters surrounding the study area (Hald & Vorren, 1984).
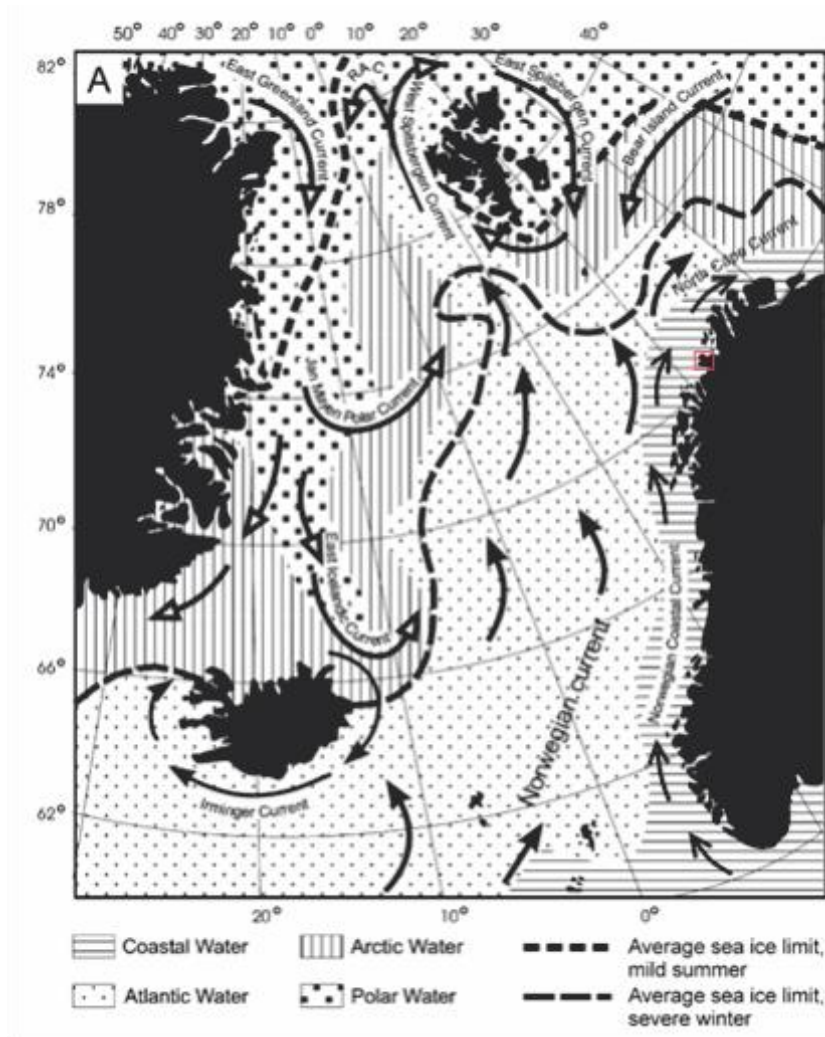
Figure 22 The Norwegian Current is an extension of the North Atlantic Drift and the Gulf Stream, transporting warm Atlantic Water to Norway by the Norwegian Current (NC). Study area is highlighted in red. From Hald et al. (2007).

The surface temperature and salinity of the coastal waters surrounding the study area has been measured at a fixed station in Loppa (Figure 23). Here, the mean annual salinities vary between 34 in the winter season and 32 in the summer months when the temperatures are highest and hence increasing the fresh water runoff. Mean annual sea surface temperatures vary between 3 °C in March and 10 °C in July, with a slow decrease in the fall and a relatively fast increase in the spring.
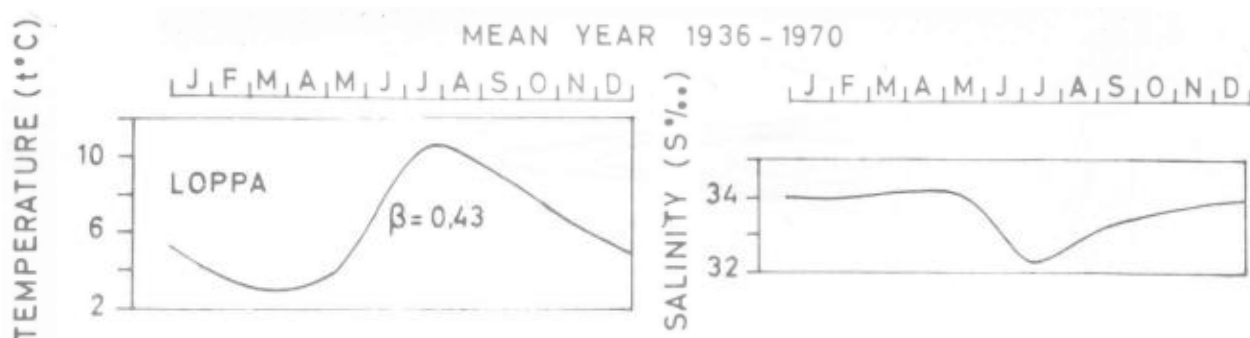
Figure 23 Mean annual sea surface temperature and salinity measured at a fixed station in Loppa from 1936 to 1970. Its position is shown in Figure. Figure from (Sætre & Ljøen, 1972).

The study area is in a region affected by climatic variability in atmospheric circulation patterns such as the North Atlantic Oscillation (NAO) and the Arctic Oscillation (AO) i.e. affecting the latitudinal position of the Polar Front (the boundary between the Polar and the Arctic Water) and the strength of the NAC (Figure 22) (B. R. Rea & Evans, 2007; Brown, 2016).

Fluctuations in the warm Gulf Stream and the heat it releases to the atmosphere in the northwestern Europe and the northern North Atlantic affect the climate (Boyle & Keigwin, 1987), Presently, the region is 5–10 ℃ warmer than the zonal mean (Monroe & Wicander, 2011).

2.6.2 Hydrography in fjords

2.6.2.1 Introduction
The long indented Norwegian coastline of 25 148 km stretches between 58° and 71° N with its fjords bordering towards the North Sea, the Norwegian Sea and the Barents Sea (OECD, 2001, 2011). Several components control the exchange of water between fjord and coast. Dynamics of temperature and salinity, tides, wind, the Coriolis' effect and the topography, as well as the availability of water, all contribute to various circulation patterns in fjords (Hansen & Rattray, 1966; Klinck et al., 1981; Howe et al., 2010). Fjords are a type of estuary: a semi-enclosed coastal inlet of water with a free connection to the open ocean inhering saline seawater by freshwater derived from land drainage (Gade, 1986; Syvitski et al., 1987). They are, however, deeper than other types of estuaries (Gade, 1986)

2.6.2.2 Circulation
Water movement in estuaries is mainly controlled by thermohaline forcing (Cottier et al., 2010). Fjords are characterized by a well-developed stratification and an exchange caused by the salinity and temperature differences in the water masses (Hansen & Rattray, 1966; Syvitski et al., 1987; Howe et al., 2010; Sælen, 2016). They often inhere what is known as *fjord estuarine circulation* (Figure 24). It is equal to partially mixed estuaries, with a surficial plume of freshwater entering at the fjord head and saline water entering at the fjord inlet (Skei, 1983). The stratification of the water masses consist of; an estuarine surface layer (in the upper 5-50 m), an intermediate layer (between the surface water and the sill), and basin water (deeper than the sill). This stratification is often well defined near the freshwater source, with progressively higher mixing rate and hence reduced stratification further out (Hansen & Rattray, 1966). Water with lower salinity is transported out from the fjord in the surface layer, originating from riverine freshwater input. The thickness of the surface layer varies with the width of the fjord, the proximity to the freshwater source and the discharge in the rivers. A compensating current of denser water is often present in the intermediate layer, with the strength of the current defined by the density differences between the outer and inner water masses (Syvitski et al., 1987; Howe et al., 2010). The Basin water may consist of a relatively still-standing water mass sporadically exchanged by barotropic tidal currents spilling ocean water over the sill (Farmer & Freeland, 1983).
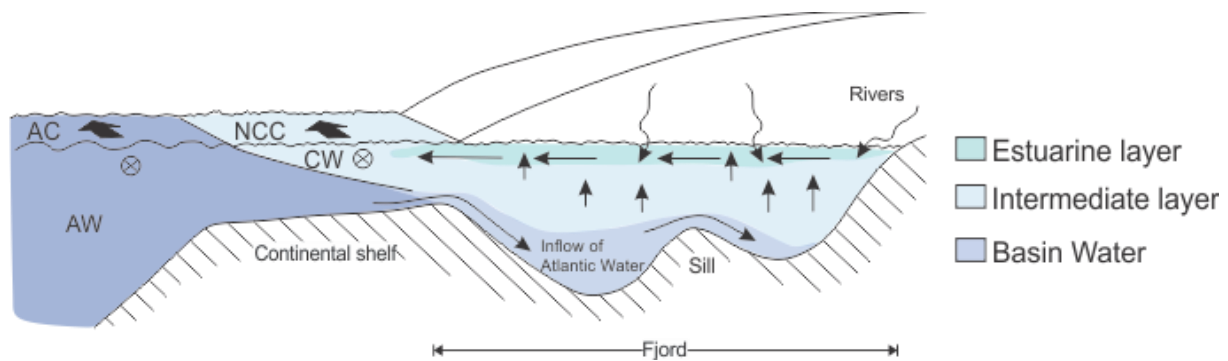
Figure 24 Fjord circulation and the northward flowing Atlantic Current (AC) and Norwegian Coastal Current (NCC); Atlantic Water (AW) and Coastal Water (CW), respectively. A steep density gradient separates the estuarine- and intermediate layer, with a gradually deeper halocline further distal from the freshwater input due to the increased mixing (Cottier et al., 2010). Modified after Gade (1986) and Mangerud et al. (2006).

Stratification in a fjord changes seasonally (Syvitski et al., 1987; Cottier et al., 2010). When the fjord is ice free, wind forcing gives rise to upwelling and strong surface circulation (Cottier et al., 2010). The well-developed stratified circulation of temperate fjords in the summertime may be opposed with a lack of estuarine circulation in the winter when run-off is limited and circulation prohibited (Syvitski et al., 1987). A more defined stratification occur progressively from June when the snowmelt begins to increase towards a peak around September (Figure 16). Cooling of the surface layer in winter may result in a vertical circulation due to increased densities of the overlying water masses, renewing the basin water (Sælen, 2016).

Alongshore winds cause large changes in the volume of water in a fjord, as opposed to cross-shore winds (Klinck et al., 1981). Several Arctic fjords are affected by very strong katabatic winds along the axis of the fjord and may lead to a pile up of water by the fjord mouth (Cottier et al., 2010). This may result in an opposite flow direction in the intermediate layer, which might contribute to deep water renewal in the basins. In the Arctic region circulation caused by wind dominates when the fjord is free from sea ice and can cause internal rotational circulation rotation (Cottier et al., 2010).

2.6.2.3 The effect of present sills on the circulation

If a sills are present, a three-layered stratification occurs such as described above. Some fjords have more prominent sills than others, affecting the oxygen supply and renewal of the basin water (Syvitski et al., 1987; Sælen, 2016). Renewal of the basin water may occur by barotropic tidal currents spilling over the sills, by meteorological forcing causing horizontal pressure gradients or by direct shelf processes pushing dense water over the sill (Figure 24) (Farmer & Freeland, 1983). The frequency of deep water renewal depends on the height of the sill because favorable conditions forcing the denser external water to flow over may be caused by cyclic tidal waves or infrequent intensity of storm surges every year or so. If the sill is to shallow, anoxic conditions may occur, affecting the possibility for life to take place in the basins (Farmer & Freeland, 1983). Sea-level change will enhance or restrict this water exchange (Howe et al., 2010). The restricted deep-water renewal may also affect the sedimentary environment (Skei, 1983). Sills constrain the fjord basins, and hence reduce the loss of sediment off shore and increase the storage capacity of the fjord (Ballantyne, 2002).

2.6.2.4 The effect of circulation on the sediment distribution

The Coriolis' Effect deflect surface currents to the right in the northern hemisphere (Garrison, 2009). Surface currents flow out of the fjord and are hence deflected to the right hand side of the fjord. The incoming denser, and hence deeper waters are also constrained to the right side

of the fjord and are, thus, deflected to the opposite fjord side compared to the fresh surface water. This circulation will affect the sedimentation in the fjord (Syvitski, 1989; Howe et al., 2010) (Figure 25). As most of the sediment are transported into the fjords by the rivers (Skei, 1983), the highest sedimentation rate will be on the right side from the fjord head.
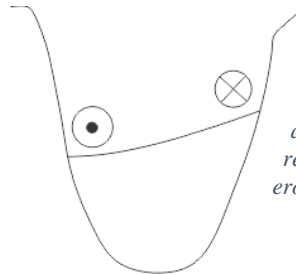
Figure 25 Due to the Coriolis Effect, outward lowing currents deflect to the right hand side (in the Northern Hemisphere). Inward flowing, denser (and hence deeper flowing) currents also deflect to the right hand side, thus to the opposite side of the outward flowing. As the main contribution of sediment arrive from the rivers making up the outward flowing current, accumulations of sediment often occur in higher rates at the right hand side. In periods of relatively high riverine discharge, the outward flowing current may increase in velocity, hence eroding instead of depositing.

As the mean sea level in fjords remains constant, the outflowing total water volume exceeds that of the incoming seawater due to the addition of riverine input (Klinck et al., 1981; Talley, 2011). The outward flowing current velocity is therefore greater than the inward, and the sediment distribution may vary according to the strength of this. In periods of high runoff discharge, the outward flowing current velocity will increase and may instead lead to erosion on the right hand side, transporting the sediment further out. The size fraction of the transported sediment is also distributed by the varying strength of current at various locations in the fjord.

2.6.3   Hydrography in the fjords of the Bergsfjord peninsula

Tides and wind are expected to dominate the circulation in the fjords in the study area, overriding the effect from the estuarine circulation (Sælen, 2016). The effect of wave action is probably relatively small compared to the other dominating effects. It might not affect Jøkelfjorden at all due to its sheltered position away from the ocean. Because sea ice is seasonally present, at least in the inner fjords, it could restrict the estuarine circulation. Winds may, however, be stronger in the winter time, and katabatic winds may blow out the fjords, still increasing the circulation. Sills are locally present in all fjords, but the fjords have not been reported as anoxic, thus basin water renewal is not restricted. The fjords comprising the study area are in a periglacial environment with proglacial and fluvial rivers entering the fjords.

2.7 Sediment sources

2.7.1   Introduction

Sediment deposited in the fjords are stratigraphic archives representing the marine, terrestrial and atmospheric environment in the source, transport and depositional area of the past and the present (Howe et al., 2010). Bedrock is exposed to chemical and physical weathering and eroded by glaciers and rivers before it is transported by the same means or by wind, currents or floating ice bergs. Finally, it is deposited in a low- or high-energy environment. It all leave traces in the size, sorting and shape of the grains (Nichols, 2009).

2.7.2   Processes

A lot of processes affect the sedimentation in both glaciated and non-glaciated fjords, these are summed up in Figure 26. Due to the continuous reworking and redeposition of sediment, the observed distribution may be caused by a combination of several processes (e.g. Holtedahl & Bjerkli, 1975).
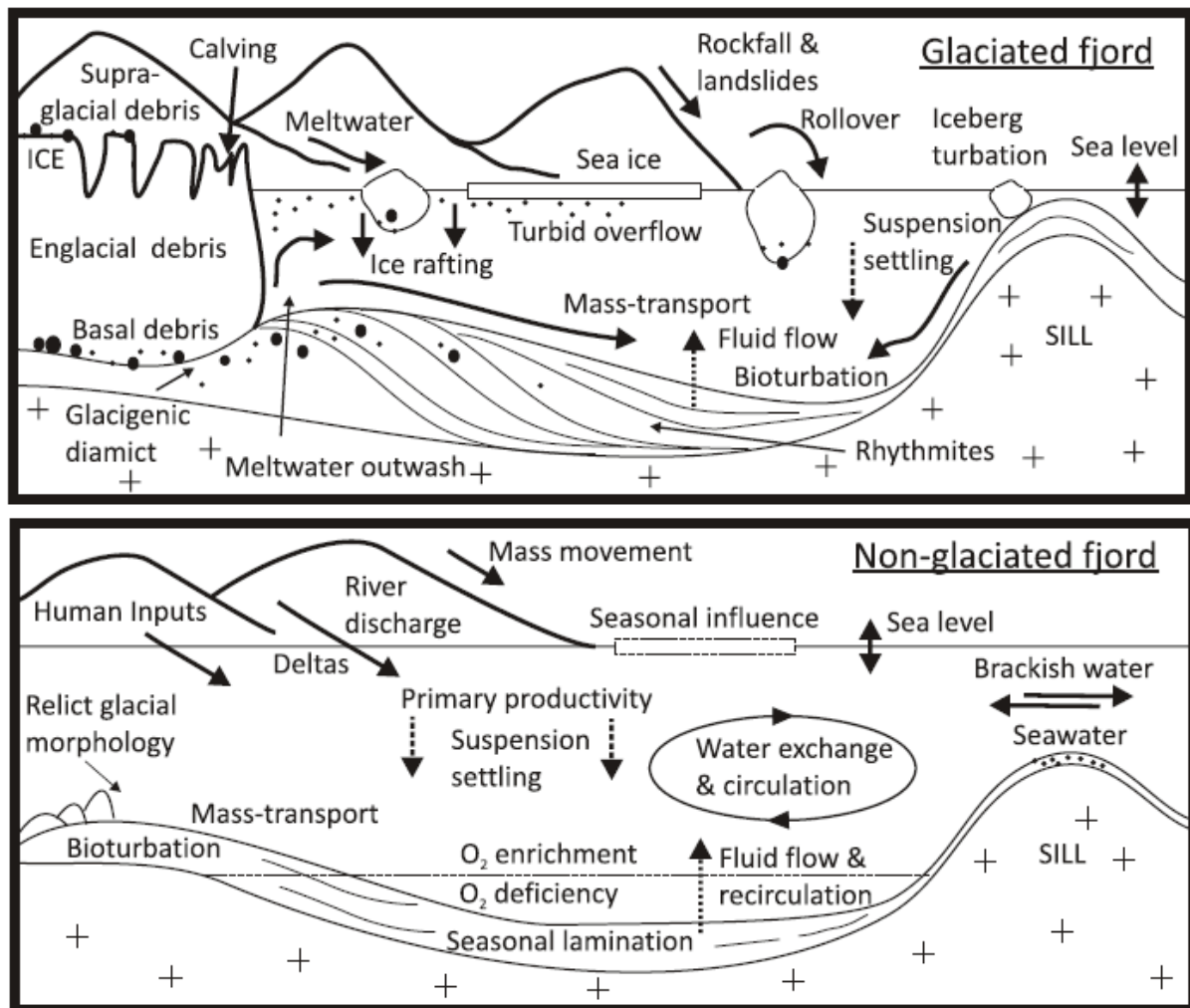
Figure 26 Summary of sedimentary processes in glaciated and non-glaciated fjords. In modern temperate fjords, sediment supply is controlled by river discharge. Figure after Howe et al. (2010).

Generally, coarser sediment is deposited with a higher proximity to the glacier margin or the fjord head and the finer fractions carried further out (Nichols, 2009). Rivers and ocean currents sort the grains, distributing them after size based on the strength of the current transporting them (Hjulström, 1939). Typically,the grain size of fjord sediment decreases with depth and the net sediment accumulation rate is usually higher in fjord basins than along the shores (Holtedahl & Bjerkli, 1975). Seasonal increase in precipitation and temperature increase the discharge in rivers due to additional run-off and melting of snow and ice. The strength of the ocean currents also vary with time, affecting the distribution of the sediment. Finer sediment fractions are transported in suspension and is capable of travelling greater distances than the coarser before settling (Syvitski et al., 1987).

In glaciated fjords the largest contribution of sediment supply occur due to the high discharge in the sub- and englacial streams developing through the summer (Benn & Evans, 2014). Sediment may be brought to the fjord by sediment plumes entering subglacially, washing out sediment below sea level, or by melt-out of the sediment incorporated in the ice (Figure). B. R Rea and Brian Whalley (1994) studied the subglacial ice of Øksfjordjøkelen, and found a concentration in basal debris to vary between 0.005 and 15.38 %. Glaciers calving into the fjord create ice bergs transporting incorporated sediment far away from its source. Sea ice may also contribute to a sporadic grain size distribution by transporting sediment. Rafted

37

detritus are poorly sorted sediment with a variety of angularities distributed by ice bergs, algae and sea ice (Figure). Mackiewicz et al. (1984) identify *ice rafted detritus, IRD*, as isolated particles > 177 µm, however they point out that glacier proximal sediment may be of similar sizes. Hence, largely opposing the natural grain size distribution caused by current and discharge velocities.
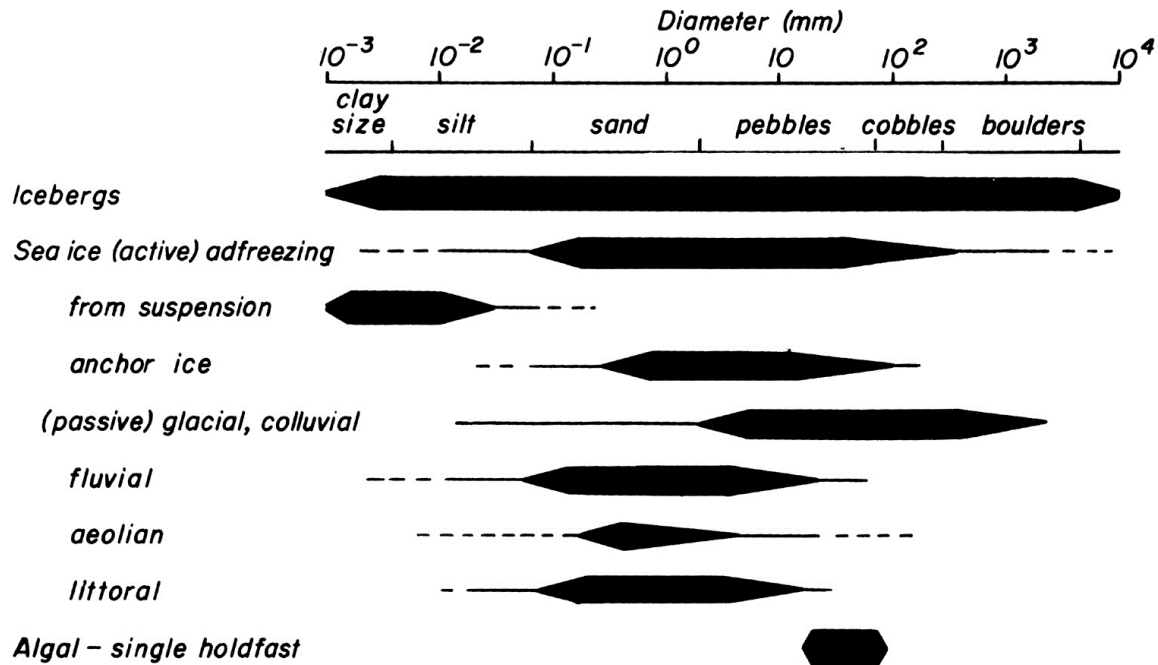
Figure 27 Mediums rafting detritus in fjords and the grain sizes of the particles. Passive = debris landing on top of the glacier and riding along when breaking off. Active = sediment brought with because it has frozen into the ice. Deposits transported by icebergs or sea ice are called IRD. These are often sub-angular, poorly sorted deposits with a mix of all grain sizes. Figure from Gilbert (1985).

In both glaciated and non-glaciated fjords gravity mass-movement processes deposit sediment directly into the fjord. Sea ice and glaciers in the fjords restrict direct deposits from gravity mass-movements. Instead, it may be transported as IRD. In northern Norway, mass movements due to slope failure along the steep sides of the fjords are common (Vorren et al., 2007). Weathering processes such as freeze-thawing processes, snow avalanches or debris flows are typical. Slope instability may also occur below water inside the fjord as high sediment supply settle in slopes steeper than the angle of repose (Syvitski et al., 1987). Sediment creep, slide, or flow as debris flows and turbidity flows, transporting coarse sediment into the basins and to areas of normally low sedimentation rates (Howe et al., 2010). Mass-movement activity generally increase in climatic periods favoring glacier build up (Gilbert, 1985). However, postglacial isostatic rebound caused seismicity that may have initiated rock avalanches and other types of large scale mass-movements such as rock falls to occur in the Holocene (e.g. Dehls et al., 2000b). Rock falls into the fjord may cause tsunamis, or tsunamis may generate offshore entering the fjords and stirring up the sediment e.g. (R. Bøe et al., 2004). Mass-wasting events may result in a variety of deposits (e.g. turbidites), generally with an erosive lower boundary with unsorted sediment and shell fragments deposited on top.

Fjord deposits consist of both organic and inorganic; marine and terrestrial detritus. The transport of inorganic marine sediment by inflowing seawater is, however, considered negligible (Skei, 1983). In oxic fjords, more than 90 % of the deposits generally consist of terrestrial inorganic material (Syvitski et al., 1987). Sparse vegetation in the catchment area

may limit the input of organic terrestrial material, but some pollen, leaves etc. probably find their way. In addition to stirring the sediments, the marine biota leaves behind datable traces (tests) essential for stratigraphic reconstructions. Most often, the dominant sediment contribution in fjord deposits are inorganic sand, silt and clay, supplied from rivers (Skei, 1983).

The biological productivity is controlled by the environment. Various species have different preferences with the general climate and living conditions affecting its capability to survive (Nichols, 2009). Preserved remains of previously present species may give indications on the climate of the past e.g. (Kucera, 2007). Benthic foraminifera dominate in fjords as planktonic foraminifera generally prefer water with a higher salinity (Howe et al., 2010). Bioturbation can cause considerable disturbances in the sediment, especially when the sedimentation rate is low (c. 1-3 cm/ka) (Dowdeswell, 1987).

A summary of the parameters affecting the sedimentation both direct or as secondary effects may be seen in Table 2.

Table 2 Parameters affecting sedimentation in fjords. Adapted from (Syvitski et al., 1987).

Parameters	Effect	Effect on sedimentation
Glacial	Relative Sea level, warm- vs. cold based glaciers, glacier-fjord contact, calving, seasonal variability, advance and retreat	Erosion, sediment supply, IRD, till, water discharge in rivers, retain water and sediment, reworking of sediment
Fluvial	Discharge, transport rate, freshwater, stratification, delta,	Sediment supply, turbidity, bed load, suspension
Climatic	glacier movement (calving, retreat, advance), sea ice, thermal stratification, wind, production of biomass, ocean/fjord current	Till, seasonal variability, sedimentation rate, distribution of sediment, inorganic/organic ratio
Geographic	Fjord dimensions, isostasy, tides, Coriolis' effect, contact with ocean	Reworking of sediment, distribution of sediment
Geotechnical	Slope failures, gravity mass-movements and seismicity and tsunamis	Reworking of sediment, sedimentation rate
Biological	Burrowing, chemical composition	Reworking of sediment, inorganic/organic ratio

Whether glaciers produce more sediment when advancing, retreating or during still-stands is generally not agreed upon (Ballantyne, 2002). However, fluctuating glaciers will create a higher energy environment and events of higher sediment input (such as floods, jøkuhllaups and mass-wasting) will be more frequent (Gilbert, 1985).

2.7.3 Evolution of fjord deposits
The evolution of typical sediment infill in Norwegian fjord is seen in Figure 28 and Figure 29. Gilbert (1985) model is valuable for understanding the process of formation of deglacial deposits in fjords, showing facies depositing during glacier fluctuation (Figure 28). Long periods of still-standing glacier fronts result in thicker till deposits and prominent morainal banks, short still-standing periods result in several smaller moraines and till cover subsequently depositing in the fjord, while a rapid glacier retreat leave no prominent till deposit (Corner, 2006).

The depositional style and regimes of the different evolutionary stages, including the postglacial stages of sea level regression and deltaic build up is described in Figure 29; *Degradational* fluvial terracing occur at times of relative sea level fall, *aggradation* is the upward building, depositional style occurring furthest away from the input of sediment, but is present in all stages. *Prograding* fluvial deltas are present when the glacier is not in direct contact with the fjord, building outwards. The shoreline moves laterally according to the position of the glacier and the delta, and vertically due to the eustatic sea level and the isostatic uplift of the crust, as seen by the shoreline trajectory in Figure 29.

2.7.4 Sedimentation rates
Sedimentation rates typically average ~1-10 mm per year, with occasional events of higher sedimentation (Skei, 1983; Howe et al., 2010). The amount of sediment put into fjords depends on the size of the catchment area and the forces working here. Sedimentation rates increase with a greater sediment supply along with increasing discharge of the rivers. A glacial erosive force in the catchment area produce more sediment available for transport, and increased precipitation and melt rates increase the discharge. Sedimentation rates are generally higher at the river outlets than further distal.

2.7.5 Rythmites
Seasonal variations in e.g. sedimentation rates may produce visible laminae or layering in the deposits. The larger the seasonal climate variations, the greater the likelihood of present rythmites. River discharge often vary with the seasons, hence river-transported terrigenous sediment is seasonally dependent (Skei, 1983). Flood pulses generally occur at times when high precipitation- and melting rates occur simultaneously, so does jøkulhlaups and gravity mass-wasting and typically result in abrupt sedimentation. Organic productivity is also generally seasonally dependent as may be seen in colors or the chemical composition. As mentioned, sea-ice may temporarily reduce the input of sediment, and lamina or layering may be produced due to this seasonal limitation (Syvitski et al., 1987). As the general sedimentation rate needs to be relatively high in order to produce visible rythmites, an increased proximity to the river outlets increase the possibility for these to occur.
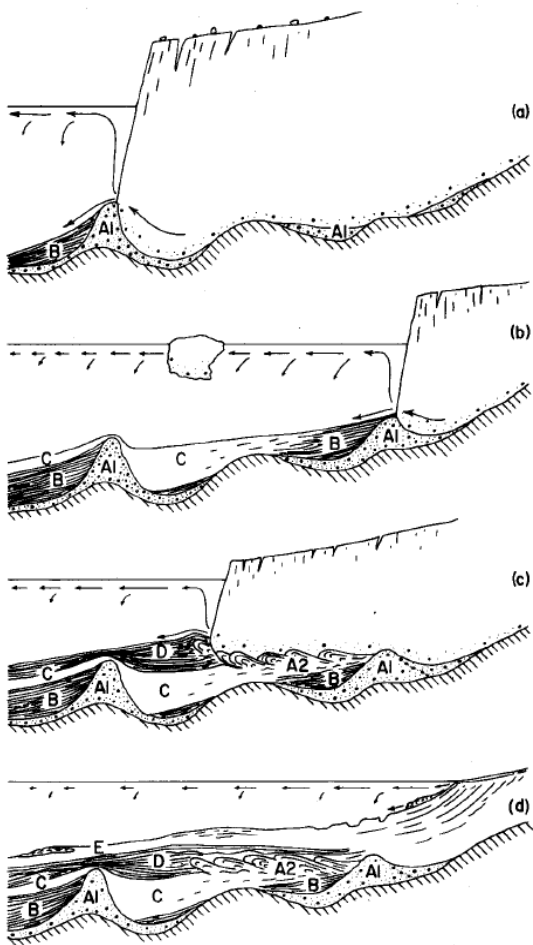
Figure 28 Facies and mechanisms processing a general sequence of glacial and glacimarine sediment in a typical glaciated fjord environment. Each figure represent different climatic environment; (a) glacial still-stand, (b) glacial retreat and calving glaciers, (c) glacial advance, and (d) glacier withdrawn from the fjord. Sub-glacial sediment plumes deposit massive ice-contact till without structures (Facies A1) and proximal stratified glacimarine sediment (Facies B). Readvancing glaciers modify the deposits into the deformed deposit illustrated as Facies A2. Facies C and E comprise of unstratified, low-energy deposits, suggesting less active glaciers, possibly not even present in the catchment area during the deposition of Facies E. The stratified Facies D represent a reactivation of the high-energy environment with a higher sedimentation rate and coarser material deposited than in C and E indicating an increased proximity to the glacier margin. Interpreted from fjords at Baffin Island by (Gilbert, 1985).
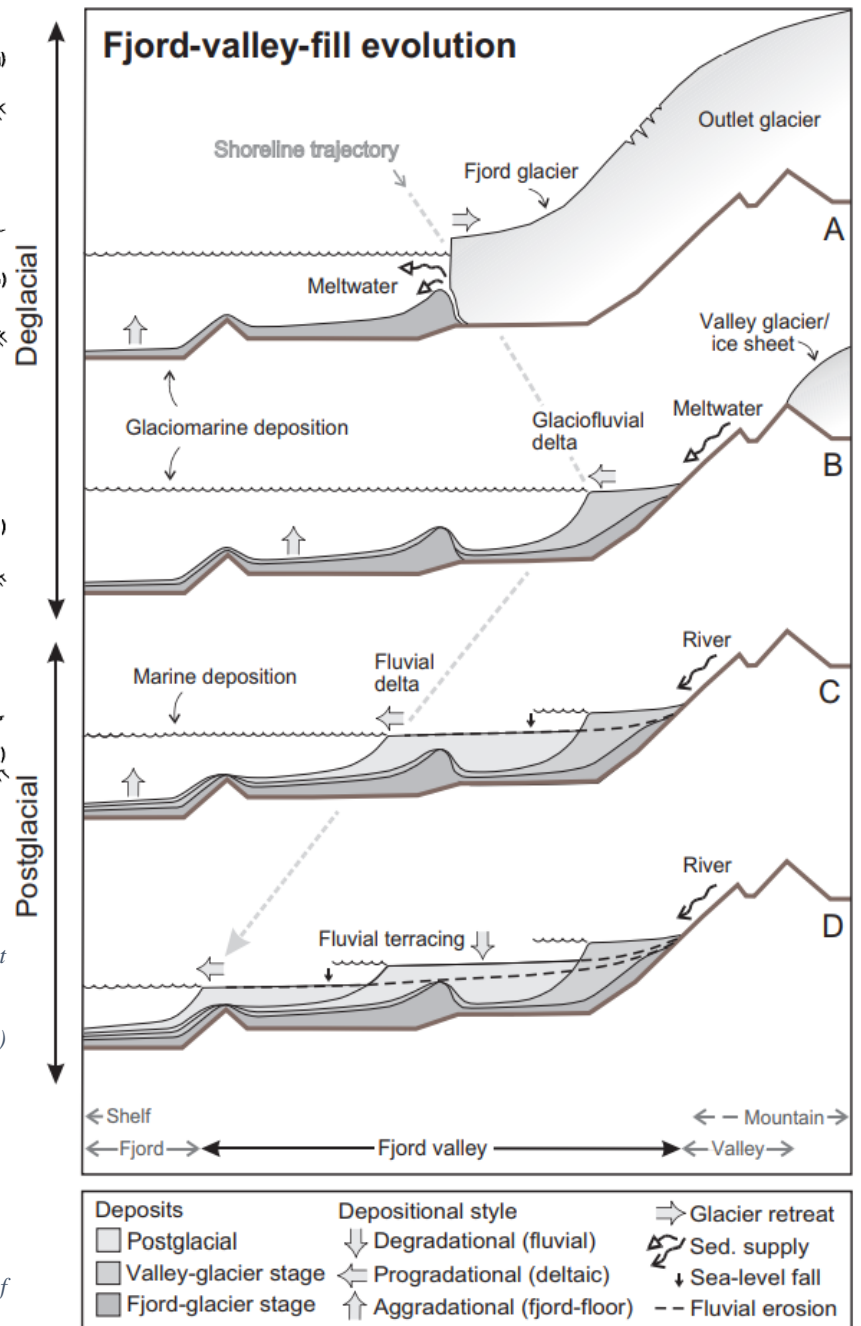
Figure 29 Illustration of the evolution of fjord-valley infill. A) a fjord-glacier stage (as in Figure 13; a, b and c), B) valley-glacier stage represent a depositional regime affected by glaciers confined to the upstream valley, introducing the effect of glaciofluvial rivers and deltaic deposits at the fjord head, C) and D) postglacial stages with sea level regression building out deltas and creating fluvial terraces. From Corner, 2006.

3   Material and Methods

High-resolution seismic data (chirp) and three sediment gravity cores provide the basis for this study (Figure 30). The data were collected during an educational cruise on R/V Helmer Hanssen arranged by UiT in 2012 (Forwick & Rasmussen, 2012).
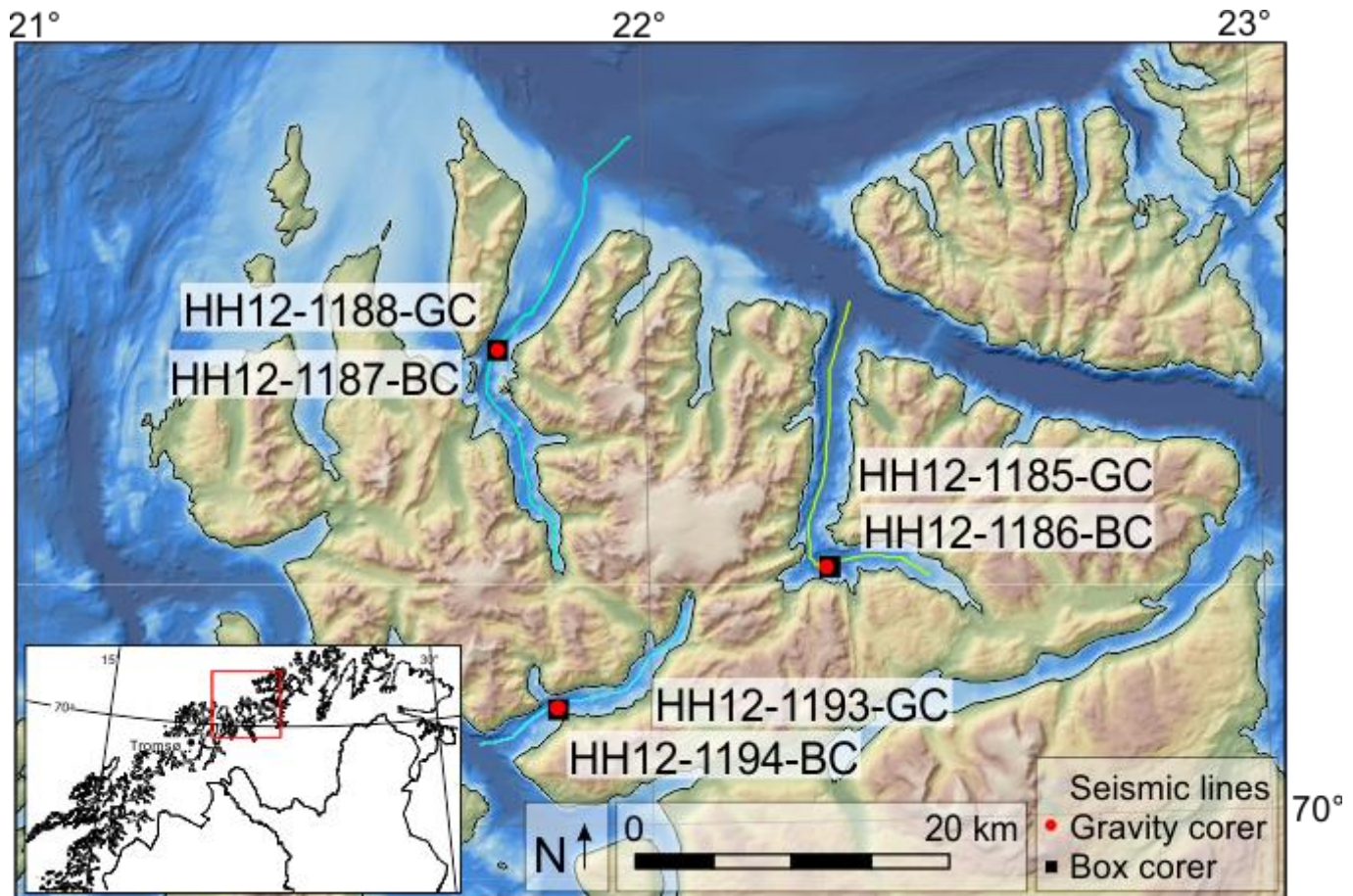
Figure 30 Show the location of the composite chirp lines in each fjord as well as the location of the box- and gravity cores retrieved. HH12-1185-GC and HH12-1186-BC are located in Øksfjorden, HH12-1188-GC and HH12-1187-BC in Bergsfjorden, and HH12-1193-GC and HH12-1194-BC in Jøkelfjorden. Modified after Jan P. Holm.

3.1 Seismic profiling (chirp)

On board the vessel a hull mounted EdgeTech 3300-HM sub-bottom sonar profiler (4*4 array) is used when retrieving high-resolution 2D seismic profiles (chirp data). A single echo sounder sends out acoustic energy in a range of frequencies, providing 6-10 cm vertical resolution of the sub-seabed (EdgeTech, 2016). The frequency spectrum in this survey were 2.0-12.0 kHz lasting for 3 ms (Forwick & Rasmussen, 2012). This profiler is recommended used in water depths down to 3000 m with typical penetrations ranging between 6 and 80 m depending on the P-wave velocity of the sediment measured (EdgeTech, 2015).

During the survey the weather was generally good with gentle winds and calm sea. The velocity of the vessel was 7-9 kn. With respect to the fish farms in the area all chirp data were collected with a signal strength reduced to 25 %. (Forwick & Rasmussen, 2012).

Reflections occur at vertical changes in acoustic impedance (Z) and depend on the density and the P-wave velocity of the sediment. The two-way-time (TWT) of the reflected acoustic pulse is recorded and may be converted into distance to the reflection by the function:

$$Distance = \frac{Velocity\ \left(\frac{m}{s}\right) * TWT\ (s)}{2}$$

P-wave velocities of the sediment retrieved by gravity coring were later measured for this purpose. However, the velocities vary a lot and are largely unreliable due to the low P-wave amplitudes. Therefore, velocities of 1500 m/s are used when calculating the distance between the reflections (Forwick & Vorren, 2010). The P-wave velocity of the water in the area is assumed to be 1500 m/s as the distance to the water/sediment interface match with the depth measured at the stations after calibrating it with CTD-data obtained preceding each core retrieval.

Due to the approximate beam width of 22º (EdgeTech, 2016) occasional side echo occur in the chirp data and are recognized by weaker reflections abruptly intruding stronger reflections such as the sea floor reflection. Multiples are delayed repetitions of a reflection and are recognized by the reversed polarity compared to the primary reflection with the shortest TWT. (K. Andreassen, 2015). Both artefacts are kept in mind when interpreting the chirp data.

3.2 Box- and Gravity Coring

Three gravity cores were retrieved, one from each fjord (Figure 30). The location of the coring sites were decided based on the chirp data collected (Table 4). In addition one box core were retrieved at each station (Table 3).

The gravity corer is a 6 m long steel barrel with a plastic liner (outer diameter 11 cm, inner diameter 10 cm). In total, the gravity corer weigh 1900 kg. After retrieval the plastic liner was cut into sections (~1 m), cleaned, covered with plastic caps, taped, labelled and stored at 4 ℃.

Table 3 Box-core stations and specifications. Modified after (Forwick & Rasmussen, 2012).

Station	Date	Time (UTC)	Location	Latitude [N] Longitude [E]	Water depth [m]	Comments
HH12-1186-BC	14/10-12	1300	Øksfjorden	70°08.668' 022°17.347'	237	-box almost full (3 cm from top), retrieved one tube HH12-1186BC, 49 cm long, 4 surface subsamples 0-1 cm for live foraminifera A-D
HH12-1187-BC	14/10-12	1859	Bergsfjorden	70°16.072' 021°45.210'	206	-box 38 cm, retrieved one tube HH12-1187BC, 32 cm long, 4 surface subsamples 0-1 cm for live foraminifera A-D
HH12-1194-BC	15/10-12	0940	Jøkelfjorden	70°03.954' 021°50.475'	195	-box 53 cm, retrieved one tube HH12-1194BC, 49 cm long, 4 surface subsamples 0-1 cm for live foraminifera A-D

Table 4 Gravity-core stations and their specifications Modified after (Forwick & Rasmussen, 2012).

Station	Date	Time (UTC)	Location	Latitude [N] Longitude [E]	Water depth [m]	Recovery [cm]	Comment
HH12-1185GC	14/10-12	1228	Øksfjorden	70°.08.650' 022°17.296'	237	441	5 sections, smelly
HH12-1188GC	14/10-12	1919	Bergsfjorden	70°16.046' 021°45.283'	204	366	4 sections
HH12-1193GC	15/10-12	0908	Jøkelfjorden	70°04.032' 021°50.742'	193	480	5 sections, core cutter/catcher – stored in bag, oriented.

3.3 Laboratory analysis

3.3.1 *Physical properties – MSCL scanning*

Prior to splitting, the physical properties of the cores were measured using a GEOTEK Multi Sensor Core Logger (MSCL-S) (Figure 31). Gamma ray attenuation, P-wave velocity, P-wave amplitude and magnetic susceptibility (MS) were measured. From the obtained data, wet-bulk density, acoustic impedance and fractional porosity may be calculated (Chapter 5.2).

One section is logged at a time, being pushed through the sensors by a stepwise motor. The sampling is conducted from top to bottom at an interval of every 1 cm lasting 10 s (0.1 SI). A laser measures the length of the core (Ellingsen). The cores were kept in room-temperature for about 24 hours before the measurements were conducted in order to diminish any change in the physical parameters (Tomas et al., 1997).
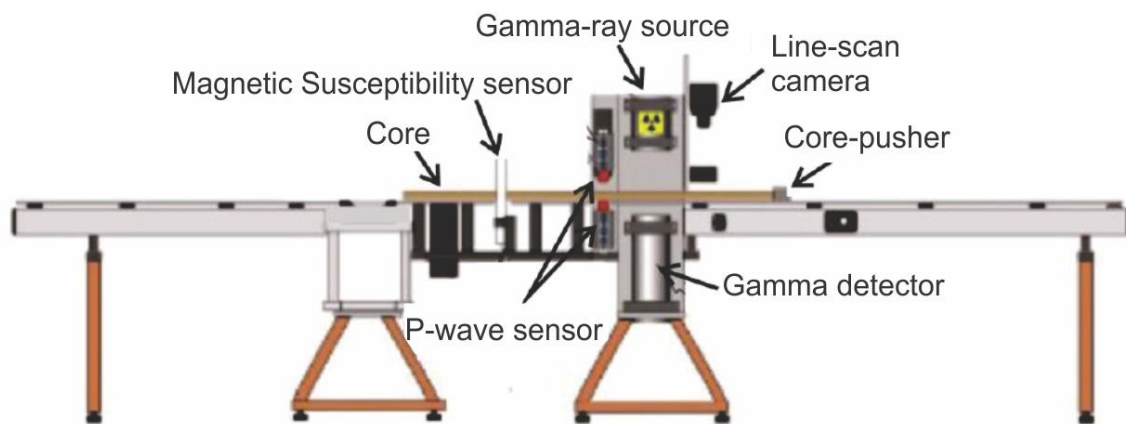
Figure 31 GEOTEK Multi Sensor Core Logger (MSCL-S) and its most important components. After (GEOTEK, 2017).

3.3.1.1 Gamma-ray attenuation (wet-bulk density and fractional porosity)

Wet-bulk density (ρ) is defined as the mass of all particles (*M*) divided by the volume (*V*) it makes up:

$$\rho = \frac{M}{V}$$

Volume includes particle and pore space, hence the density is dependent on the element composition of the sediment as well as compaction.

I order to obtain the gamma ray attenuation, radioactive gamma (γ)-rays are sent through the core section. A ^{137}Cs source is sent out with an energy of 0,662 MeV with an opening of 5 mm. From the amount sent out and the amount received at the detector, the mass of the sediment may be calculated by the amount of γ-rays attenuated. The diameter of the liner is measured and hence wet bulk density may be calculated. It is wet bulk because the sections are unopened. The gamma source is calibrated every week and the detector calibrated before every logging by inserting a density-calibration section.

Fractional porosity is calculated from the same measurements.

Density generally increase at the section ends due to the extra plastic the caps provide. This is ignored when analyzing the data, and the highest peaks are removed for the presentation.

3.3.1.2 P-wave velocity, P-wave amplitude and core diameter
An ultrasonic transmitter transmits low-frequent primary (P)-waves, compressional waves, propagating through the material measured. A P-wave is sent out on one side and detected on the opposite side of the core section. The time it takes for the acoustic signal to propagate through the liner is measured. The P-wave velocity is given by:

$$Vp = \frac{d}{t}$$

Where V_p is the P-wave velocity, d the diameter of the core and t, travel time of the p-wave. Deviations from the given diameter are measured by a laser and used in the calculations. Measurements with an accuracy of 50 ns = 1.5 m/s is obtained.

The composition, density and porosity of the material affect the velocity of the P-wave. Hence, the velocity in combination with the other parameters measured may say something about the composition of the material.

In addition, the receiver measures the intensity of the signal, given as the P-wave amplitude. This reflects the contact between the sensor and the plastic liner. It is important with a high amplitude, as the P-wave velocity may not be representative if the signal is lost. An attempt to increase the amplitude was made by putting water on the liner throughout the entire time of the logging.

P-wave amplitudes below 100 are not valid, and hence velocities of 1500 m/s were used when estimating the depth to the reflectors in the seismic signal (Chapter 3.1).

3.3.1.3 Acoustic impedance
Acoustic impedance (*Z*) may be calculated from the wet-bulk density and the P-wave velocity of the sediment.
$$Z = V * \rho$$

This may be used to track changes in the composition. When conducting seismic data, it is the change in acoustic impedance that reflects the acoustic signal, making up the reflectors.

3.3.1.4 Magnetic susceptibility (MS)
Magnetic susceptibility (MS) is a measure of the materials ability to magnetize when placed beneath a magnetic field. This gives an indication of the composition of the sediment as changes in MS may correlate with changes in the origin of the sediment and/or the environment it is deposited in (GEOTEK, 2014). Minerals originating from terrestrial sources generally comprise of material with a higher MS than that originating in the ocean (Richter et al., 2006). In addition, magnetic minerals are generally made up of denser elements, hence increasing the weight of the particles (Nichols, 2009). Stronger currents may deposit heavier material, thus MS is also an indication on the strength of the bottom currents (Rasmussen et al. 1996; Kissel et al. 1999).

MS is measured by a Barlington loop sensor (MS2C) mounted onto the MSCL. A resolution of 3-4 cm is obtained (Ellingsen). An oscillator circuit produce a magnetic field, and any material with MS will cause a change in the oscilliation circuit (GEOTEK, 2014). This information is converted into SI-values, showing relative changes throughout the core.

Unlikely increasing values were removed due to assured mistakes in the equipment. Especially high values were given at the section boundaries and hence removed.

3.3.2 Splitting and opening the cores

The cores were opened in September 2017 using a Marinetechnik Kawohol core liner saw (Figure 32). They were opened from top to bottom as the sediment are already contaminated this way during retrieval. The vibrating blades help in separating the halves.
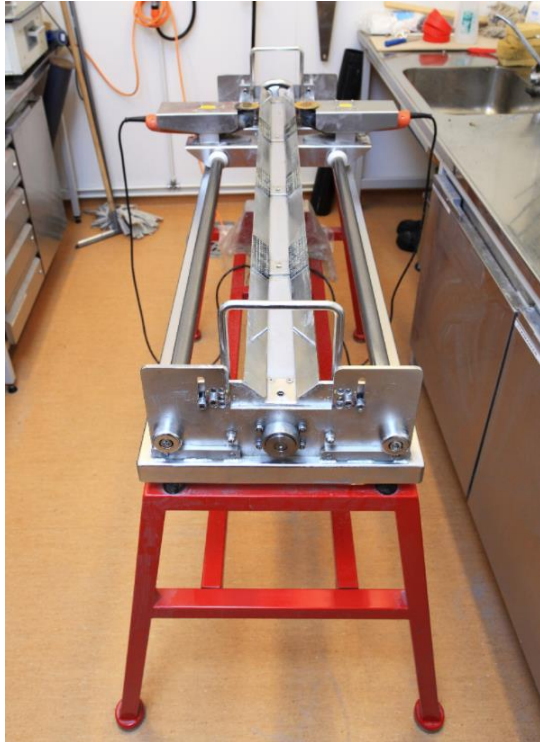
Figure 32 The Marinetechnik Kawohol core liner saw in the laboratory at the Institute for Geoscience, UIT. Photo by T. Dahl et al. .

Separation continued by using a 5V, 15W, Carl Zeiss electro-osmotic knife, *a negatively loaded electrode* attracting water and hence lubricating the knife. The cores are cleaned and the sediment surfaces are made even before labeling, packing and storing. The nicest looking half is chosen as the work section, the other is archived. Both halves are stored at 4 °C. All the sections were well-filled and the opening was successful.

3.3.3 X-ray scanning

The GEOTEK MSCL X-ray Computed Tomographic imaging machine (Figure 33) were used to make X-ray radiographic scans for each half core section, including the archive part of the opened cores. 16-bit images with a resolution up to 60 microns were produced. X-ray imaging is a preferred method as records on the internal structures are obtained without ruining them (Orsi et al., 1994).

Figure 33 The Geotek MSCL X-ray Computed Tomographic imaging machine laboratory at the Institute for Geoscience, UIT. Photo by (T. Dahl et al.).

Each section is radiated with X-rays as a detector measure the attenuation of the rays through it. Different components absorb and scatter the transmitted x-rays differently. The main parameter affecting the attenuation of the X-rays is density. Density increase along with increasing grain size and higher atomic numbers in the lithology (Tanaka et al., 2011). Attenuation may also be affected by physical parameters such as water content, compaction and porosity (St-Onge et al., 2007). These relative variations are recorded and depicted in black-and-white images. In negative images components with high attenuation (higher densities) appear darker than components with low attenuation (lower density).

The split core is denser in the center due to its thickness, hence a zero angle 11 cm split cross core setting is used. Radiographic images are taken every 20 mm with the transmission of 120kV and 225 µA X-rays. The x-ray machine calibrates itself.

As the X-ray images are taken at 20 mm intervals and the images are stitched together, some artefacts may be induced. Because the artefacts occur at the same intervals they are ignored when interpreting the images. The lids also produce some artefacts, but are easily overseen as the position of these are known.

The X-ray radiographic images are processed by choosing a negative image and adjusting the contrast and amount of light, making it easier to examine the variations in density. Different settings for each image are used in the presentation and the fact that the relative attenuation occur per section has to be kept in mind when studying them. The images are also stretched laterally in order to be able to present the entire core on one page and still spot some variations (Chapter 5.2).

3.3.4   Visual descriptions and logging

Visual descriptions were made after opening. Immediate observations such as smell and black spots indicating presence of sulphide were noted. These spots are a result of reduced sulphate by bacteria action (Friedman *et al.* (1992), and will oxidize and disappear some hours after it is exposed to air. Color descriptions were made after "The Munsell Soil Colour Charts" 1995), and any visual structures and changes in grain size were mentioned. Shells, shell fragments, clasts, pore spaces and any sign of bioturbation and other variations in density

were identified in the X-ray images of both the archive and the work half section. All the descriptions were drawn into mm-sheets and later digitalized using CorelDRAW 2017 for the presentation (Chapter 5.2).

The electro-osmotic knife left imprints along the edges of the sections. Hence, the edges of the images were cut off for the presentation, the center of the core sections are in addition less prone to disturbances in the sediment during coring and opening.

What is identified as is mostly recognized in the top of the core sections, thus possibly being due to general disturbances, and hence may not always represent bioturbation.

The photographic and radiographic images are correlated depth-wise according to what was measured (manually and using the MSCL) and stretched laterally for the presentation.

3.3.5   X-Ray Fluorescence (XRF) core scanning
All the work-halves were scanned and photographed using the Avaatech XRF core scanner (Figure 34). The principle of XRF-scanning is the generation of a secondary radiation, fluorescence, when radiated by X-rays. Electrons are ejected when irradiated and are subsequently replaced from outer orbits in the atom, causing an excitation of the atom. The excess energy the outer electron possess is released, a secondary radiation. Each element has a characteristic fluorescing energy, hence allowing for identification of the elements in the sample (Forwick, 2013).

Figure 34 The mobile Avaatech XRF core skanner at the Institute for Geoscience, UIT. Photo by (T. Dahl et al.).

X-rays are produced by a cathode emitting electrons toward an anode inside a vacuum-chamber filled with Helium. The acceleration rate of the electrons depend on the voltage between them, and the amount of electrons depend on the electric current in the cathode. In this survey two runs were made for each core; (1) 10 kV, 1000 µA, no filter, to measure light

elements from Mg to Co, and (2) 30 kV, 2000 µA, Pd-thick filter, to measure medium-heavy elements from Ni to Mo. A measurement was made every 10 mm lasting 10 s.

The He-chamber allow for better detection of the fluorescence than air. This is closely monitored as the foil protecting it may break and/or the He-flow may cease due to lack of gas in the container. Contamination of the foil separating the chamber and the measured sample is prevented by covering the sample measured with a 4 µm plastic foil.

The total counts per second (CPS) should be ~190,000 for 10 kV and ~50,000 for 30 kV. Not all elements have high enough abundance for the counts to be reliable (Croudace et al., 2006). Counts above 10,000 are reliable for the 10 kV run, counts above 3,000 are reliable for the 30 kV run (Forwick, 2013).

It is the pulses of energy characteristic for the respective element that has been counted, not its concentration. Therefore, ratios are produced to see variations in abundance along the core section. Various elements above the detection limit are divided on the sum. The sum is based on the most abundant elements counted at the particular depth for each run. According to Forwick (2013) some elements should not be used and are therefore ignored. These are Chloride, Rubidium and Silver.

The ratios give valuable information on the paleo environment. Variations in the ratios occur due to variations in the source of the sediment, sedimentary processes, biological productivity, deposition and re-depositional processes. Elements studied in this thesis and the information they may provide are summed up in Table 5.

Table 5 Elements used when creating ratios based on the XRF-analysis and the information they may provide. References occur continuously in the table. Elements below the detection limit of the instrument are ignored.

Element	Information
Sulfur (S)	Pronounced sulfur enrichment can reflect the presence of surficial layer of solid sulfate related to the oxidation of dissolved sulfides in the pore water after core opening (Chéron et al., 2016).
Titanium (Ti)	Proxy for terrestrial weathering of pre-Cambrian bedrock (Bakke et al., 2009). Associated with clay-minerals and basaltic sources (Richter et al., 2006). Resistant, non-reactive. High abundance associated with turbidite-bases (Croudace et al., 2006)
Potassium (K)	K, Si and Rb often correlate. Indicate the contribution of minerals from weathered continental crust, thus terrestrial input (Richter et al., 2006). Associated with clay-minerals in tubidite-muds (Croudace et al., 2006).
Rubidium (Rb)	Rb is commonly associated with detrital clay (Croudace et al., 2006) Glaciofluvial material derived from contemporaneous glacial erosion should display higher Rb/Sr-ratios, than deposits from mass-wasting events (Vasskog et al., 2011).
Bromine (Br)	Exists in seawater, variation may indicate variations in the contribution of fresh-water input.
Zirconium (Zr)	Indicate the contribution of minerals from weathered bedrock, thus terrestrial input. High abundance associated with turbidite-bases (Croudace et al., 2006).
Strontium (Sr)	Sr/Ca-ratios define the relative presence of aragonite (high Sr) vs. calcite (low Sr) (Richter et al., 2006). Sr is most likely to be entrained in mass-wasting events, such as pre-Holocene glacigenic material (till), weathered material or re-deposited glaciofluvial material (Vasskog et al., 2011). Sediment deposited by mass-wasting events should display a lower Rb/Sr-ratio than the background sedimentation due to a higher content of chemically weathered material and a lower content of glacially derived detrital clay (Vasskog et al., 2011).
Silicon (Si)	If the Si/Sum- ratio correlate with that of K and Rb, it may indicate the contribution of minerals from weathered bedrock, thus terrestrial input (Kylander et al., 2011). If not, it is an important indicator for biological productivity by diatoms (Croudace et al., 2006).
Calcium (Ca)	Preserved biogenic material comprise of calcium carbonates. Fe/Ca-ratios reflect variations in terrestrial vs. biological contribution (Croudace et al., 2006; Richter et al., 2006). The ratios are used to separate glacial/interglacial cycles in the Northern Atlantic. A higher abundance of Ca occur during interglacials due to a larger biological productivity in such periods (Richter et al., 2006). However, higher meltwater discharges may occur during interglacial periods and hence may provide a larger supply of terrestrial material. (?) Carbonate bedrock in the catchment area may also affect the ratios.
Iron (Fe)	If Fe correlate with Ti, redox-reactions have not affected the Fe-content, and hence reflect variations in terrestrial sediment contribution and not diagenetic iron-enrichments (Richter et al., 2006)

Secondary radiation through water and air reduce the element intensities, especially lighter elements such as Al and Si are affected (Tjallingii et al., 2007). Hence, the cores are made as even as possible and kept in room temperature for the surface to dry before conducting the measurements. This also reduces reflections in the photographs taken. One very small boulder was removed from the bottom of core HH12-1193-GC in order to make the section as even as possible.

The core halves were photographed with the Jai L-107CC 3 CCD RGB Line Scan Camera with a resolution of 70 μm. All photos were taken under similar light conditions in order to eliminate variations at the section boundaries. Abrupt changes in color at section boundaries are ignored due to possible variations in thickness of the split sections and hence distance to the light source in the XRF-scanner. The images are stretched laterally in order to present the entire core on one page and still spot some variations (Chapter 5.2).

A catchment area for each gravity core station were inferred in order to evaluate the source of the main elements found in the sediment (Figure 19). This may provide information when interpreting the origin (terrestrial and/or marine) of the sediment. Table 6 show the element composition of the bedrock in the area and in which fjord it may be transported to when eroded. Figure 3 where used to evaluate the various rock types in each catchment area.

Table 6 Relevant elements the bedrock in the study area comprise of and how they may be distributed in the catchment areas of the fjords. Element composition of the various rock types are based on information in (Deer et al., 1992). Main elements are outside the brackets.

Main rock type	Precence of	Minerals	Elements	Catchment area
Metasandstone	Quartzite, Arkose	Feldspar, Quartz, Mica	Si, K (Rb, Sr, Fe, Ca)	Jøkelfjorden Bergsfjorden
Mica- gneisses and schists	Garnet-mica schists, Staurolite, Kyanite, Sillimanite, Garnet	Mica, Garnet	K, Si, Fe (Ca)	Bergsfjorden
Gneisses	Amphibolite, Hornblende gneisses, Mica gneisses, Garnet	Amphibole, Plagioclase feldspar, Hornblende, Quartz, Feldspar Mica, Garnet	Si, Ti, K, Ca (Fe)	Bergsfjorden, Jøkelfjorden, Øksfjorden
Gabbro and Amphiobolite		Amphibole, Plagioclase feldspar, Pyroxene, Hornblende	Ca, Si (Fe)	Bergsfjorden, Jøkelfjorden, Øksfjorden
Ultramafic Peridotite	Olivestone, Pyroxenite	Olivine, Pyroxene	Si (Ca, Fe)	Bergsfjorden, Jøkelfjorden, Øksfjorden
Alkaline Syenite	Syenite, Quartz Syenite	Alkali Feldspar, Quartz	K, Si (Fe, Ca)	Bergsfjord, Øksfjorden
Alkaline Carbonatite and Limestone	Marble, Carbonate Mica Schists, Limestone, Carbonate Silica-Schists and Gneisses, Graphite Schists w/ white Quartzite	Calcite	Ca, Fe, K, Si	Bergsfjorden, Jøkelfjorden

3.3.6   *Grain size particle distribution analysis*

A grain size analysis was performed using the Beckman Coulter LS 13 320 Multi-Wavelength Laser Diffraction Particle Size Analyzer (Figure 35) after the preparation of samples.

Samples were taken every 5 cm with an addition of more frequent sampling at interesting depths. All together 290 samples were taken; 90 samples from HH12-1185-GC, 10 samples from HH12-1186-BC, 7 samples from HH12-1187-GC, 75 samples from HH12-1188-GC, 98 samples from HH12-1193-GC, and 10 samples from HH12-1194-BC. As samples were taken at 5 cm intervals, the depth yield is the minimum depth of the sample and down maximum 1 cm more. All samples were treated with 20 % HCl and 20 % H_2O_2 in a pre-heated VWB 18 Thermal Bath in order to remove $CaCO_3$ and oxidize organic matter, respectively. After each treatment the samples were cleaned with distilled water and centrifuged with an Eppendorf Centrifuge 5702 (4000 rpm) for 4 minutes, three times. All of this treatment were carried out in a fume hood. Subsequently the samples were dried in a cabinet drier.

Samples of 0.2 g were extracted and mixed with 20 ml distilled water and put on a shaking table for at least 24 hrs. Before the samples were run a few drops of Calgon were added to the sample and the beaker were put in a Branson 200 ultrasonic cleaner for 3-8 min. Directly after, the sample were added to the Particle Size Analyzer (Figure 35) to count the amount of different grain size fractions. The Polarization Intensity Differential Scattering (PIDS) proved too low for the first samples and so 0.5 g samples were measured instead (excess pre-treated sediment was still available). 0.5 g is a suitable amount when the mean grain size is around 80 µm. When the mean grain size is less than 50 µm, the PIDS is too high.

Figure 35 Beckman Coulter LS 13 320 Multi-Wavelength Laser Diffraction Particle Size Analyzer in the laboratory at the Institute for Geoscience, UIT. Photo by (T. Dahl et al.).

The sample is put into a rotating tub of water where the laser count and measure the size of each grain between 0.4µm and 2000µm. A 2 mm sieve filters out the larger grain sizes that will disturb the instrument. Three runs are performed on each sample showing the amount of grains per fraction. A mean of these runs are used when processing and presenting the data. Grain-size statistics were extracted using GRADISTAT Excel-software (Blott & Pye, 2001). The distribution were both unimodal and multimodal (several peaks in the amounts of the particle size fractions). The primary mode is the dominating peak and hence is assumed to represent the matrix. The difference between mean and mode values are demonstrated in Figure 36.
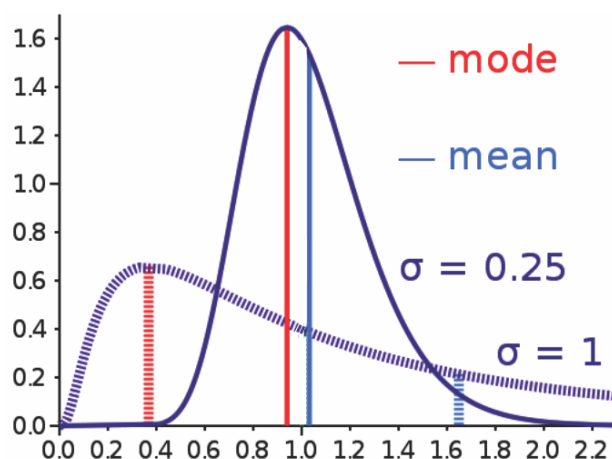
Figure 36 Simple unimodal graphs showing the comparison of mean and mode. Mode is the x-value with the highest y-value, mean is the x-value with mean of the range in the y-axis.

The width of the lithological logs represent the dominating size fraction, thus the matrix at the measured depth, equivalent to the primary mode of the size fractions. A larger width represents a larger fractional mode. All the cores have a matrix comprising of either silt or

sand. In addition, because most depths inhere multimodal values, the mean grain size is presented in order to notice these variations. Both scales show the lower boundary, separating the main grain size fractions of silt (si) and sand (S), at 2 and 63 µm, respectively. The classification of sediment grain sizes used in this thesis are after Udden (1914) and Wentworth (1922) (Table 7).

Table 7 Classification of grain size fractions modified after Udden (1914) and Wentworth (1922).

Grain Size (phi)	Grain Size (mm)	Descriptive term	Group
		Very Large	
-10	1024	Large	
-9	512	Medium	Boulder
-8	256	Small	
-7	128	Very small	
-6	64	Very coarse	
-5	32	Coarse	
-4	16	Medium	Gravel
-3	8	Fine	
-2	4	Very fine	
-1	2	Very coarse	
0	1	Coarse	
1	microns 500	Medium	Sand
2	250	Fine	
3	125	Very fine	
4	63	Very coarse	
5	31	Coarse	
6	16	Medium	Silt
7	8	Fine	
8	4	Very fine	
9	2	Clay	

Based on the fractions measured, each sample were divided into a textural group based on the classification after Folk (1954) (Figure 37); Silty sand (50-90 % sand and a silt/clay-ratio > 2), sandy silt (10-50 % sand and a silt/clay-ratio > 2, silt (a silt/clay-ratio > 2, sand < 10 %). Textural groups are added to the lithological logs in order to spot variations not seen when only studying the primary mode or the mean grain size. The figures used when presenting the textural groups are after NGU (2017) (Figure 46).
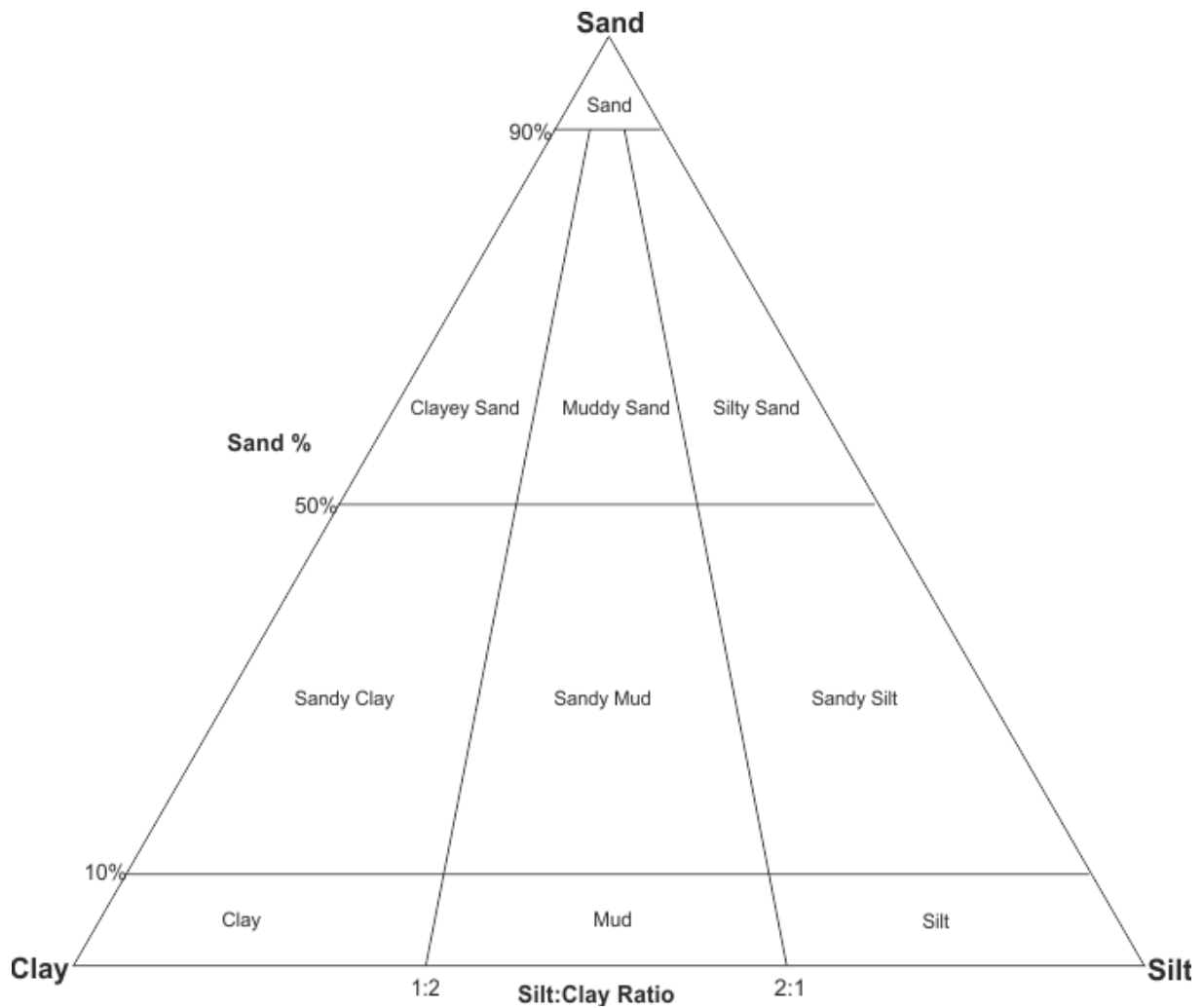
Along with the lithological logs and the mean grain size with depth, a presentation of the detailed measurements of all the sub-fractions (Table 7) is given in stacked area diagrams to show the amounts [%] of grains present in each core (Figure 47, Figure 49 and Figure 51). Samples containing detritus > 2 mm are noted with an asterix, and the lithological log adapted when the measured primary mode does not represent the observed grain size.

Sources of error

There is a possibility that some samples were contaminated and that the smaller particles were lost due to effervescence when treated with HCl and H_2O_2. However, this happened to almost all the samples to some degree (Table 8), and so the loss would be similar down core. Due to the high CO_3-content in the samples reacting with HCl, it is likely that some grains contained carbonates in their bedrock composition and thus were dissolved when treated with HCl. Some part of the particle fractions are probably also lost when washed and centrifuged after the acid-treatment. Flocculation is attempted reduced when shaking the sample in water and adding Calgon and put in the ultrasonic bath, this is however impossible to prevent from occurring and hence all samples probably contain smaller fractions than the ones measured. The occurance of flocculation and loss of finer fractions are more likely than fragmentation of the grains when handled.

Especially the samples from Bergsfjorden, HH12-1187-BC and the upper samples of HH12-1188-GC, reacted vigorously with both the HCl- and the H_2O_2-treatment. So did the additional sample retrieved in a coarser layer at 204 cm.

Table 8 Reaction with HCl and H_2O_2. X: Vigorous effervescence, x: bubbles, -: minor/no reaction.

Core reacting	HCl	H_2O_2
HH12-1185-GC	x	x
HH12-1186-BC	x	x
HH12-1188-GC	X	X
HH12-1187-BC	X	X
HH12-1193-GC	-	x
HH12-1194-BC	-	X

4   Radiocarbon dating, calibration and sedimentation rates

4.3   Dating fossils

In order to construct a chronostratigraphic sequence of the three cores and be able to correlate the environmental conditions in the different areas, dating is needed. The method is based on a theory of a known half-life of the radioactive isotope ^{14}C decaying after death e.g. (Ruddiman, 2007). Accelerator Mass Spectrometry (AMS) is used to calculate ^{14}C ages of preserved calcium carbonate remains found along with the sediment. A ^{14}C "Libby half-life" of 5568 ± 30 years is used when calculating conventional radiocarbon ages (e.g. Stuiver & Polach, 1977; Stuiver & Reimer, 2018).

Fossils observed in the X-ray images were retrieved and sediment rinsed off before the shells were weighed and labeled. Whole shells were preferred as well as fossils at depths above and below variations in density and color. Trine Dahl carried out the species recognition. A variation of molluscs; bivalves and gastropods, and one foraminifera were dated using AMS-technology. 9 samples were dated at NTNU: The National Laboratory of Age Determination with a 1 MV Tandetron from High Voltage Engineering Europa B.V (Nadeau et al., 2015), 3 samples were dated at the AMS dating facility at the Alfered Wegener Institute (AWI), with a Ionplus AG MICADAS (Gentz et al., 2017). NTNU needed at least 23 mg, while AWI even managed to date the foraminifera of 1.9 mg. Table 9 show the species, at which depth they were retrieved and the weight of the combined samples.

Table 9 The dated samples are presented along with their laboratory reference numbers, weight and species.

Core	Depth [cm]	Lab.	Lab. Ref. nr.	Species	Weight [g]	Comment
HH12-1185-GC	61	NTNU	TRa-12752	Thyasira sp.	0.024	One side of bivalve, broke when obtained
HH12-1185-GC	350	NTNU	TRa-12753	Yoldia hyperborea	0.239	Right side of bivalve
HH12-1188-GC	163	NTNU	TRa-12754	Yoldia hyperborea	0.0367	One side of bivalve, broke when obtained
HH12-1188-GC	175	NTNU	TRa-12755	Yoldiella (lucida)	0.0238	Several sides of bivalves
HH12-1188-GC	260	NTNU	TRa-12756	Nuculana pernula	0.054	Right side of bivalve
HH12-1188-GC	356	NTNU	TRa-12757	Gastropo Lacunidae Lacuna sp.	0.397	
HH12-1193-GC	75	NTNU	TRa-12758	Gastropo Lacunidae Gibbula cineraria	0.171	
HH12-1193-GC	211	NTNU	TRa-12759	Astarte sulcata	1.12	Left side of bivalve
HH12-1193-GC	254	AWI	1538.1.1	Yoldiella lenticula	0.0088	Right side of bivalve
HH12-1193-GC	288	NTNU	TRa-12760	Astarte sp., Yoldiella lenticula, Yoldiella sp.	0.031	Right and left, Whole + right, Left side + fragment of right
HH12-1193-GC	408	AWI	1540.1.1	Triloculina tricarinata	0.0019	
HH12-1193-GC	458	AWI	1539.1.1	Yoldiella lenticula	0.0057	Whole

4.4   Calibrations

Radiocarbon ages do not directly equate to calendar years due to the atmospheric variations in the ^{14}C concentration e.g. (Mangerud, 1972; Reimer et al., 2013), and hence calibration is needed. Due to the development of nuclear weapons and testing in the 20th century, calibrated ages are referred to as cal. yrs. BP, thus the calibrated age before 1950 CE (Common Era) (Bradley, 2013). (Reimer et al., 2013) describe the improvement of Marine13, the most up to date calibration curve, used when calibrating the marine ^{14}C-dates achieved from the AMS-dating. The Northern Hemisphere calibration is well defined by dendrochronological databases from 0 to 13,900 cal. yrs. BP (Reimer et al., 2013).

Due to the reservoir effect of the oceans and its increase with higher latitudes, a marine reservoir age (MRA) / an *apparent age* is subtracted when the radiocarbon age is calibrated (Bradley, 2013). The marine calibration incorporates a time-dependent global MRA correction of about 400 years (Stuiver & Reimer, 2018). A regional deviation, ΔR, is yield to

correct for the global MRA. For Northern Norway a ΔR of 71 +/- 21 is used to correct samples retrieved in coastal waters below a depth of 100 m (Mangerud et al., 2006).

4.5   Limitations

Contamination of the organic material is probably the largest source of error. In addition, redeposited sediment may transport material with already decayed radiocarbon, thus give older ages. An attempt to date whole shells diminish the probability for dating redeposited material, as it is likely to break into fragments during redeposition. In situ material has a greater probability of being preserved.

As mentioned, variations in the atmospheric concentration of ^{14}C caused by variation in the rate of radiocarbon production in the atmosphere affect the curves used for calibration (Bowman, 1990). Several parameters affect the production such as; (1) cosmic-ray fluctuations caused by stellar phenomena, solar activity, changes in the geomagnetic field, meteorite collisions and nuclear testing, (2) variations in exchange rate of radiocarbon between reservoirs due to variations in temperature, humidity, sea level, ocean salinity, circulation and capacity and (3) variations in the total amount of carbon dioxide present due to introduction by volcanic activity and human industry, as well as the sink capacity of sedimentary reservoirs (Bradley, 2013). Insight in all of these factors are continuously investigated and hence are the reason why the calibration curves are frequently updated. The calibration curves have several plateaus due to this variation (e.g. Hughen et al., 2000).

Difficulties in deciding on the MRA for the samples lead to another source of error. The ocean circulation affect the MRA and hence geographical variations are large. Surface waters will have a lower MRA than deeper as the contact with the atmosphere occur more frequent closer to the atmosphere. Upwelling of deep water, prevented contact with the atmosphere due to sea ice and the general variation in the circulation occur both over space and time (Bradley, 2013). Mangerud et al. (2006) measured ΔR values on stationary molluscs along the Norwegian coast and found that they are latitude dependent and increase northwards. Hence the ΔR of 71 ± 21 used on shells and benthic foraminifera seem reasonable to apply on the samples measured in this study.

Some species are capable of transferring themselves up and/or down the sediment, hence produce a source of error in the data. Especially the foraminifera retrieved from HH12-1193-GC at 408 cm depth is capable of moving vertically (Table 9).

Lots of assumptions are made and a lot of varying factors may affect the ^{14}C concentration in any material. One last assumption is the need for the relationship between ^{14}C and its daughter isotope, ^{12}C to have been constant through time in all living organisms (Bradley, 2013). However, the dendrochronological databases go far enough back to make the ages measured in this study reliable.

5 Results

In the following chapter all the results from the measurements conducted are presented. First, the seismostratigraphic data is presented along with a description of the fjord geomorphology. Second, the lithostratigraphic data obtained through laboratorial work are given and the units decribed. Thirdly, the results from the radiocarbon datings are given along with estimated sedimentation rates.

5.1 Large scale bathymetry and seismostratigraphy

Here, the chirp-data collected October 14th-15th, 2012, by R/V Helmer Hanssen (Forwick & Rasmussen, 2012) is presented. A general geomorphological description of each fjord is made along with an identification of sedimentary facies in the basins. The seismic 2D line was interpreted using PETREL and Corel Draw.

5.1.1 Large scale bathymetry

Scales of the geomorphology are summed up in Table 10, with estimations based on assumed sediment velocities, the measured distances and TWT retrieved from the seismic data.

Table 10 A summary of the dimensions in the fjords. Ø: Øksfjorden, B: Bergsfjord, J: Jøkelfjorden, B: Basin, sB: Sub-basin, S: Sill. Progressively distal features of the seafloor are denoted by increasing numbers.

Basin or sill	Depth [m b.s.l.]	Width [m]	Length [km]	Height [m]	Maximum sediment thickness [m]
ØB1	237	-	6	-	42
ØsB1	159	-	2.7	-	42
ØsB2	237	2.7	2.6	-	24
ØS1	133	-	1.7	96	25
ØB2	278	2	9.5	-	55
ØS2	222	-	0.4	46	-
ØS3	250	-	0.3	24	-
BB1	97	1	3.3	-	17
BS1	44	1.5	0.2	115	-
BB2	162	1.5	5.3	-	24
BS2	120	1	0.3	61	-
BB3	230	4	8.5	-	18
BS3	71	1	4	92	14
BB4	139	3	3	-	14
BS4	118	1.5	0.4	24	5
JB1	125	1	7	-	12
JS1	45	2	2	51	4.5
JB2	193	1.5	4	-	23
JS2	162	-	0.3	23	-

Accumulations of sediment generally increase in the depressions of the seafloor, hence sediment is trapped as it is transported out the fjords. The lowest sediment accumulations are observed over the sills.

5.1.2 Acoustic reflectors

Seismic reflections are produced by interfaces of changing acoustic impedance (Z), the product of density and velocity of the material measured (Chapter 3.3.1.3). The reflections are presented with an x-axis giving the two-way-time (TWT) [ms], representing the time between the transmitted and received seismic signal, along the path of the vessel [km] on the y-axis.

The structure of the reflections are defined by the paleo-topography and the processes of formation, deposition and erosion (Stoker et al., 1997). Observed reflections are presented in Figure 38. Three main reflection configurations occur, separated by their type and quality (e.g. strength and continuity); (1) *stratified reflections* reflect abrupt vertical contrasts in Z, e.g. the continuous water-sediment interface is often particularly sharp and easily recognizable. Vague, stratified reflections may indicate a minor change in the lithology or a layer too thin to be properly detected. The stratified reflections may be continuous to disrupted (Grundvåg, 2016). (2) *Acoustically transparent intervals* represent no detected variation in Z, thus no reflection is produced. This may imply a homogenous unit, or if no subsequent reflection occur: an acoustically impenetrable material, (3) *Chaotic reflections* represent discontinuous interfaces and probably represent poorly sorted deposits.

A combination of the reflection configurations are observed in the seismic data (Figure 38). The reflections vary from being planar to rugged, often smooth to undulating. The strength of the reflections also vary from vague to prominent. A reflection may inhere lateral transitions from continuous to discontinuous, from vague to prominent, and from chaotic to acoustically impenetrable. The combination of the reflection configurations and the geometry of the sequences, give the basis for classifying the facies.
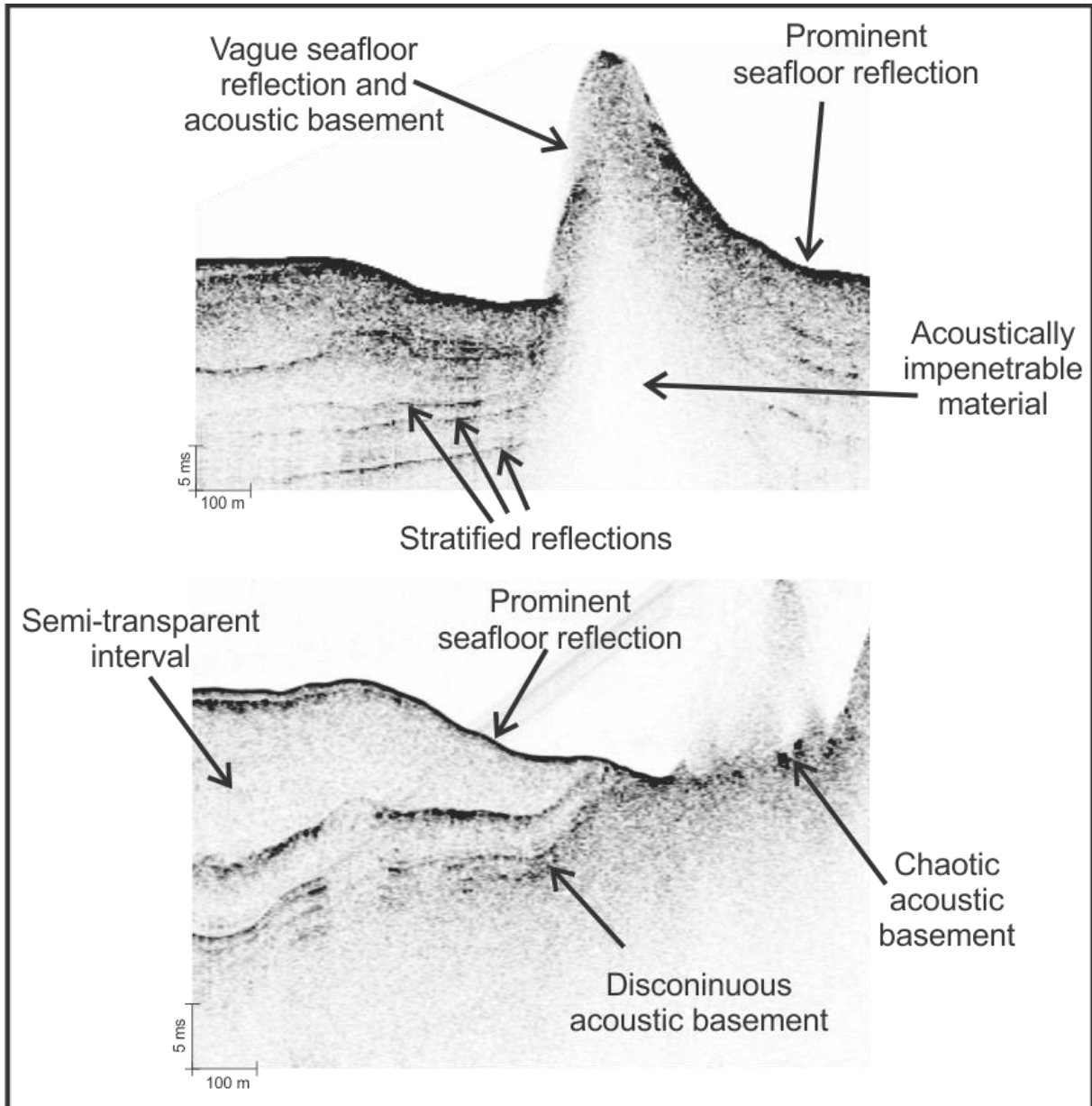
Figure 38 A summary of various reflections observed in the seismic data. A steeper gradient of the sea floor generally produce less prominent reflections than gentler sloping surfaces. Acoustically transparent intervals may represent homogeneous units and/or acoustically impenetrable material. Stratified reflections may be vague or prominent, continuous or discontinuous.

The sea floor reflection is often the most easily recognized reflection. It is the first, generally strong, reflection detected, caused by the greater density in sediment compared to the water. Deeper continuing reflections generally occur at interfaces between homogenous sediment units with varying p-wave velocity and/or density.

5.1.2.1   *Acoustic basement, R1*

The last semi-continuous reflector is the top of the *acoustic basement*, or R1. It represents the depth at which the seismic signal is attenuated due to impenetrable material below, represented by acoustically transparent intervals. This may indicate underlying bedrock or morainal deposits (Hjelstuen et al., 2009).

Its occurrence range from the seafloor to the bottom of the infilled sediment. It represents the boundary between overlying sediment or water and the underlying impermeable acoustic basement. A general undulating reflector is inferred, implying sills and basins subsequently filled with sediment. Its continuation is difficult to detect in the deeper basins due to the general attenuation of the seismic signal with increasing depth. It is most easily recognized when it protrudes the sedimentary sequences, and make up the seafloor. The reflection is generally less prominent it dipping slopes (Figure 38).

The configuration of the reflection varies between being chaotic, disrupted or vaguely continuous. An example of a vaguely continuous acoustic basement is the lower boundary of the facies F1 in Figure 39. Examples on discontinuous and chaotic reflectors are given in Figure 38.

5.1.3   *Acoustic facies*

The acoustic facies recognized in the seismic data are described herein. Classifications are based on the reflector configuration and geometry of these, along with an analysis of the stratigraphic sequences and their assumed characteristics and process of formation. Continuous reflections are studied, e.g. the seafloor and internal reflections. An attempt to identify the acoustic basement is executed. Low-resolution bathymetric data area a useful contribution to the vertical data as a means of interpreting the horizontal extension of the sea floor morphology.

A p-wave velocity of 1500 m/s is assumed for the water in all the three fjords as this fit with the depth yield for the coring stations in the cruise report by Forwick and Rasmussen (2012). Likewise for the sediment, a mean p-wave velocity of 1500 m/s was used when calculating the thicknesses in the data (e.g. Hjelstuen et al., 2009; Forwick & Vorren, 2010). The chirp lines and the coring stations are correlated in Chapter 6.1.

An overview of the acoustic facies recognized in the seismic profiles are presented in Figure 39, and are further described in the following chapters. The same facies are inferred to appear in all the fjords, but are denoted with a letter in order to separate which fjord it is found in when described.
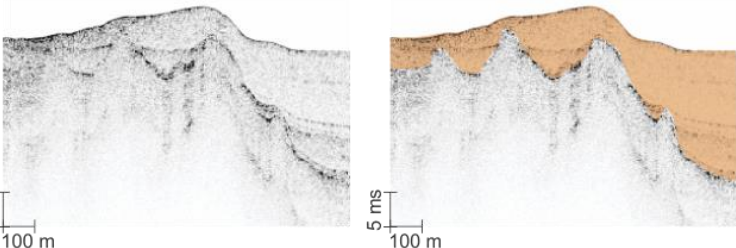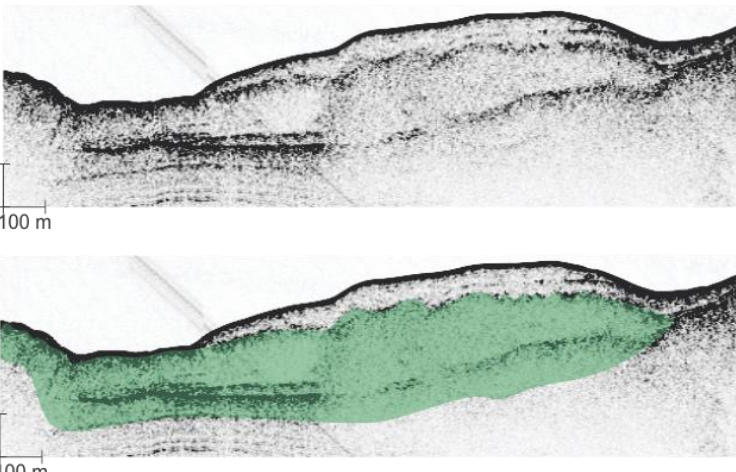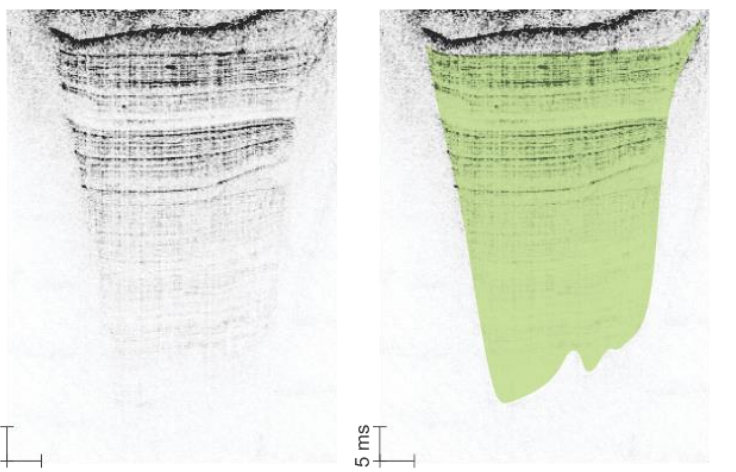
Acoustic facies	Example of facies with and without interpretation	Character of facies
F3		Acoustically semi-transparent units separated by parallel to wavy, semi-continuous internal reflectors. Sheet drape. Low energy deposit.
F2		Acoustically semi-transparent to chaotic units, separated by strong, undulating and disrupted reflectors. Internal reflectors referred to as hummocky to chaotic. Mounded onlapping fill/ fan-complex High-energy deposit.
F1		Acoustically stratified facies with continous, parallel internal reflectors. Onlapping fill trapped in depressions. Low energy deposit.

Figure 39 Overview of the acoustic facies recognized in the seismic data and the characters they possess. F1: Facies 1, F2: Facies 2, F3: Facies 3. The internal configuration, external geometry and continuity of the reflectors are inferred, along with the energy of the environment it is assumed to have been deposited in. 5 ms ≈ 3.75 m.

5.1.3.1   Seismic Facies 1

The facies observed deepest in the basins is the seismic Facies 1 (F1) (Figure 39). It is mostly recognized in Øksfjorden (Figure 41), with a minor presence in the inner Langfjorden (Figure 43). It varies between being 3 to 9 m b.s.f.

Generally, the configuration of the facies comprise of continuous, densely spaced, parallel stratification, onlapping the sides of the basins it fills in. The layers are generally 75 to 15 cm thick, possibly thinner. In Øksfjorden, the thickness of F1 is observed to be more than 50 m at its thickest.

Internal reflections are gradually attenuated with depth, thus a vague continuous stratification is inferred as the base. However, it is possible that it continues deeper than what is detected.

The upper boundary is generally pronounced, following the planar geometry of the rest of the internal reflectors.

5.1.3.2   Seismic Facies 2

The seismic Facies 2 (F2) is observed in all the three fjords. The upper boundary of the facies range from making up the seafloor, to being buried maximum 7, 11 and 13 m beneath the sea floor (Figure 41, Figure 43 and Figure 45, respectively).

Both the upper and lower reflection of the F2 vary between being pronounced and vague, generally not following the same geometry, but both are undulating (Figure 39).

F2 is separated into units separated by undulating and disrupted reflectors. Some of the units inhere a lobate geometry, pinshing out to the sides. The internal reflectors are seen to onlap at some terminations, but is generally complex. The intervals between the broad, chaotic and undulating reflectors inhere a semi-transparent to chaotic configuration.

One to three units are observed in the basins containing F2.

5.1.3.3   Seismic Facies 3

At the top of the other facies, the seismic Facies 3 (F3) is detected, as the youngest facies in the fjords (Figure 39). Either as patches or a sheet drape filling in and smoothing out the undulating upper boundary of F2. Parallel to wavy, continuous internal reflectors, sometimes slightly vague, separate acoustically semi-transparent units. Up to six units are observed to overly each other (JB2, Figure 45).

F3 drape the underlying irregular bottom reflector, either onlapping, pinching out toward the sides or truncating toward the fjord mouth.

The upper boundary of the facies always represent the seafloor, and is the facies inferred to have been captured in the all the gravity cores.

5.1.4 Øksfjorden

The 17.6 km long seismic line retrieved in Øksfjorden is presented in Figure 41 along with an interpretation of observed facies based on an analyze of the reflection configurations.

Two main basins (ØB1 and ØB2) are inferred from both the low-resolution bathymetry (Figure 40) and the seismic line (Figure 41). These are separated by the most prominent sill (ØS1). ØB1 comprises two sub-basins (ØsB1 and ØsB2). The inner fjord has an undulating bathymetry, gradually deepening out towards ØsB2, 237 m b.s.l. where core HH12-1185-GC was retrieved. ØsB2 is approximately 2.7 km wide, 2.6 km long and almost 100 m deep from ØS1. The sediment infill in this basin is approximately 24 m thick at its thickest. Several rivers enter directly into the semi-enclosed basin.

ØB2 is also gradually deepening out the fjord, stretching 10 km from ØS1 to the break 285 m b.s.l. where it meets Stjernsundet. Two minor sills (ØS2 and ØS3) are observed in both the bathymetry and the seismic line, rising 40 and 20 m above the surrounding sea floor, respectively. The basin is not constrained by an outer shallow sill.
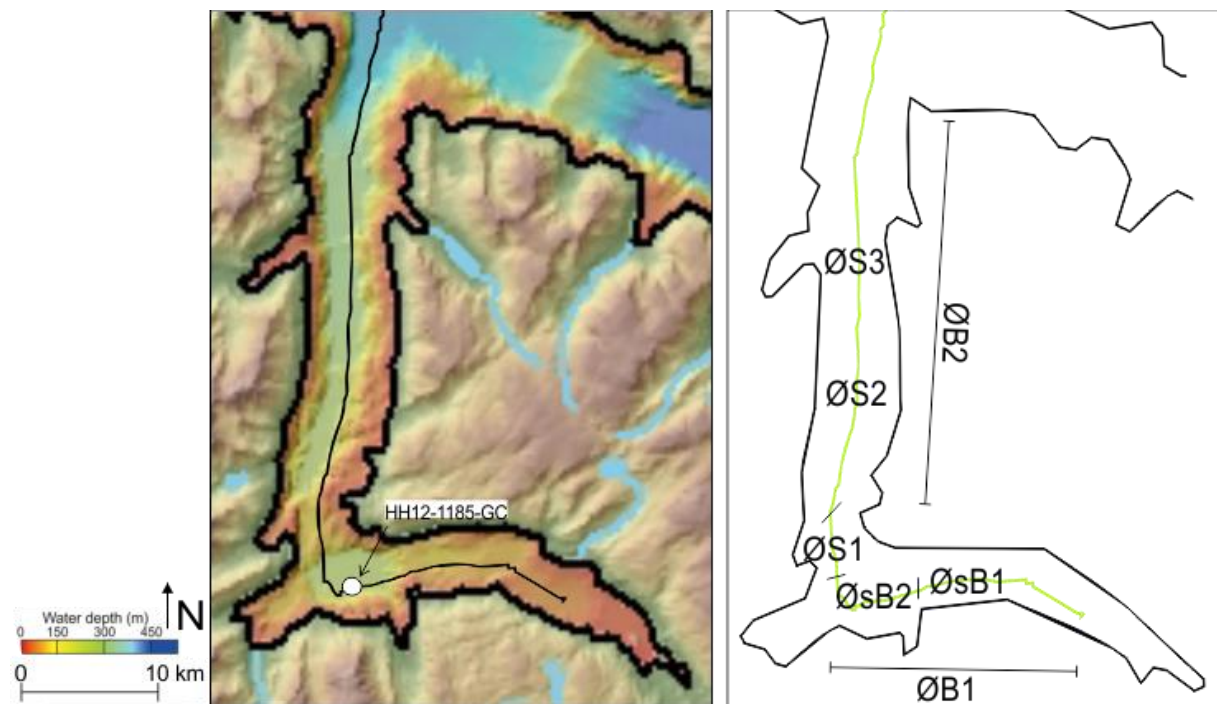
Figure 40 Low-resolution bathymetric data and the position of core HH12-1185-GC. Seismic composite line inferred in the bathymetry and in a simple wireframe of the coastline. Ø: Øksfjorden, B: Basin, sB: Sub-basin, S: Sill. Increasing numbers denoted with reduced proximity to the fjord head. Bathymetric data after Jan. P. Holm (Forwick & Rasmussen, 2012).

Figure 41 (next page) The upper profile presents the seismic chirp data retrieved from Øksfjorden in 2012 (Forwick & Rasmussen, 2012). The lower profile include interpretations of acoustic facies and large-scale fjord geomorphology. The location of the gravity core HH12-1185-GC is given, and the basin it is retrieved from highlighted in the zoom-in. The sperm whale show what is inferred to be the water column, not to scale. Note the vertical exaggeration in the seismic data. The outer fjord is to the north. Ø: Øksfjorden, B: Basin, sB: Sub-basin, S: Sill. Increasing numbers are denoted out the fjord.
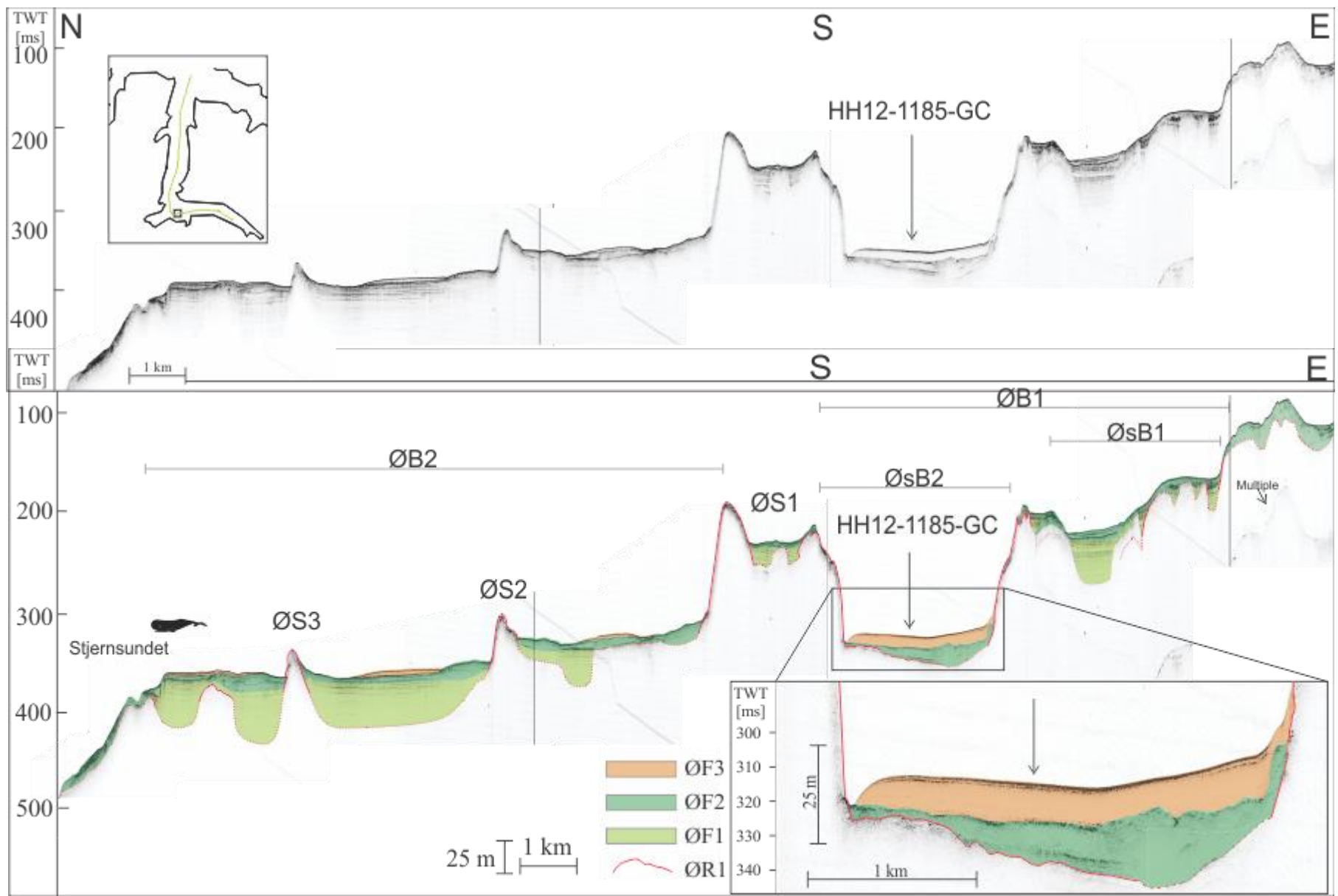
5.1.4.1   Acoustic basement – Reflection ØR1

ØR1 is the top of the acoustic basement in Øksfjorden, with a varying occurrence from the seafloor and beneath the sediment infill 60 m b.s.f. It is most easily recognized when it protrudes the sedimentary sequences at the sills (ØS1, ØS2 and ØS3). The continuous red line represent stronger reflections of ØR1, "dashed" lines indicate the vague continuations.

5.1.4.2   Øksfjorden Facies 1

The lower boundary to the facies ØF1 is interpreted to represent the acoustic basement, ØR1. ØR1 is not very prominent below ØF1, hence thicker deposits than the detected may exist in the basins. ØF1 is the thickest of all the sequences with over 50 m detected. The inner reflection configuration of the interpreted facies are continuous and inhere an almost planar stratification, parallel to sub-parallel. In some of the basins the stratification is inferred to onlap, thinning towards the basin side walls. ØF1 is recognized in all basins except sub-basin ØsB2. The undulating acoustic basement is generally evened out by the facies ØF1, and is assumed to control the location and thickness of the deposits. The sedimentary sequences are probably trapped in the initial depressions in the undulating base. At the top an erosional unconformity is inferred representing the bottom of the seismic facies ØF2.

5.1.4.3   Øksfjorden Facies 2

ØF2 overlies ØF1, or directly on top of the acoustic basement, ØR1, as in basin ØsB2. The sequence is recognized in all basins. ØF2 is more chaotic than the other facies observed in the fjord, and stratification is generally absent. Some inner reflections occur. These are slightly chaotic, vague to prominent, continuous to discontinuous, varying from hummocky to sub-parallel in configuration, creating units pinching out to the sides. The internal reflection configuration of the units are chaotic to semi-transparent. All together, the thicknesses of the facies vary from 3 to 18 m, with a trend of decreasing thicknesses distally in the basins. The thickness of the internal units vary from 3 to 11 m at the center, thinning toward the sides.

5.1.4.4   Øksfjorden Facies 3

ØF3 is found in sub-basin ØsB2 and in ØB2, on top of ØF2. It is thickest in basin ØsB2, up to 10 m. It is generally acoustically transparent, with some stratification. Three internal reflections are recognized in basin ØsB2. The thinnest facies is found in the basin ØB2, occurring in patches at the center of the sub-basins. Seemingly, a structural truncation in the outer parts of the basins and onlapping onto the inner basin wall are indicated.

5.1.5 *Bergsfjorden*

The 26.8 km long seismic line is shown in Figure 42 and Figure 43, was retrieved from Langfjorden and Bergsfjorden. Studying the seismic it may seem as if three major and one minor sill separate several basins in the fjord. Whether or not these sills are fjord-crossing sills remains unsupported by the low-resolution bathymetry data. However, it is assumed that these are cross-fjord sills, because the reflection patterns on either side of the sills are different, suggesting different styles of sediment distribution. Furthermore, inner-fjord sills are common features in fjords (e.g. Chapter 5.1.4; 5.1.6; Corner (1980)). BS1, towers more than 100 m above the surrounding sea floor and hence possibly constrain the innermost basin, BB1.

The innermost part of Langfjorden. The basin BB1, has a relatively high relief configuration in the sea floor. The 3.3 km long basin, BB1, is shallow, but is still about 50 m deep relative to BS1. It contains approximately 17 m of deposited sediment. Basin BB2 is 5.3 km long with sediment thicknesses up to 24 m. BB3 is the deepest basin in the fjord, with the deepest point, 230 m b.s.l. south of the coring station. The undulating sea floor deepens out the fjord toward this point, before a gradual elevation towards BS3. Across the fjord, BB3 is approximately 4 km wide and 8.5 km long along the fjord. It is 160 m deep relative to BS3 with varying sediment thicknesses up to about 18 m. The water depth increases drastically at the mouth of Bergsfjorden, towards Sørøysundet situated almost 200 m deeper.
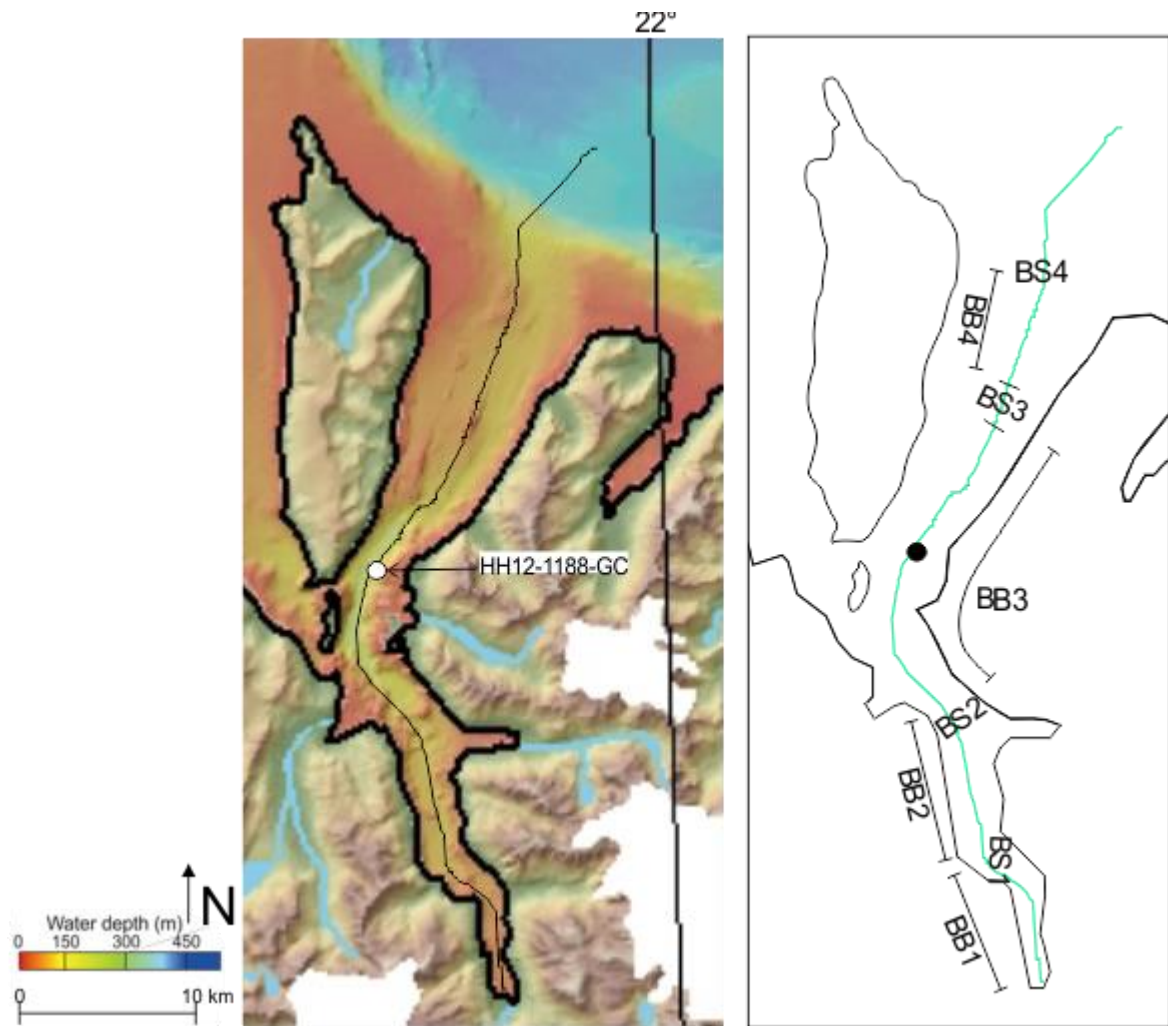
Figure 42 Low-resolution bathymetric data and the position of core HH12-1188-GC. Seismic composite line inferred in the bathymetry and in a simple wireframe of the coastline. BB: Bergsfjorden Basin, sB: Sub-basin, S: Sill. Increasing numbers denoted with reduced proximity to the fjord head. Bathymetric data after Jan. P. Holm (Forwick & Rasmussen, 2012).

Figure 43 (next page) The upper profile presents the seismic chirp data retrieved from Bergsfjorden in 2012 (Forwick & Rasmussen, 2012). The lower profile include interpretations of acoustic facies and large-scale fjord geomorphology. The location of the gravity core HH12-1188-GC is given, and the basin it is retrieved from is highlighted in the zoom-in. The orca show what is inferred to be the water column, not to scale. Note the vertical exaggeration in the seismic data. The outer fjord is to the north. BB: Bergsfjorden Basin, sB: Sub-basin, S: Sill. Increasing numbers are denoted increasingly out the fjord.
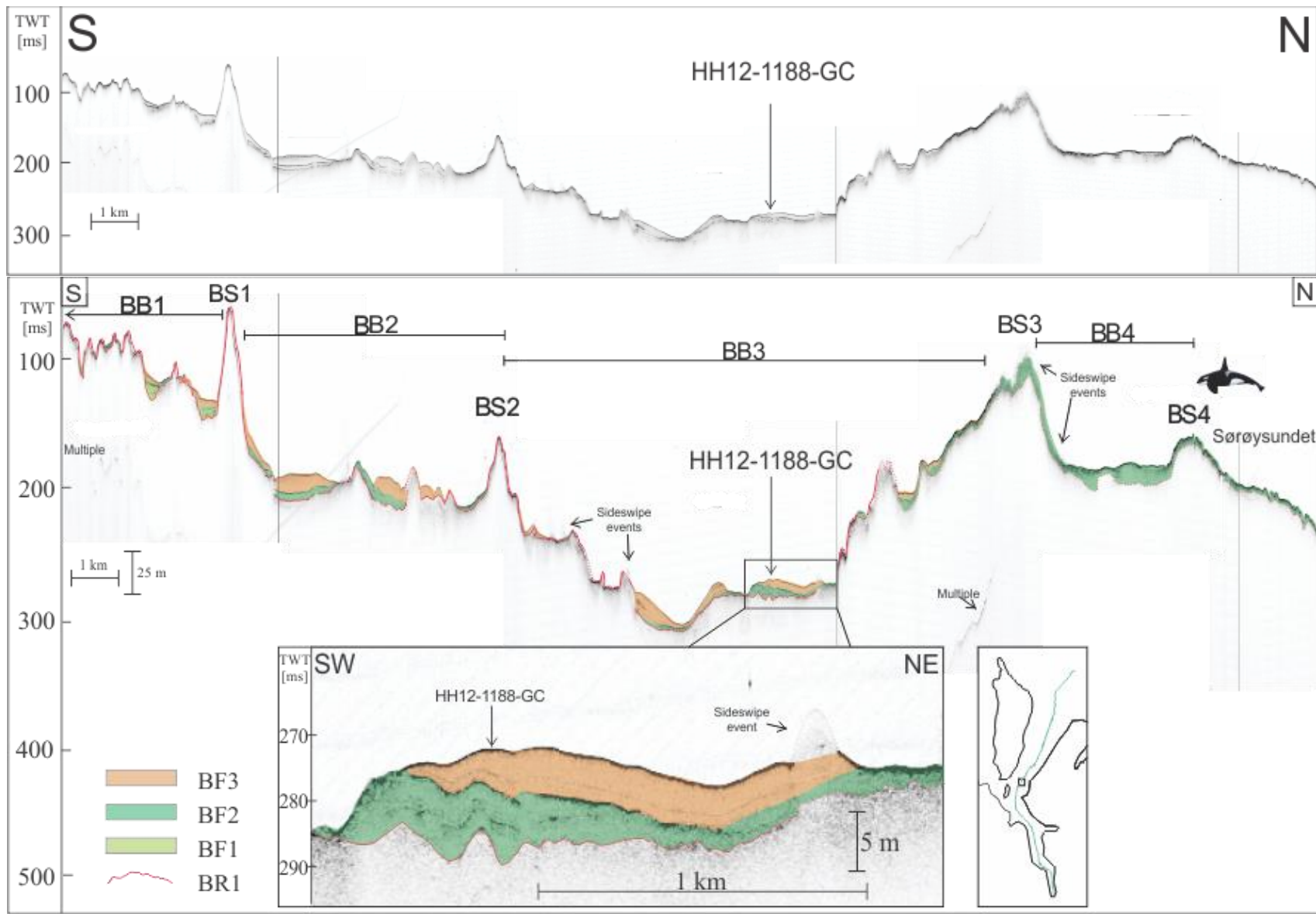
5.1.5.1   Acoustic basement – Reflection BR1

Occurrences of the acoustic basement, BR1, range from the seafloor to 24 m b.s.f. It is generally deeper in the basins, undulating, and control the general morphology of the fjord. The acoustic basement make up the geometry of the sills and basins, subsequently filled with sediment.

5.1.5.2   Bergsfjorden Facies 1

In the basin BB1, facies BF1 is observed to make up the lower sedimentation in the two sub-basins. It has a maximum thickness of 12 m in the innermost basin, and 5 m in the next. 200 horizontal m are observed in the seismic profile in the innermost basin, 400 m in the next. The continuous parallel stratification is observed to fill in the acoustic basement beneath, onlapping the side walls..

5.1.5.3   Bergsfjorden Facies 2

The facies BF2 is recognized in all basins in the seismic profile. With the exception of the innermost basin BB1 where it overlies BF1, it is deposited directly on top of the acoustic basement. Some stratification in the generally semi-transparent configuration of the internal reflections is inferred. The stratification is continuous in BB2 and in the highlighted sub-basin, generally following the geometry of the upper prominent boundary, onlapping the side wall. In the other basins, the inner reflections are rather chaotic, discontinuous and undulating, hummocky to complex, with little systematic terminations.

The thickness of the facies generally increase in the distal basins, from approximately 1 m in the innermost sub basin to around 7 m in the highlighted sub-basin. Units with thicknesses ranging from 2 to 4 m are generally observed in all basins, often thinning distally. Over the sills BS3 and BS4 and in the basin BB4, BF2 is chaotic, with a vague lower boundary, possibly attenuating the seismic signal as it comprise of impenetrable material.

The relatively strong upper boundary of the facies represent the interface to the overlying and hence younger facie BF3, or directly to the overlying water, representing the seafloor.

5.1.5.4   Bergsfjorden Facies 3

The lower boundary of the facies BF3 comprise of a strong, undulating reflection configuration. Some inner stratification occur, generally following the trend of the upper boundary reflection, being sub-parallel in its configuration. The internal intervals are generally acoustically transparent. BF3's upper strong boundary represent the water-sediment interface. The facies is inferred to be generally filling in the undulating unconformity below.

In the deepest part of BB3, accumulations up to 9 m are observed. The facies onlap the sediment or the acoustic basement below, except in the highlighted sub-basin where it seems to be truncating northward (Figure 43).

5.1.6 Jøkelfjorden

The approximately 15.1 km long seismic line reveals two basins separated by one prominent sill (JS1) in the middle of the fjord (Figure 44 and Figure 45). A lower relief of the seafloor affect the configuration of the fjord geometry.

The inner part of the fjord is characterized by a slightly undulating, low-relief morphology between 85 and 120 m b.s.l. Basin JB1 is approximately 50 m deep, 7 km long and 1 km wide, narrowing toward the fjord head. Maximum 12 m of sediment is observed in the basin. Basin JB2 is the basin from where the core HH12-1193-GC was retrieved, 193 m b.s.l. The 4 km long basin is around 1.5 km wide with a maximum sediment thickness of approximately 23 m. JB2 terminates at a sill about 160 m b.s.l., before the depth of the seafloor increase down to 340 m b.s.l. into Kvænangsfjorden.
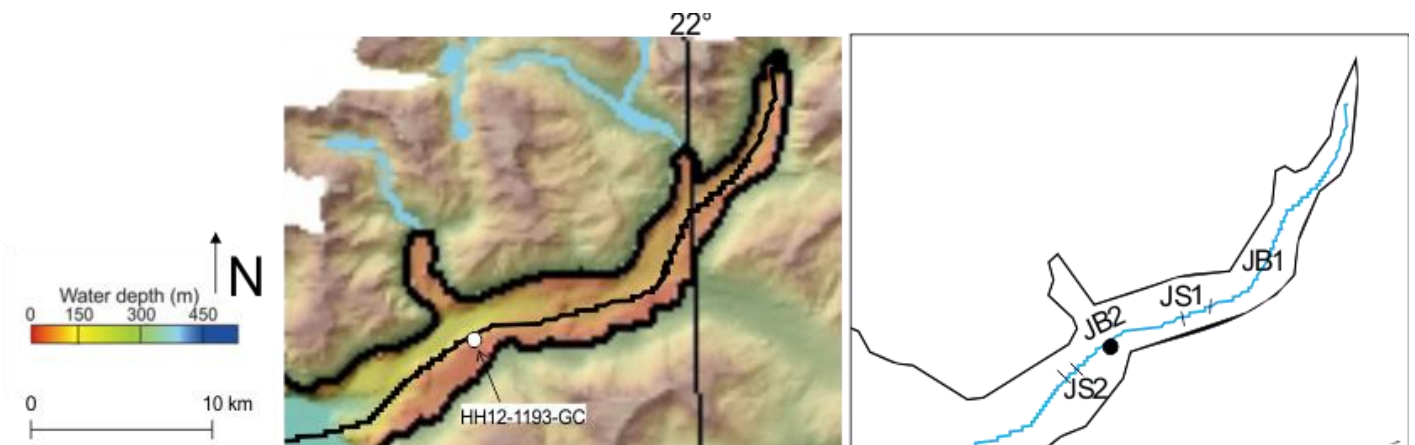
Figure 44 Low-resolution bathymetric data and the position of core HH12-1193-GC. Seismic composite line inferred in the bathymetry and in a simple wireframe of the coastline. J: Jøkelfjorden, B: Basin, sB: Sub-basin, S: Sill. Increasing numbers denoted with reduced proximity to the fjord head. Bathymetric data after Jan. P. Holm (Forwick & Rasmussen, 2012).

Figure 45 (next page) The upper profile presents the seismic chirp data retrieved from Jøkelfjorden in 2012 (Forwick & Rasmussen, 2012). The lower profile include interpretations of acoustic facies and large-scale fjord geomorphology. The location of the gravity core HH12-1193-GC is given, and the basin it is retrieved from highlighted in the zoom-in. The halibut show what is inferred to be the water column, not to scale. Note the vertical exaggeration in the seismic data. The outer fjord is to the west. J: Jøkelfjorden, B: Basin, sB: Sub-basin, S: Sill. Increasing numbers are denoted out the fjord.
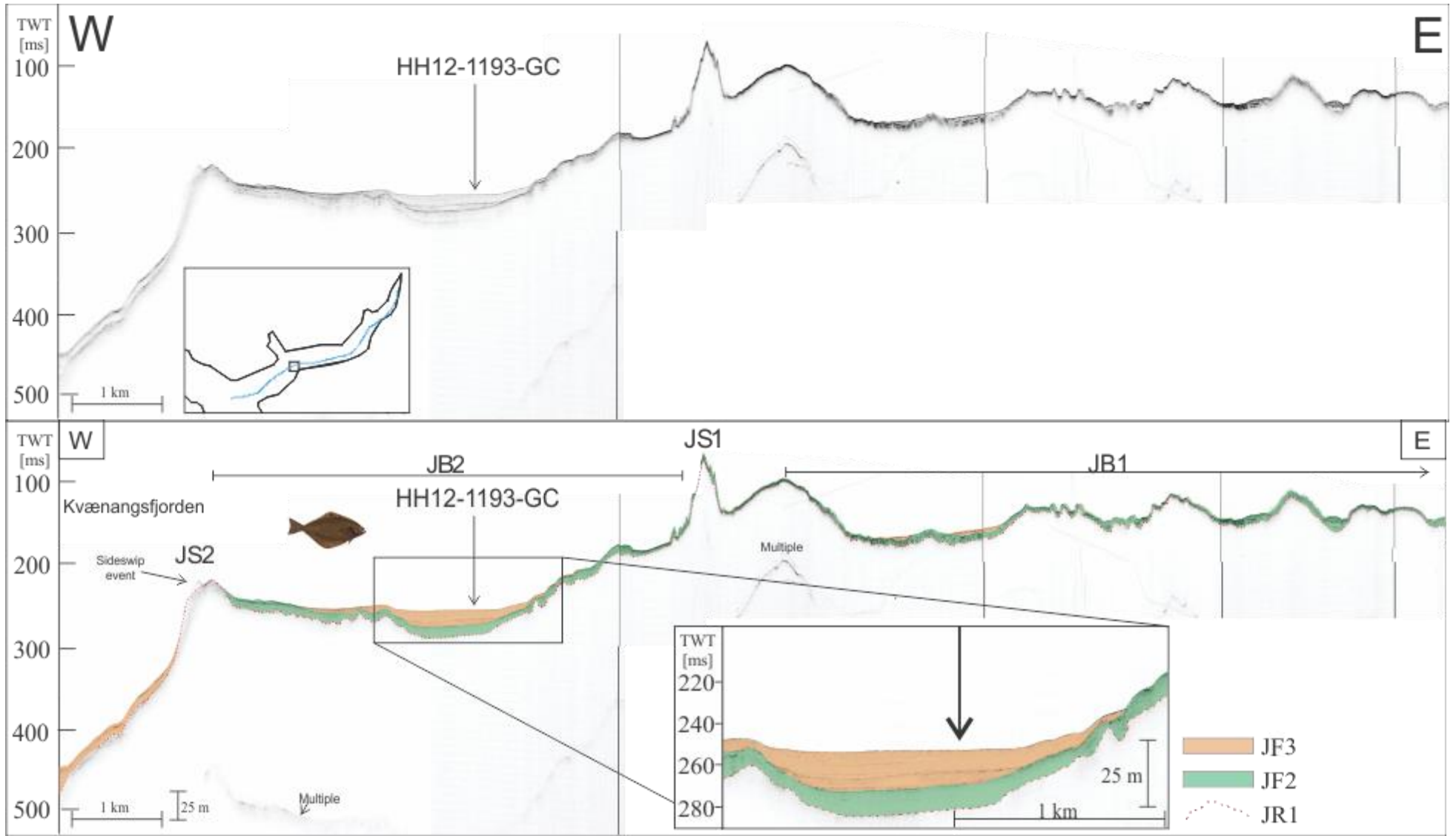
5.1.6.1 Acoustic basement – Reflection JR1

The acoustic basement may not be continuously traced, but an attempt to recognize a vague reflection was carried out. This range between making up the seafloor to occur 22 m b.s.f.

5.1.6.2 Jøkelfjorden Facies 2

A general concordance on top of the lower undulating base characterize the facies JF2. The facies is found to drape the acoustic basement in the entire fjord, with thicknesses measuring between 1 to 4 m in the basin JB1, and between 2 to 9 m in the basin JB2. The thinnest accumulation of the facies is draping the center sill, JS1 with about 1.5 m of the deposit described as facies JF2.

The reflection configuration of the entire facies is generally chaotic in the innermost basin, to almost semi-transparent in JB2. Some fan complex units are observed in the innermost basin, with a generally rugged upper boundary. The outer basin contain an upper boundary being more undulating, and seemingly slightly closer in charcter to the overlying facies JF3.

5.1.6.3 Jøkelfjorden Facies 3

A lower continuous reflection make up the base for the facies JF2, an onlapping infill of stratified sediment. The stratification is parallel to sub-parallel, with thicknesses varying between 8 to 2 m, thinning toward the basin sides.

The general reflection configuration is semi-transparent to transparent, separated by at least two continuous reflections. All together, the units in JB2 together make up 15 m at its thickest, thinning toward the sides of the basin. Thin patches of the facies are found in the inner sub-basins, filling in the depressions in the undulating bathymetry.

5.2 Lithostratigraphy

Herein, the gravity cores have been described based on visual observations, X-ray imaging, physical characteristics, grain size distribution and geochemical composition. The data was retrieved as described in Chapter 3.3, and is described from bottom (oldest) and up. A summary of the location of the gravity cores and the ranges of the physical properties are given in Table 11. A legend for the presented data is seen in Figure 46.

Table 11 Summary of the location of the gravity cores and the physical properties measured in the laboratory.

Fjord	Øksfjord		Bergsfjord		Jøkelfjord	
Coring station	HH12-1185-GC		HH12-1188-GC		HH12-1193-GC	
Latitude [N]	70°.08.650'		70°16.046'		70°04.032'	
Longitude [E]	022°17.296'		021°45.283'		021°50.742'	
Water depth [m]	237		204		193	
Recovery [cm]	441		366		480	
	Min	*Max*	*Min*	*Max*	*Min*	*Max*
Density [g/cm]	1.28	1.67	1.32	1.90	1.36	2.28
MS [$SI * 10^{-5}$]	10	132	11	40	29	338
AI [$g*m*cm^{-3}s^{-1}$]	1160	2560	1429	3324	1320	3747
P-wave Velocity [m/s]	891	1651	932	1772	897	1693
P-wave Amplitude	0	100	0	99	0	100
Fractional porosity	0.62	0.85	0.49	0.83	0.27	0.80
Fe/Ca-ratio	1.34	2.48	0.47	3.60	2.24	5.56
Fe/SUM	0.40	0.53	0.27	0.63	0.41	0.65
Ca/SUM	0.18	0.30	0.15	0.56	0.10	0.20
Grain size mode [μm]	16	169	38	96	5	518
Grain size mean [μm]	16	119	31	250	7	202
Age [cal. yrs. BP]	0	6392	0	11085	0	12341
Sed. rate [cm/ka]	48.5	55.6	21.5	77.0	15.9	51.2
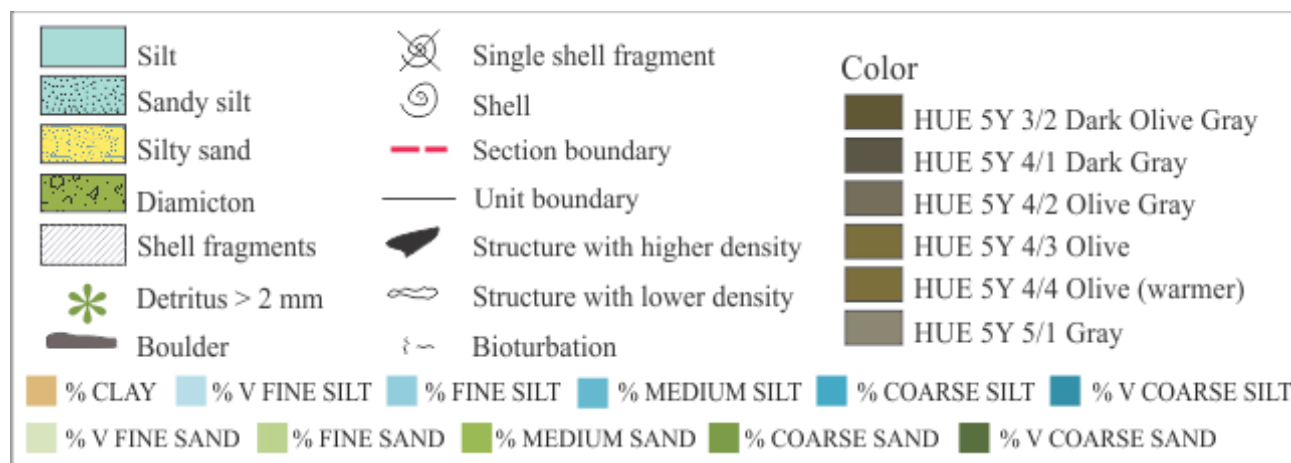
Figure 46 Legend for the presentation of the data retrieved from laboratory work. Textural groups are after (NGU, 2017). Color descriptions are after "The Munsell Soil Colour Charts" 1995).

5.2.1 Core HH12-1185-GC
The entire core HH12-1185-GC consists of massive mud; mainly sandy silt and silt, with the exception of a layer of silty sand around 50 cm down the core (Figure 47).

5.2.1.1 Visual properties
The color changes gradually from Olive Gray to Olive throughout the entire core, with the exception of a 2 cm thin upper Gray layer (Figure 47). Directly after opening some black marks presumably consisting of sulphide were observed in the uppermost section. Most of these oxidized over time, except for a layer between 54 and 52 cm b.s.f.

5.2.1.2 Physical properties
In the X-ray images, the lower 10 cm of the core is depicted as darker than the rest of the section, thus inhering a relatively higher density than the overlying deposit (Figure 47). The increased density at the bottom 10 cm may reflect compaction of the sediment, and probably prevented the gravity core from penetrating deeper. Reduced loading of overlying sediment closer to the seafloor probably causes the relatively steady decrease in density up the core. 2 cm thick layers of increased density is seen between 54 and 52 cm, and in the uppermost 2 cm.

Some larger clasts are observed sporadically throughout the entire core (very small boulder at 404-407 cm b.s.f., and gravel at 344, 317, 249, 239, 176, 123-125, 104, 64 and 8 cm b.s.f.). Lines of lower densities possibly represent bioturbation, or they are caused by the reduced loading after retrieval, as these are mostly recognized mostly in the top of the core sections. Shells were observed in the entire core, with less occurrences in the lower 2 m of the core. Five skew, undulating planes were observed in the upper section.

The density is generally decreasing up core, with small variations from 1.75 to 1.25 g/cm^3. A slightly larger increase is inferred from around 280 cm b.s.f. and up. As inferred from the X-ray images, peaks of higher density occur at the very coarse gravel at 123 cm b.s.f., at the 2 cm thick layer 52-54 cm down core and at the upper 2 cm. Decrease in density occur from around 395 to 375 and around 61 cm b.s.f. The latter possibly due to the large shell found at 61 cm b.s.f. Fractional porosity is general opposite proportional to the density, varying from 60 % at the bottom, toward 80 % in the top.

Magnetic susceptibility increase at the boulder around 405 cm b.s.f, and is steady until an increase around 70 cm b.s.f, peaking at the bed recognized in the other physical properties, 54-52 cm b.s.f., the clast at 8 cm b.s.f. and at the top bed. An interval of decreasing MS is seen 395-375 cm b.s.f., coinciding with the decrease in density observed.

The P-wave amplitude is mostly too low for the P-wave velocity measured to be valid, and hence also includes the acoustic impedance.

Slightly larger grain size fractions are inferred above 300 cm b.s.f., with continuous variations. Peaks of positive variations in the mean grain size occur around 405, 300, 190, 180, 145, 52 and 1 cm b.s.f.

Figure 47 (next page) Characteristics of the physical properties of core HH12-1185-GC. Variations in the data inferred to be related to the section boundaries have been removed.

| [cm b.s.f.] | Photo | Color | Bioturbation | Lithological log | Mean grain size | Density [g/cm³] | Fractional porosity [%] | P-wave velocity [m/s] | Grain size fraction [%] |

Age [cal.yrs. BP]

1,197 ± 73

6,392 ± 89

X-ray Shells Sulfide si S si S Acoustic impedance [g*m*cm⁻³s⁻¹] Magnetic susceptibility [SI * 10⁻⁵] P-wave amplitude Clay Silt Sand

78
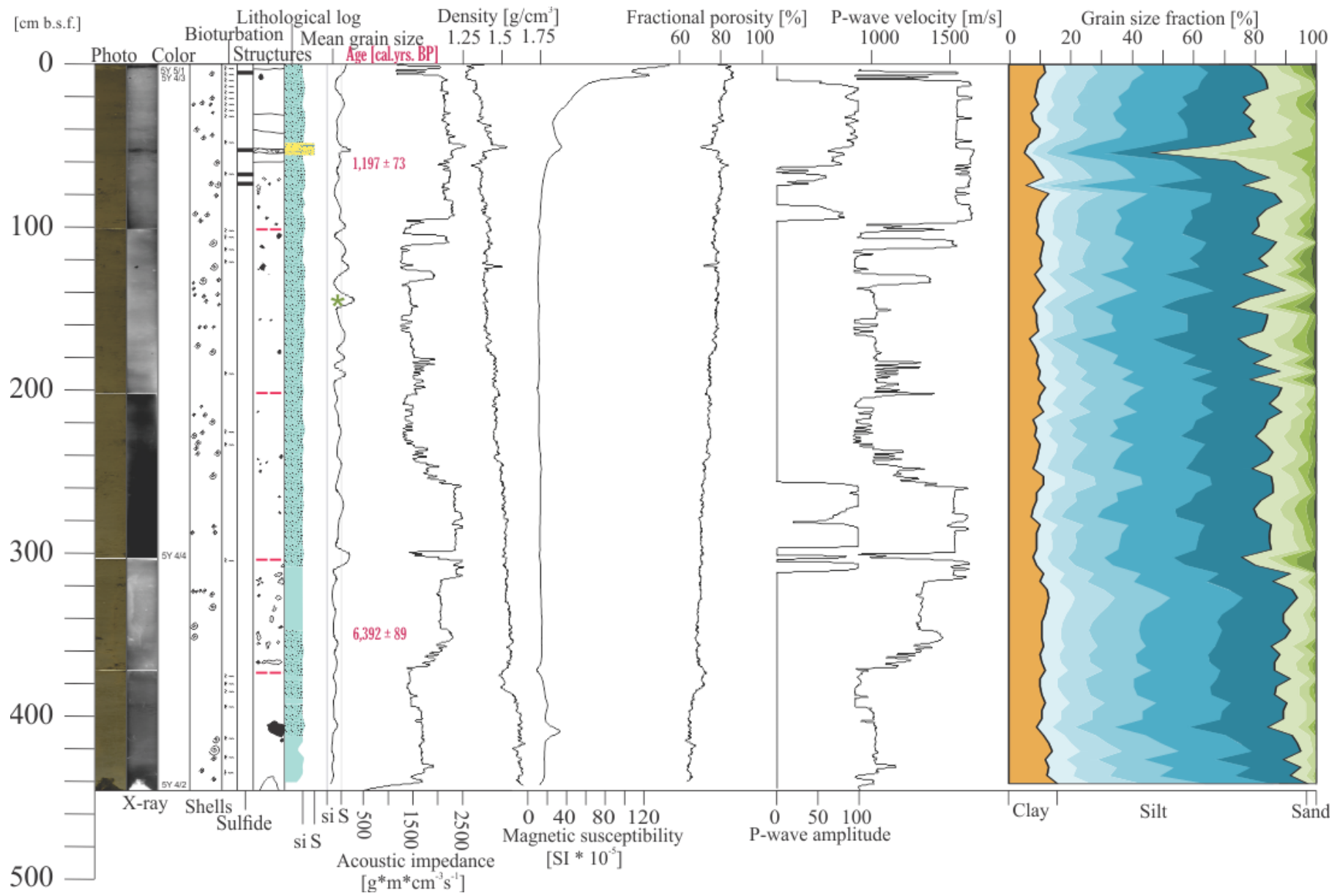
5.2.1.3   Geochemical properties

The bottom 30 cm inhere a trend of an upward decrease of the K/SUM-, Si/SUM- and Fe/SUM-ratios, and an increase in the Ca/SUM-ratio (Figure 48). Above this, all geochemical ratios are generally stable up the core before a break around 280 cm b.s.f. The exception is the Si/SUM-ratio, continuing the slightly decrease up the core, and the Ca/SUM-ratio with a slight increase.

At 280 cm b.s.f., the Ca/SUM changes from being gradually increasing below, to gradually decreasing above. Fe/SUM and K/SUM follow an opposite trend relative to Ca/SUM. A vague indication of changing regimes around 210 cm b.s.f. is observed. Here, K/SUM change toward decreasing ratios. Si/SUM changes from a minor decrease to a slightly greater decrease. Ca/SUM is more stable above.

From 110 cm b.s.f. and upward, larger variations in the geochemical ratios are observed, with the largest variations around 53 cm b.s.f., and at the very top. At 53 cm b.s.f., positive peaks in the Ti/SUM-, Sr/SUM- and Fe/SUM-ratios are inferred, along with negative peaks in the K/SUM-, Br/SUM and Ca/SUM-ratios. At the uppermost 2 cm, an increase in Si/SUM, Ca/SUM, Ti/SUM and Sr/SUM, and a decrease in Br/SUM and Fe/SUM.

Figure 48 (next page) Characteristics of the geochemical properties of core HH12-1185-GC.
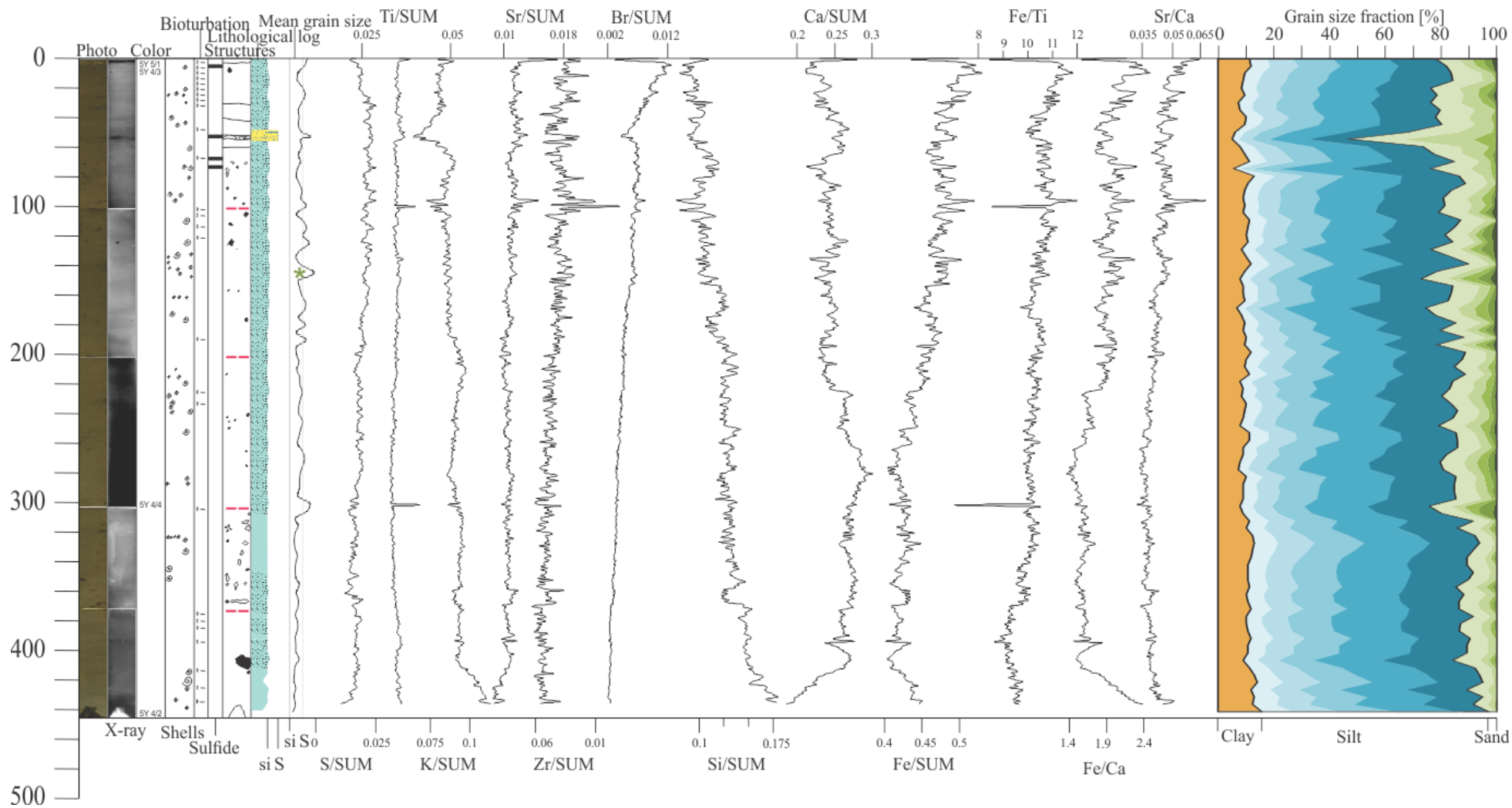
5.2.2 Core HH12-1188-GC
The entire core HH12-1188-GC consists of massive mud; mainly sandy silt and silty sand (Figure 49).

5.2.2.1 Visual properties
The color changes gradually from Olive Gray to Olive throughout the entire core (Figure 49). Sulphide was observed visually in the upper- and lowermost section. Section 1 and 3 smelled of sulphide a long time after opening. The most pronounced observation was the layer at 203-204 cm b.s.f. with a lot of visible shell fragments present.

5.2.2.2 Physical properties
In both the X-ray images and visually, a lot of shell fragments where observed in the top 240 cm (Figure 49). Intact shells were observed in the entire core with a generally equal abundance throughout the core. A pronounced layer of increasing amounts of fragments were observed at 203 cm b.s.f., with increasing densities. In addition, a skew plane of higher density is seen in the X-ray images between 306 and 309 cm b.s.f. Few sporadic clasts are found; two small gravels in the lower 5 cm, three clasts around 320, one at 240, one at 120, four around 50 and one around 20 cm b.s.f. No clasts > 2 mm were in the grain size samples. Only one case of bioturbation is observed, at 110 cm b.s.f.

The density is slightly increasing up the core until around 240 cm b.s.f., where a transition into decreasing densities are inferred. Positive peaks in density is seen at the skew plane around 307 and at the pronounced shell fragment layer 203 cm b.s.f., matching with the observed density in the X-ray images. Negative density peaks are seen at depths where large shells are observed in the X-ray. Fractional porosity is generally opposite proportional to the density, varying from 50 % to 70 %.

From the bottom of the core and up 15 cm, the magnetic susceptibility increase. In addition, the MS increase at the inferred layers mentioned above, despite a general trend of decreasing values up the core from 350 cm b.s.f. and up. Around 40 cm b.s.f., MS increase a lot, until a slight decrease initiated 4 cm b.s.f.

The P-wave amplitude is mostly too low for the P-wave velocity measured to be valid, and hence also includes the acoustic impedance.

A finer grain size fraction is inferred at the bottom of the core, gradually increasing in size up to around 200 cm b.s.f. The increase is steeper above 290 cm b.s.f. A peak of larger fractions occur at 203 cm b.s.f. before a drop around 190 cm b.s.f. Generally, stable grain sizes are seen above 180 cm b.s.f. Finer grain size fractions are also observed at the very top 10 cm. Silt and clay content generally decrease above 240 cm b.s.f.

Figure 49 (next page) Characteristics of the physical properties of core HH12-1188-GC. Most of the variations in the data that are inferred to be related to the section boundaries have been removed.
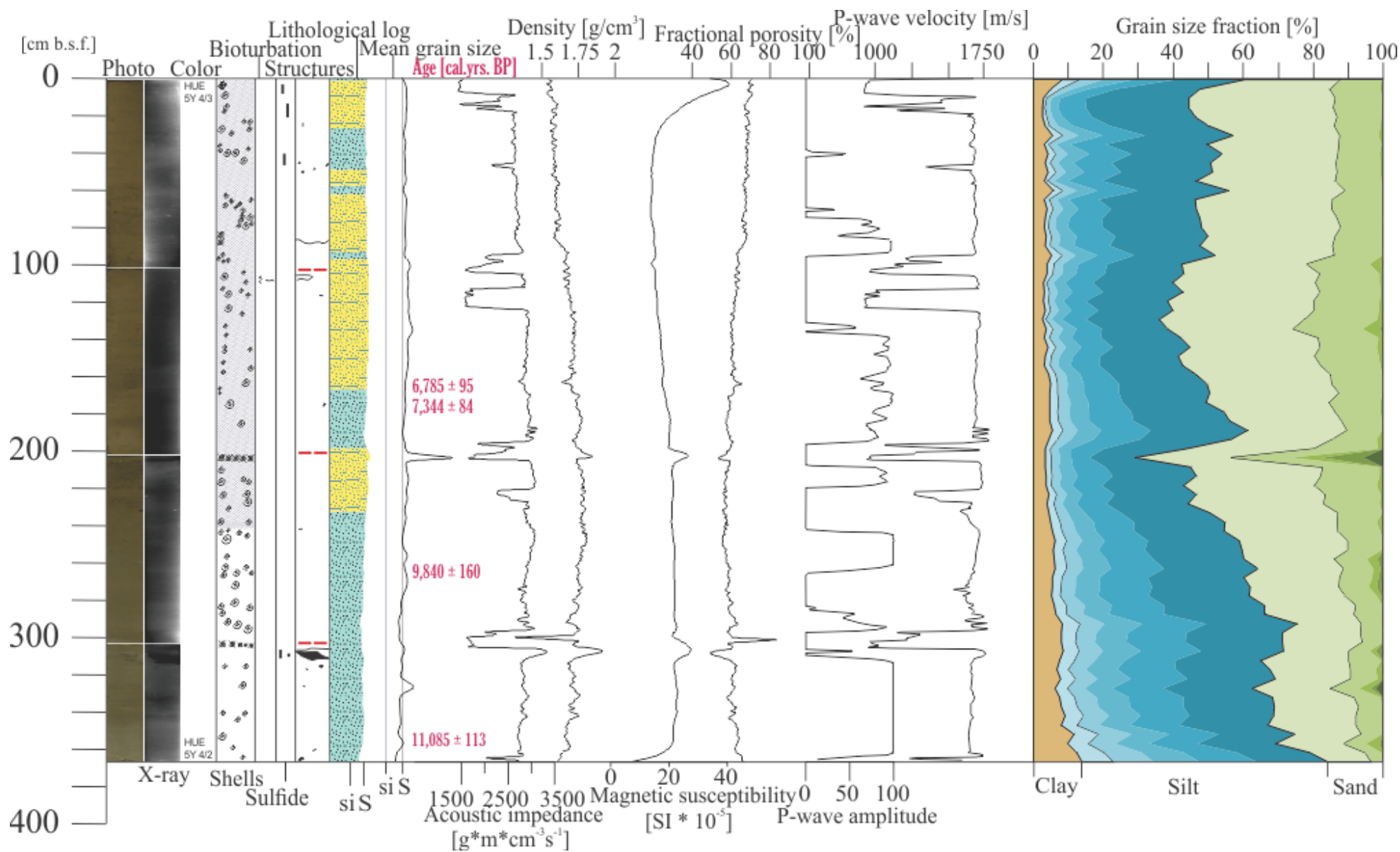
5.2.2.3 Geochemical properties

Above 350 cm trends of decreasing Ti/SUM, K/SUM, Si/SUM and Fe/SUM are observed along with an increasing Ca/SUM, up until 240 cm b.s.f. (Figure 50). Larger variations are caused by the layer 203 cm b.s.f. Above 170 cm b.s.f., the ratios continue the trend of a gradual change from earlier, but with less short term variations. Around 150 cm b.s.f. and up, more stable composition of the sediment are inferred.

The layer with a lot of shell fragments present at 203 cm b.s.f., generally inhere a trend of decreasing Ti, K, Si, and Fe, and increasing Ca.

Figure 50 (next page) Characteristics of the geochemical properties of core HH12-1188-GC.
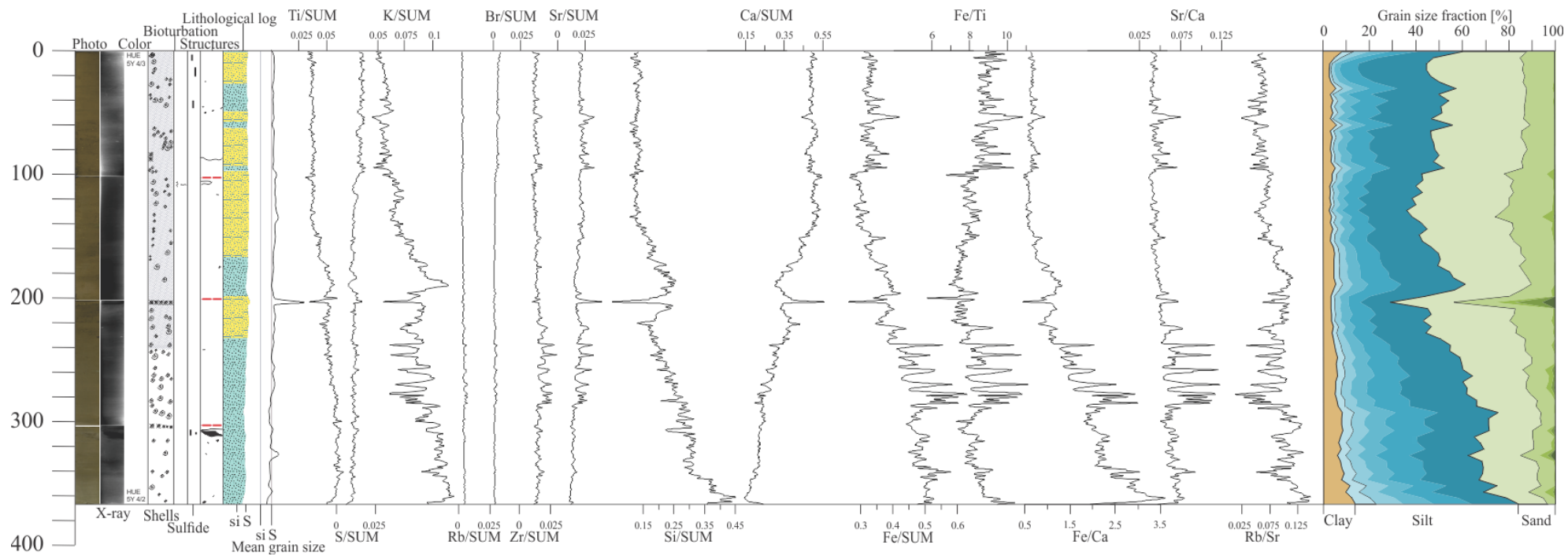
5.2.3 Core HH12-1193-GC
The core HH12-1193-GC, consists of 30 cm of diamicton at the bottom, with an upper 440 cm of massive mud; mainly sandy silt and silt (Figure 51). A boulder was removed at the very bottom when the pictures were taken. This is indicated in the lithological log.

5.2.3.1 Visual properties
The change in color in the core is conspicuous (Figure 51). A change from Gray to Dark Gray, to Olive Gray to Dark Olive Gray is seen up the core. Sulphide were noticed on the color and the smell in the upper 20 cm of the core.

5.2.3.2 Physical properties
The X-ray images show a very high abundance of clasts throughout the core, increasing in size and abundance up the core (Figure 51). The largest clasts are seen in the bottom diamicton, in a layer around 385 cm b.s.f., and above 235 cm b.s.f. A higher abundance of shells are also observed in the upper 235 cm, sporadically occurring below (e.g. 310-280 cm b.s.f.). Not much bioturbation has been observed.

Varying densities are inferred in the lower diamicton up until 450 cm b.s.f., possibly due to the large variation in the deposit with grain sizes from clay to boulder. Directly above the diamicton, a 15 cm thick layer with a steeply decreasing density gradient occurs. Above 436 cm b.s.f., a steady density around 1.6 g/cm^3 is observed, before slightly decreasing from 250 cm b.s.f. and up. Fractional porosity is generally opposite proportional to the density, varying from 40 % at the bottom toward 80 % at the top.

The magnetic susceptibility generally follow the trend of the density; varying up until 449 cm b.s.f., steeply decreasing upward to 436 cm b.s.f., and relatively steady above approximately 360 cm b.s.f. A slight increase is however observed above 2 cm b.s.f.

The P-wave amplitude is mostly too low for the P-wave velocity measured to be valid, and hence also the acoustic amplitude. However, high P-wave amplitudes in the deepest section validate the P-wave velocity measured, showing steeply decreasing velocities in the upward fining layer between 450 and 436 cm b.s.f.

The diamicton from the bottom of the core to 450 cm b.s.f. comprise of grain sizes too large to be measured by the laser diffraction analyzer. However, samples of the finer fractions were retrieved, confirming the presence of all grain sizes. Above this, grain sizes decrease up to a layer without any sand at all between 426 and 416 cm b.s.f, before an increase in the grain sizes until a peak 366 cm b.s.f.. Above this, relatively steady grain sizes are inferred, slightly peaking at 325, 285, 195 and 135 cm b.s.f.
395

Figure 51 (next page) Characteristics of the physical properties of core HH12-1193-GC. Variations in the data related to the section boundaries are removed.
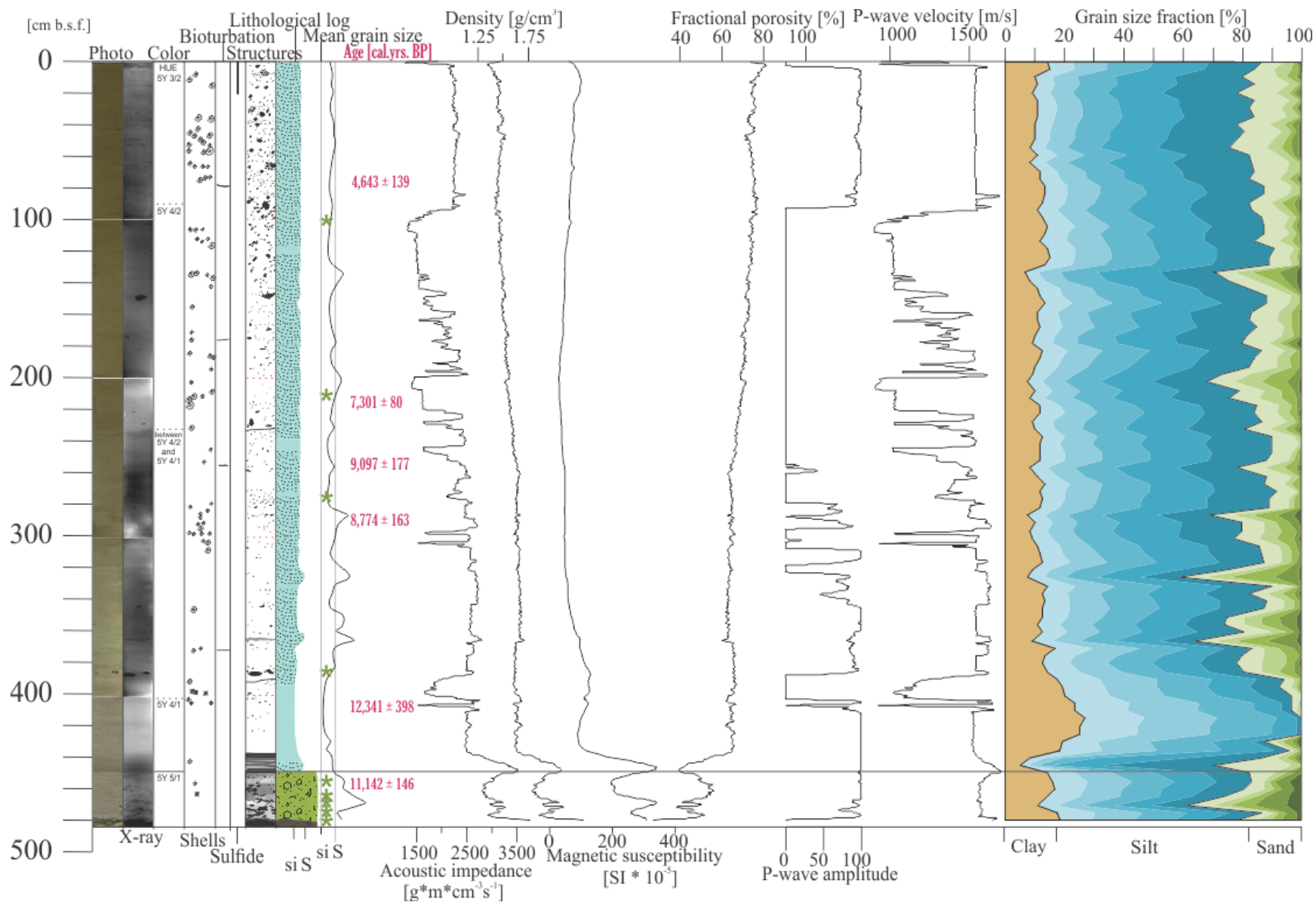
5.2.3.3 Geochemical properties
In the lower diamicton, all geochemical ratios vary a lot (Figure 52). In the 15 cm above 450 cm b.s.f., an upward increase in K/SUM, and Fe/SUM occur, along with a decrease in Ti/SUM, Zr/SUM, Sr/SUM, Si/SUM and Ca/SUM.

Above 436 cm b.s.f., generally stable ratios are inferred, except a decrease in Fe/Ca, K/SUM and Si/SUM, until 235 cm b.s.f. Above this, K/SUM and Si/SUM continue decreasing, along with a small increase in Br/SUM and Fe/SUM. The rest of the geochemical ratios are generally continuing at the same level up the core.

The peaks in the ratios around 40 cm b.s.f. are presumably due to a large clast of lower density observed in the X-ray image of the archive half section.

Figure 52 (next page) Characteristics of the geochemical properties of core HH12-1193-GC.
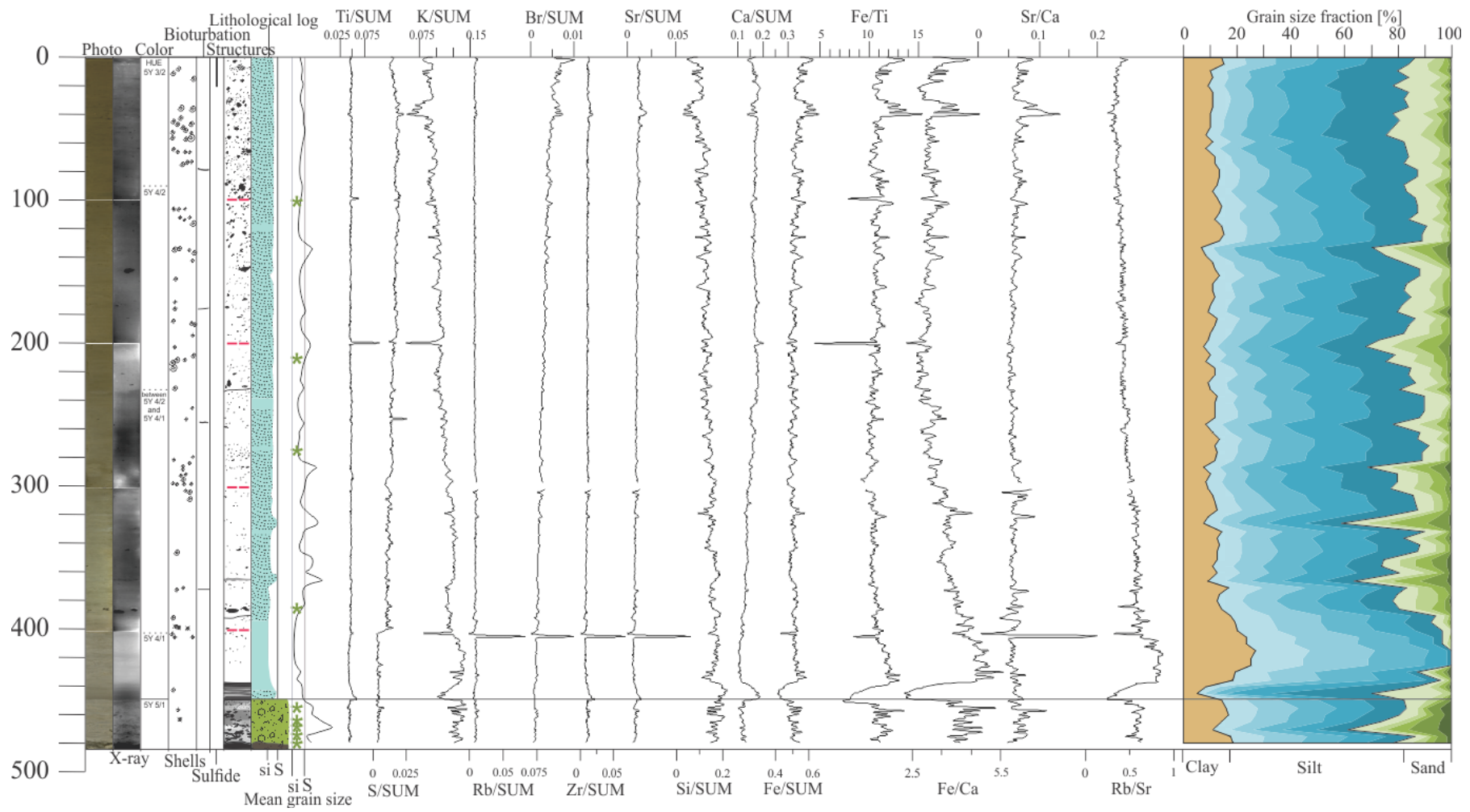
5.3 Chronostratigraphy

5.3.2 Results from the dating and calibration

The complete tables received from AWI and NTNU are presented along with the calibration curves in the Appendix A. Table 12 show the ^{14}C ages and the calibrated age BP. A ΔR of 71 +/- 21 is applied when calibrating, as mentioned in Chapter 4.4. The calibrated ages are also presented along with the physical properties in the previous figures (Figure 47, Figure 49 and Figure 51).

Generally, younger sediment are subsequently deposited on top of the older. Some ages in the core HH12-1193-GC, reveals redeposition of older sediment. It is obvious that some of the dated material is not deposited in situ as older dates are found above younger at several locations. This is further discussed in Chapter 6.3.2.

Table 12 Present the ^{14}C age received from NTNU (TRa) and AWI (no letters in lab. Ref. nr.) and the calibrated ages BP with their standard deviation (σ1) from the Marine13 calibration curve (Stuiver et al., 2018). 71 ± 21 is used as ΔR (Mangerud et al., 2006)

Core	Depth [cm]	Lab. Ref. nr.	^{14}C age	Cal. age BP [1σ]
HH12-1185-GC	61	TRa-12752	1690 ± 15	1197 ± 73
HH12-1185-GC	350	TRa-12753	6055 ± 20	6392 ± 89
HH12-1188-GC	163	TRa-12754	6395 ± 20	6785 ± 95
HH12-1188-GC	175	TRa-12755	6885 ± 25	7344 ± 84
HH12-1188-GC	260	TRa-12756	9185 ± 25	9839 ± 160
HH12-1188-GC	356	TRa-12757	10,135 ± 25	11085 ± 113
HH12-1193-GC	75	TRa-12758	4535 ± 20	4643 ± 139
HH12-1193-GC	211	TRa-12759	6850 ± 20	7301 ± 80
HH12-1193-GC	254	1538.1.1	8554 ± 60	9097 ± 177
HH12-1193-GC	288	TRa-12760	8315 ± 20	8774 ± 163
HH12-1193-GC	408	1540.1.1	10,922 ± 129	12,341 ± 398
HH12-1193-GC	458	1539.1.1	10,209 ± 68	11,142 ± 146

5.3.3 Average linear sedimentation rates

Estimations of the average linear sedimentation rate between each determined age is calculated (Table 13). A constant sedimentation is assumed for the estimates. Thus, presence of abrupt greater accumulations of sediment provide larger estimations of the average sedimentation rate than what is actually the case. An assumption of sedimentation up until 2012 CE is expected and hence 62 years are added when estimating the age intervals, as the calibrated ages yield refer to prior to 1950 CE (Chapter 4.3). Calculations are made without the standard deviation of the calibrated ages. Sedimentation rates have not been calculated for the inverted ages.

Table 13 Calculated sedimentation rates for depth intervals between dated materials. 62 years have been added when presenting the age interval as the calibrated dates are presented as ages prior to 1950 CE, and the sedimentation is expected to have occurred up until retrieval. Age reversals are inferred for some of the dated samples from core HH12-1193-GC, and hence sedimentation rates are not calculated for this interval.

Core	Depth interval [cm]	Age interval [cal. yrs. BP]	Years of sedimentation	Linear sedimentation rate [cm/ka]
HH12-1185-GC	61-0	1259-0	1259	48.5
HH12-1185-GC	350-61	6454-1259	5195	55.6
HH12-1188-GC	163-0	6847-0	6847	23.8
HH12-1188-GC	175-163	7406-6847	560	21.4
HH12-1188-GC	260-175	9901-7406	2495	34.1
HH12-1188-GC	356-260	11,147-9901	1246	77.1
HH12-1193-GC	75-0	4705-0	4705	15.9
HH12-1193-GC	211-75	7363-4705	2659	51.2
HH12-1193-GC	288-211	8836-7363	1473	52.3

5.3.4 Age estimates

Age estimates may be inferred between dated shells based on the average linear sedimentation rates. If an age estimate of a depth beneath any dated material, extrapolating the deepest rate may be used. Correlations between depths in the gravity core and ages [cal. yrs. BP] may be seen in Figure 53. A continuous average linear extrapolation of the lowermost, reliable ages are inferred in the figure.

Figure 53 Each colored line represent separate average linear sedimentation rates. Extrapolated linear sedimentation are seen as black lines. These are extrapolated from the lower average linear sedimentation rate inferred to be valid (thus, not inverted).

Depths between dated material further discussed in Chapter 6, may be seen in Table 14.

Table 14 Estimation of ages based on the sedimentation rates calculated by the calibrated ages of shells. Extrapolated age estimates from the calculated sedimentation rate above the closest dated shell are noted with an asterix.

Core	Depth [cm]	Estimated age [cal. Yrs. BP]
HH12-1185-GC	2	41 ± 73
HH12-1185-GC	40	824 ± 73
HH12-1185-GC	54	1114 ± 73
HH12-1185-GC	70	1358 ± 89
HH12-1185-GC	200	3695 ± 89
HH12-1185-GC	280	5133 ± 89
HH12-1185-GC	300	5493 ± 89
HH12-1185-GC	411	$7488 \pm 89*$
HH12-1188-GC	4	168 ± 95
HH12-1188-GC	25	1050 ± 95
HH12-1188-GC	40	1680 ± 95
HH12-1188-GC	170	7111 ± 84
HH12-1188-GC	203	8166 ± 160
HH12-1188-GC	240	9252 ± 160
HH12-1188-GC	351	$11,020 \pm 113$
HH12-1193-GC	2	125 ± 139
HH12-1193-GC	25	1568 ± 139
HH12-1193-GC	150	6109 ± 80
HH12-1193-GC	220	7477 ± 80
HH12-1193-GC	235	7760 ± 163

The deepest average linear sedimentation rates from Table 13 were extrapolated in order to estimate the age of the bottom of the core and the boundary to underlying facies and/or units as interpreted from the depth inferred in the seismic data. These may be seen in Table 15. Estimates were only made for F3, as sedimentation rates probably change with changing facies. HH12-1193-GC inhere interchangeable age estimates with depth, hence non of the extrapolated ages were used. HH12-1188-GC are inferred to be in contact with F2, hence an extrapolation of the age of the contact is estimated. Internal reflections are observed in the seismic data of ØF3, beneath the core HH12-1185-GC. Estimations of the ages of these are therefore made, as well is the age of the F2/F3 contact.

Table 15 Extrapolated age estimates based on the thicknesses derived from the seismic data or the bottom of the cores, and the average linear sedimentation rate calculated as in Table 13.

Core	Depth [cm]	Estimated age [cal. Yrs. BP]
HH12-1185-GC	441	8269 ± 89
HH12-1185-GC	591	9088 ± 89
HH12-1185-GC	786	$12,593 \pm 89$
HH12-1185-GC	861	$13,941 \pm 89$
HH12-1188-GC	366	$11,214 \pm 113$

All estimated ages are maximum ages due to possible events producing abnormally large sediment accumulations.

6   Discussions

6.1 Correlation of seismo- and lithostratigraphy

Chirp data is in here correlated with the gravity cores based on the depths inferred by the TWT and velocities. Some of the reflectors in the seismic data may represent variations in the physical properties observed in the cores.

The gravity cores do not penetrate the entire body of sediment detected in the seismic data, hence exclusively the shallowest seismostratigraphic facies are present in the cores. However, internal reflections occur, possibly representing short-lasting events of mass redeposition. Pronounced and apparent reflectors observed in the uppermost facies are inferred in the seismic data.

6.1.1 Øksfjorden

The reflection pattern in ØF3 at the core site is predominantly transparent, with the exception of a single reflection close to the seafloor (Figure 54). The lithology of core HH12-1185-GC is mainly uniform except from the coarser layer with higher density and peaks in the geochemistry around 54 cm b.s.f., estimated to date back to approximately 1100 cal. yrs. BP (Figure 47, Figure 48 and Table 14). I suggest that the coarser interval at 54 cm leads to changes in the physical properties causing the reflection observed on the chirp profile. This indicates that the reflection represents an approximately 2 cm thick mass transport deposit that can be traced over a distance of approximately 2.5 km (Figure 54). The extrapolated age to the top of ØF2 is maximum 13,940 cal. yrs. BP (Table 15).
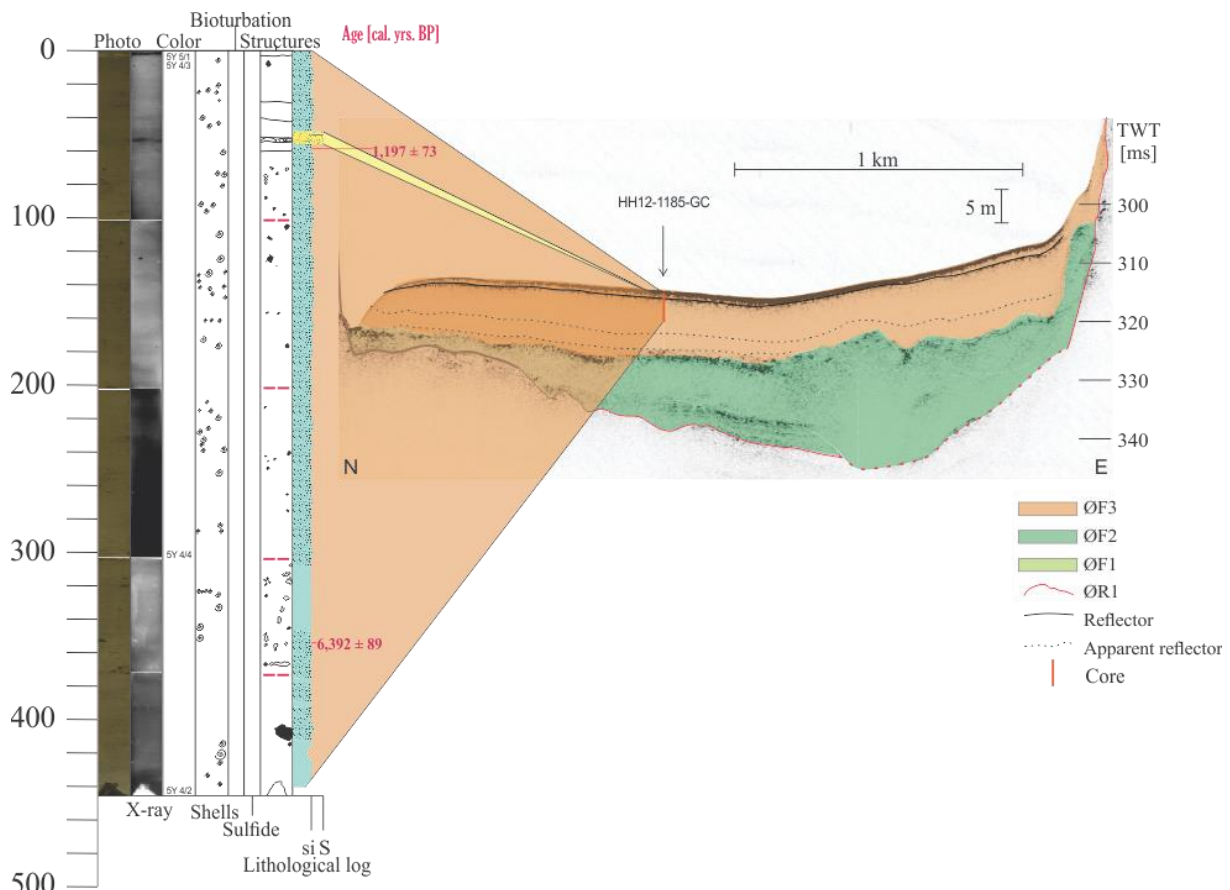
Figure 54 Seismic data from the sub-basin ØsB2 in Øksfjorden correlated with gravity core HH12-1185-GC.

6.1.2 Bergsfjorden

The mainly uniform core HH12-1188-GC is inferred to penetrate the entire facies BF3 (Figure 55). One reflector is observed in the predominantly transparent seismic facies, traced 1.5 km laterally. I suggest that this reflector correlate with the increased density 240 cm b.s.f., approximately 9250 cal. yrs. BP, inferred from the gravity core (Figure 49 and Table 14). The estimated age of the bottom of the core is 11,210 cal. yrs. BP (Table 15), and hence provides a minimum age for the deposition of BF2.
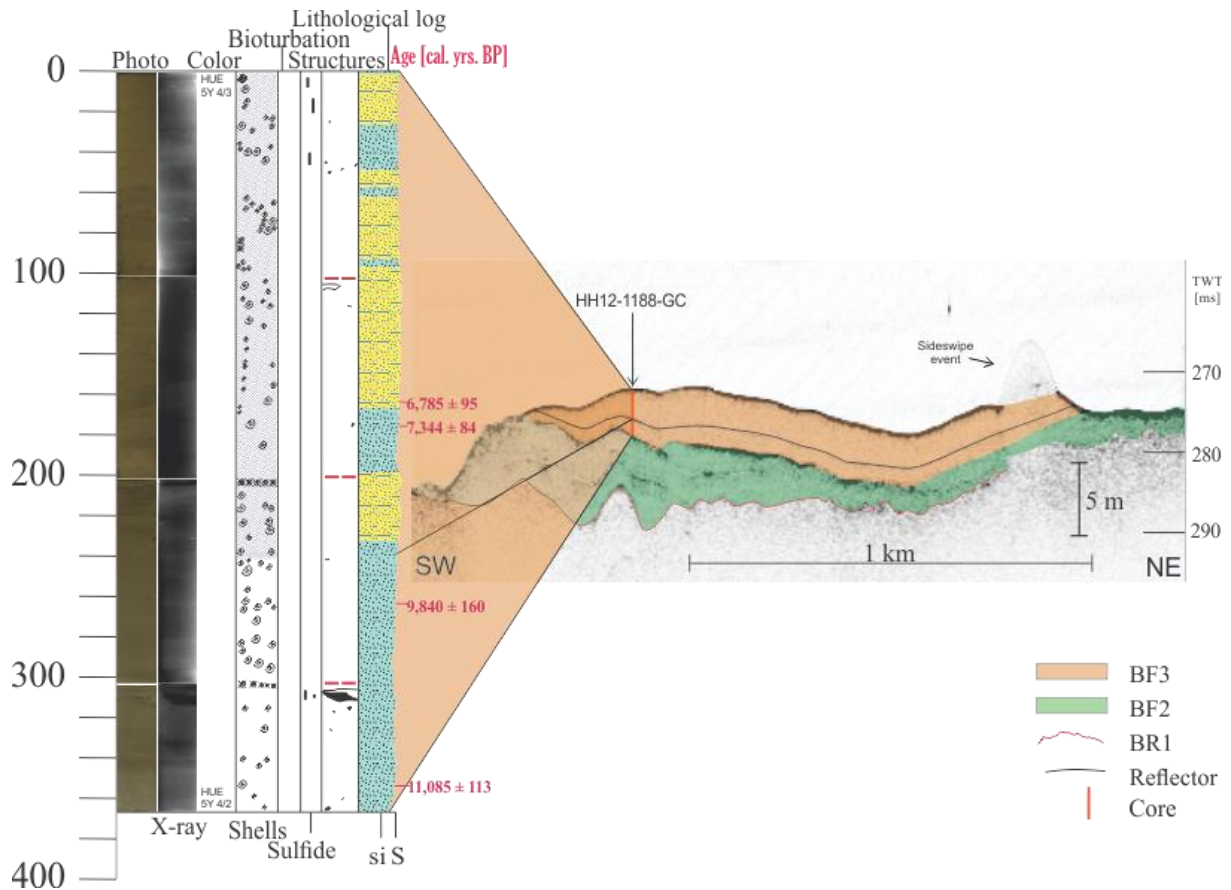
Figure 55 Seismic data from the highlighted part of BB3 in Bergsfjorden (Figure 43) correlated with gravity core HH12-1188-GC.

6.1.3 Jøkelfjorden

The change in color, density, geochemistry and MS at 235 cm b.s.f. in the core HH12-1193-GC (Figure 51 and Figure 52), estimated to have occurred 7770 cal. yrs. BP (Table 14), correlate well with the depth down to the uppermost reflector in the facies JF3 (Figure 56). The great change in physical and geochemical properties detected in the bottom of the core is not as easily correlated with the seismic data. This may be due to possible variations in deeper velocities, hence depth translations may be incorrect. Or, the vessel conducting the samples may have drifted to a more shallow area where the sediment deposit is thinner (e.g. toward southeast) during the coring. A possibility is to correlate 436 cm b.s.f. in the core with the apparent reflector and 449 cm b.s.f. with the stronger reflection directly below, both around 260 ms.

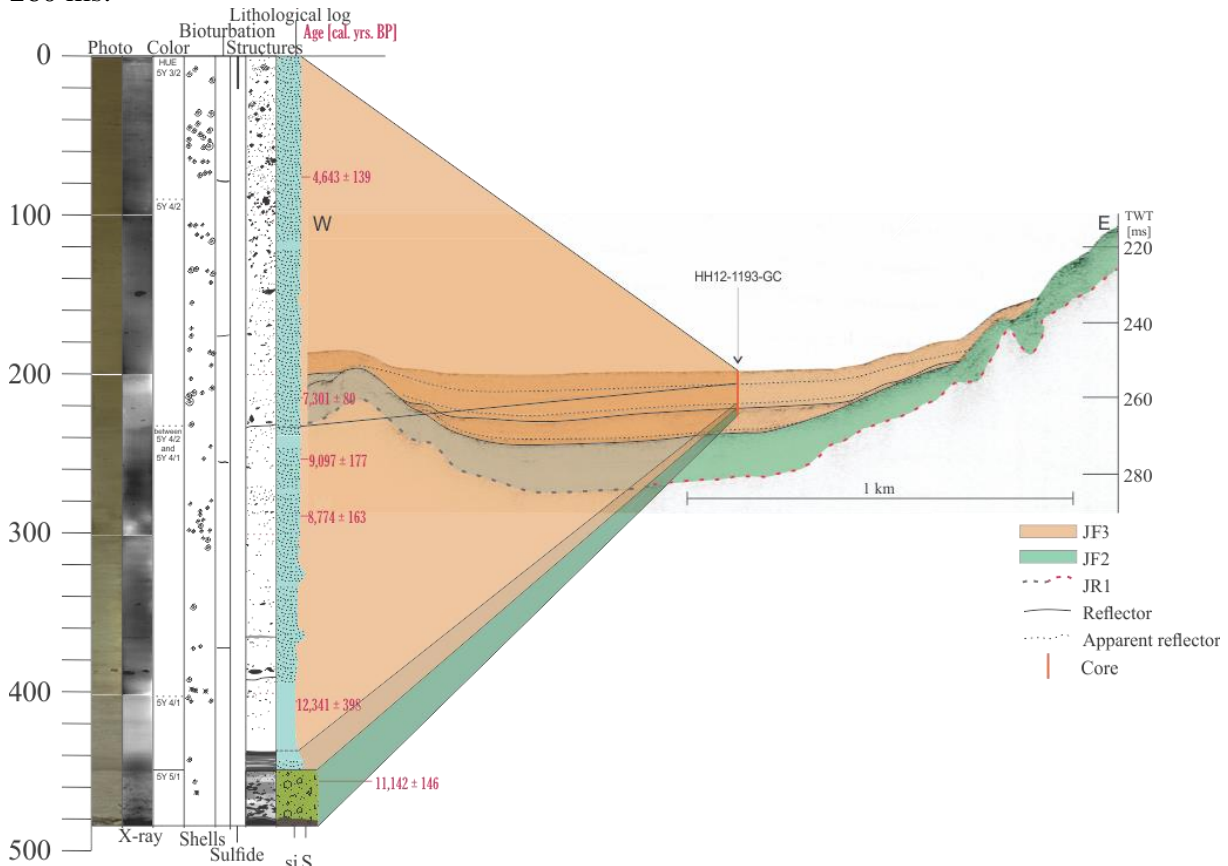*Figure 56 Seismic data from the basin JB2 in Jøkelfjorden correlated with gravity core HH12-1193-GC. The depth inferred by the TWT is possibly not correct as no reflector were found to correlate with the great change in physical properties observed in the core (Figure 51). Hence, the penetration is interpreted to extend deeper than the estimated correlation.*

96

6.2 Interpretations of the lithology

Interpretations of the source of the sediment supply has been conducted based on the lithostratigraphic analyses (Chapter 5.2) and the estimation of ages (Chapter 5.3). Physical properties may provide information as seen in Table 5.

6.2.1 Øksfjorden

At the very bottom of the core HH12-1185-GC, an age of 8270 cal. yrs. BP is estimated (Table 15). Here, high K/SUM, Si/SUM and Fe/Ca-ratios (Figure 48) imply a terrestrial sediment source (Croudace et al., 2006; Richter et al., 2006; Kylander et al., 2011). Decreasing ratios imply a transition toward increasingly larger marine impact until an estimated age of 7490 cal. yrs. BP (Table 14). Subsequently, between 7490 cal. yrs. BP and 5130 cal. yrs. BP (Table 14), a steady trend of relatively high Ca-ratios and low Fe-ratios are observed (Figure 48).

Signs of progressively increased terrestrial sediment supply is inferred from the Fe/Ca and grain size (Figure 48) after 5130 cal. yrs. BP; larger grain sizes imply an increased proximity to the sediment source, mainly inferred to be of fluvial origin (Syvitski et al., 1987; Howe et al., 2010), Fe is mainly derived from land and Ca mainly originate from calcareous organisms in the ocean (e.g. Croudace et al., 2006). In addition, the overall change in color also implies a small change towards increasing input of terrestrial sediment supply up the core.

The increasing Br/SUM-ratios after the event at 54 cm b.s.f. (Figure 48) may imply a lower input of fresh water from around 1110 cal. yrs. BP. This may be explained by an increase in the fjord circulation, decreasing river discharges and/or increasing sea level. This event is further described in Chapter 6.3.2.

MS progressively increase from around 25 cm b.s.f. (Figure 47), and thus also implies increased dominance of terrestrial sediment and a higher proximity to the source after 825 cal. yrs. BP (Table 14). An interpretation of this is made in Chapter 6.4.4.

The reduced occurrence of shells beneath 3700 cal. yrs. BP can imply different climatic environments not preferred by the specous observed further up.

6.2.2 Bergsfjorden

The geochemistry in the core HH12-1188-GC, generally infer a gradual transition from terrestrially affected sediment supply toward more marine up to around 240 cm b.s.f. (Ti/SUM, K/SUM, Si/SUM and Fe/SUM decrease, Ca/SUM increase) (Figure 50) (Croudace et al., 2006; Richter et al., 2006; Kylander et al., 2011). In addition, the Rb/Sr-ratio show a higher degree of glacigenic input of detrital clay below 170 cm b.s.f. than above (Vasskog et al., 2011). A possible "transition zone" between larger variations in the conditions below and quite steady conditions above is inferred from the geochemistry between 240 and 170 cm b.s.f., estimated to have occurred between 9250 and 7110 cal. yrs. BP (Table 14).

Density progressively increase up to ca 240 cm b.s.f., before decreasing toward the top (Figure 49). Glacial sediment often consists of poorly sorted, inorganic, finer fractions, recognized by higher densities (Bakke et al., 2005). The increase in grain size above 240 cm b.s.f. may imply a higher proximity to the sediment source, and/or stronger currents/higher discharge. Above 240 cm b.s.f., progressively decreasing MS is observed, along with a higher abundance of shells above this depth.

As the general trend implies a marine supply in the top, stronger fjord circulation and the lack of glacially grinded sediment are concluded to cause the grain size variation initiated around 9,252 ± 160 cal. yrs. BP.

All signs support an interpretation of increasing marine sediment supply up the core except the variation in color. However, the olivine color can have been caused by the varying grain size, and not the change in environment.

A progressively small decrease in MS is observed, before abruptly increasing around 40 cm b.s.f (Figure 49), at time estimated to be 1,680 ± 95 cal. yrs. BP (Table 14). In addition, a positive peak in MS is observed around 4 cm b.s.f., thus 168 ± 95 cal. yrs. BP.

6.2.3 Jøkelfjorden

Some of the lower ages are neglected, as these are inverted and presumably comprise of redeposited material (Table 12). The presence of possible erosional surfaces and shell fragments, along with the inverted age around 9100 cal. yrs. BP make the lowermost reliable age of the core to be around 8780 cal. yrs. BP (Figure 51), hence sedimentation rates are only calculated down to this (Table 13).

The bottom consist of a diamicton up until 450 cm b.s.f. (Figure 51). Its poorly sorted, coarser grained material show high density and MS, along with similar geochemical values as the massive mud above 436 cm b.s.f. (Figure 52). The thin laminated layer between these seem to comprise of a different geochemistry with peaks of less Fe/SUM, K/SUM and Rb/Sr, and more Ca/SUM and Si/SUM, and hence a different composition. A different sediment source is therefore assumed for this upward fining laminated mud, and is further described in Chapter 6.3.2.

Between 390 and 240 cm b.s.f., a minor increase in Ca/SUM is inferred along with a decrease in Fe/SUM, K/SUM and Si/SUM, indicating progressively increased marine contribution to the sediment supply (Figure 52) (Croudace et al., 2006; Richter et al., 2006; Kylander et al., 2011).

At around 240 cm b.s.f., at an extrapolated age of 7770 cal. yrs. BP (Table 14), an abrupt change in color and density is seen from (Figure 45). Above, progressively stable sediment compositions are observed along with increasing input of IRD, stable Fe/Ca and slightly decreasing densities (Figure 51 and Figure 52). This implies a stable origin of the sediment supply, as explained in Chapter 6.3.4.

The exception is between 43 and 25 cm b.s.f., with an uppermost age estimation of 1570 cal. yrs. BP (Table 13). It is observed to have a similar geochemistry as the lowermost diamicton (Figure 52), and hence the sediment is assumed to originate from a similar source.

A slightly more grey color is observed in the upper 2 cm. Increased MS and the decrease in the Fe/Ca-ratio (Figure 51 and Figure 52) imply increasingly marine supply of sediment (Croudace et al., 2006; Richter et al., 2006). According to calculations of the sedimentation rate, the upper 2 cm have been deposited around the past 125 years. As the ages inferred from the sedimentation rates are maximum ages, and the standard deviation is ±139, the layer may have been deposited after the glacier stopped calving into the fjord (Askheim, 2016).

6.3 Sedimentary processes and environments

The analyses of chirp data (Chapter 5.1) and the sediment cores (Chapter 5.2) indicate that mainly four sedimentary processes occur in the fjords of this study. These are:

1) Open marine environments (suspension settling)
2) Mass wasting
3) Glacier-proximal environments
4) Deltaic processes

6.3.1 Open marine environments (suspension settling)

Terrigenous hemipelagic sediment deposit in open marine environments by suspension settling. They comprise of both organic and inorganic material, mainly transported by rivers but also tidal currents. More than 50 % is derived from land and less than 30 % is calcareous (Nichols, 2009). The organic material mainly originate from primary production in the fjord, but also by incoming currents from the ocean or from land by rivers and wind (Wassmann et al., 1996).

Hemipelagic sediment mainly comprises finer grain size fractions (Nichols, 2009). Finer grain sizes are capable of staying in suspension for a longer distance than coarse (Syvitski et al., 1987). This results in higher sedimentation rates, and hence thicker deposits comprising of larger grain sizes closer to the source. As the sediment mainly have fluvial origin, the sedimentation may vary with the seasonal variation in river discharge (Skei, 1983; Syvitski et al., 1987). Higher flow rates of water result in larger grain size fractions able to stay in suspension and hence being transported further out (Hjulström, 1939). Occasional increase in current flow may, therefore, produce layers or lamina of larger grain sizes.

Hemipelagic sediment is deposited in relatively low-energy regimes, hence draping the base even though it is very undulating. Rugged surfaces are smoothed out when depressions are filled in, onlapping the basin walls. The deposits are observed as quite homogenous, seen by the transparent intervals, but are separated by reflectors probably representing higher energy environments.

Facies 3 is interpreted to mostly contain fluvially derived hemipelagic sediment deposited in an open marine environment mostly by suspension settling, with some redeposition caused by mass flows and eroding currents. The acoustically semi-transparent units draping the undulating base generally reflect the interpretation of a fluvially derived deposit in a low-energy environment (Figure 39). The parallel to wavy, semi-continuous internal reflectors are inferred to consist of increased amounts of IRD or minor local mass flows redepositing the sediment. Some places, the facies is observed as thinner patches pinching out to both sides in some basins (ØB2 in Figure 41 and JB1 in Figure 45), hence reflecting transportation from a river entering at the side of the fjord, sometimes derived by deltaic processes or mass flows.

ØF3 in Øksfjorden is interpreted to mainly consist of fluvially derived deposits as several rivers enter at the side of the fjord. A similar interpretation goes for BF3 in Bergsfjorden. However, it is generally more affected by a marine input of organic material due to the proximity to the ocean. In Jøkelfjorden, fluvially derived deposits are interpreted for JF3, however with a larger occurrence of IRD.

Truncation of the Facies 3 is also observed in Øksfjorden and Bergsfjorden (ØsB2 in Figure 54 and BB3 in Figure 43). This may be a result of strong bottom currents where the sediment presumably is removed due to erosion. The Coriolis effect may result in deeper, inward flowing

currents constrained to the right hand side (Skei, 1983; Syvitski et al., 1987; Howe et al., 2010), possibly causing the truncation in Øksfjorden in the basin ØsB2 (Figure 54). The same explanation may have caused the truncation observed in basin BB3 in Bergsfjorden (Figure 43). Truncation is not observed in Jøkelfjorden, presumably due to the lower marine influence as it is sheltered by Kvænangsfjorden.

From the seismostratigraphy it is evident that the thicknesses of the deposits not only vary with distance to the source, but also with the topography. Topography is a large controlling factor, resulting in thinner deposits draping the sills, and thicker deposits in depressions. This is due to the circulation of the currents in the fjords (Syvitski et al., 1987). In the BB2 in Bergsfjorden and ØsB2 in Øksfjorden, the hemipelagic sediment is observed to have been relocated further into the center of the basins (Figure 43 and Figure 54). Slumping/sliding from the inner basin walls probably occurred due to the reduced capability for sediment to deposit in steeper slopes (Figure 63).

6.3.2   Mass flows

Mass wasting due to slope failure on land are common in northern Norway (Vorren et al., 2007). Rock avalanches and smaller mass wasting of rock are inferred to have occurred frequently after the deglaciation as the ice-support diminished and the isostatic uplift was rapid (Bradwell & Stoker, 2016). Seismic activity associated with the isostatic uplift is likely to have triggered large scale mass wasting (e.g. Blikra, 1999). Facies 2 is interpreted to mostly contain largescale rock slope deposits due to the geometry of the seismic reflections and the interpreted erosional base (Chapter 5.1.3.2). Mapping of soil covers made by NGU (2018a) supports the occurrence of mass wasting in the fjords (Figure 57). Investigations of largescale unstable rock slopes are scheduled in the area (NGU, 2018c, 2018b).
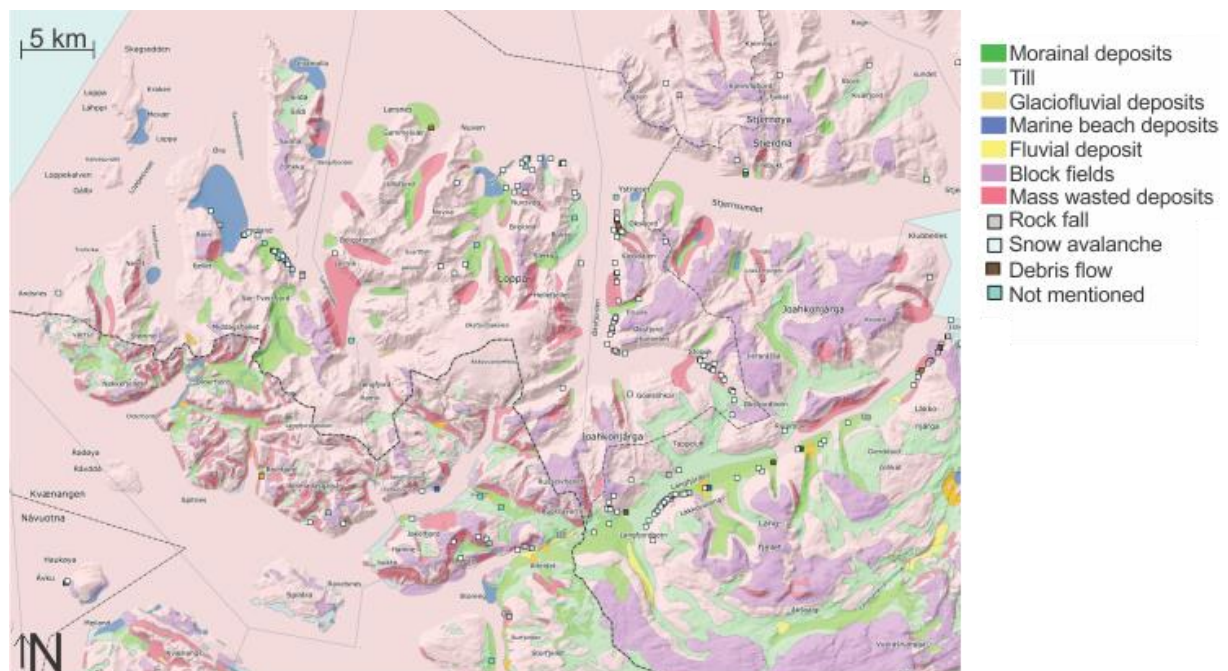
Figure 57 Soil map covering Bergsfjorden peninsula. Mass wasted deposits are mapped in Øksfjorden and Bergsfjorden, and historical mass wasting events inferred. The historical data is however not precise, and the exact locations not known. Modified after (NGU, 2018a).

Several factors may trigger redeposition caused by submarine mass flows (e.g. Holtedahl & Bjerkli, 1975; Syvitski et al., 1987; Hambrey, 1994; Howe et al., 2010). In addition to mass wasting of rock into fjords, snow avalanches and icebergs calving into the fjords are other examples of processes stirring up the already deposited sediment. A combination of high-

relief topography and high sediment supply may cause slope failure due to compaction, over-loading or over-steepening of slopes (Syvitski et al., 1987). Even tsunamis and sea level change may trigger submarine mass flows.

Debris flows are dense mixtures of more sediment than water and may occur subaerially or submarine, and all grain sizes may be present. *Turbidity currents* are less dense than debris flows and are usually turbulent, sorting the grains it comprises of, from clay to gravel. A combination of these flows may occur in a submarine slide, with a turbidity current initiated by the debris flow, and hence *turbidites* may deposit on top of debris flow deposits. (Nichols, 2009). Both are high-energy events, however energy is lost further distal to the source, and sediment is deposited.

Hemipelagic sediment is also associated with turbidity currents. Finer material is kept in suspension after the coarser has been deposited and are transported by currents deposited as sheet drape, fining upwards (Nichols, 2009). The turbidity currents may flow several hundred km, and are not prohibited by non-sloping bases, as they are driven forward due to the density differences between the turbidity current and the water. Sometimes, no sign on basal erosion is observed due to a lower energy regime (e.g. Hjelstuen et al., 2009), thus it settles as any other suspended material.

Bouma (1962) presented an idealized turbidity deposit "the Bouma sequence" (Figure 58). The coarsest sediment are deposited fist, hence the overall gradation of the deposit is upward fining. Proximal turbidites contain coarser grain sizes. A high abundance of Ti/SUM and Zr/SUM often correlate with turbidite bases, and K/SUM is often associated with clay minerals within (Croudace et al., 2006). Rb/Sb ratio should be lower than if the material was glaciofluvially derived (Vasskog et al., 2011).
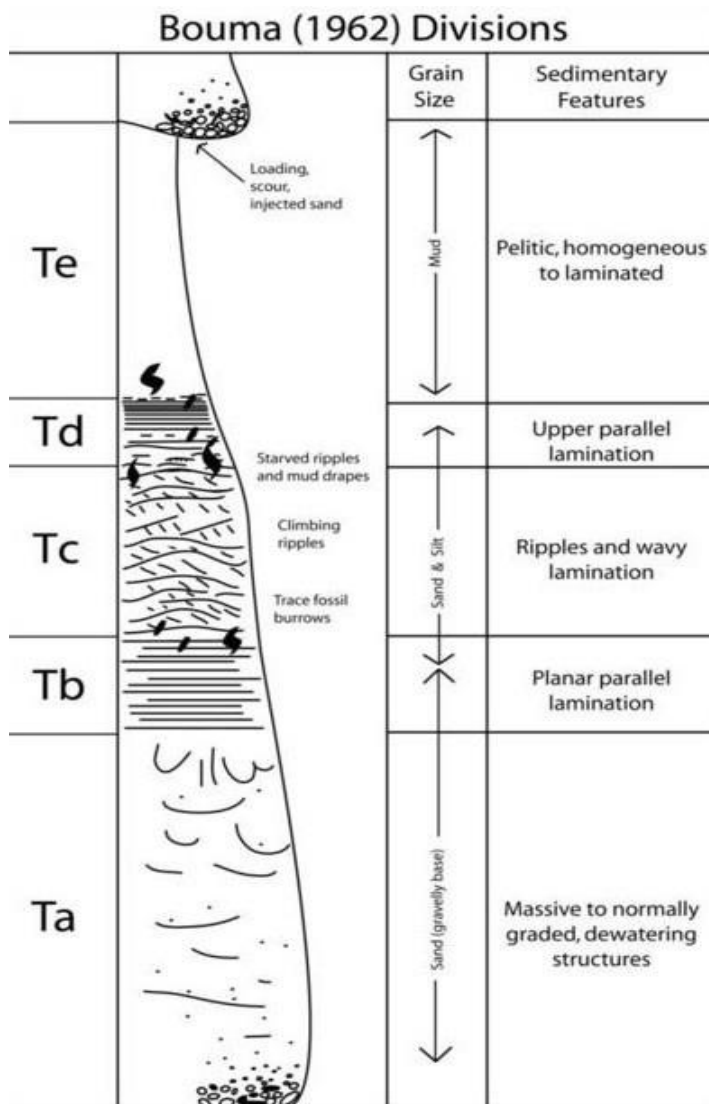
Figure 58 The Bouma sequence (1962) presenting the lithostratigraphy of an idealized turbiddite. All sequences are rarely present.

6.3.2.1 Jøkelfjorden

In Jøkelfjorden, a diamicton is located in the bottom of the core HH12-1193-GC, up to 450 cm b.s.f., and possibly continue below the core (Figure 51). The large variation in composition relative to the overlying laminated mud between 450 and 436 cm b.s.f., infer that the events originate from separate sources (Figure 52).

The gravity core is retrieved less than 1 km from what is inferred to be a fan deposit on land below the river Golpeelva (Figure 59). The coarse material in the bottom of the sequence coincide with a high proximity to the source, hence it is likely that it originated from the river. An increasing Rb/Sr-ratio in the bottom of the core may imply that the material is derived glaciofluvially (Vasskog et al., 2011). Evans et al., (2002) observed the coarse-grained delta located at Jøkelfjordeidet (Figure 59), and inferred that progradation of distal sediment originating from a retreating glacier in the surrounding highlands may be the origin of the delta. The diamicton in the bottom is therefore interpreted to originate from a previously proglacial river entering the fjord where Golpeelva enters today, indicating a small glacier at Dusjárga where a lake is found today (Figure 59). It is interpreted to comprise of a debris flow deposit due to the large mix, up to coarse grain sizes. It could have been an entrainment of water suddenly

102

flooding out of the glacier, a jökulhlaup (Benn & Evans, 2014), or a general increased input of sediment during periods of accelerated glacier retreat (Evans et al., 2002).

Observations of Carbonatite Limestone in the bedrock is observed on the northern side of the fjord (Figure 3). Peaks of increased Ca/SUM and Si/SUM in the laminated layer (Figure 52) may possibly indicate input from either Tverrfjorden or Skalsadalen including Carbonatite Limestone (Table 6). A decrease in Fe/SUM may be explained by the presence of Iron in all bedrock comprising the Bergsfjord peninsula, though probably less in the Carbonatite Limestone. The same accounts for K/SUM. In addition, increased amounts of Potassium is associated with turbidite-bases (Croudace et al., 2006), hence giving an explanation on the origin of the layer. The decrease in Rb/Sr indicate a mass wasting event (Vasskog et al., 2011). This is supported by the inverted ages of the dated material. A possible advance in an outlet glacier of either Øksfjordjøkelen or Langfjordjøkelen may have induced mass wasting into the fjord, causing a turbidite to deposit on top of the diamicton. Or, it may have originated from other types of mass wasting that may possibly have occurred from the northern, steep fjord side (Figure 59).

The layer between 450 and 436 cm b.s.f. may therefore represent either Tb or Td (Figure 58) in a turbidite. The missing ripples (Tc) may be explained by rapid deposition (Nichols, 2009). An overlying layer of upward-fining massive mud (Figure 52) imply that Te is present until maybe around 390 cm b.s.f. (Figure 58). In the latter layer, the geochemistry show an abrupt return to the geochemical conditions as *prior to* the laminated mud, before slowly returning to the conditions *in* the laminated mud (Figure 52).

The age of the events are estimated to be at least 8780 cal. yrs. BP (Table 14).
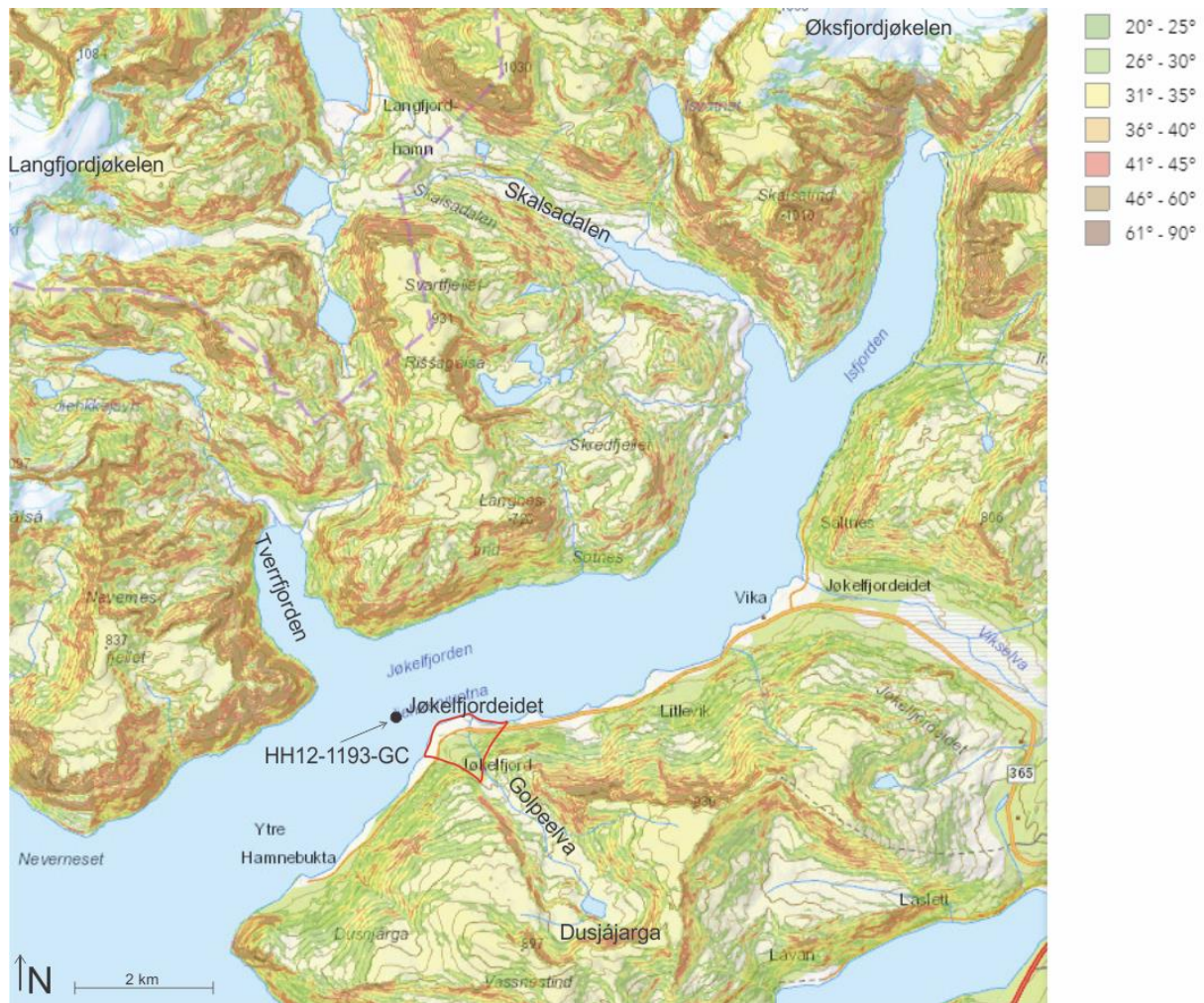
Figure 59 Slope gradient map of Jøkelfjorden. The fan deposit at Jøkelfjordeidet in the end of Golpeelva is inferred in red, 34 m a.s.l.. Modified after (NGI, 2017).

6.3.2.2 Øksfjorden

In Øksfjorden, an event with increased density, MS and grain sizes and an erosive base is observed around 53 cm b.s.f. (Figure 47). Possibly, it represents a mass flow event estimated to have occurred around 1110 cal. yrs. BP (Table 14). A negative peak in Br/SUM (Figure 48) suggests high fresh water input. Increased terrestrially affected sediment supply is also inferred from the geochemical ratios in Figure 48. The event may have occurred due mass wasting from land associated with increased fresh water input (e.g. snow avalanche, jökulhlaup or debris flow). A second explanation is given in Chapter 6.3.4.

The upper 2 cm of the same core in Øksfjorden is also observed to contain dense material with increased MS, somewhat larger grain sizes, a drop in Br/SUM and an erosive base (Figure 47 and Figure 48). However, the overall geochemistry implies a different origin of the sediment relative to the earlier event (Figure 48). An assumption is made that the sediment deposited at once quite recently the past 100 years by redeposition of sediment more influenced by marine supply. It is possibly caused by; a submarine mass flow event initiated due to mass wasting related to increased input of fresh water, redeposition due to trawling, or it may be related to dumping or other anthropogene actions.

The steeply dipping sediment to the east of the core station in Øksfjorden may indicate sliding surfaces (Figure 54). A possibility is that the two events occurred as a result of failure in over-steepened deposits triggered by e.g. overloading, seismicity or tidal waves.

104

6.3.2.3 Bergsfjorden
The southern part of BB3 in Bergsfjorden is interpreted to contain mass wasted deposits originating from the sides of the fjord (Figure 57). In addition, submarine slides within BB2 may have deposited BF3, inferred by the geometry of the reflectors, pinching out of the deposit, and hence imply a sideward origin.

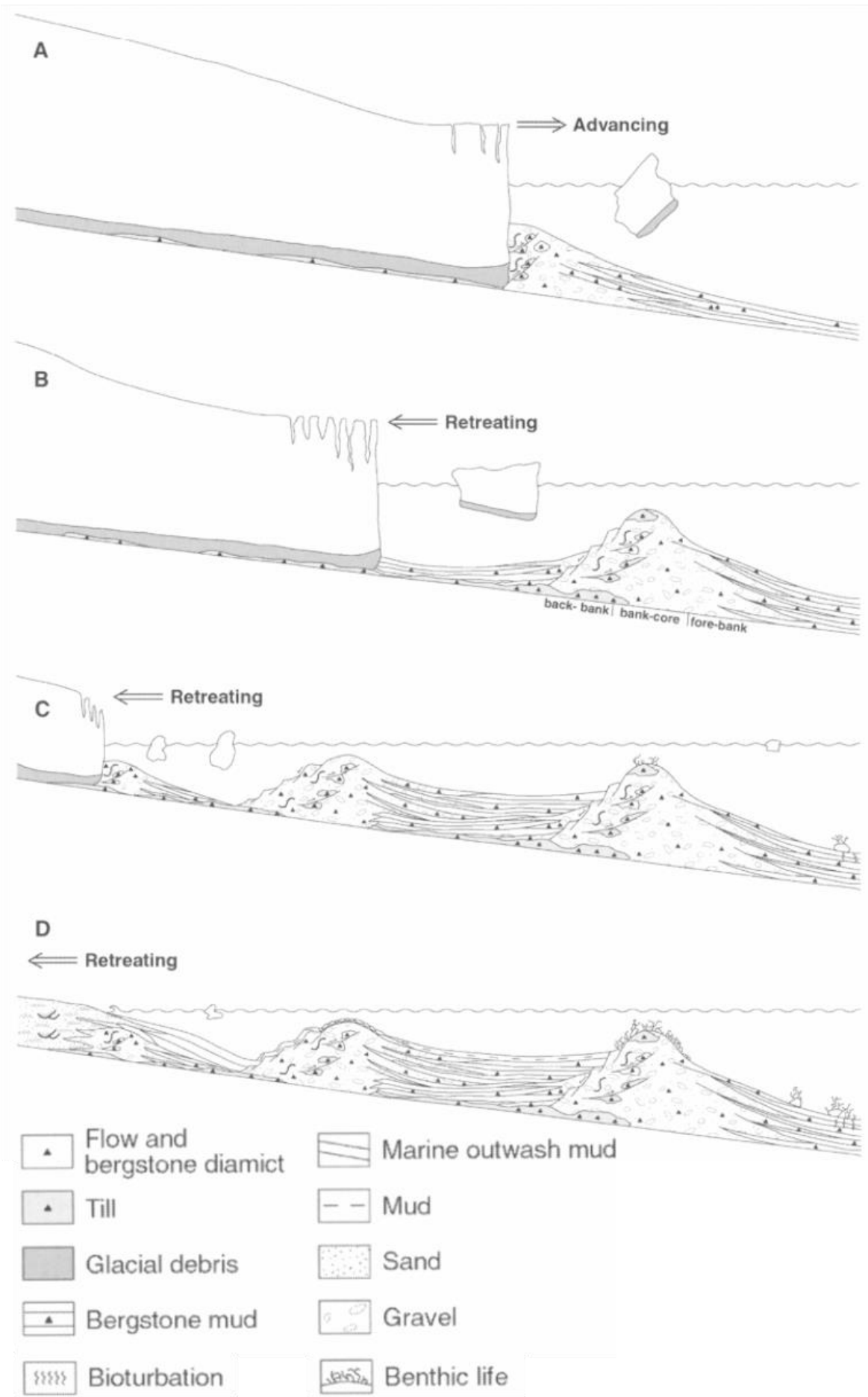In Bergsfjorden an event is observed around 203, with increased densities, grain sizes, Ca/SUM and the amount of fragmented shells along with decreased Ti/SUM, K/SUM, Si/SUM, and Fe/SUM (Figure 49 and Figure 50). An increased input of marine supply of sediment is inferred in the period (Croudace et al., 2006), possibly also associated with submarine mass wasting explaining the input of shell fragments and the increased densities and grain sizes. The event occurred around 8200 cal. yrs. BP.

6.3.3   Glacier-proximal environments
Glacimarine hemipelagic sediment originates from proglacial outwash proximal to a glacier front, as described in Chapter 2.7. It comprises similar deposits as sequences that settled from suspension, except from more frequent occurrence of IRD, and it inheres a higher frequency of reflectors.

Powell and Cooper (2002) (and references therein) showed the retreat of temperate glaciers and the stratigraphic sequence of sediment it may deposit in fjords (Figure 60). Ice-contact and ice-proximal deposition include complex facies of all grain sizes (Gilbert, 1985). Morainal banks of coarser sediment are deposited as elevated ridges at the margins of glacier termini, often at the initial sills of bedrock as it halts there. The *back-bank* (Figure 60B) consists of poorly sorted diamicton with geometries caused by the removed support as the glacier retreats and hence collapse in the deposit toward the fjord head. The *fore-bank* (Figure 60B) mainly comprise of gravity flow sand interstratified with finer grain sizes transported in suspension by overflows. *Proglacial outwash deposits* deposit proglacially as fans or onlapping infill in front of the morainal bank, filling in between these (Figure 60C). Overflows occur as sediment is expelled sub- or englacially, floating to the surface as turbulent plumes containing both coarse and fine sediment in suspension, transporting it out the fjord (Figure 28) (Mackiewicz et al., 1984; Syvitski, 1989). It interacts with the diurnal tides and is affected by the diurnal and annual meltwater discharge and the sediment concentration in the glacial streams (Powell & Cooper, 2002). Subglacial and englacial streams inhere a lot lower velocities in the discharge when entering water than when they drain out on land (Boulton, 1990). Underflows occur only when the sediment concentration is too high for the sediment plume to rise after entering the fjord (Mackiewicz et al., 1984).

Figure 60 (next page) Facies associated with a hypothetical glacier advance and retreat in profile. The morainal banks and the outwash deposit between these are recognized in Øksfjorden. Modified after (Powell & Cooper, 2002).

A

Advancing

B

Retreating

back-bank | bank-core | fore-bank

C

Retreating

D

Retreating

	Flow and bergstone diamict		Marine outwash mud
	Till		Mud
	Glacial debris		Sand
	Bergstone mud		Gravel
	Bioturbation		Benthic life

106

Glacigenic deposits include till deposits, moraines and IRD, indicating glacial contact within the fjord. Till is incorporated in the glacier and is melted out as the glacier halts or retreats. Ice calving into the fjord melt out till as the iceberg floats out the fjord, dumping it with a random distribution based on the path of the iceberg. An input of IRD may be observed by a bimodality of the grain size fractions, indicating several sediment sources as the fractions in between them are missing. IRD is inferred to be interlayered with the proglacial outwash deposits (Figure 60C) (Mackiewicz et al., 1984; Powell & Cooper, 2002).

In Øksfjorden, ØF1 is inferred to represent outwash deposits due to the dense lamination and a similar configuration to that of e.g. Gilbert (1985); Powell and Cooper (2002); Hjelstuen et al. (2009). The internal reflectors probably consist of coarser grain sizes, as this will imply both higher densities and velocities inferred in the seismic profile (Figure 41). Some of the elevated acoustic basement and some of Facies 2 may possibly contain morainal bank or till deposit, as these are likely to contain poorly sorted, chaotic diamicton with a chaotic reflection configuration. A separation between mass wasted deposit and till is, however, difficult to conclude with the data at hand. However, where Facies 2 is deposited on top of Facies 1, mass wasting is assumed. As it would been likely to observe a second succession of Facies 1 overlying Facies 2 if this was till (e.g. Hjelstuen et al., 2009).

In Jøkelfjorden, a lot of IRD is observed throughout the entire core. The sand fractions observed in the gravity core from Øksfjorden are assumed to have occurred after the glacier retreated from the fjord and hence may instead represent detritus rafted by local sea ice or transported by slumping from the steep basin sidewalls. High IRD fluxes are observed to be related to rapid glacier retreat (Mackiewicz et al., 1984; Dowdeswell et al., 1994; Vorren & Plassen, 2002). Isolated grains of medium sand and larger sand fractions occur in Bergsfjorden from around 11,000 cal. yrs. BP, reoccurring about every 1000 year, possibly indicating IRD (Mackiewicz et al., 1984). A period without IRD is seen between about 4200 and 1700 cal. yrs. BP, presumably indicating little glacial impact on the sediment supply in Bergsfjorden in this period.

6.3.4   Deltaic processes
Several rivers enter Øksfjorden close to the basin ØsB2 (Figure 41); Eastern and western Kjoselva, Tverrelva, Kolsokkerelva and several smaller streams. The basin represent the turn of the fjord, with a 10 m deposit of hemipelagic ØF3. Prograding deltas generally have thick upward coarsening successions in the prodelta area, as the source of the sediment continuously gets closer as the delta builds out (Nichols, 2009). Core HH12-1185-GC possesses smaller grain-size fractions in the bottom, increasing above 300 cm b.s.f., probably indicating a prograding delta (Figure 47). ØsB2 is interpreted to crosscut the lower part of a delta foreset. Progradation of a delta may occur as the delta gradually builds out at a steady sea level. But it may also possibly indicate a drop in sea level, as this also coincides with the change in geochemistry and color toward an environment more affected by terrestrial input (Croudace et al., 2006). Ca/SUM changes from being gradually increasing below, to gradually decreasing above (Figure 48). Fe/SUM and K/SUM follow an opposite trend relative to Ca/SUM. The changing Ca/SUM may also imply a lower strength of the incoming Atlantic Water current. Either way, the change is estimated to have occurred about 5130 cal. yrs. BP (Table 14).

Deep-water deltas are prone to mass-wasting events as the extensive delta slope is relatively steep (Reading & Richards, 1994), and may be another explanation for the event at 54 cm b.s.f. An interpretation of the ØF3 to contain deltaic deposits may also coincide with the

thicker deposit observed in the sub-basin ØsB2 relative to the other fjords (Figure 54). As more rivers enter here, an increased fluvial input with increased sediment supply transport sediment mainly settling from suspension. Fluvially transported inorganic sediment is normally freshly weathered and of local origin (Skei, 1983).

In Jøkelfjorden, a coarse-grained delta fan at the bottom of Gopneelva (>20º) is inferred (Figure 59) (Evans et al., 2002). It is likely to represent the *topset* of a Gilbert-type delta, a coarse grained deep-water delta (Nichols, 2009). Below the sea surface, a steeper *foreset* (>30º), contain frequently occurring debris flows and turbidity currents. This result in the deposition of interlayered suspension deposition and turbidites in the *bottomset/prodelta* area (Figure 61) (Nichols, 2009). The morphology may be similar to the Alta Delta, except at a smaller scale and hence lower sedimentation rates (Corner et al., 1990). Or, it may represent a gravel-rich submarine fan decending into the fjord, overlain by sediment mainly settling from suspension (Figure 62).
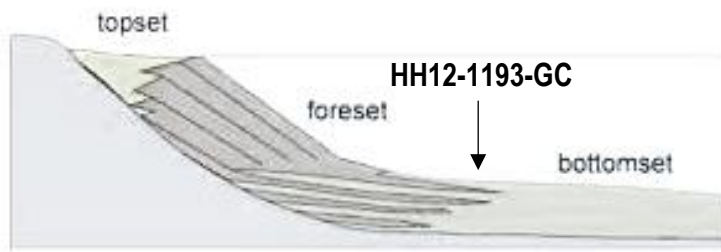
Figure 61 Cross section of a typical Gilbert type delta. They are coarse grained and prograde into deeper water, especially at times of decreasing sea level. Aggradation occur in the bottomset with interlayering of mass wasted debris and suspension settled deposits. It is in the transition between the foreset and the bottomset the core HH12-1193-GC is interpreted to have been retrieved from. Modified after Nichols (2009).
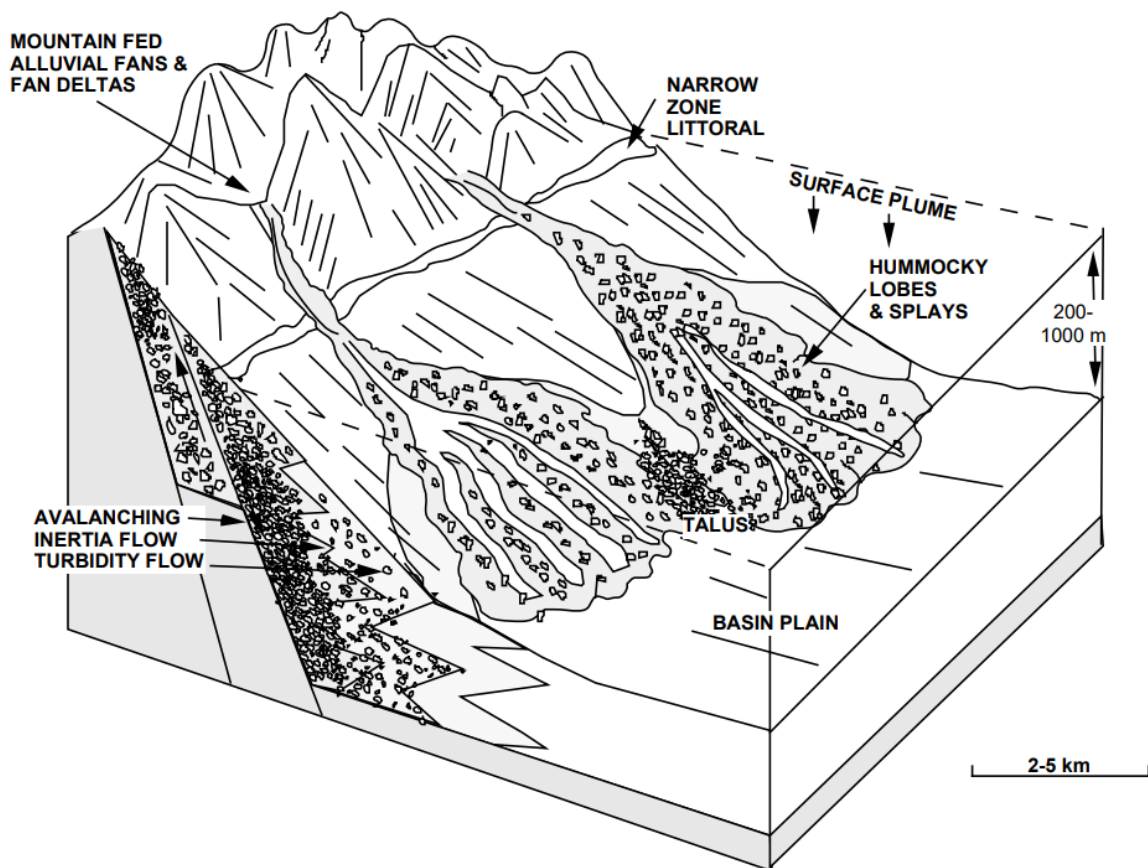
Figure 62 Gravel-rich submarine fan with hummocky lobes of mass wasted debris interlayered with turbidites and surface plume deposits of suspended sediment. Core HH12-1193 can possibly represent the bottomset, with the core penetrating the uppermost finer deposits settled by suspension and the top of a debris lobe. Figure after Reading and Richards (1994).

6.3.5 Interpretation of the sedimentology

A summary of the facies interpretation has been made in (Figure 63).
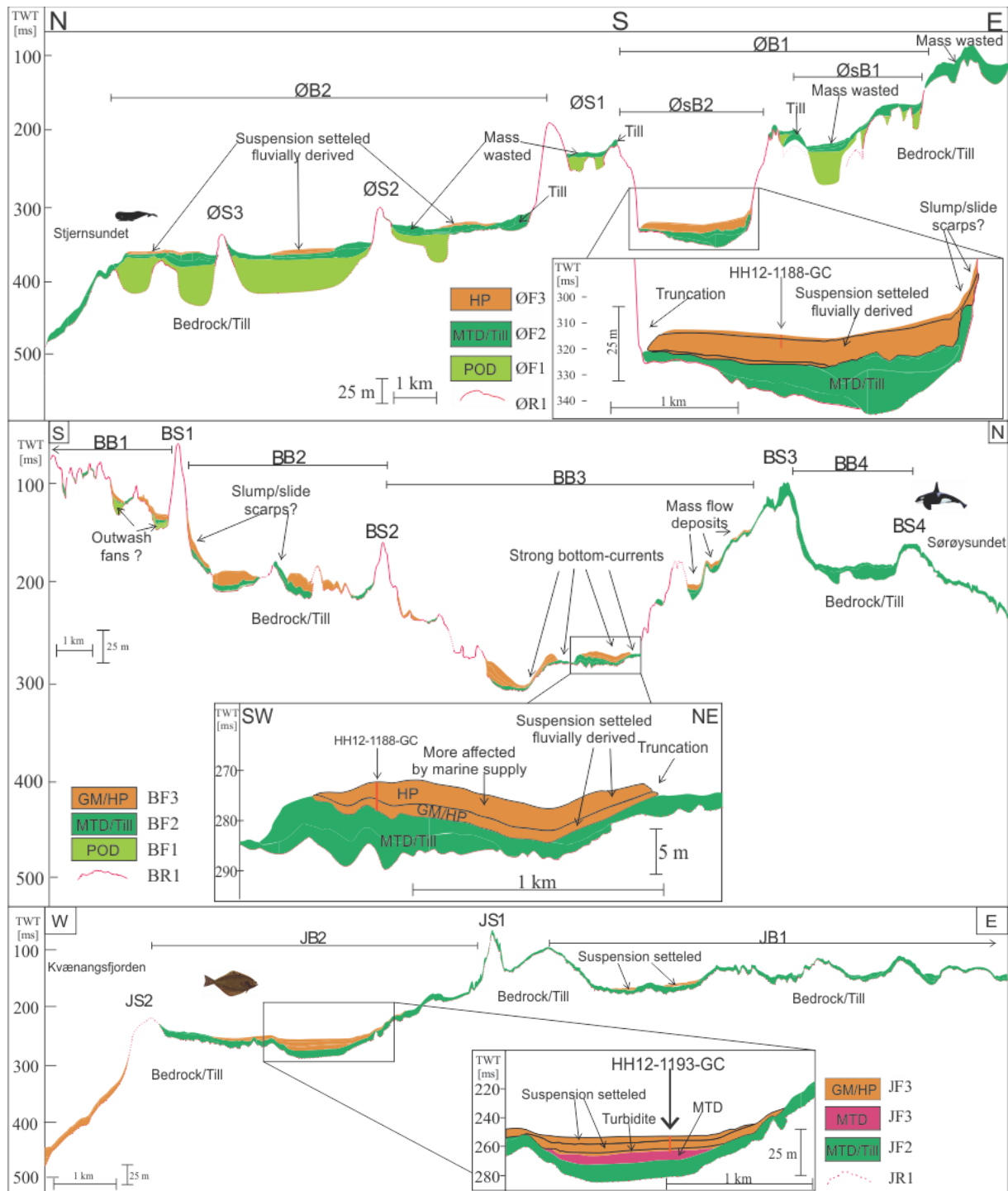
Figure 63 Facies interpretations of Øksfjorden, Bergsfjorden and Jøkelfjorden, respectively. Arrows point out interpretations made for single units, and the legends infer the composition of the facies. GM: Glacimarine, HP: Hemipelagic, MTD: Mass Transported Deposit, POD: Proglacial Outwash Deposit. Names of basins and sills are explained in Figure 41, Figure 43 and Figure 45. Note the different scales of the fjords.

The acoustic basement is interpreted to represent bedrock or till (Figure 63).

Facies 1 is interpreted to consist of proglacial outwash deposits, mainly recognized in Øksfjorden (ØF1 in Figure 41). It is inferred to have filled in depressions directly in front of the morainal banks deposited by the glacier front such as described by (Gilbert, 1985; Powell & Cooper, 2002). This may be seen by the continuous, parallel internal reflectors onlapping a vaguely continuous acoustic basement reflector. The stratification is interpreted to be a result of variation in grain sizes as the discharge of the sub- and englacial streams vary diurnally in strength. Hence, increased sediment concentration and size of the grains are inferred to cause changing density and velocity of the deposit, and thus are acoustically reflected. IRD also contribute to larger grain sizes. Similar deposits may also occur in BB1 in Bergsfjorden due to similar reflection configurations (Figure 43).

The chaotic units making up Facies 2 is interpreted to consist of mass transported deposits or till in all the fjords (ØF2, BF2 and JF2, Figure 63). When deposited directly on top of Facies 1 it is inferred to be mass transported deposits, also seen by the mounded onlapping infill of the reflection geometry (Figure 39). Otherwise, separation will not be possible from the data at hand.

As Facies 3 contain semi-transparent units with a sheet-drape geometry, it is interpreted to contain hemipelagic sediment settled from suspension. Mainly in an open marine environment with the largest sediment supply being of fluvial origin. Increased glacimarine input is inferred in Jøkelfjorden due to the high abundance of IRD. BF3 is interpreted to consist of increasingly more marine affected sediment supply in the top. The semi-continuous internal reflectors are interpreted to have been deposited in a higher energy environment, possibly by local mass flows.

Jøkelfjorden contain mass transported deposits in the bottom of Facies 3, inferred by the gravity core retrieved from basin JB2 (Figure 47). The unit contains a mounded onlapping reflection geometry, but with almost similar internal reflector configuration as the other units of Facies 3. It is observed to extend 1 km laterally (Figure 59). As other units making up Facies 3 in the other fjords is also observed to pinch out to the sides with a "patchy" geometry (e.g. in BB2), some of these may indicate similar composition as that of Jøkelfjorden, thus mass transported deposits. This interpretation fit with that of Hjelstuen et al. (2009) in Nordfjord.

A higher degree of redeposition of Facies 3 is inferred from the reflection geometry of the facies succession in Bergsfjorden. Both from the mounded onlapping infill configuration, and the possibility of present slide scars (Figure 63). Similarly, a slide scar may be inferred from ØsB2 in Øksfjorden, possibly representing the event recorded around 1110 cal. yrs. BP (Figure 54).

6.3.6 Comparison of the sedimentary processes in the three fjords

As the fjords comprising the Bergsfjord peninsula are aligned in all directions and the topography vary alot, it is only rational that the fjords have had separate histories of development. In addition, the core sites do not have equal proximity to their source and hence different processes affect the sedimentation at site. All the fjords are however affected by sedimentation by several processes, mainly originating from the sides of the fjords.

6.3.6.1 Large scale morphology

Øksfjorden has a gradual decrease in the depth to the sea floor, gradually increasing towards the fjord mouth. So do the other fjords, however Bergsfjorden contain a deeper basin in the center of the fjord (BB3). Jøkelfjorden has an undulating inner basin (JB1), however the depth do not vary considerably before on the outside of the sill JS1. Bergsfjorden is inferred to have the highest relief of the three fjords, however the seismic profile may be misleading, as it is observed to include local elevations of the sea floor not crossing the fjord transversally. Øksfjorden is the deepest of the fjords, with water depths reaching 400 m b.s.f. (Figure 1).

Fjord circulation depend greatly on the topography of the fjord and are very much constrained by sills crossing the fjord. An elevated fjord mouth is inferred by the seismic profile from Bergsfjorden. However, Bergsfjorden has a higher proximity to the ocean relative to the other, especially the coring site of the core HH12-1188-GC. It is also the widest of the three fjords, making it easy for Atlantic Water to enter (Figure 24). This is seen by the truncation of many of the units making up the sediment originally deposited by suspension settling. A possibility is that strong bottom currents of Atlantic Water intrude trough the shallow but wide Sandlandsfjorden as well.

The sheltering of Jøkelfjorden, elevated higher above Kvænangsfjorden than any of the other fjords are elevated above their outer basins, may constrain the fjord circulation more than the presence of an outer sill. Jøkelfjorden is the most narrow of the three fjords. From the low-resolution bathymetry data it may be inferred that the basin is more shallow on the right hand side (toward the fjord mouth). This may be explained by high runoff discharge, increasing the outward flowing current strength and depth. Mainly, it concludes the low impact of inflowing bottom water that would have eroded on the opposite side due to Coriolis (Syvitski et al., 1987).

The main sill in Øksfjorden (ØS1), is observed to cross the entire fjord transversally, however truncation of the suspended sediment deposit infer that deep Atlantic Water bottom currents enter and erode in the basin ØsB2 (Gade, 1986). The sill probably increase the erosion by increasing the water velocity as the denser bottom water descends down the side of the sill (Farmer & Freeland, 1983). The storage capacity is probably also increased in the basin as sediment probably is trapped (Ballantyne, 2002). This may be the reason for the high sedimentation rates recorded in the core HH12-1185-GC in Øksfjorden.

6.3.6.2 Sedimentation of Facies 3

The average sedimentation rate in the core retrieved from Øksfjorden is the highest measured of the three cores, averaging 50 cm/ka (Table 13). It is relatively stable down the core (Figure 53), but variations may have been missed due to fewer datings. The highest rates, of 77 cm/ka, are however observed in the bottom of the core retrieved from Bergsfjorden, up until around 10,000 cal. yrs. BP, when the sed rate is subsequently reduced toward approximately 20 cm/ka in the top (Table 13). Measurements traced as far back in time is however not obtained from the other cores, except extrapolated values (Figure 53). The average linear sedimentation rate in Jøkelfjorden are around 50 cm/ka until about 5000 cal. yrs. Ka, when it is reduced to 15 cm/ka (Table 13). Overall, the sedimentation rates are not expected to have been linear due to the presence of mass wasted deposits in all fjords.

The sediment in Facies 3 is mainly inferred to have been deposited by suspension settling (ref til der sier det) with the presence of mass wasted debris. As inferred by the sedimentation rates, the thickness of the deposits vary between the basins were the gravity cores are

retrieved from and between the various basins within each fjord. The thickest deposit settled by suspension is observed in Øksfjorden within basin ØsB2 (Figure 54), with almost 10 m. Similar thicknesses may be seen in some of the basins in Bergsfjorden, except not in the deposit where the gravity core where retrieved, reaching down to the underlying facies about 4 m below the sea floor. Basin JB2 in Jøkelfjorden comprise sediment deposited by suspension settling reaching approximately 4.5 m down below the sea floor, inferred by the gravity core retrieved from here. Depth calculations from the seismic profile (Figure 45), however infer around 10 m of deposit, as this probably is obtained somewhat closer to the source than the core. Even though Øksfjordjøkelen does not seem to have its main drainage down Vestre Kjoselva, sediment may be supplied by inward flowing currents bringing sediment originating from Øksfjordjøkelen draining down Bac'cavuonvag'gi, as well as sediment transported into the inner fjord (Figure 19). The greater thickness in Øksfjorden is probably caused by the trapping of sediment due to the outer sill. In Bergsfjorden, more sediment is probably transported further out the fjord by surface currents from where the core is retrieved. Trapping of sediment in Bergsfjordvatnet may also reduce the sediment supply. The great thickness in Jøkelfjorden may be interpreted as caused by a high supply of sediment from many sources as both Øksfjordjøkelen, Langfjordjøkelen and several lakes drain into the fjord. The high IRD supply from the calving glacier at the fjord head and the proximity to Golpeelva, may also cause the thickness of the deposit.

6.3.6.3 Mass wasting
All the fjords are generally observed to contain mass transported deposits, both inferred by Facies 2 when it overlies Facies 1, and as thinner deposits in-between the suspended sediment in Facies 3 and possibly also in Facies 1 (Figure 63). The mass transported deposits of Facies 2 generally include great volumes filling in the entire basins, but with a generally equal thickness in all the fjords and basins. All basins are observed to contain mass transported deposits, with thicknesses varying between 1 and 10 m.

6.3.6.4 Glacier-proximal deposits
Proglacial outwash deposits are mainly observed in Øksfjorden, possibly because the acoustic signal is attenuated beneath thick, overlying deposit in the other fjords. This interpretation is maintained due to the lack of observed proglacial outwash deposits in ØsB2, and as the deposit filling in the basin is generally of the same thickness as in the basins of Bergsfjorden. A similar explanation is interpreted for Jøkelfjorden, however the generally high input of IRD may have caused the acoustic signal to have been attenuated at a shallower stage than in Øksfjorden. In Øksfjorden the proglacial outwash deposits reach thicknesses up to 50 m.

The thickness of the proglacial outwash deposits may imply that a lot of the deposit beneath the acoustic basement is in fact part of morainal bank deposits.

6.3.6.5 Deltaic deposits
Several larger rivers enter the fjords (Chapter 2.4), possibly building out deltas as the sediment supply probably is very high due to the large amount of paraglacial deposit (Ballantyne, 2002). Deltas are often related to fjord processes, often building out at the fjord head if the morphology of the terrain allows for it (Syvitski et al., 1987).

Separation between deltaic deposits and deposits settled from suspension in an open marine environment are difficult as both mainly settle from suspension. Mass flows may be more frequent in a deltaic environment, however this is not always the fact as slumping inside basins and redeposition by other means also may occur in more distal environments. It may be

possible that the delta below Gopneelva (Figure 59) continue into the fjord as a gravel-rich submarine fan that was active when glaciers were present in the highlands above, supplying a great deal of sediment during rapid retreat (Evans et al., 2002). The debris lobe entering the fjord may then later have been covered by a turbidite originating from somewhere else in the fjord, before sediment settled from suspension and IRD deposited on top.

In Øksfjorden, the deposit in basin ØsB2 is interpreted to crosscut the lower part of a delta foreset (Chapter 6.3.4). However, influence from sediment transported in suspension from rivers entering both further out and in the fjord is likely to be as large or possibly larger than the influence from the river entering at Austre and Vestre Kjoselva (Figure 19). A progradation possibly occurred around 5130 cal. Yrs. BP. All though, the lack of high-resolution bathymertry and seismic profiles makes it difficult to conclude the origin of the changing physical and geochemical composition of the sediment retrieved in the core HH12-1185-GC (Figure 47 and Figure 48).

6.3.6.6 Correlation of the physical and geochemical properties in the gravity cores
The average linear sedimentation rates estimated in Table 13 and Figure 53 were used to correlate the most prominent changes in the gravity cores (Figure 64). This were made in order to compare the conditions in the fjords in the approximately similar time frames. As the sedimentation rate may have varied a lot through time, correlations of events may be made for a larger timeframe than what is obtained by the linear average. Care must therefore be made when comparing events between fjords even though they are located as close as in this study. The cores correlate back to around 8270 cal. yrs. BP.
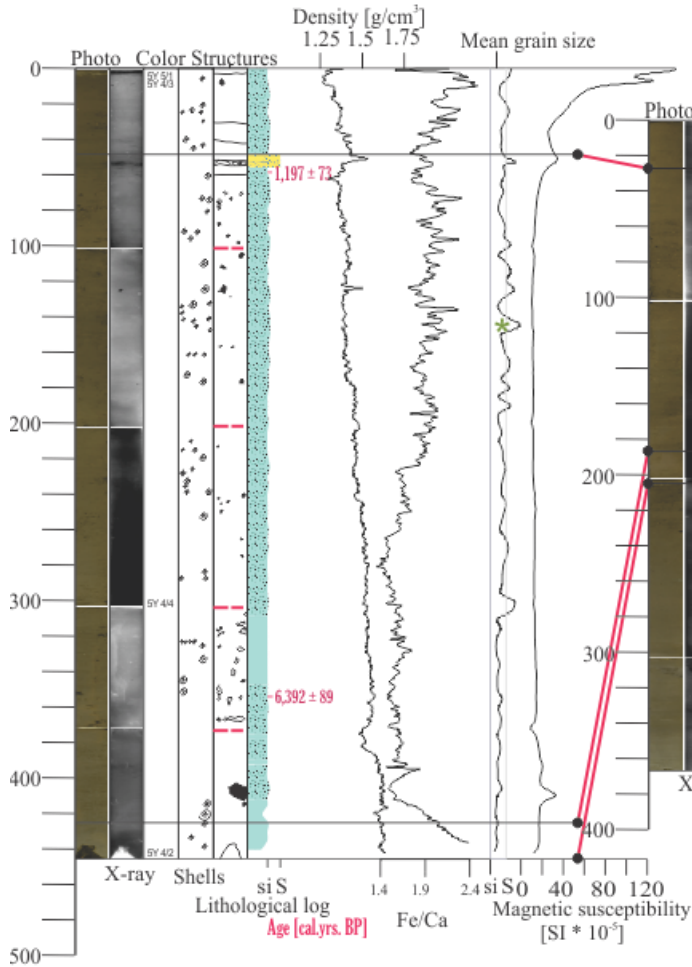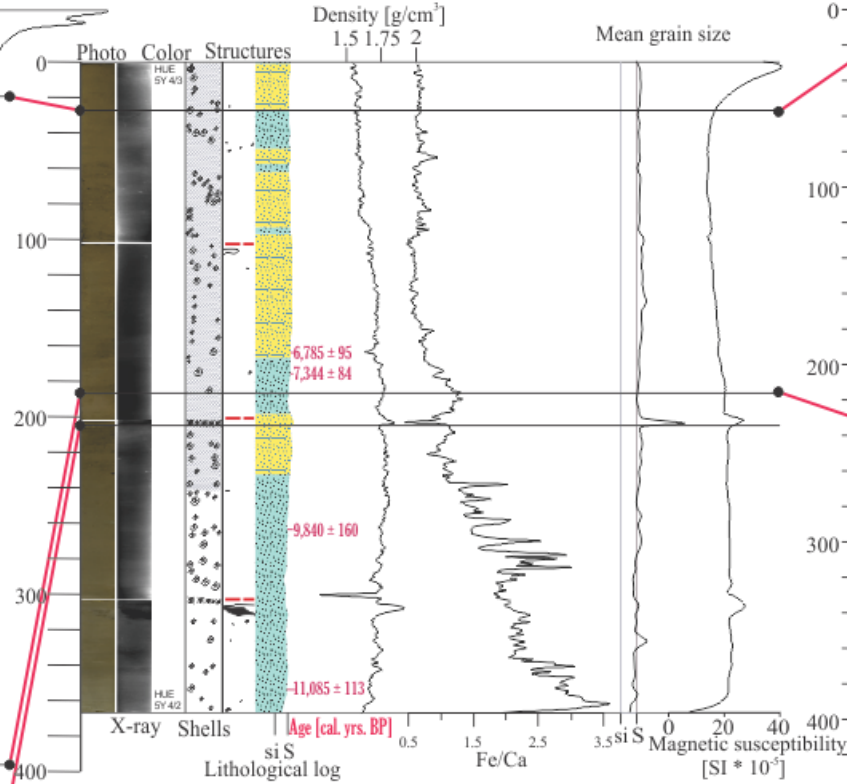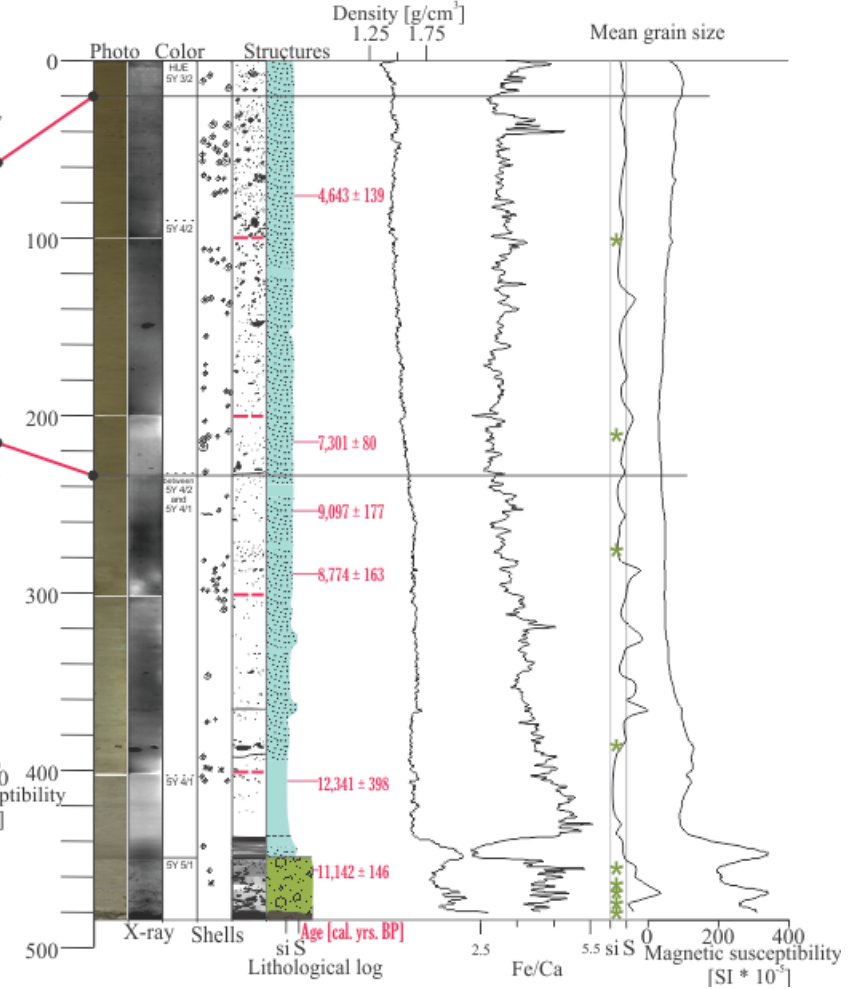
Figure 64 Correlation of depth inferred by the estimated linear sedimentation rates. Depth of important processes are correlated, and the most important physical properties included. Legend as in Figure 46. Red lines imply equal age estimates.

The bottom of the core HH12-1185-GC retrieved from Øksfjorden presumably represent a period with increased influence by terrestrial sedimentation around 8270 cal. yrs. BP (Chapter 6.2.1). The following period probably resulted in an increased input of melt water when the glaciers retreated back to its previous termination. This may have induced the mass flow observed in core HH12-1188-GC shortly after as it correlates with the 8200-event observed in Bergsfjorden. This supports the argument of a closer proximity to the source of the sediment in Øksfjorden, probably caused by an advance in glacier extent. Further interpretations are included in Chapter 6.4.2

Following is the changing conditions observed in Jøkelfjorden in core HH12-1193-GC, estimated to date back to 7770 cal. yrs. BP (Chapter 6.2.3). This correlates with the conditions inferred to represent somewhat increasing input of terrestrial input in Bergsfjorden, observed by the peak in Fa/Ca-ratio in this period. An interpretation may be that glaciers retreated slightly as seen by the decrease in grain size in Bergsfjorden and the probable decrease in proximity in Øksfjorden. Possibly, the source of the changing conditions in Jøkelfjorden may have occurred due to a final diminishing of the glacier inferred to have been located in Dusjajarga upstream of the Golpeelva draining down to Jøkeleidet (Figure 59).

The overall high Fe/Ca and low Ca/SUM-ratios of Jøkelfjorden illuminate the fact that the fjord is constrained from the ocean, relative to the other fjords (Table 11). The opposite is observed for Bergsfjorden, with low Fe/Ca and high Ca/SUM-ratios.

The mass flow event observed in Øksfjorden interpreted to be related to mass wasting with increased fresh water input (Chapter 6.2.2) seem to correlate with the initiation of an increase in MS is Bergsfjorden (Figure 64). An isolated clast is also observed in core HH12-1188-GC, hence supporting the argument of a relation to increased fresh water input, if being an IRD. The clast may however have a different explanation than being brought there by an iceberg, separating the two events.

The overall coarser grain sizes in the core HH12-1188-GC from Bergsfjorden (Figure 64) may be explained by a higher discharge in the river entering down from Bergsfjordvatnet (Figure 19). The smaller grain size fractions in Øksfjorden may oppositely be explained by lower discharges in the rivers with the highest proximity

6.4 Climatic/Environmental periods

6.4.1 > 11,200 cal. yrs. BP

Vorren & Plassen, 2002 found an onset of an atmospheric warming and a sea level rise caused by the large input of melt water and a marked recession before the Skarpnes event approximately 14.2 ka cal. yrs. BP, (corresponding to the moraine in Stjernsundet Figure 6). Further, they found that the outlet glaciers (e.g. Astafjord) retreated to the fjord head or further inland during Allerød (40 km inland from the YD termination). A readvance until the outer limit of YD after approximately 12.1 ka cal. yrs. BP, and a retreat from here after 11.2 ka cal. yrs. BP is found in Astafjorden, Balsfjorden and Lyngen (Forwick & Vorren, 2002; Vorren & Plassen, 2002; Fimreite et al., 2001). Andersen et al., (1981) also suggested that all moraines correlated with the Tromsø-Lyngen substage were deposited prior to 11.2 ka cal. yrs. BP.

The deglaciation of the fjords comprising this study probably occurred before 13.5 ka cal. yrs BP, corresponding to the deglaciation of Altafjorden, directly north of the study (Stokes et al., 2014). During this retreat of the Øksfjordjøkelen ice cap, its glacier outlets terminated in the fjords, probably halting at the sills. At times of still stand or re-advance predating the deglaciation, morainal banks/ice-contact till and deformed deposit presumably deposited in front of the glacier (Gilbert, 1985), making up some parts of Facies 2. Facies 1 can presumably imply proglacial outwash plumes stratified with IRD, filling in the basins in Øksfjorden and in the inner part of Bergsfjorden. These are inferred to be progressively younger with decreasing distance to the glacier outlets, with the youngest presumably dating back to the Younger Dryas advance 12.1 ka cal. yrs. BP (Andersen, 1980; Corner, 1980; Andersen et al., 1995; Vorren & Plassen, 2002; Vorren et al., 2007; Stokes et al., 2014), as the termination of the glacier has been concluded by Evans et al. (2002) to have been located at the fjord heads (Figure 11). The observation of Facies 1 in the easternmost part of Øksfjorden (sub-basin ØsB1, Figure 41) can possibly imply that a separate glacier outlet entered somewhere in the inner part of Øksfjorden, depositing a proglacial outwash plume here.

After the glacier retreated from the Younger Dryas termination, mass wasting probably deposited some of what is observed as Facies 2 (Figure 63). In Øksfjorden, the extrapolated age of the top of this is 13.9 ka cal. yrs. BP and in Bergsfjorden 11.2 ka cal. yrs. BP. The age in Bergsfjorden is most reliable as the gravity core retrieved from here is inferred to penetrate all the way down to the facies, however the retreat may not have been synchronous (e.g. Stokes et al., 2014). Forwick and Vorren (2002) found mass deposits that they assumed deposited in the period between 10.2 and 9.7 ka cal. yrs. BP, at times of sea level rise and increased seismicity due to isostatic rebound. Increased seismic activity is expected in periods of steep uplift gradients (Bøe et al., 2000). Blikra 1999, Blikra & Longva 2000, Blikra et al., 2001 and Dehls et al 2000 infer a period between 10.9 and 10.4 ka cal. yrs. BP with increased slope failure, and particularly rock avalanches, as a result of seismic activity. The fjords in the area have had a progressive isostatic rebound following the Younger Dryas termination (Figure 13 and Figure 14) (Evans et al., 2002). Today's rate average 1 mm/yr (Dehls et al., 2000a; Fjeldskaar et al., 2000), hence rebound of the past is inferred to have been very large (Figure 12).

6.4.2   11,200 cal. yrs BP – 7000 cal. yrs. BP

11,090 cal. yrs BP is the oldest reliable age in this study, found in the core HH12-1188-GC, 3.5 m below the sea floor. It represents the lower boundary of Facies 3 and the preserved deposits of hemipelagic mud settled from suspension. A progressively increased supply of marine sediment is inferred until 4.2 ka cal. yrs. BP in Bergsfjorden, and until 7.5 ka cal. yrs. BP in Øksfjorden.

According to reconstructed equilibrium line altitudes of Svartfjelljøkelen by Eeg (2012), increased input of glacial sediment into Bergsfjordvatnet occurred between 9 and 7 ka cal. yrs BP. She connects this to a retreat of the glacier, and hence increased discharge in the proglacier rivers and availability of glacial sediment (Eeg, 2012). This probably reflects the variations observed around the same time in the "transition period" between increasingly more marine input and stable marine input in Bergsfjorden. Bergsfjordvannet drains into Bergsfjorden only a few km south of the coring station in this study. Hence, the fluctuations in Svartfjelljøkelen is inferred to affect Bergsfjorden. Øksfjordjøkelen has probably not affected the fjord after it terminated into Langfjorden in basin BB2 around 12.1 ka cal. yrs. BP (Figure 11) (Evans et al., 2002). As Svartfjelljøkelen is a lower lying, smaller ice cap than Øksfjordjøkelen, climate variations probably intensified the fluctuations, and the glacier probably retreated at an earlier stage than Øksfjordjøkelen. This is represented by the early transition towards increased marine sediment supply in Bergsfjorden. However, the coring station in Bergsfjorden is located closer to the ocean, and will of course generally have a larger marine element composition than the other coring stations.

In Jøkelfjorden, mass wasting has been estimated to have occurred before 8.8 ka cal. yrs. BP. One local mass movement event dating back to approximately 8.7 ka cal. yrs. BP have been found in Balsfjord (Forwick og Vorren 2002) and possibly correlates with that in Jøkelfjorden. It may be explained by a period of increased seismicity due to uplift in the region.

A period of Svartfjelljøkelen glacier advance has been observed by Eeg, 2012 between 8.3 and 8 ka cal. yrs. BP. She infers this to coincide with the 8200-cooling event (Klitgaard-Kristensen et al., 1998), interpreted to be a result of a massive lake burst of Lake Agassiz from the Laurentide ice sheet (Barber et al., 1999; Teller, 2013) related to variations in the thermohaline circulation (Boyle & Keigwin, 1987; P. U. Clark et al., 2002) and freshwater forcing (P. U. Clark et al., 2001). The increasing grain sizes around 8.2 ka cal. yrs in Bergsfjorden may imply the same cooling event. In Øksfjorden, the core HH12-1185-GC reaches a depth estimated to be 8.3 ka cal. yrs. BP. It is interpreted to include a time period of increased terrestrial supply of sediment, possibly indicating the same. The inverted age around 260 cm b.s.f. in HH12-1193-GC along with the peak in grain size and minor decrease in Rb/Sr, may possibly imply a mass wasting event (Vasskog et al., 2011). Mass-movement activity generally increase in climatic periods favoring glacier build up (Gilbert, 1985). Hence, the events in the bottom of the gravity core in Jøkelfjorden may also reflect the cooling event around 8.2 ka cal. yrs. BP as mass wasting has been recorded in several other fjords around the same time (R. Bøe et al., 2004).

6.4.3   7000 cal. yrs. BP – 5000 cal. yrs. BP

In Jøkelfjorden the origin of the sediment is relatively steady from around 7.8 ka cal. yrs. BP (Chapter 6.2.3). A similar trend in Øksfjorden show a steady origin of the sediment supply between 7.5 and 5.1 ka cal. yrs. BP (Chapter 6.2.1). The lower input of IRD between approximately 7.5 and 6.1 ka cal. yrs. BP observed in Jøkelfjorden may be explained by a smaller glacier cover caused by high summer temperatures and/or reduced winter precipitation resulting in very small glaciers in Norway (Vorren et al., 2007; Nesje et al., 2008). The presence of IRD throughout the entire core may, however indicate that glacier ice did exist throughout the period. Eeg (2012) observed little or no glacial input in Bergsfjordvatnet between 7.0 and 5.2 ka cal. years BP (Eeg, 2012). In core HH12-1188-GC, this is supported by one single clast around 7.3 ka cal. yrs. BP, and one around 5 ka cal. yrs. BP, along with an observed steady sediment source (Figure 49). The isolated clasts presumably represent IRD from ice floating down the river from Bergsfjordvatnet, or calving icebergs from an outlet glacier entering the fjord further inward (Figure 19).

6.4.4   5000 cal. yrs. BP – present

Continuously, relatively steady origin of sediment is inferred for both Bergsfjorden and Jøkelfjorden in this period (Chapter 6.2.2 and 6.2.3). In Øksfjorden, increased influence by terrestrial sediment with slightly coarser grain size fractions are inferred to have been supplied after 5.1 ka yrs. BP (Chapter 6.2.1). This imply a closer proximity to its sediment source than before. As the hemipelagic mud is interpreted to have been deposited by suspension settling in a prodeltaic environment, progradation caused by decreased relative sea level or increased sediment supply is interpreted to have caused this variation. A second interpretation may be an advance in the glacier outlet entering Bac'cavuonvag'gi (Figure 19), increasing the input of larger grain size fractions as it is transported by the inward flowing currents. Increased strength in the inward flowing current of Atlantic Water may alone work as a third, plausible explanation for increased grain sizes, as an increased circulation in the fjord will increase the capability of transporting coarser grain sizes.

In Jøkelfjorden, a decrease in sediment supply is inferred after around 5.0 ka cal. yrs. BP, seen by the decrease in the sedimentation rate (Figure 53). The increasing abundance of IRD from around this time may together with the decreased sedimentation rate imply rapid retreat of surrounding glaciers (Mackiewicz et al., 1984; Dowdeswell et al., 1994; Vorren & Plassen, 2002), reducing the proximity to the source and hence also the sediment supply.

Relatively steady sedimentary environments are observed after 4.2 ka cal. yrs. BP in Bergsfjorden, 5.1 ka cal. yrs. BP in Øksfjorden and 5.0 ka cal. yrs. BP in Jøkelfjorden. After this, mass flow events and IRD may have caused minor variations in the sediment supply, however not correlating between the fjords.

No particular sign of a glacier advance in the Little Ice Age has been observed except an increase in MS in Bergsfjorden from about 1.0 ka cal. yrs. BP and around 825 cal. yrs. BP in Øksfjorden. It is plausible that these correlate as a variation in sedimentation rates may be reflected in the age estimates (Table 14). The increase in MS may imply an increase in terrestrial sediment supply (Bakke et al., 2005) This may possibly have been caused by an increase in glacier extent, assuming that larger glaciers produce more sediment. The assumption that larger glaciers produce more sediment may be argumented against (e.g. Ballantyne, 2002).

6.5 Summary of deglaciation and the development

Powell and Cooper (2002) created a model for deposition of morainal banks and proglacial outwash plumes (Figure 60). However, the model imply that all sills comprise of till, either reworked or directly deposited in front of the glacier as it fluctuated. It is, however, likely that the sills comprise of bedrock and hence therefor result in halts of the glacier terminus as it quickly retreats. When a glacier looses contact with the bed due to a minor decrease in ELA, it quickly calves inward until it reaches contact with the sea floor again, often when it reaches the next sill (Vorren & Plassen, 2002). Thus, sills may not just comprise of till, but may actually cause the termination at the particular location. It can however be likely that sills may have been deposited on generally low-relief sea floor within the fjord at an earlier stage.

The conceptual model created by Plassen and Vorren (2002) is interpreted to further explain the deposition of sediment similar to those observed in the fjords of this study, especially in Øksfjorden (Figure 65). Both of these models were used when creating the interpretation of the deglaciation in the fjords comprising the Bergsfjorden peninsula.
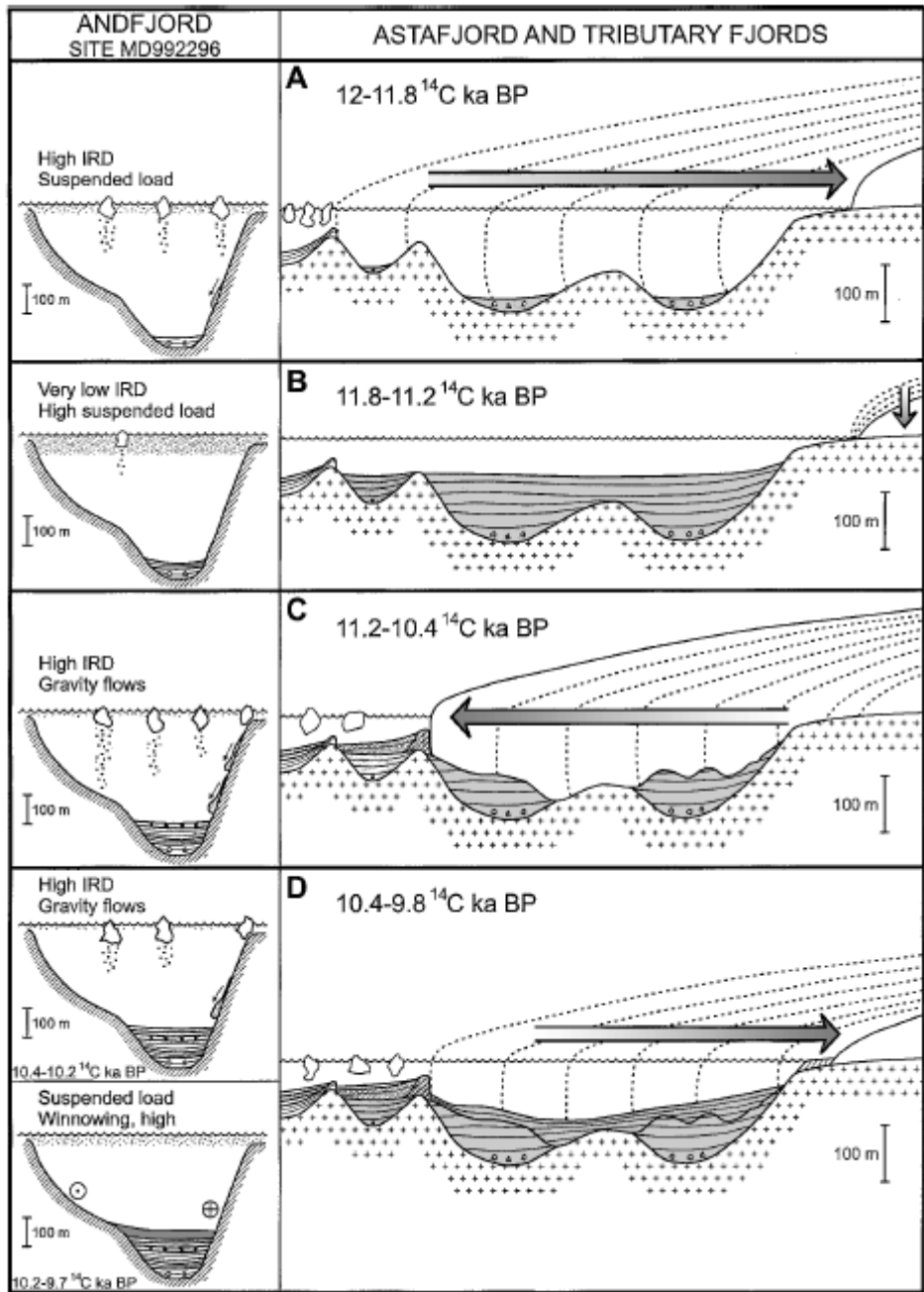
Figure 65 Conceptual model showing recession in Astafjorden before the onset of the Younger Dryas stadial. A similar fluctuation may have occurred in the fjords comprising this study. Figure after Vorren and Plassen (2002).

Each following glaciation resulted in a redeposition of the sediment already present in the fjords, transporting it further off shore. Thus, fjords in Norway inhere sediment deposited after the last deglaciation (Syvitski et al., 1987).

As all the facies are represented in Øksfjorden a conceptual model of the development of the sediment is illustrated in Figure 67-69. Facies 1 is either mostly preserved in Øksfjorden or at least give the highest resolution in the seismic signal.
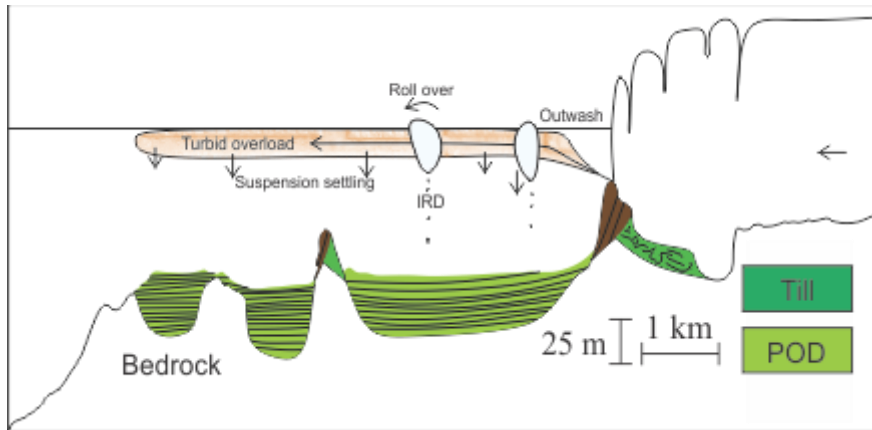
Figure 66 Conceptual model of infilling of proglacial outwash deposit and till. The illustation is based on information from Hambrey (1994); Powell and Cooper (2002); and Vorren and Plassen (2002).
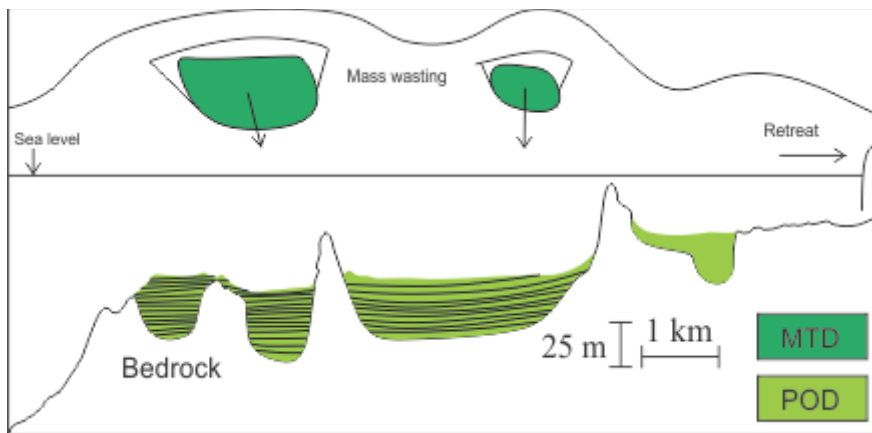
Figure 67 Conceptual model showing the increased mass wasting processes occurring after the deglaciation due to increased seismicity

Figure 68 Conceptual model of suspension settling and deltaic processes. Fluvial sediment is the main origin of the deposit. Some mass flows may occur from land but also within the basins. Some proglacial activity may sporadically occur, such as ice floats and increased terrestrial input from proglacial rivers.

Assuming that the Weischelian ice streams removed all earlier deposit, only sediment deposited during and after the deglaciation of the fjords are present in the fjords (Ottesen et al., 2005; Rydningen et al., 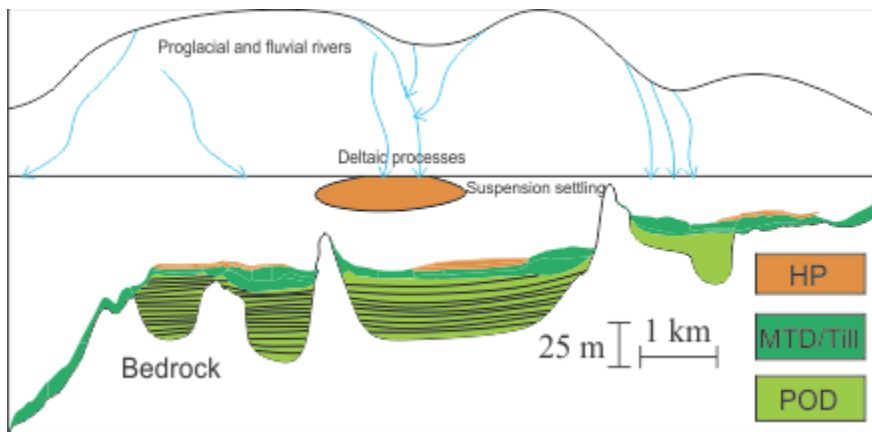2013). F1 presumably deposited during the deglaciation, in a stepwise manner (Figure 66). Hence, the sills are interpreted to mark temporary glacier terminations depositing proximal outwash fans in the basins with a progressively decreasing age closer to the fjord head. The age of the till is progressively younger further in the fjord. The overlying F2 is interpreted to comprise of mass wasted deposits triggered by the increased seismicity in post-glacial times (Figure 67). Subsequently after F2, F3 is inferred to have deposited by suspension settling and prograding deltaic processes originating from fluvial and proglacial rivers (Figure 68).

7 Conclusions

- Low-resolution bathymetric data, high-resolution seismics (chirp) and multi-proxy analyses of three gravity cores from the Bergsfjorden peninsula were analysed and integrated with the purpose of evaluating the sedimentary processes and paleo-environments in the fjords Øksfjorden, Bergsfjorden and Jøkelfjorden.

- The low-resolution bathymetry and chirp data reveal that Øksfjorden and Jøkelfjorden comprise two main basins, whereas Bergsfjorden contains three basins that are separated by sills. The main basins are also divided into sub-basins confined by locally elevated topography.

- Both Bergsfjorden and Øksfjorden show signs of incoming bottom currents. Jøkelfjorden are more restricted from the ocean and the fjord estuarine circulation is therefore inferred to be limited.

- The chirp data reveal three seismostratigraphic facies;
  o F1: Stratified with densely spaced parallel reflectors with an onlapping infill, primarily occurring in depressions/basins. They are interpreted to be deposited in a sedimentary environment with repeated changes of the physical conditions, e.g. in a glacier-proximal environment.
  o F2: Chaotic units with a mounded onlapping geometry, interpreted to be composed of mass-transport deposits or till.
  o F3: Acoustically semi-transparent units draping the underlying sediment. Deposition occurred presumably in a low-energy environment from suspension settling in an open marine environment where sediment input mainly originated from fluvial input, with the presence of IRD.

- The multi-proxy analyses of the sediment cores includes the measurements of physical properties (e.g. wet-bulk density, magnetic susceptibility), lithological descriptions, XRF core scanning and grain-size distribution analyses. The results reveal that the cores mainly contained hemipelagic massive mud with isolated IRD and shells of seismostratigraphic Facies 3. However, coarser intervals representing mass-transport deposits occurred occasionally.

- The core location in Øksfjorden are mainly affected by suspension settling of fluvially derived sediment supply. The same accounts for Jøkelfjorden, except from a great abundance of IRD retrieved from the until recent calving from Øksfjordjøkelen. The core location in Bergsfjorden have closer proximity to the ocean and hence have a higher influence of marine sediment supply.

- The oldest reliable age, 11,090 cal. yrs. BP, derived from Bergsfjorden, suggest that the fjord was deglaciated prior to this time. Furthermore, this date imply that large-scale mass-transport event took place shortly before this time. This mass-transport event could have been triggered by seismicity caused by high rates of isostatic rebound following the deglaciation of the fjords.

- Isolated clasts, inferred to be IRD, were observed throughout the entire core retrieved from Jøkelfjorden, indicating that Øksfjordjøkelen has maintained a reasonable extent after at least 8.7 ka cal. yrs. BP.

- Increasing grain size in Bergsfjorden, changes in geochemistry suggesting increased terrestrial supply to Øksfjorden, as well as a mass-transport activity in Jøkelfjorden occurred around around 8.2 ka cal. yrs. These changes may correlate to an advance of Svartfjelljøkelen (compared with Eeg, 2012), including an advance in the outlet glaciers of Øksfjordjøkelen.

- The lithological record from Bergsfjorden indicates sedimentation in an exclusively open-marine environment between 7.3 and 5.0 ka cal. yrs. BP, suggesting that glacial activity was limited or absent. This supports terrestrial investigations concluding with little or no glacial input into Bergsfjordvatnet between 7.0 and 5.2 ka cal. yrs. BP (Eeg, 2012).

- Relatively steady sedimentary environments are observed after 4.2 ka cal. yrs. BP in Bergsfjorden, 5.1 ka cal. yrs. BP in Øksfjorden and 5.0 ka cal. yrs. BP in Jøkelfjorden. After this, mass flow events and IRD may have caused minor local variations in the sediment supply.

8   Recommendations for future studies

Sediment from what is inferred to contain proglacial outwash deposits in Øksfjorden and Bergsfjorden may reveal the complete deglaciation of the fjord. In order to study this, more gravity cores are needed in the combination with higher resolution bathymetry data and more seismic lines. Data like this may also conclude if the sills are comprised of moraine or mass wasted deposits.

Volume estimations of mass wasted deposits in the fjords should be obtained along with continued age estimates of these. Future studies of unstable rock slopes should be conducted as the history show that the generally resistant rock may fail if utterly triggered. Determinations of the origin of the mass wasted deposit in the past should also be included in a study like this.

Geological mapping is generally important to obtain, e.g. as the composition of the bedrock affects the sedimentation of the fjords, especially when analyzing XRF-data and evaluating if the sediment is of marine or terrestrial origin.

The assumption made that Øksfjordjøkelen withstood the climatic variations that have occurred through the past 8.7 ka cal. yrs. BP need further proof in order to be concluded. Younger end moraines on land are generally easier to date and help in evaluating the fluctuations in glaciers. Hence, it is suggested that the work of Evans et al. (2002) should be continued, obtaining regional sea level curves and dating the moraines crosscutting the shore lines.

I addition, mapping of previously present glacier fields may also help in evaluating the sedimentary processes and environment of the past.

References

Andersen, B. G. (1965). Glacial chronology of western Troms, north Norway. *Geological Society of America Special Papers, 84*, 35-54.

Andersen, B. G. (1968). Glacial geology of western Troms, North Norway. *Norges Geologiske Undersokelse, 256*, 1-160.

Andersen, B. G. (1980). The Deglaciation of Norway after 10,000 Bp. *Boreas, 9*(4), 211-216.

Andersen, B. G., Mangerud, J., Sørensen, R., Reite, A., Sveian, H., Thoresen, M., & Bergstrøm, B. (1995). Younger Dryas ice-marginal deposits in Norway. *Quaternary International, 28*, 147-169.

Andreassen, K. (2015). Marine Geophysics. Lecture notes for GEO-3123, University of Tromsø.

Andreassen, L. M., Elvehøy, H., Kjøllmoen, B., & Engeset, R. V. (2016). Reanalysis of long-term series of glaciological and geodetic mass balance for 10 Norwegian glaciers. *The Cryosphere, 10*(2), 535-552.

Andreassen, L. M., Winsvold, S. H., Paul, F., & Hausberg, J. E. (2012). *Inventory of Norwegian Glaciers* (38-2012). Retrieved from NVE (Norwegian Water Resources and Energy Directorate): http://publikasjoner.nve.no/rapport/2012/rapport2012_38.pdf

Angell, H., (1891), Bang, A., (1891), Munthe, O., (1892), . . . (1902) (Cartographer). (1907). Bergsfjorden [Topographic Quadrangle map]. Retrieved from https://www.kartverket.no/historiske/gradteigtr/jpg300dpi/gradteigtr_s4_1907-1.jpg

Askheim, S. (2016). Øksfjordjøkelen. *Store Norske Leksikon (SNL)*.

Bakke, J., Lie, Ø., Nesje, A., Dahl, S. O., & Paasche, Ø. (2005). Utilizing physical sediment variability in glacier-fed lakes for continuous glacier reconstructions during the Holocene, northern Folgefonna, western Norway. *The Holocene, 15*(2), 161-176.

Ballantyne, C. K. (2002). Paraglacial geomorphology. *Quaternary Science Reviews, 21*(18-19), 1935-2017.

Barber, D. C., Dyke, A., Hillaire-Marcel, C., Jennings, A. E., Andrews, J. T., Kerwin, M. W., . . . Morehead, M. D. (1999). Forcing of the cold event of 8,200 years ago by catastrophic drainage of Laurentide lakes. *Nature, 400*(6742), 344.

Benn, D., & Evans, D. J. (2014). *Glaciers and glaciation*: Routledge.

Blott, S. J., & Pye, K. (2001). GRADISTAT: a grain size distribution and statistics package for the analysis of unconsolidated sediments. *Earth surface processes and Landforms, 26*(11), 1237-1248.

Bondevik, S., SVENDSEN, J. I., & Mangerud, J. (1997). Tsunami sedimentary facies deposited by the Storegga tsunami in shallow marine basins and coastal lakes, western Norway. *Sedimentology, 44*(6), 1115-1131.

Boulton, G. (1990). Sedimentary and sea level changes during glacial cycles and their control on glacimarine facies architecture. *Geological Society, London, Special Publications, 53*(1), 15-52.

Bowman, S. (1990). *Radiocarbon dating* (Vol. 1): Univ of California Press.

Boyle, E. A., & Keigwin, L. (1987). North Atlantic thermohaline circulation during the past 20,000 years linked to high-latitude surface temperature. *Nature, 330*(6143), 35.

Bradley, R. S. (2013). *Paleoclimatology: Reconstructing Climates of the Quaternary*: Elsevier Science.

Bradley, R. S., & Jonest, P. D. (1993). 'Little Ice Age'summer temperature variations: their nature and relevance to recent global warming trends. *The Holocene, 3*(4), 367-376.

Bradwell, T., & Stoker, M. (2016). Glacial sediment and landform record offshore NW Scotland: a fjord–shelf–slope transect through a Late Quaternary mid-latitude ice-stream system. *Geological Society, London, Memoirs, 46*(1), 421-428.

Brown, J. (2016). *Ocean circulation: prepared by an Open University course team*: Elsevier.

Bryhni, I. (2015, 10.27). Paleisk Overflate. Retrieved from https://snl.no/paleisk_overflate

Buhl-Mortensen, L. (2006). *Kartlegging av bunnmiljø og biomangfold i MAREANO*. Retrieved from Havforkningsinstituttet: https://www.hi.no/filarkiv/2006/02/Nr.6_2006_Mareano_mai_juni_2006.pdf/nb-no

Bøe, P. (2011). Geologi og mineralogi på Sørøya i Finnmark. Retrieved from http://www.hasvik.kommune.no/geologi-og-mineralogi-paa-soeroeya-i-finnmark.246319-37123.html

Bøe, R., Longva, O., Lepland, A., Blikra, L. H., Sønstegaard, E., Haflidason, H., . . . Lien, R. (2004). Postglacial mass movements and their causes in fjords and lakes in western Norway. *Norwegian Journal of Geology/Norsk Geologisk Forening, 84*(1).

Bøe, R., Rise, L., Blikra, L. H., Longva, O., & Eide, A. (2003). Holocene mass-movement processes in Trondheimsfjorden, Central Norway. *Norwegian Journal of Geology/Norsk Geologisk Forening, 83*(1).

Chéron, S., Etoubleau, J., Bayon, G., Garziglia, S., & Boissier, A. (2016). Focus on sulfur count rates along marine sediment cores acquired by XRF Core Scanner. *X-Ray Spectrometry, 45*(5), 288-298.

Chroston, P. N., Brooks, M., & Sellevoll, M. A. (1976). A seismic refraction line across the Seiland igneous province, northern Norway. *Nor. Geol. Tidsskr., 56*, 211-216.

Clark, J. A., Farrell, W. E., & Peltier, W. R. (1978). Global Changes in Postglacial Sea Level: A Numerical Calculation 1. *Quaternary Research, 9*(3), 265-287.

Clark, P. U., Archer, D., Pollard, D., Blum, J. D., Rial, J. A., Brovkin, V., . . . Roy, M. (2006). The middle Pleistocene transition: characteristics, mechanisms, and implications for long-term changes in atmospheric pCO2. *Quaternary Science Reviews, 25*(23-24), 3150-3184.

Clark, P. U., Marshall, S. J., Clarke, G. K., Hostetler, S. W., Licciardi, J. M., & Teller, J. T. (2001). Freshwater forcing of abrupt climate change during the last glaciation. *science, 293*(5528), 283-287.

Clark, P. U., Pisias, N. G., Stocker, T. F., & Weaver, A. J. (2002). The role of the thermohaline circulation in abrupt climate change. *Nature, 415*(6874), 863.

Corner, G. D. (1980). Preboreal deglaciation chronology and marine limits of the Lyngen-Storfjord area, Troms, North Norway. *Boreas, 9*(4), 239-249.

Corner, G. D. (2006). A transgressive-regressive model of fjord-valley fill: stratigraphy, facies and depositional controls.

Corner, G. D., Nordahl, E., Munch-Ellingsen, K., & Robertsen, K. (1990). Morphology and Sedimentology of an Emergent Fjord-Head Gilbert-Type Delta: Alta Delta, Norway. *Coarse-grained deltas*, 153-168.

Cottier, F. R., Nilsen, F., Skogseth, R., Tverberg, V., Skarðhamar, J., & Svendsen, H. (2010). Arctic fjords: a review of the oceanographic environment and dominant physical processes. *Geological Society, London, Special Publications, 344*(1), 35-50.

Croudace, I. W., Rindby, A., & Rothwell, R. G. (2006). ITRAX: description and evaluation of a new multi-function X-ray core scanner. *Geological Society, London, Special Publications, 267*(1), 51-63.

Crozier, M. J. (2010). Deciphering the effect of climate change on landslide activity: A review. *Geomorphology, 124*(3-4), 260-267.

Dahl, R., Bergstrøm, B., Blikra, L. H., & Svean, H. (2004). Og landet steg. In R. Dahl & H. Svean (Eds.), *Ka dokker mein førr stein!: geologi, landskap og ressurser i Troms*: Norges geologiske undersøkelse.

Dahl, S. O., & Nesje, A. (1996). A new approach to calculating Holocene winter precipitation by combining glacier equilibrium-line altitudes and pine-tree limits: a case stud from Hardangerjokulen, central southern Norway. *The Holocene, 6*(4), 381-398.

Dahl, T., Hald, I., Forwick, M., & Monsen, K. Laboratory facilities. Retrieved from h[ttps://uit.no/om/enhet/artikkel?p_document_id=380017&p_dimension_id=88137&men=28927](https://uit.no/om/enhet/artikkel?p_document_id=380017&p_dimension_id=88137&men=28927)

Deer, W. A., Howie, R. A., & Zussman, J. (1992). *An introduction to the rock-forming minerals* (Vol. 696): Longman Scientific & Technical Hong Kong.

Dehls, J. F., Olesen, O., Olsen, L., & Blikra, L. H. (2000a). Neotectonic faulting in northern Norway; the Stuoragurra and Nordmannvikdalen postglacial faults. *Quaternary Science Reviews, 19*, 1447-1460.

Dehls, J. F., Olesen, O., Olsen, L., & Blikra, L. H. (2000b). Neotectonic faulting in northern Norway; the Stuoragurra and Nordmannvikdalen postglacial faults. *Quaternary Science Reviews, 19*(14-15), 1447-1460.

Dowdeswell, J. A. (1987). Processes of glacimarine sedimentation. *Progress in Physical Geography, 11*(1), 52-90.

Dowdeswell, J. A., Whittington, R. J., & Marienfeld, P. (1994). The origin of massive diamicton facies by iceberg rafting and scouring, Scoresby Sund, East Greenland. *Sedimentology, 41*(1), 21-35.

EdgeTech. (2015). 3300 Hull Mount Sub-bottom Profiler, User Hardware Manual. *0016732_REV_A*.

EdgeTech. (2016). 3300 Hull Mount Sub-bottom Profiling System. Retrieved from h[ttps://www.edgetech.com/wp-content/uploads/2016/03/3300-brochure-022916.pdf](https://www.edgetech.com/wp-content/uploads/2016/03/3300-brochure-022916.pdf)

Eeg, T. T. (2012). *En rekonstruksjon av variasjoner i breutbredelse gjennom holosen på Svartfjelljøkelen, Bergsfjordhalvøya. En studie basert på proglasiale innsjøsedimenter og kvartærgeologisk kartlegging.* The University of Bergen,

Ellingsen, E. KOKEBOK MSCL 3.0.

Evans, D. J. A., Rea, B. R., Hansom, J. D., & Whalley, W. B. (2002). Geomorphology and style of plateau icefield deglaciation in fjord terrains: the example of Troms-Finnmark, north Norway. *Journal of Quaternary Science, 17*(3), 221-239. doi:10.1002/jqs.675

Fairbanks, R. G. (1989). A 17,000-year glacio-eustatic sea level record: influence of glacial melting rates on the Younger Dryas event and deep-ocean circulation. *Nature, 342*(6250), 637.

Fairbridge, R. W. (1961). Eustatic changes in sea level. *Physics and Chemistry of the Earth, 4*, 99-185.

Farmer, D. M., & Freeland, H. J. (1983). The physical oceanography of fjords. *Progress in oceanography, 12*(2), 147-219.

Fjeldskaar, W., Lindholm, C., Dehls, J. F., & Fjeldskaar, I. (2000). Postglacial uplift, neotectonics and seismicity in Fennoscandia. *Quaternary Science Reviews, 19*, 1413-1422.

Folk, R. L. (1954). The distinction between grain size and mineral composition in sedimentary-rock nomenclature. *The Journal of Geology, 62*(4), 344-359.

Forwick, M. (2013). How to use XRF core scanner data acquired with the Avaatech XRF core scannerat the Department of Geology, University of Tromsø.

Forwick, M., & Rasmussen, T. L. (2012). *CRUISE REPORT on R/V Helmer Hanssen, October 11th-13th & October 13th-16th 2012, about joint educational cruises in the courses GEO-3111 Reconstructing Marine Climate and Environments, GEO-3121 Marine Geology and GEO-3122 Micropaleontology.* Retrieved from Department of Geology, University of Tromsø (UIT), Norway:

Forwick, M., & Vorren, T. O. (2002). Deglaciation history and post-glacial mass movements in Balsfjord, northern Norway. *Polar Research, 21*(2), 259-266.

Forwick, M., & Vorren, T. O. (2010). Stratigraphy and deglaciation of the Isfjorden area, Spitsbergen. *Norwegian Journal of Geology/Norsk Geologisk Forening, 90*(4).

Fossen, H. (2009, 02.14.2009). Isobaser. Retrieved from https://snl.no/isobaser

Fowler, A., & Hennessy, K. (1995). Potential impacts of global warming on the frequency and magnitude of heavy precipitation. *Natural Hazards, 11*(3), 283-303.

Francey, R. J., Trudinger, C. M., Van Der Schoot, M., Law, R. M., Krummel, P. B., Langenfelds, R. L., . . . Andres, R. J. (2013). Atmospheric verification of anthropogenic CO 2 emission trends. *Nature Climate Change, 3*(5), 520.

Friedrich, M., Kromer, B., Spurk, M., Hofmann, J., & Kaiser, K. F. (1999). Paleo-environment and radiocarbon calibration as derived from Lateglacial/Early Holocene tree-ring chronologies. *Quaternary International, 61*(1), 27-39.

Friis-Christensen, E., & Lassen, K. (1991). Length of the solar cycle: an indicator of solar activity closely associated with climate. *science, 254*(5032), 698-700.

Gade, H. G. (1986). Features of fjord and ocean interaction. In *The Nordic Seas* (pp. 183-190): Springer.

Garrison, T. S. (2009). *Oceanography: An Invitation to Marine Science*: Cengage Learning.

Gattuso, J.-P., Hansson, L., Brewer, P. G., Hoegh-Guldberg, O., Kleypas, J. A., Pörtner, H.-O., & Schmidt, D. N. (2011). Ocean acidification: background and history. *In: Climate Change 2014: Impacts, Adaptation, and Vulnerability. Part A: Global and Sectoral Aspects. Contribution of Working Group II to the Fifth Assessment Report of the Intergovernmental Panel on Climate Change*, 129-131.

Gellatly, A. F., Gordon, J. E., Whalley, W. B., & Hansom, J. D. (1988). Thermal regime and geomorphology of plateau ice caps in northern Norway: observations and implications. *Geology, 16*(11), 983-986.

Gentz, T., Bonk, E., Hefter, J., Grotheer, H., Meyer, V., & Mollenhauer, G. (2017). *Establishment of routine sample preparation protocols at the newly installed MICADAS 14C dating facility at AWI.*

GEOTEK. (2014). Geotek Core Logging Systems. Retrieved from http://www.geotek.co.uk/products/magsusc/

GEOTEK. (2017). MSCL-S: Multi-Sensor Core Logger. Retrieved from http://www.geotek.co.uk/wp-content/uploads/2017/06/MSCL-S.pdf

Gilbert, R. (1985). Quaternary glaciomarine sedimentation interpreted from seismic surveys of fiords on Baffin Island, NWT. *Arctic, 38*(4), 271-280.

Goudie, A., Lewin, J., Richards, K., Anderson, M., Burt, T., Whalley, B., & Worsley, P. (2005). *Geomorphological Techniques*. London and New York: Routledge, Taylor & Francis Group.

Grundvåg, S.-A. (2016). GEO-3123 fall 2016 Seismic facies analysis.

Grønlie, O. (1951). On the rise of sea and land and the forming of strandflats on the west coast of Fennoscandia. *Norsk Geologisk Tidsskrift, 29*, 26-63.

Hald, M., Andersson, C., Ebbesen, H., Jansen, E., Klitgaard-Kristensen, D., Risebrobakken, B., . . . Telford, R. J. (2007). Variations in temperature and extent of Atlantic Water in the northern North Atlantic during the Holocene. *Quaternary Science Reviews, 26*(25), 3423-3440.

Hald, M., & Vorren, T. O. (1984). Modern and Holocene foraminifera and sediments on the continental shelf off Troms, North Norway. *Boreas, 13*(2), 133-154.

Halvorsen, R., Andersen, T., Blom, H. H., Elvebakk, A., Elven, R., Erikstad, L., . . . Ødegaard, F. (2009). Naturtyper i Norge – Teoretisk grunnlag, Prinsipper for inndeling og definisjoner. *Naturtyper i Norge, 1*(210.).

Hambrey, M. J. (1994). *Glacial environments*: UBC Press.

Hansen, D. V., & Rattray, M. (1966). New dimensions in estuary classification. *Limnology and Oceanography, 11*(3), 319-326.

Haug, G. H., Sigman, D. M., Tiedemann, R., Pedersen, T. F., & Sarnthein, M. (1999). Onset of permanent stratification in the subarctic Pacific Ocean. *Nature, 401*(6755), 779.

Hermansen, H. O. (2015). Sedimentære avsetningsmiljøer og deglasiasjonshistorie i Ersfjorden, Kvaløya, Troms fylke. M. Sc. Thesis. 157.

Hjelstuen, B. O., Haflidason, H., Sejrup, H. P., & Lyså, A. (2009). Sedimentary processes and depositional environments in glaciated fjord systems—Evidence from Nordfjord, Norway. *Marine Geology, 258*(1-4), 88-99.

Hjulström, F. (1939). Transportation of detritus by moving water: Part 1. Transportation.

Holtedahl, H. (1967). Notes on the formation of fjords and fjord-valleys. *Geografiska Annaler: Series A, Physical Geography, 49*(2-4), 188-203.

Holtedahl, H., & Bjerkli, K. (1975). Pleistocene and recent sediments of the Norwegian continental shelf (62 N-71 N) and the Norwegian Channel area. *Nor. geol. unders, 316*, 241-252.

Hopkins, T. S. (1991). The GIN Sea—A synthesis of its physical oceanography and literature review 1972–1985. *Earth-Science Reviews, 30*(3-4), 175-318.

Howe, J. A., Austin, W. E. N., Forwick, M., Paetzel, M., Harland, R., & Cage, A. G. (2010). Fjord systems and archives: a review. *Geological Society, London, Special Publications, 344*(1), 5-15. doi:10.1144/sp344.2

Hughen, K. A., Southon, J. R., Lehman, S. J., & Overpeck, J. T. (2000). Synchronous radiocarbon and climate shifts during the last deglaciation. *science, 290*(5498), 1951-1954.

IPCC. (2014). *Climate Change 2014: Synthesis Report. Contribution of Working Groups I, II and III to the Fifth Assessment Report of the Intergovernmental Panel on Climate Change*. Retrieved from [Core Writing Team, R.K. Pachauri and L.A. Meyer (eds.)]. IPCC, Geneva, Switzerland:

Jacoby, G. C., & D'Arrigo, R. (1989). Reconstructed Northern Hemisphere annual temperature since 1671 based on high-latitude tree-ring data from North America. *Climatic Change, 14*(1), 39-59.

Jakobsson, M., Ingólfsson, Ó., Long, A. J., & Spielhagen, R. F. (2014). The dynamic Arctic. *Quaternary Science Reviews, 92*, 1-8. doi:10.1016/j.quascirev.2014.03.022

Kartverket (Cartographer). Retrieved from http://www.norgeskart.no/#!?project=seeiendom&layers=1004,1015&zoom=9&lat=7801484.97&lon=764489.44

Kartverket. (2017, 05.19). Arealstatistikk for Norge. Retrieved from https://kartverket.no/kunnskap/fakta-om-norge/Arealstatistikk/Arealstatistikk-Norge/

Kessler, M. A., Anderson, R. S., & Briner, J. P. (2008). Fjord insertion into continental margins driven by topographic steering of ice. *Nature Geoscience, 1*(6), 365.

Kjøllmoen, B., Olsen, H. C., & Svaerd, R. (2000). Langfjordjøkelen i Vest-Finnmark.

Klinck, J. M., O'Brien, J. J., & Svendsen, H. (1981). A simple model of fjord and coastal circulation interaction. *Journal of Physical Oceanography, 11*(12), 1612-1626.

Klitgaard-Kristensen, D., Sejrup, H. P., Haflidason, H., Johnsen, S., & Spurk, M. (1998). A regional 8200 cal. yr BP cooling event in northwest Europe, induced by final stages of the Laurentide ice-sheet deglaciation? *Journal of Quaternary Science, 13*(2), 165-169.

Kottek, M., Grieser, J., Beck, C., Rudolf, B., & Rubel, F. (2006). World map of the Köppen-Geiger climate classification updated. *Meteorologische Zeitschrift, 15*(3), 259-263.

Krauskopf, K. B. (1954). Igneous and metamorphic rocks of the Øksfjord area, west Finnmark. *Norges geologiske Undersøkelse, Arbok, 188*, 29-50.

Kucera, M. (2007). Chapter six planktonic foraminifera as tracers of past oceanic environments. *Developments in marine geology, 1*, 213-262.

Kylander, M. E., Ampel, L., Wohlfarth, B., & Veres, D. (2011). High-resolution X-ray fluorescence core scanning analysis of Les Echets (France) sedimentary sequence: new insights from chemical proxies. *Journal of Quaternary Science, 26*(1), 109-117.

Lund, B., Näslund, J.-O., Connor, C., Chapman, N., & Connor, L. (2009). Glacial isostatic adjustment: implications for glacially induced faulting and nuclear waste repositories. *Volcanic and tectonic hazard assessment for nuclear facilities*, 142-155.

Mackiewicz, N. E., Powell, R. D., Carlson, P. R., & Molnia, B. F. (1984). Interlaminated ice-proximal glacimarine sediments in Muir Inlet, Alaska. *Marine Geology, 57*(1-4), 113-147.

Mangerud, J. (1972). Radiocarbon dating of marine shells, including a discussion of apparent age of recent shells from Norway. *Boreas, 1*(2), 143-172.

Mangerud, J., Bondevik, S., Gulliksen, S., Hufthammer, A. K., & Høisæter, T. (2006). Marine 14C reservoir ages for 19th century whales and molluscs from the North Atlantic. *Quaternary Science Reviews, 25*(23-24), 3228-3245.

Mareano. (2006a). Kornstørrelses fordeling. Retrieved from http://www.mareano.no/kart/mareano.html#maps/3328

Mareano. (2006b). Marint landskap. Retrieved from http://www.mareano.no/kart/viewer/#maps/3314

Mareano. (2018). Regionale landformer. Retrieved from http://www.mareano.no/kart/mareano.html#maps/3327

Marthinussen, M. (1960). Coast and fjord area of Finnmark. In *Geology of Norway* (Vol. 208, pp. 416-429): Norges Geologiske Undersökelse.

Marthinussen, M. (1962). C14-datings referring to shore lines, transgressions, and glacial substages in northern Norway. *Nor. geol. unders, 215*, 37-67.

Monroe, J. S., & Wicander, R. (2011). *The changing earth: exploring geology and evolution*: Cengage Learning.

The Munsell Soil Colour Charts. (1995). In *Macbeth. Kollmorgen Instruments Corp. New York*.

Nadeau, M.-J., Vaernes, E., Svarva, H. L., Larsen, E., Gulliksen, S., Klein, M., & Mous, D. J. (2015). Status of the "new" AMS facility in Trondheim. *Nuclear Instruments and Methods in Physics Research Section B: Beam Interactions with Materials and Atoms, 361*, 149-155.

Nesje, A. (2017, 05.28). Bre Erosjon. Retrieved from https://snl.no/bre-erosjon

Nesje, A., Bakke, J., Dahl, S. O., Lie, Ø., & Matthews, J. A. (2008). Norwegian mountain glaciers in the past, present and future. *Global and Planetary Change, 60*(1-2), 10-27.

Nesje, A., & Whillans, I. M. (1994). Erosion of Sognefjord, Norway. *Geomorphology, 9*(1), 33-45.

NGI (Cartographer). (2017). Bratte områder Norge. Retrieved from https://geodata.ngi.no/arcgisportal/apps/webappviewer/index.html?id=fd597e0179fe479b9274d95a90b00931

NGRIP, Andersen, K. K., Azuma, N., Barnola, J.-M., Bigler, M., Biscaye, P., . . . Fischer, H. (2004). North Greenland Ice Core Project. High-resolution record of Northern Hemisphere climate extending into the last interglacial period. *Nature, 431*(7005), 147.

NGU (Cartographer). (2011). Nasjonal berggrunnsdatabase [Bedrock map]. Retrieved from http://geo.ngu.no/kart/berggrunn/?lang=Norsk&Box=712066:7760532:831362:7844155&map=Berggrunn%2EN250%2Emed%2Elineamenter%2Eog%2Efjellskygge

NGU. (2017, 12.05). Presentasjonsregler: Bunnsedimenter (Kornstørrelse), Detaljert. Retrieved from http://www.ngu.no/upload/Kartkatalog/Presentasjonsregler_Marin_SedimentKornstorrelseDet.pdf

NGU. (2018a). Løsmasser og skredhendelser. Retrieved from http://geo.ngu.no/kart/losmasse/?lang=Norsk&Box=729638:7776225:805407:7828650&map=L%2Esmasser:%2EL%2Esmassekart%2Emed%2Esymboler

NGU. (2018b). Tjørnatinden, Dusnjarga, Vassnestind, Koppartind og Låvan Under Kartlegging. Retrieved from http://geo.ngu.no/kart/ustabilefjellparti/

NGU. (2018c). Undersøkte ustabile fjellparti. Retrieved from http://geo.ngu.no/kart/ustabilefjellparti/?lang=Norsk&Box=508403:7587165:1011468:7939800&map=Ustabile%2Efjellparti%2E%2E%2Eunders%2Ekt%2Eomr%2Ede

Nichols, G. (2009). *Sedimentology and stratigraphy*: John Wiley & Sons.

NVE (Cartographer). (2006). Breatlas. Landsat. Breregion ID 2 [Glacier Area map]. Retrieved from https://temakart.nve.no/link/?link=breatlas

NVE. (2018a). Klimaprodukter bre Langfjordjøkelenen 54. Retrieved from http://glacier.nve.no/viewer/CI/no/nve/ClimateIndicatorInfo/54

NVE. (2018b). Nedbørsfelt. Retrieved from https://temakart.nve.no/link/?link=nedborfelt

OECD. (2001). Environmental Performance Reviews Norway.

OECD. (2011). Environmental Performance Reviews: Norway 2011.

Olsen, J. A. (2015). Sedimentære avsetningsmiljøer og deglasiasjonshistorie i Ersfjorden, Kvaløya, Troms fylke. M.Sc. Thesis. 162.

Orsi, T. H., Edwards, C. M., & Anderson, A. L. (1994). X-ray computed tomography: a nondestructive method for quantitative analysis of sediment cores. *Journal of Sedimentary Research, 64*(3).

Ottesen, D., Dowdeswell, J., & Rise, L. (2005). Submarine landforms and the reconstruction of fast-flowing ice streams within a large Quaternary ice sheet: the 2500-km-long Norwegian-Svalbard margin (57–80 N). *Geological Society of America Bulletin, 117*(7-8), 1033-1050.

Overpeck, J., Hughen, K., Hardy, D., Bradley, R., Case, R., Douglas, M., . . . Jennings, A. (1997). Arctic environmental change of the last four centuries. *science, 278*(5341), 1251-1256.

Pharaoh, T., MacIntyre, R., & Ramsay, D. (1982). K-Ar age determinations on the Raipas suite in the Komagfjord Window, Northern Norway. *Norsk Geologisk Tidsskrift, 62*(1), 51-57.

Porter, S. C. (1989). Some geological implications of average Quaternary glacial conditions. *Quaternary Research, 32*(3), 245-261.

Powell, R. D., & Cooper, J. M. (2002). A glacial sequence stratigraphic model for temperate, glaciated continental shelves. *Geological Society, London, Special Publications, 203*(1), 215-244.

Ravelo, A. C., Andreasen, D. H., Lyle, M., Lyle, A. O., & Wara, M. W. (2004). Regional climate shifts caused by gradual global cooling in the Pliocene epoch. *Nature, 429*(6989), 263.

Raymo, M. (1992). Global climate change: a three million year perspective. In *Start of a Glacial* (pp. 207-223): Springer.

Raymo, M. (1994). The initiation of Northern Hemisphere glaciation. *Annual Review of Earth and Planetary Sciences, 22*(1), 353-383.

Rea, B. R., & Brian Whalley, W. (1994). Subglacial observations from Øksfjordjøkelen, north Norway. *Earth surface processes and Landforms, 19*(7), 659-673.

Rea, B. R., & Evans, D. J. A. (2007). Quantifying climate and glacier mass balance in north Norway during the Younger Dryas. *Palaeogeography, Palaeoclimatology, Palaeoecology, 246*(2-4), 307-330. doi:10.1016/j.palaeo.2006.10.010

Rea, B. R., Whalley, W. B., Rainey, M. M., & Gordon, J. E. (1996). Blockfields, old or new? Evidence and implications from some plateaus in northern Norway. *Geomorphology, 15*(2), 109-121.

Reading, H. G., & Richards, M. (1994). Turbidite systems in deep-water basin margins classified by grain size and feeder system. *AAPG bulletin, 78*(5), 792-822.

Reimer, P. J., Bard, E., Bayliss, A., Beck, J. W., Blackwell, P. G., Ramsey, C. B., . . . Friedrich, M. (2013). IntCal13 and Marine13 radiocarbon age calibration curves 0–50,000 years cal BP. *Radiocarbon, 55*(4), 1869-1887.

Richter, T. O., Van der Gaast, S., Koster, B., Vaars, A., Gieles, R., de Stigter, H. C., . . . van Weering, T. C. (2006). The Avaatech XRF Core Scanner: technical description and applications to NE Atlantic sediments. *Geological Society, London, Special Publications, 267*(1), 39-50.

Roberts, D. (Cartographer). (1973). Atlas73 1:250 000 [Bedrock]. Retrieved from http://www.ngu.no/upload/Publikasjoner/Kart/B250/Hammerfest.pdf

Roberts, R. J., Corfu, F., Torsvik, T. H., Ashwal, L. D., & Ramsay, D. M. (2006). Short-lived mafic magmatism at 560–570 Ma in the northern Norwegian Caledonides: U–Pb zircon ages from the Seiland Igneous Province. *Geological Magazine, 143*(06), 887-903. doi:10.1017/s0016756806002512

Robins, B., & Gardner, P. (1975). The magmatic evolution of the Seiland Province, and Caledonian plate boundaries in northern Norway. *Earth and Planetary Science Letters, 26*(2), 167-178.

Rossby, T. (1996). The North Atlantic Current and surrounding waters: At the crossroads. *Reviews of Geophysics, 34*(4), 463-481.

Ruddiman, W. F. (2007). *Earth's Climate: Past and Future*: W. H. Freeman.

Rydningen, T. A., Vorren, T. O., Laberg, J. S., & Kolstad, V. (2013). The marine-based NW Fennoscandian ice sheet: glacial and deglacial dynamics as reconstructed from submarine landforms. *Quaternary Science Reviews, 68*, 126-141.

Sandersen, F., & Domaas, U. (2014). *Utarbeidelse av detaljerte faresonekart Loppa Kommune*. Retrieved from http://webfileservice.nve.no/API/PublishedFiles/Download/201301392/1691277

seNorge (Cartographer). (2018). Klima [Climate maps]. Retrieved from http://www.senorge.no/index.html?p=klima

Shuster, D. L., Ehlers, T. A., Rusmoren, M. E., & Farley, K. A. (2005). Rapid glacial erosion at 1.8 Ma revealed by 4He/3He thermochronometry. *science, 310*(5754), 1668-1670.

Skei, J. (1983). Why sedimentologists are interested in fjords. *Sedimentary geology, 36*(2-4), 75-80.

Sollid, J., Andersen, S., Hamre, N., Kjeldsen, O., Salvigsen, O., Sturød, S., . . . Wilhelmsen, A. (1973). Deglaciation of Finnmark, North Norway. *Norsk geografisk tidsskrift-Norwegian Journal of Geography, 27*(4), 233-325.

St-Onge, G., Mulder, T., Francus, P., & Long, B. (2007). Chapter two continuous physical properties of cored marine sediments. *Developments in marine geology, 1*, 63-98.

Stephens, M. B., Furnes, H., Robins, B., & Sturt, B. A. (1985). Igneous activity within the Scandinavian Caledonides. *The Caledonide orogen—Scandinavia and related areas, 2*, 641-643.

Stewart, I. S., Sauber, J., & Rose, J. (2000). Glacio-seismotectonics: ice sheets, crustal deformation and seismicity. *Quaternary Science Reviews, 19*(14-15), 1367-1389.

Stoker, M. S., Pheasant, J. B., & Josenhans, H. (1997). Seismic methods and interpretation. In *Glaciated Continental Margins* (pp. 9-26): Springer.

Stokes, C. R., Corner, G. D., Winsborrow, M. C., Husum, K., & Andreassen, K. (2014). Asynchronous response of marine-terminating outlet glaciers during deglaciation of the Fennoscandian Ice Sheet. *Geology, 42*(5), 455-458.

Stuiver, M., & Polach, H. A. (1977). Discussion reporting of 14 C data. *Radiocarbon, 19*(3), 355-363.

Stuiver, M., & Reimer, P. (2018). CALIB Manual - Chapter 1, Rev 5.0.

Stuiver, M., Reimer, P. J., & Reimer, R. W. (2018). CALIB 7.1 [WWW program]. Retrieved from http://calib.org

Sturt, B. A., Pringle, I. R., & Roberts, D. (1975). Caledonian nappe sequence of Finnmark, northern Norway, and the timing of orogenic deformation and metamorphism. *Geological Society of America Bulletin; 2012, 86*(5), 710-718.

Syvitski, J. P. M. (1989). On the deposition of sediment within glacier-influenced fjords: oceanographic controls. *Marine Geology, 85*(2-4), 301-329.

Syvitski, J. P. M., Burrell, D. C., & Skei, J. M. (1987). *Fjords: processes and products*: Springer-Verlag.

Syvitski, J. P. M., & Shaw, J. (1995). Sedimentology and geomorphology of fjords. In *Developments in sedimentology* (Vol. 53, pp. 113-178): Elsevier.

Sælen, O. H. (2016). Fjord: vannforhold.

Sætre, R., & Ljøen, R. (1972). The Norwegian coastal current.

Talley, L. D. (2011). *Descriptive physical oceanography: an introduction*: Academic press.

Tanaka, A., Nakano, T., & Ikehara, K. (2011). X-ray computerized tomography analysis and density estimation using a sediment core from the Challenger Mound area in the Porcupine Seabight, off Western Ireland. *Earth, planets and space, 63*(2), 103-110.

Teller, J. T. (2013). Lake Agassiz during the Younger Dryas. *Quaternary Research, 80*(3), 361-369.

Tjallingii, R., Röhl, U., Kölling, M., & Bickert, T. (2007). Influence of the water content on X-ray fluorescence core-scanning measurements in soft marine sediments. *Geochemistry, Geophysics, Geosystems, 8*(2).

Tomas, C., Seibold, E., Berger, W., Weber, M. E., Niessen, F., Kuhn, G., & Wiedicke, M. (1997). Calibration and application of marine sedimentary physical properties using a multi-sensor core logger. *Marine Geology, 136*(3-4), 151-172.

Udden, J. A. (1914). Mechanical composition of clastic sediments. *Bulletin of the Geological Society of America, 25*(1), 655-744.

Vasskog, K., Nesje, A., Støren, E. N., Waldmann, N., Chapron, E., & Ariztegui, D. (2011). A Holocene record of snow-avalanche and flood activity reconstructed from a lacustrine sedimentary sequence in Oldevatnet, western Norway. *The Holocene, 21*(4), 597-614.

Vorren, T. O., Mangerud, J., Blikra, L. H., Nesje, A., & Sveian, H. (2007). *Landet blir til: Norges geologi*: Norsk geologisk forening.

Vorren, T. O., & Plassen, L. (2002). Deglaciation and palaeoclimate of the Andfjord-Vågsfjord area, North Norway. *Boreas, 31*(2), 97-125.

Walcott, R. (1972). Past sea levels, eustasy and deformation of the earth. *Quaternary Research, 2*(1), 1-14.

Wassmann, P., Svendsen, H., Keck, A., & Reigstad, M. (1996). Selected aspects of the physical oceanography and particle fluxes in fjords of northern Norway. *Journal of Marine Systems, 8*(1-2), 53-71.

Wentworth, C. K. (1922). A scale of grade and class terms for clastic sediments. *The Journal of Geology, 30*(5), 377-392.

Whalley, W. B., Gordon, J. E., & Gellatly, A. F. (1989). Effects of topographic and climatic controls on 19th and 20th century glacier changes in the Lyngen and Bergsfjord areas, North Norway. 153-172.

Whalley, W. B., & Parkinson, A. F. (2016). Visitors to 'the northern playgrounds': tourists and exploratory science in north Norway. *Geological Society, London, Special Publications, 417*(1), 83-93.

Whalley, W. B., Rea, B. R., & Rainey, M. M. (2004). Weathering, blockfields, and fracture systems and the implications for long-term landscape formation: some evidence from Lyngen and Øksfordjøkelen areas in north Norway. *Polar Geography, 28*(2), 93-119. doi:10.1080/789610120

Whalley, W. B., Rea, B. R., Rainey, M. M., & McAlister, J. J. (1997). Rock weathering in blockfields: some preliminary data from mountain plateaus in North Norway. *Geological Society, London, Special Publications, 120*(1), 133-145.

Winsborrow, M. C., Andreassen, K., Corner, G. D., & Laberg, J. S. (2010). Deglaciation of a marine-based ice sheet: Late Weichselian palaeo-ice dynamics and retreat in the southern Barents Sea reconstructed from onshore and offshore glacial geomorphology. *Quaternary Science Reviews, 29*(3-4), 424-442.

Winsvold, S. H. (2017). Mapping glaciers using time-series of remote sensing data.

Winsvold, S. H., & Andreassen, L. M. (2015). Breendringer i hele Norge. *KLIMA - Et magasin om klimaforskning fra CICERO*.

Yr. (2018). Klimastatistikk for Norge. Retrieved from https://www.yr.no/sted/Norge/klima.html

Zachos, J., Pagani, M., Sloan, L., Thomas, E., & Billups, K. (2001). Trends, Rhythms, and Aberrations in Global Climate 65 Ma to Present. *science, 292*(5517), 686-693. doi:10.1126/science.1059412

Østrem, G., & Haakensen, N. (1993). Glaciers of Norway.

Østrem, G., Haakensen, N., & Melander, O. (1973). Glacier atlas of northern Scandinavia. *22*.

Appendix A

Results from the radiocarbon dating from both NTNU and AWI may be seen in Table 1 and Table 2, respectively. Calibrations using CALIB 7.1 (Stuiver et al., 2018) and a ΔR of 71 +/- 21 (Mangerud et al., 2006) are presented below.

Table 1 Radio carbon dating conducted by Marie-Josée Nadeau, Martin Seiler and the rest of the staff at the NTNU University Museum, The National Laboratory for Age Determination.
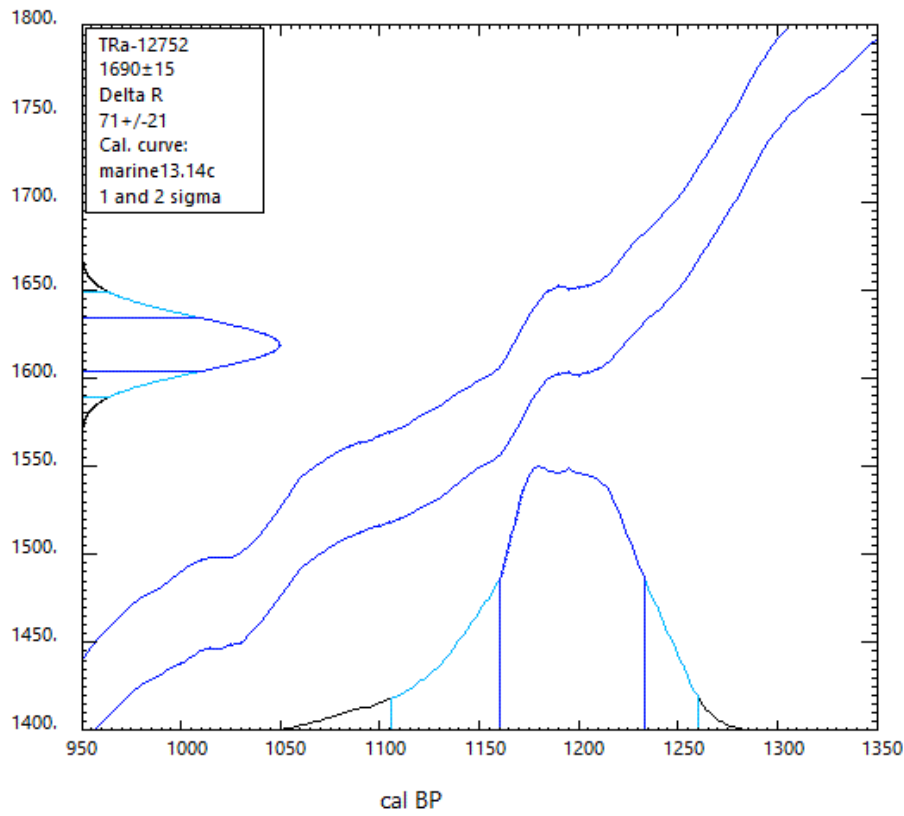
NTNU nr.	Sample Name	Fraction	% C	^{14}C content (pMC)	^{14}C Age (rounded)	δ^{13}C (from AMS system)
TRa-12752	HH12-1185GC 1W Thyasia sp., 61cm	Shell. Intet materiale igjen. H-container.,CaCO3	7.0	81.01 ± 0.16	1690 ± 15	-8.1 ± 0.2 ‰
TRa-12753	HH12-1185GC 4W Yoldia hyperborea, 350 cm	Shell.,CaCO3	8.0	47.07 ± 0.11	6055 ± 20	-0.2 ± 0.6 ‰
TRa-12754	HH12-1188GC 2W Yoldia hyperborea, 163 cm	Skjell.,CaCO3	9.0	45.12 ± 0.11	6395 ± 20	-2.2 ± 0.6 ‰
TRa-12755	HH12-1188GC 2W Yoldiella (lucida), 175 cm	Shell. Intet materiale igjen.,CaCO3	3.0	42.44 ± 0.12	6885 ± 25	-3.0 ± 0.4 ‰
TRa-12756	HH12-1188GC 3W Nuculana pernula, 260 cm	Skjell.,CaCO3	8.0	31.87 ± 0.09	9185 ± 25	-1.8 ± 0.4 ‰
TRa-12757	HH12-1188GC 4W Gastropo Lacunidae Lacuna sp., 356 cm	Skjell.,CaCO3	9.0	28.31 ± 0.08	10135 ± 25	-2.0 ± 0.2 ‰
TRa-12758	HH12-1193GC 1W Gastropo Lacunidae Gibbula cineraria, 75 cm	Skjell.,CaCO3	8.0	56.87 ± 0.15	4535 ± 20	1.6 ± 0.5 ‰
TRa-12759	HH12-1193GC 3A Astarte sulcata, 211 cm	Skjell.,CaCO3	8.0	42.61 ± 0.10	6850 ± 20	-0.2 ± 0.7 ‰
TRa-12760	HH12-1193GC 3AW Astarte sp., Yoldiella lenticular, Yoldiella sp., 288 cm	Shell. Intet materiale igjen.,CaCO3	8.0	35.51 ± 0.09	8315 ± 20	-0.6 ± 0.4 ‰

Table 2 Radio carbon dates obtained by the staff at the AMS dating facility at the Alfered Wegener Institute (AWI), Torben Gentz and Gesine Mollenhauer.
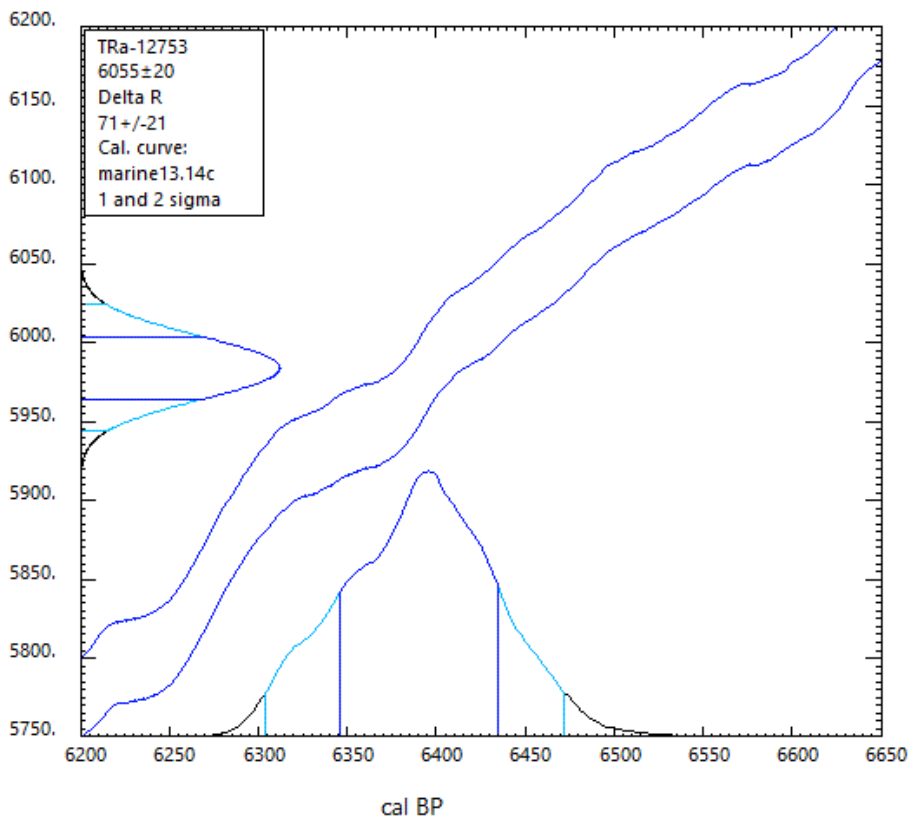
AWI nr.	Sample label	Species	^{14}C counts	^{12}C (µA)	^{14}C/^{12}C (10^{-12})	+-(%)	Age (y)	+-(y)	Magazine label	Date/Time
1538.1.1	HH12-1193-GC_#3_254cm	Yoldiella lenticula	233 158	20.0	0.3999	0.21	**8 554**	60	180323TG_FOR	23.03.2018 17:30:28 CET
1539.1.1	HH12-1193-GC_#5_458cm	Yoldiella lenticula	136 830	15.5	0.3243	0.27	**10 209**	68	180323TG_FOR	23.03.2018 18:17:53 CET
1540.1.1	HH12-1193-GC_#51_408cm	Triloculina tricarinata	8 379	7.2	0.2813	1.09	**10 922**	129	180125HG_CHS	25.01.2018 15:54:40 CET

Radiocarbon Age vs. Calibrated Age

TRa-12752
1690±15
Delta R
71+/-21
Cal. curve:
marine13.14c
1 and 2 sigma

cal BP

Radiocarbon Age vs. Calibrated Age

TRa-12753
6055±20
Delta R
71+/-21
Cal. curve:
marine13.14c
1 and 2 sigma

cal BP

Radiocarbon Age vs. Calibrated Age

TRa-12754
6395±20
Delta R
71+/-21
Cal. curve:
marine13.14c
1 and 2 sigma

cal BP

Radiocarbon Age vs. Calibrated Age

TRa-12755
6885±25
Delta R
71+/-21
Cal. curve:
marine13.14c
1 and 2 sigma

cal BP

Radiocarbon Age vs. Calibrated Age

TRa-12756
9185±25
Delta R
71+/-21
Cal. curve:
marine13.14c
1 and 2 sigma

cal BP

Radiocarbon Age vs. Calibrated Age

TRa-12757
10135±25
Delta R
71+/-21
Cal. curve:
marine13.14c
1 and 2 sigma

cal BP

Radiocarbon Age vs. Calibrated Age

TRa-12758
4535±20
Delta R
71+/-21
Cal. curve:
marine13.14c
1 and 2 sigma

cal BP

Radiocarbon Age vs. Calibrated Age

TRa-12759
6850±20
Delta R
71+/-21
Cal. curve:
marine13.14c
1 and 2 sigma

cal BP

Radiocarbon Age vs. Calibrated Age

TRa-12760
8315±20
Delta R
71+/-21
Cal. curve:
marine13.14c
1 and 2 sigma

cal BP

Radiocarbon Age vs. Calibrated Age

1538.1.1
8554±60
Delta R
71+/-21
Cal. curve:
marine13.14c
1 and 2 sigma

cal BP

Radiocarbon Age vs. Calibrated Age

1539.1.1
10209±68
Delta R
71+/-21
Cal. curve:
marine13.14c
1 and 2 sigma

cal BP

Radiocarbon Age vs. Calibrated Age

1540.1.1
10922±129
Delta R
71+/-21
Cal. curve:
marine13.14c
1 and 2 sigma

cal BP
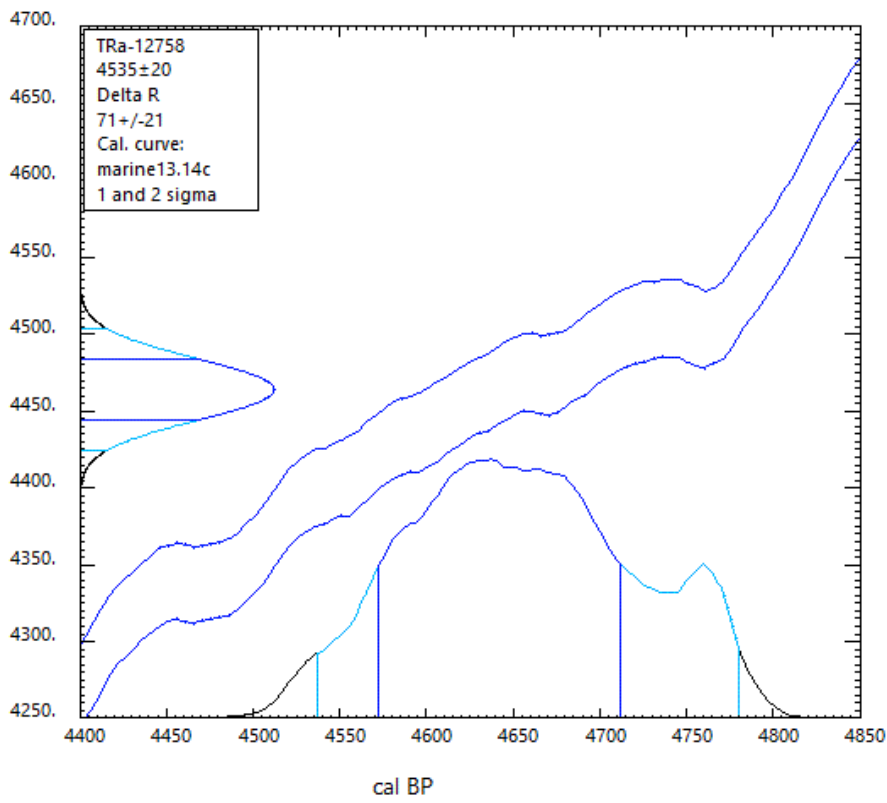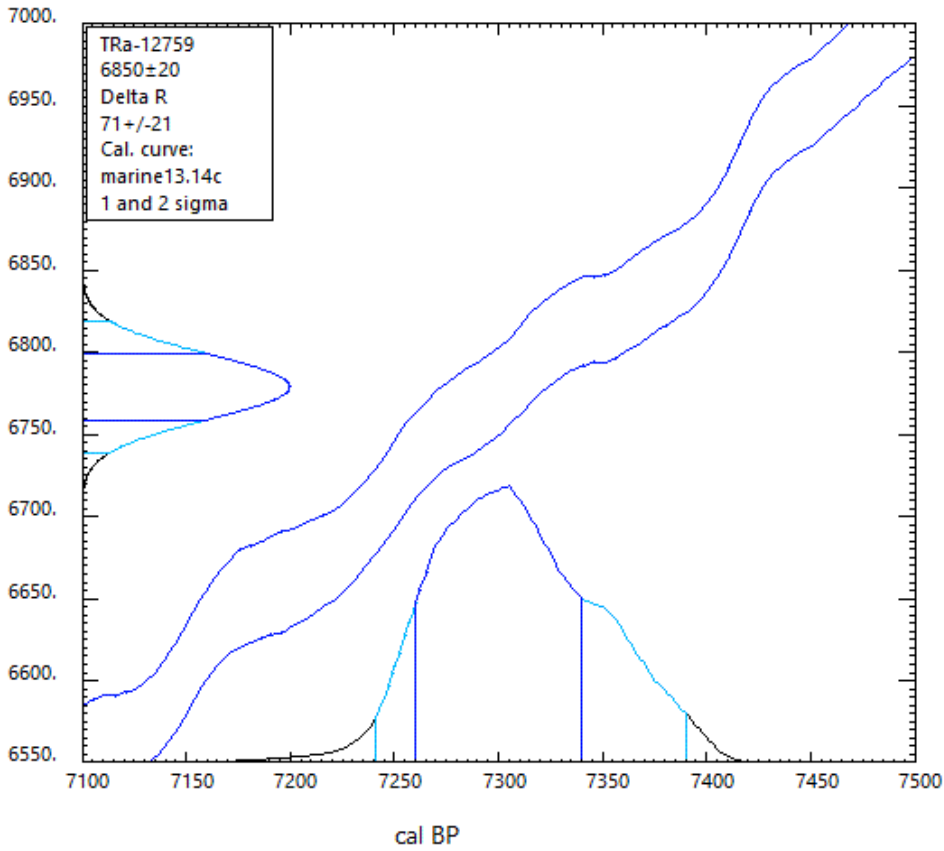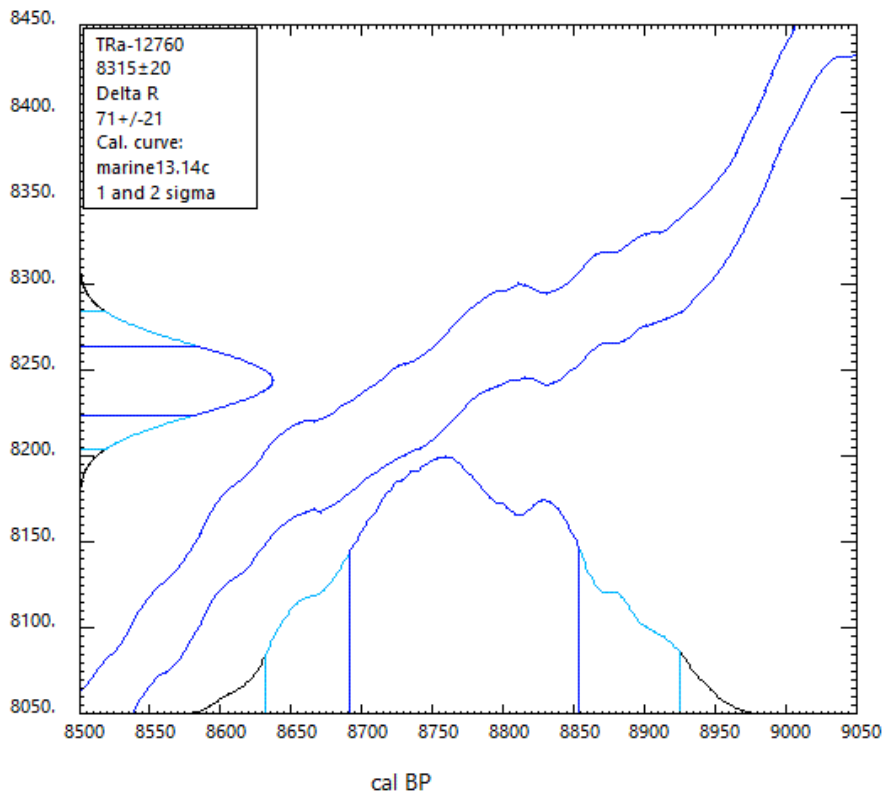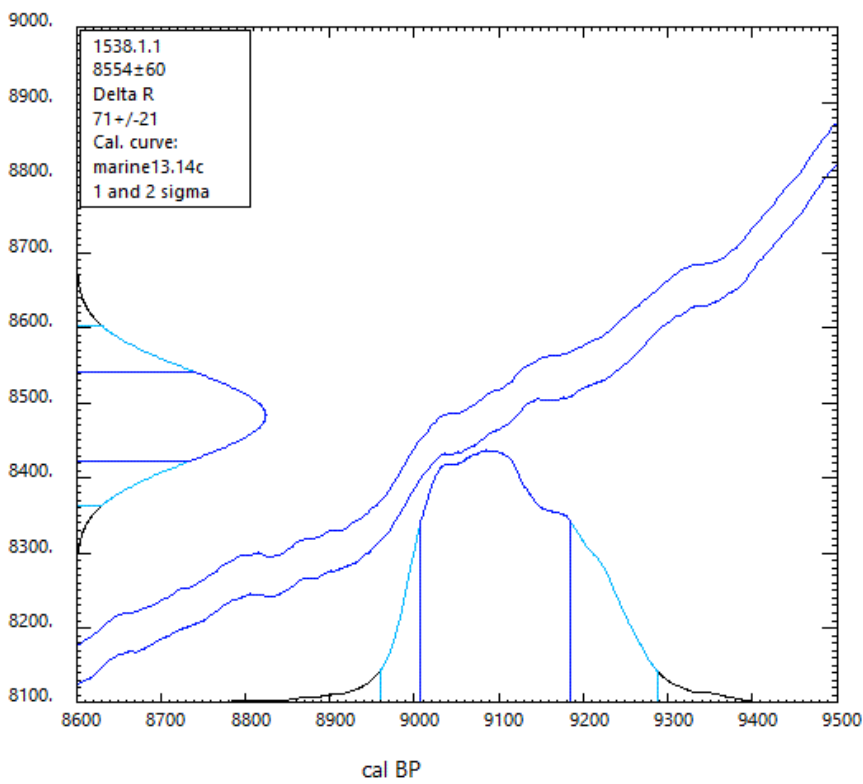
Mangerud, J., Bondevik, S., Gulliksen, S., Hufthammer, A. K., & Høisæter, T. (2006). Marine 14C reservoir ages for 19th century whales and molluscs from the North Atlantic. *Quaternary Science Reviews, 25*(23-24), 3228-3245.

Stuiver, M., Reimer, P. J., & Reimer, R. W. (2018). CALIB 7.1 [WWW program]. Retrieved from http://calib.org